Experiments on Separation Shear Layer Instabilities in Hypervelocity Flows

Thesis by
Wesley Minlai Yu

In Partial Fulfillment of the Requirements for the
Degree of
Doctor of Philosophy

CALIFORNIA INSTITUTE OF TECHNOLOGY
Pasadena, California

2024
Defended May 8, 2024

Wesley Minlai Yu
ORCID: 0000-0002-1133-3199

ACKNOWLEDGEMENTS

My work would have been impossible without the three professors in the Caltech Hypersonics Group. I would first like to thank my advisor, Professor Joanna Austin, for welcoming me into her group and for her invaluable guidance and support throughout my time as a student. Working in her lab has been an absolute privilege and I have learned so much from her over the years. Most importantly, she fosters an excellent lab culture and always makes sure to prioritize her students' well-being. I will be forever grateful to her for going above and beyond as an advisor and making my many years as a graduate student so enjoyable. Next, I need to extend my thanks to Professor Joe Shepherd. He has been an amazing source of guidance over the years, and always gives insightful advice on everything from practical lab experience to complex fluid mechanics problems or why my optics refuse to behave how I expected. I feel lucky to have him around to steer me in the right direction. Finally, I must express my gratitude to Professor Hans Hornung. He is one of the most amazing scientists and teachers I have ever met, with a huge breadth of knowledge and an incredible physical intuition for complex phenomena in the hypersonics field. His office door is always open, and even when faced with some basic questions, he is patient and takes the time to explain without making us feel embarrassed, while taking great interest in our research and hobbies.

Thanks also goes to Professor Guillaume Blanquart, firstly, for being on my candidacy and thesis committees, and, secondly, for letting us join his group presentation lunches. It was great fun being able to learn about everyone else's research and also present at these meetings. He always asks inquisitive questions that inspire critical thinking and gives helpful suggestions, all while never failing to liven up a room with his quick wit and humor.

Next I have to acknowledge my current labmates in the Caltech Hypersonics Group: Ying Luo, Michael Stramenga, Alex Acosta, Jorge Rodríguez Gutiérrez, and William Feasey. They have been exceptional colleagues and even better friends! To the past members of the group: Matt Leibowitz, Nelson Yanes, Joel Lawson, Galina Shpuntova, Mallory Neet, and Ilan Grossman, thank you for making me feel at home from day one, and teaching me so much over the years. I am so fortunate to have had student mentors like them to guide me through the early years of my PhD. Additionally, I need to thank the past and present members of the Explosion Dynamics Laboratory: Jean-Christophe Veilleux, Silken Jones, Conor Martin, Charline Fouchier,

Donner Schoeffler, and Branson Davis. Our close and shared lab spaces let us interact frequently, and being able to bounce ideas off one another and have quick discussions greatly benefited me as an scientist. Finally, I have to give a shout out to my first-year cohort and colleagues from all across campus. Running the GALCIT masters gauntlet with my now lifelong friends made the late night homework sessions somewhat bearable and always fun!

I would also like to acknowledge our collaborators from the Thermofluids, Energy, and Propulsion Systems Laboratory at Stanford University: Professor Ronald Hanson, Christopher Strand, Julian Girard, Peter Finch, and Tal Schwartz. We had the opportunity to work together over six experimental campaigns spanning four years. They brought their expertise in absorption spectroscopy to our facilities and I had an absolute blast working with and learning from them.

Special thanks goes to Bahram Valiferdowsi and Noel Esparza-Duran, the research engineers who make it possible to run the absolute beast that is T5. Bahram welcomed me with a warm smile and loud laughter from my first day, and always took the time to explain every little detail about T5. When Noel took over three years ago, he impressively picked everything up at a blistering pace and research continued without a hitch. I have learned a lot from the both of them, and am grateful for the many hours they spent to make sure my research went smoothly. I also need to thank the GALCIT machinists: Ali Kiani and Brandon Nilles. Their wide expertise in all kinds of fabrication techniques was an invaluable resource to have.

We are fortunate to have such a capable administrator, Liza Bradulina, managing all of our lab logistics and day-to-day operations. Without her, none of what we do would be possible. I also want to thank the rest of the GALCIT and MCE administrative staff who have helped facilitate my research and other department activities: Christine Ramirez, Jamie Meighen-Sei, Barbara Slater, and Kristen Bazua.

Beyond the realm of GALCIT, the Caltech Chamber Music Program has been a vital part of my time here. I need to thank Martin and Nancy Chalifour, Maia Jasper-White, Robert Ward, Glenn Price, Cindy De Mesa, and the countless student musicians on campus for making all of it possible.

To all my friends from El Paso and Austin, thank you for staying in touch. I have not been back home as much as I should, and those who have visited me here in Pasadena bring a bit of home to me every time. I always enjoy reminiscing on our

high school and college years, and getting to see you and where you are today always puts a smile on my face.

To Kiva, my partner and best friend, thank you for always being there for me. You have made me a better person, filled my life with laughter, and kept my toughest moments bearable. The distance between us has been difficult, and I have missed you dearly all these years we have lived apart. I count the days until the next chapter of our lives, and I am so excited to start our new adventure together.

Finally, to my Mom and Dad, thank you for loving me, for supporting me in all my endeavors, and letting me explore anything my curiosity desired (no matter how far-fetched). From teaching me algebra, to showing me all the tiny organisms in a drop of pond water under a microscope, to watching Star Trek with me after dinner, you shared your passions with me and opened my eyes to the beautiful world of scientific discovery. Most importantly, you instilled in me to do the things I love and encouraged me on the days when those things became difficult. All of my accomplishments today are a direct result of the opportunities that you gave me growing up, and for that I am eternally grateful.

This work was partially supported by the Air Force Office of Scientific Research (AFOSR) awards FA9550-19-1-0219 and FA9550-21-1-0080 with Drs. Ivett Leyva and Sarah Popkin as program officers, and FA9550-23-1-0446 with Dr. Michael Berman as program officer.

ABSTRACT

Shock–boundary layer interactions (SBLI) are complex fluid dynamic phenomena that occur when shocks are generated near corners and irregular geometries on vehicles flying near or above supersonic speeds, causing external flow distortion and possible boundary layer separation. Accurate prediction of the mean and unsteady SBLI surface interaction is imperative to avoid failure from highly localized aerodynamic and heating loads, and loss of authority near a control surface. For hypersonic flight-enthalpy matched conditions, current SBLI simulations tend to under-predict thermal loads and have significant disagreements with ground-based experiments in separation location, and location and magnitude of peak heating. These discrepancies are potentially largely due to uncertainties in the modeling and recreation of the coupled real-gas (thermochemical) molecular and gas dynamic processes. To address this issue, efforts have been placed on developing and validating thermochemical gas models, which presents a need for off-surface experimental data. The disagreement between simulations and high-enthalpy ground test experiments have also highlighted the need to better characterize the freestream thermodynamic, velocity, and noise conditions.

Extensive freestream characterization of the T5 Free-Piston Reflected Shock Tunnel was performed over the course of numerous experimental campaigns using high-speed shadowgraph/schlieren imaging, static and pitot pressure probes, tunable diode laser absorption spectroscopy (TDLAS), and focused laser differential interferometry (FLDI). Accurate time-resolved static pressure measurements are key to characterizing the operation and freestream thermodynamic state in hypervelocity reflected shock tunnels, through both direct measurement and for interpretation of TDLAS signals. A series of three static pressure probes were built for use in T5 at a range of conditions from 8–16 MJ/kg stagnation enthalpies, and measurements agreed well with TDLAS-inferred pressure and numerical simulations of the static probe response. At higher enthalpy conditions, TDLAS measurements showed a substantial decrease in freestream temperature ($\sim$1000 K) while velocity was constant. This finding motivated the need for a method to characterize the arrival time and degree of driver gas contamination in T5. An opposing-wedge detector was designed to leverage the sensitivity of the canonical Mach stem flow to the freestream γ, such that the flow would choke at a prescribed increase in γ corresponding to the arrival of a specific mole fraction of monatomic driver gas. With high-speed

schlieren/shadowgraph imaging, driver gas arrival times and mole fractions were obtained for the 8 MJ/kg test condition.

Informed by these freestream characterization experiments, near-surface FLDI measurements of instabilities in a separation shear layer on a 25°–55° double-cone model were performed with simultaneous static pressure and freestream tunnel noise measurements in hypervelocity conditions. Three main frequency regimes were considered: i) low-frequency content associated with Kelvin-Helmholtz instabilities and streamwise acoustic disturbances along the shear layer, ii) a strong medium-frequency (peak ~370–450 kHz) signal associated with shear layer instabilities communicating with the model surface, and iii) high-frequency features associated with Mack (second-mode) disturbances. Length scaling arguments are discussed for each case, informed by axisymmetric simulations of the mean flow over the double-cone. A ray-tracing model was used to simulate the FLDI response to certain disturbances. The low-frequency Kelvin-Helmholtz and streamwise acoustic disturbance frequencies did not vary beyond uncertainty bounds along the shear layer. The medium-frequency content had a clear dependence on the local separation height, with the mean frequency decreasing with streamwise position. The high-frequency Mack mode disturbances were only observed in some experiments, suggesting the disturbance is limited only to within the shear layer, making detection difficult if any bulk shear layer motion occurs relative to the FLDI beam positions. This study provides the first known FLDI data on shear layers in hypervelocity flows, together with simultaneous freestream characterization, with the aim to inform future experiments in hypervelocity ground testing facilities and high-resolution numerical simulations.

PUBLISHED CONTENT AND CONTRIBUTIONS

Yu, W. M., Luo, Y., Austin, J. M., Hornung, H. G., Finch, P. M., Schwartz, T., Strand, C. L., and Hanson, R. K. (2024). "High-frequency static pressure measurements in the T5 reflected shock tunnel". In: *AIAA SciTech 2024 Forum*. Orlando, FL: AIAA. DOI: 10.2514/6.2024-2884.

Yu, W. M., Luo, Y., Austin, J. M., Hornung, H. G., Finch, P. M., Schwartz, T., Strand, C. L., and Hanson, R. K. (2023). "Comparison of static pressure measurement techniques in the T5 free-piston reflected shock tunnel". In: *The 34th International Symposium on Shock Waves*. [Accepted]. Daegu, Korea: ISSW34.

Yu, W. M., Austin, J. M., and Hornung, H. G. (2022a). "Freestream static pressure measurements in the T5 reflected shock tunnel". In: *AIAA SciTech 2022 Forum*. San Diego, CA: AIAA. DOI: 10.2514/6.2022-1658.

Yu, W. M., Luo, Y., Austin, J. M., and Hornung, H. G. (2022b). "Temporal freestream measurements in the T5 free piston shock tunnel". In: *23rd Australasian Fluid Mechanics Conference*. [Non-Listed]. Sydney, Australia: AFMS.

The above articles by Wesley Yu contain material that is adapted for parts of Chapters 2–4 of this thesis. Chapters 2 and 3 include experimental details, data, and analyses from Yu et al. (2022a), Yu et al. (2023), and Yu et al. (2024). Experimental details, data, and analyses presented in Yu et al. (2022b) are adapted in Chapters 2 and 4.

TABLE OF CONTENTS

LIST OF ILLUSTRATIONS

LIST OF TABLES

Chapter 1

INTRODUCTION

1.1 Motivation

Shock–Boundary Layer Interactions

Shock–boundary layer interactions (SBLI) are complex fluid dynamic phenomena that occur near corners and irregular geometries found in supersonic and hypersonic vehicle designs, particularly around control surfaces. An incoming boundary layer encounters an adverse pressure gradient due to the shock associated with a compressive area change, usually leading to boundary layer separation/reattachment (and the separation shear layer), which can generate localized aerothermal heating to the vehicle surface. The inherently unsteady nature of SBLI flows makes predicting locations of peak heating and dynamic stresses difficult, which is a significant issue for vehicle efficiency and survivability. Additionally, when entering the hypersonic regime where the ideal gas equation of state can no longer be assumed, real-gas effects, potentially including both thermal transitions and chemical reactions –and nonequilibrium– may need to be taken into account.

The double-cone or double-wedge geometries (discussed in detail below) were developed as canonical models for hypersonic shock-boundary layer interactions in the presence of real-gas effects. The 25°–55° double-cone is sensitive to vibration-dissociation coupling and a stringent test case for thermochemical models (Olejniczak et al., 1997). After numerous studies comparing simulations and surface measurements obtained in experiments, good agreement was generally obtained in the case of low-enthalpy nitrogen hypersonic flows ($h_0 \leq \sim 4$ MJ/kg) (MacLean et al., 2007; Nompelis et al., 2003).

However, for conditions with any significant degree of dissociation, large disagreements between predictions and experiments are reported (a full discussion is included in Section 1.2). As an example, a recent effort was made to predict laminar double-cone flow under frozen, nonequilibrium, and equilibrium assumptions, with two kinetic models for reacting flow (Park two-temperature, Park (1993); MMT, Chaudhry et al. (2020a,b)) in air (Holloway et al., 2022), for comparison with experiments performed in the national CUBRC LENS-XX facility at freestream conditions up to 21.77 MJ/kg (MacLean et al., 2014). Simulations consistently

over-predicted the surface properties, with total heat flux differing by up to 30%. An investigation into the inflow conditions generated in these experiments was carried out using an inverse approach with Navier–Stokes simulations found some inconsistencies, indicating the importance of freestream characterization in these challenging experiments (Ray et al., 2023).

These discrepancies highlight the need for experimental investigations focused on i) validating kinetic rates associated with the chemical reactions occurring both in the freestream of high-enthalpy ground test facilities and in SBLI air flows at these conditions and ii) making off-surface measurements that can provide more direct information about the SBLI gasdynamics than surface heat flux and pressure.

Ground Testing and Diagnostic Considerations

Accurately modeling hypersonic flight and the associated complex shock interactions, nonequilibrium real-gas chemistry, radiative heating, and instabilities in shear and boundary layers is a challenging problem. Even assuming a thorough understanding of these phenomena, accounting for a few of them in simulations can balloon the resolution and computational time to impractical levels. Hypersonic flight testing is also limited, as it is expensive, time-consuming, and, most importantly for understanding gas dynamic phenomenona, challenging for any off-surface diagnostics. Ground testing facilities can bridge the gap between simulations and flight by generating the required flow conditions in a laboratory.

There are two main ways to perform ground testing, the first being moving a model through quiescent gas (ballistic ranges or rail-sled systems). The more common method is to induce flow over a stationary model. For low-speed flows, continuous wind tunnels are typically used for long duration test times. However, as flow velocity requirements increase, the power needed for facility operation can quickly become unsustainable. To study cold supersonic and hypersonic flows, blowdown wind tunnels and Ludwieg tubes can generate test times on the order of seconds. In order to generate hypervelocity flows to study flight-enthalpy matched real-gas effects, impulse facilities like shock tubes, reflected shock tunnels, and expansion tubes are commonly used, with test times on the orders of micro- to milliseconds (Hornung, 2010).

As discussed above, there remains a significant need to continue to characterize the gasdynamic processes used to accelerate flow to hypervelocity conditions in impulse facilities. Additionally, freestream acoustic noise is a subject of study in

such facilities as it can also affect sensitive instabilities. The work presented in this thesis focuses on experiments in the T5 Free-Piston Reflected Shock Tunnel, and various optical and probe diagnostics are employed to probe the freestream at conditions of interest, with the goal being to provide experimental data with simultaneous measurements of temporal freestream variations. More details on these methods will be discussed in Chapter 2.

Diagnostics in impulse facilities face notoriously difficult environments, as the harsh test conditions and structural loads require significant consideration for any intrusive sensors like pressure probes. Additionally, the response time of many of these sensors is insufficient to capture high-frequency features such as the Mack (second-mode) boundary layer instability, which can be on the order of 1 MHz in hypervelocity flows (Bitter, 2015; Parziale, 2013). As is the case with most fluid mechanics problems, optical techniques are an effective way to probe these flows. Historically in T5, schlieren imaging, interferometry, and emission/absorption spectroscopy have been used to study a wide array of flow geometries.

The advantages of such techniques are the non-intrusive nature of the measurement and the high-frequency response (limited only by the detector response time). The primary issue with these optical diagnostics is line-of-sight integration. The spatial non-uniformity of the flow in the test section combined with strong shock-waves exacerbating beam steering issues causes difficulty in extracting quantitative measurements from the data. One optical diagnostic that aims to minimize the impact of these issues is focused laser differential interferometry (FLDI) (Lawson and Austin, 2020; Parziale et al., 2012; Schmidt and Shepherd, 2015b). As with most interferometers, FLDI consists of two coherent beams of light that are recombined onto a photodetector, which outputs a voltage proportional to the intensity of the interference of the two beams. In a shearing interferometer, the two beams run parallel to each other, but are focused down from large beam diameters outside the test section to small foci with diameters on the order of microns at the measurement location of interest. This effectively filters out flow features like nozzle free shear layers and window boundary layers in the test section, while measuring small-scale disturbances near the test model. More on the theory and operation of this measurement technique will be addressed in Section 1.4.

One of the main goals of this thesis is to improve the confidence in experimental data collected from impulse facilities by characterizing the freestream properties in various flight-relevant conditions of interest. There is an emphasis placed on

obtaining simultaneous optical measurements in the freestream while probing near-body flows. FLDI is used to interrogate the separation shear layer on a canonical double-cone geometry while simultaneously measuring the freestream noise using a parallel FLDI beam-pair. Time-resolved freestream pressure is measured simultaneously using tunable diode laser absorption spectroscopy and a series of static and pitot pressure probes. Additionally, the degree of driver gas contamination is characterized with an opposing-wedge sensor using high-speed shadowgraph imaging. The rest of this chapter will review the theory and past work on double-cone flows, focusing on the separation region and shear layer. The experimental techniques used to probe this flowfield and characterize the freestream will also be discussed in the following sections.

1.2 Double-Cone and Double-Wedge Flows

The flowfield of interest is high-enthalpy hypervelocity flow over a double-cone geometry, shown in Fig. 1.1, reproduced with permission from Knisely (2016). The double-cone geometry was a response to uncertainties in the spanwise effects of double-wedge models and associated unsteadiness. Given the similarity of the two flowfields and that the literature has significant work studying double-wedge flowfields, studies of both geometries will be discussed.

The base flowfield is reminiscent of canonical compression ramp flows, where often a separation region forms at the corner. This is complicated by the upstream cone generating an oblique shock that impinges on the bow shock caused by the aft, large-angle cone. When the laminar boundary layer separates, it causes a separation shock to interact with the oblique shock, and a reattachment shock that then interacts with the bow shock. It is well documented that this SBLI is sensitive to the thermochemical state of the gas, making it an ideal flow for comparing experimental results to simulations (Druguet et al., 2005; Knisely, 2016; Nompelis and Candler, 2010; Nompelis et al., 2003). Beyond the academic interest in this flowfield, the geometry is common in wing-body junctions, engine inlets, and control surfaces of hypersonic vehicles, so understanding the coupling between the flow physics and thermochemistry is paramount for vehicle design. Experiments and numerical simulations have been performed on this flowfield in cold-flow and low-enthalpy conditions (Acosta et al., 2023; Hao et al., 2022; Hao and Wen, 2020; Hornung et al., 2021) and agree well with each other. However, in high-enthalpy hypervelocity conditions, agreement is poor between experiment and simulation (Druguet et al., 2005; Hao and Wen, 2018; Knight et al., 2017; Knisely, 2016; Nompelis and

Candler, 2010; Reinert et al., 2020; Swantek and Austin, 2015).

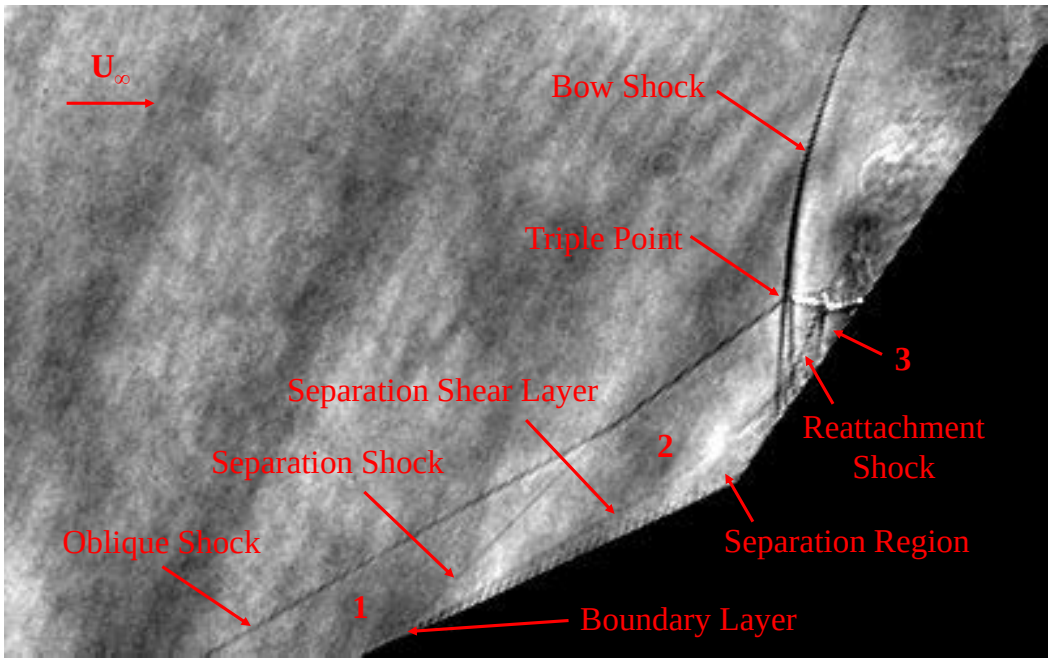

Figure 1.1: Flowfield over a 25°-55° double-cone in T5 (Knisely, 2016).

Using a cylinder generated bow shock with and oblique shock generator, the oblique/bow shock interactions were thoroughly studied and grouped into six types (I-VI) by Edney (1968). The flowfield generated by the 25°–55° double-cone in the current work is considered Type V. Davis and Sturtevant (2000) developed a scaling for the separation region over a double-wedge, which is applicable to both geometries (Huang and Inger, 1983). The scaling applied the triple-deck theory (Stewartson and Williams, 1969) to the base flow model introduced by Roshko (1993), which applies the pressure rise theory through a shear layer (Sychev, 1982). Knisely (2016) measured heat flux and performed high-speed imaging on a 25°–55° double-cone and double-wedge (Edney V) and a 25°–48° double-cone (Edney VI) in air, nitrogen, and carbon dioxide flows in T5. Good correlation was observed between the separation length and pressure, and normalized separation length collapsed well onto the scaling of Davis and Sturtevant (2000). The high-speed images of the 25°–55° are used to position the FLDI beams in this study. This will be expanded on in Chapters 2 and 5.

As discussed above, one of the main reasons for the discrepancies between experiments and numerical simulations of double-cone flows is finite-rate molecular processes in hypervelocity flows. Given that chemical and vibrational nonequilib-

rium occur simultaneously, and are also coupled, accurate simulation of these flows is difficult without sufficient experimental data to understand the thermochemistry. Some of the discrepancies (separation length, triple point motion, pressure underprediction) have been attributed to unsteadiness caused by freestream noise and vibrational nonequilibrium as well as uncertainties in nitrogen dissociation rates (Olejniczak et al., 1997, 1996). Non-Boltzmann distributions of nitric oxide (Bose and Candler, 1996) and oxygen dissociation/recombination (Candler et al., 2010) also add to the complexity of the modeling. The Park (Park, 1993) and MMT (Chaudhry et al., 2020a,b) kinetic models over-predicted heat flux when comparing to laminar double-cone flow experiments in the CUBRC LENS-XX tunnel. Ray et al. (2023) demonstrated the importance of freestream characterization with an *a posteriori* inverse approach with Navier–Stokes simulations, finding inconsistencies in the LENS-XX datasets. Part of the goals of the current work is to address uncertainties in the freestream conditions to increase confidence in the experimental data so improvements can be made to thermochemical modeling.

1.3 Separation Shear Layer Instabilities

While the mean flow over double-cones has been studied extensively both experimentally and computationally, this thesis focuses on identifying modes of intrinsic instabilities that form in the separation region and shear layer. These instabilities propagate downstream and impact the flow behavior and heating in the post-reattachment region and have significant ramifications in the global stability of the flowfield. As mentioned above, numerous studies have explored the unsteadiness of double-cone flows and highlighted the relatively low-frequency fluctuations both within in the separation region and in Region 2, but few have looked at the actual instabilities in the shear layer itself. Due to the near-body locations of such features and the small scales of the turbulent structures, they are difficult to probe experimentally and require high resolution to model the flow physics and chemistry accurately. This section will review possible modes of instability present in the shear layer discussed in Section 1.2. Additionally, the effects of nonequilibrium thermochemistry in high-enthalpy flows are considered.

Kelvin-Helmholtz Instability

Kelvin-Helmholtz instabilities arise when there are velocity or density differences across a shearing interface between two fluids. Discovered by Hermann von Helmholtz in 1868 (Helmholtz, 1868), a mathematical model was developed by

William Thomson (Lord Kelvin) in 1871 to study the formation of ocean waves (Thomson, 1871). Over the next century, Kelvin-Helmholtz instabilities were observed and studied in a wide range of fields, from small-scale medical implementations, to various engineering applications, to the atmospheric and planetary sciences. Given the breadth of the literature on these instabilities, this review will focus on the latter half of the 20th century to present efforts to understand the effects of compressibility on such shear layers and the development of coherent structures through vortex amalgamation processes. Scaling arguments for these phenomena will be discussed, with emphasis on the convective velocity and growth rate of the shear layers. To give physical context, a schematic of a canonical shear layer between two parallel inflows is shown in Fig. 1.2. In the following discussion and throughout this work, U_c refers to the convective velocity of the vortices in the shear layer, and λ refers to the wavelength of the vortices, or the distance between adjacent vortex centroids.

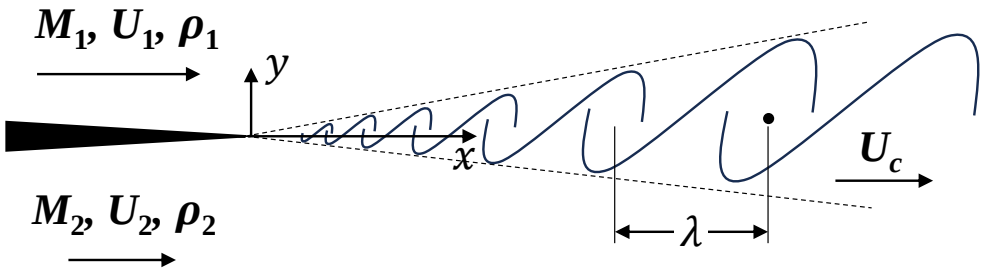

Figure 1.2: Idealized representation of large-scale structures in a shear layer.

With the advent of high-speed flight, investigations into compressibility effects on free jets and mixing layers grew in popularity. Crane studied the effects of high velocity and large temperature differences on growth rate, finding the impact of velocity to be much more dominant that temperature (Crane, 1957; Crane and Pack, 1957). Maydew and Reed investigated the turbulent mixing of free jets at a range of Mach numbers from 0.7 to 1.96, showing the growth rate is constant at subsonic speeds and decreases with increasing Mach number in the supersonic regime (Maydew and Reed, 1963). In 1974, Brown and Roshko performed flow visualization on plane turbulent mixing between nitrogen and helium streams, showing that the growth rate depended mostly on compressibility effects and not the density ratio between the two streams. They identified large coherent structures which convect at nearly constant velocity, but grow in size and spacing discontinuously due to amalgamation

with neighboring structures, such that the mean scale grows linearly with distance downstream. These interactions, called vortex pairing, were first observed by Freymuth (1966) and Winant and Browand (1974) at low Reynolds number. Another form of this mechanism was documented by Dimotakis and Brown (1976), where three vortices amalgamate into one, appropriately called vortex tripling. Moore and Saffman (1975) proposed a third mode of amalgamation called vortex tearing, where a vortex is destroyed by its neighbors and absorbed into them. This process was observed by Hernan and Jimenez (1982) and Dimotakis and Brown (1976); it was also shown that pairing was the dominant form of amalgamation. Bernal (1988) developed a statistical formulation, in both the Eulerian and Lagrangian frames, to fit the measured wavelengths of the vortices to a lognormal distribution, with standard deviations corresponding to the three types of amalgamations.

The compressible turbulent shear layer was studied in depth by Papamoschou and Roshko (1988), using combinations of helium, argon, and nitrogen gas at a variety of density and velocity ratios and Mach numbers ranging from 0.2 to 4. They defined a compressibility parameter, called the convective Mach number (M_c), in a coordinate system following the streamwise motion of the convecting vortices. Referring back to Fig. 1.2, U_c is the convective velocity of the vortices and λ is the wavelength of the vortices. Conveniently, since the vortex circulation is defined as $\Gamma = \Delta U \lambda$, where $\Delta U = U_1 - U_2$ and velocity is constant, λ can be used to describe the wavelength and circulation interchangeably, which is also constant throughout the lifetime of a vortex (Bernal, 1988). To convert this to the convective frame, the respective convective Mach numbers can be defined as:

$$\begin{aligned} M_{c_1} &= \frac{U_1 - U_c}{a_1} \\ M_{c_2} &= \frac{U_c - U_2}{a_2} \end{aligned} \tag{1.2}$$

where a_i is the sound speed of the respective fluids. As shown in Papamoschou and Roshko (1988), this coordinate system allows the two convective Mach numbers to be related by:

$$\left(1 + \frac{\gamma_1 - 1}{2} M_{c_1}^2\right)^{\frac{\gamma_1}{\gamma_1 - 1}} = \left(1 + \frac{\gamma_2 - 1}{2} M_{c_2}^2\right)^{\frac{\gamma_2}{\gamma_2 - 1}} \tag{1.3}$$

where γ_i is the ratio of specific heats. If M_{c_2} is small, and $\gamma_1 = \gamma_2$, this expression is simplified to:

$$M_{c_2} = \left(\frac{1}{q}\right)^{1/2} M_{c_1} \tag{1.4}$$

where $q = \gamma_2/\gamma_1$. Finally, the expression for convective velocity, U_c can be written as:

$$U_c = U_1\left(\frac{1 + rs^{1/2}}{1 + s^{1/2}}\right) \tag{1.5}$$

where $r = U_2/U_1$ and $s = \rho_2/\rho_1$. The growth rate, $\delta' = d\delta/dx$, is then a function of q, r, s, and M_{c_1}. Papamoschou and Roshko (1988) then showed that when normalizing the compressible pitot growth rates by the incompressible value, the ratio starts at unity and decrease with increasing M_{c_1}, asymptoting to 0.2. The clear observation was that compressibility inhibits turbulent mixing and effectively reduces the spreading rate of mixing layers. They proposed a scaling for compressible mixing layers that collapsed well for their data:

$$\delta' = \delta'_{ref}(M_c)\left(\frac{(1-r)(1+\sqrt{s})}{2(1+r\sqrt{s})}\right)\Phi(M_c) \tag{1.6}$$

where δ_{ref} is the growth rate with $U_2 = 0$, and $\Phi(M_c)$ is a function determined from experiment. This scaling method will be revisited in Chapter 5 when discussing FLDI measurements in the double-cone separation shear layer.

Results from Dimotakis (1991), Goebel and Dutton (1991) and Clemens and Mungal (1995), among others, all fit the trend presented in Papamoschou and Roshko (1988) fairly well, albeit with a fair amount of scatter. This is likely due to sensitivity to initial and boundary conditions, facility noise, and 3D effects. Dimotakis (1991) proposed a semi-empirical relation to fit the numerous datasets:

$$\Phi = 0.8e^{-M_c^2} + 0.2 \tag{1.7}$$

Aupoix (2004) performed numerical reassessments of the data, and made adjustments to zero Mach number regimes. In general, large scatter is still observed at low Mach numbers but the trends for higher Mach numbers fit Eq. 1.7. These experimental and numerical fits suggest that the effects of compressibility and density ratios still need to be further explored. While convective Mach number is a strong

similarity parameter in this problem, as growth rate clearly decreases with Mach number, it does not fully represent all the physics in shear layer flows (Smits and Dussauge, 2006).

Subsequently, significant work has been done on studying supersonic free shear layers and separation induced shear layers. Martens et al. (1994) performed flow visualization and hot-wire anemometry on a supersonic shear layer with $U_1 = 3$ to 4 and $U_2 = 1.2$, and were able to resolve fluctuations in the 10–20 kHz range ($St = 0.5$). Smith and Dutton (1999) measured convective velocity in a reattaching shear layer with $M_1 = 2.5$ and $M_2 = 2.0$ and observed U_c to be slightly higher than isentropic estimates and shocklets moving with the convecting eddies. Compressiblity effects were characterized in axisymmetric shear layers by Thurow et al. (2003), who used high-speed imaging to track coherent structures as they moved downstream and compiled a distribution of convective velocities in the shear layer. Massa and Austin (2008) numerically examined the spatial linear stability of a shear layer behind a shock triple point generated by an opposing-wedge. Hao and Wen (2020) performed numerical global stability analysis on the canonical 25°–55° double-cone, observing that the onset of global instability occurs just prior to emergence of secondary separation due to azimuthally periodic perturbations at a critical Re. More recently, burst-mode nitric oxide planar laser-induced fluorescence was used to image a similar flowfield in the Hypervelocity Expansion Tunnel (HXT) at Texas A&M University. Kelvin-Helmholtz instabilities were identified in the shear layer with frequencies in the 35–55 kHz range (Leonov et al., 2023).

Acoustic Instabilities

Another mode of instability that must be addressed are acoustic disturbances. Given that the sensitivity of FLDI to acoustic disturbances (Lawson, 2021; Parziale et al., 2012; Schmidt and Shepherd, 2015b), their role in shear layer instabilities and scaling arguments need to be discussed. A commonly investigated instability mechanism in hypersonic flows is the Mack "second-mode" (Mack, 1984), where acoustic waves are trapped in the boundary layer that effectively acts as a waveguide. The scaling given by Mack (1984) for the frequency of these disturbances is:

$$f_M = \frac{KU_E}{2\delta} \tag{1.8}$$

where K is a constant of proportionality that scales with Mach number, U_E is the boundary layer edge velocity, and δ is the boundary layer thickness. This scaling

was confirmed experimentally by Demetriades (1977) and Stetson et al. (1984). Second-mode disturbances were investigated over a slender cone in T5 by Rasheed et al. (2002), Jewell et al. (2013), and Parziale (2013), and numerically by Fedorov (2003) and Bitter (2015). More recent experiments in T5 (Hameed et al., 2022; Paquin et al., 2023) also measured second-mode instabilities on a cooled cone. These acoustic disturbances are not limited to boundary layers, however, as Butler and Laurence (2021) and Benitez et al. (2020) observed second-mode disturbances propagating through a separation shear layer on a flared cone. Pandey et al. (2022) also measured second-mode instabilities propagating through the shear layer on a cone-slice-ramp geometry in the Sandia National Laboratories Hypersonic Wind Tunnel. All three studies on second-mode instabilities in shear layers noticed lower-frequency oscillations within the shear layer.

An additional acoustic disturbance mode that needs to be considered is streamwise communication between the separation and reattachment points of the shear layer. The interaction between acoustic disturbances and vortex shedding in cylinder wakes have been studied extensively (Kim and Durbin, 1988), but work in the supersonic and hypersonic regimes is still limited. Schmidt and Shepherd (2015a) measured the fluctuations in the wake shear layer behind cylinders of varying diameter. When scaled by the shear layer length, the Strouhal number collapsed to an approximate value of 0.48, suggesting that oscillations in the supersonic flow outside of the separation region are driven by acoustic signals propagating in the subsonic region. This mode was investigated numerically by Hinman and Johansen (2018) and scaling arguments were developed to describe this flowfield. Awasthi et al. (2022) performed high-speed focusing schlieren in the wake of a Mach 3 circular cylinder and observed broadband standing waves due to the aeroacoustic resonance in the wake caused by interaction between wake instabilities and upstream propagating acoustic waves. Another numerical study by Pirozzoli and Grasso (2006) showed oscillatory motion of the separation point induced by acoustic disturbances propagating upstream through the shear layer. In these cases, the shear layer would be the main length scale of interest, so the associated frequency would scale as:

$$f_{SW} = \frac{a}{2L_{sep}} \tag{1.9}$$

where a is the local sound speed. These scalings will be revisited in Chapter 5 during the discussion of the experimental results in the context of different instability modes on the double-cone separation shear layer.

Shear Layer Instabilities

The low-frequency Kelvin-Helmholtz instabilities and high frequency second-mode disturbances have been explored extensively in supersonic and hypersonic flows. However, stability analyses studies have shown the existence of medium-frequency shear layer instabilities. Mack (1990) used linear, inviscid stability theory to calculate spatial amplification rates at Mach 3 for sinuous and varicose modes of single wake and jet flows. It was observed for confined shear layers that the lowest sinuous mode was the most unstable, including both subsonic and radiating disturbances. Jackson and Grosch (1989) showed that for parallel compressible mixing layers, if the Mach number exceeds a critical value, there are two groups of unstable waves. The "fast" group has phase speeds greater that 0.5 and is supersonic relative to the stationary stream, while the "slow" group has phase speeds less than 0.5 and is supersonic relative to the moving stream.

While the nature of these instabilities is still not well understood, more recent experimental studies have measured such medium-frequency features along separation shear layers (Benitez et al., 2020; Butler and Laurence, 2021; Pandey et al., 2022). An important length scale to consider when investigating these medium-frequency instabilities in the separation shear layer is the local distance of the shear layer to the wall. Since the separation region is largely subsonic, disturbances along the shear layer are communicated to the wall, causing shifts in the second-mode frequency and generating additional instabilities at lower frequencies. These frequencies would thus scale as:

$$f_H = \frac{a}{2H(x)} \tag{1.10}$$

where H is the local separation distance from the wall in the wall-normal direction, which is clearly a function of x. Using FLDI, high-speed schlieren, and surface-mounted pressure transducers, Pandey et al. (2022) noticed a slight decrease in the second-mode frequency and lower-frequency flapping (15–60 kHz) along the separation shear layer and attributed it to the growing distance between the shear layer and the model surface. Butler and Laurence (2021) observed lower frequency content (60–90 kHz) in the shear layer independent of the second-mode, which agrees well when compared with the scaling using $H(x)$. Benitez et al. (2020) also observed frequencies in the 50–170 kHz range and attributed it to shear layer instabilities. While no conclusive causes for these frequency shifts and additional

instabilities are given in these studies, the importance of the separation region height scaling is shown.

High-Enthalpy Effects

A final consideration for shear layer instabilities is the effect of nonequilibrium thermochemistry on shear layer behavior. As mentioned in Section 1.2, the flowfield is sensitive to chemical and vibrational nonequilibrium. A source of discrepancy between experiment and simulation is likely linked to these effects on the instabilities in the shear layer. Shin and Ferziger (1993) performed numerical simulations of a compressible and reacting mixing layer, showing that multiple supersonic modes exist for both non-reacting and reacting flows when the disturbance phase velocity is supersonic relative to the freestream. As observed by Papamoschou and Roshko (1988) these supersonic modes become less unstable with increasing Mach number, but additionally, Shin and Ferziger noticed more instability with increasing heat release. They also concluded that convective Mach number is not a universal parameter for describing compressing reacting shear layers. In a numerical study of a shear layer behind a triple point, Massa and Austin (2008) observed that thermochemical nonequilibrium also had a destabilizing effect on shear layer perturbations for all convective Mach numbers from 0.341 to 1.707. Their analysis considered the evolution of the molecular vibrational quantum distributions during the instability growth by examining the perturbation eigenfunctions. Oxygen and nitrogen maintained a Boltzmann distribution of vibrational energy, but nitric oxide, as expected, had high degrees of nonequilibrium. The differences between translational and vibrational temperature eigenfunctions also increased with convective Mach number.

The current work aims to use FLDI to measure various modes of instability a shear layer where significant amounts of chemical and vibrational nonequilibrium are expected (Knisely, 2016). This is in the hope that the experimental data can inform computational models of such flows and move towards a better understanding of the coupling of thermochemistry to the shear layer behavior, and eventually to the mean hypervelocity flow over the double-cone geometry.

1.4 Focused Laser Differential Interferometry

History of FLDI

In the most basic sense, FLDI behaves like most optical interferometers, responding to optical path differences between the two beams. More specifically, the path differences are caused by variations in the refractive index n, which can be linearly

related to the density, ρ, of the gas using the Gladstone-Dale relation:

$$n = K\rho + 1 \tag{1.11}$$

where K, the Gladstone-Dale constant, depends on the wavelength of the light (Gladstone and Dale, 1863; Merzkirch and Gersten, 1987). While this relation was developed empirically, the Lonrenz-Lorentz relation was derived independently through first principles by Ludwig Valentin Lorenz and Hendrik Lorentz (Gardiner et al., 1981; Kragh, 1991):

$$R_L = \left(\frac{n^2 - 1}{n^2 + 2}\right)\left(\frac{1}{\rho}\right) \tag{1.12}$$

As before with K, the constant R_L depends on wavelength; most of which is tabulated in Gardiner et al. (1981). The main conclusion from these relations is that FLDI effectively measures density fluctuations in the region of interest, with the spatial resolution determined by the beam spacing Δx (usually on the order of 100 µm). With modern commercially available photodetector bandwidth reaching into the GHz range, this makes FLDI an ideal instrument to probe small-scale near-body density fluctuations in hypervelocity flows.

FLDI was first proposed by Smeets and George (1973), but the limited laser, photodetector, and data acquisition technology of the time kept the technique from gaining much traction. There was growing interest in the 1990's and early 2000's to measure high-speed small-scale disturbances, but ultimately, non-focusing laser differential interferometry (LDI) was used. After another decade, FLDI was finally deployed in T5 by Parziale et al. (2012) to measure freestream tunnel noise. Parziale further demonstrated the usefulness of FLDI for measuring cone boundary layer acoustic instabilities in T5 and extensively characterized the response of FLDI (Parziale, 2013; Parziale et al., 2014, 2015b).

Since then, FLDI has seen an exponential growth in popularity in the fields of supersonic and hypersonic flows, and limited use in hypervelocity flows. With modern availability of relatively low-cost and easily deployable optical components, it has proven to be a useful tool in characterizing density disturbances in ground testing facilities. Schmidt and Shepherd (2015b) developed a transfer function approach to characterize the frequency response of FLDI. Settles and Fulghum (2016) measured freestream disturbances in the AEDC Hypervelocity Wind Tunnel

9 and the Penn State Supersonic Wind Tunnel with comparisons with hot-wire anemometry. Ceruzzi and Cadou used FLDI to measure the frequency content in turbulent jets and wall boundary layers in a Mach 2.6 tunnel (Ceruzzi and Cadou, 2017, 2019; Ceruzzi et al., 2020; Ceruzzi and Cadou, 2022). Ceruzzi also made Mach 18 density and velocity measurements in Tunnel 9 and analyzed the spatial sensitivity of FLDI (Ceruzzi et al., 2021a,b). Houpt and Leonov (2018) developed a planar FLDI system to measure close to a model surface without any beam clipping. In an extensive characterization study, Lawson furthered the understanding of FLDI response to shock-waves and various density disturbances, using numerical simulations and benchtop experiments with turbulent jets and ultrasonic acoustic beams (Lawson and Austin, 2023a,b; Lawson et al., 2019, 2020; Lawson, 2021). FLDI was also utilized to characterize freestream acoustic noise in the Hypervelocity Expansion Tube at Caltech and the von Kármán Gas Dynamics Facility Wind Tunnel D (Lawson and Austin, 2020; Lawson et al., 2022; Lawson, 2021). Bathel and Weisberger both used FLDI to measure cone and flat plate instabilities, respectively, in the NASA Langley 20-Inch Mach 6 Air Tunnel (Bathel et al., 2020; Weisberger et al., 2020, 2019). Benitez developed and characterized FLDI in the Purdue Unviversity Mach 6 Quiet Tunnel, measuring transitional boundary layer profiles and also simulating FLDI response over axisymmetric models (Benitez et al., 2024; Benitez and Jewell, 2022; Benitez et al., 2021, 2023). Hameed characterized FLDI using a vibrating cylindrical lens and a turbulent jet (Hameed and Parziale, 2021, 2022), and also deployed multi-point FLDI in T5 to measure second-mode instabilities on a cooled cone (Hameed, 2023; Hameed et al., 2022). At the Sandia Hypersonic Wind Tunnel, Pandey et al. (2022) used a scanning FLDI system to probe second-mode disturbances propagating through the shear layer of a cone-slice-ramp geometry.

FLDI Theory and Signal Interpretation

FLDI is technically just a subset of LDI, a common diagnostic used in a wide variety of fields. The main difference between FLDI and traditional LDI is the focusing of the beams to small ($<10\mu m$) diameters at the region of interest, decreasing the interferometer's sensitivity to density disturbances further away from the focal plane. It is this feature that reduces the effects of the line-of-sight integration issues mentioned in 1.1, as the final signal at the photodetector comes primarily from a small sensitive region near the foci. There are various methods to generate this beam geometry, so the optical configuration used in this study, similar to Parziale et al.

(2012) and Lawson et al. (2019), is shown in Fig. 1.3. The components in this setup are labeled as followed: L = laser, B = beam waist, QWP = quarter-wave plate, WP_i = Wollaston prisms, F_i = focusing lenses, LP = linear polarizer, PD = photodetector. More on the details of experimental setup and expansions to double-FLDI (DFLDI) will be discussed in Chapter 2, so the rest of this section will focus on the signal interpretation of a base FLDI setup.

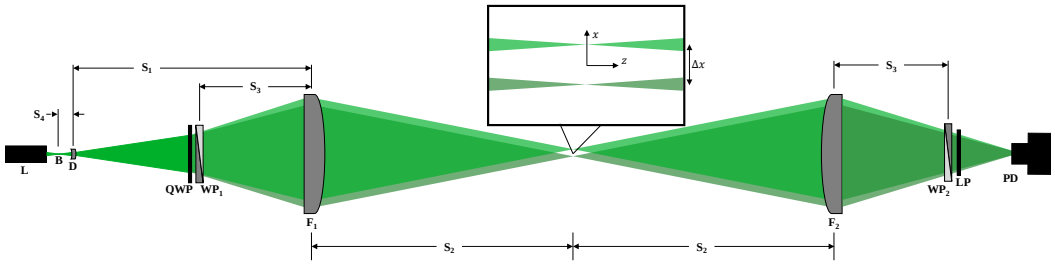

Figure 1.3: Schematic of a standard FLDI setup.

Much like classical interferograms, a fringe pattern is produced by this setup, but the Wollaston prisms are arranged such that an "infinite-fringe" configuration is achieved, where a only a single fringe is visible, and changes in phase cause the entire beam to darken and brighten. With this setup, the beam can then be focused onto a photodetector and produces a voltage signal that scales with the interference intensity of the FLDI. Details on the alignment process and optical arrangement needed to achieve this are discussed in Lawson (2021).

For many applications, analyzing the raw voltage is sufficient to extract frequency content of density disturbances, or cross-correlating two voltage traces from DFLDI to measure velocity. However, there is additional quantitative information in the FLDI signal that can still be extracted. Fundamentally, the FLDI responds to refractive index changes, and as discussed earlier, linearly scales with density. Thus, the response to a density gradient $\Delta\Phi(t)$ is proportional to $\Delta\rho/\Delta x$. To quantify the density disturbances in T5, Parziale et al. developed a simple analytical relation to estimate $\Delta\rho$ between two FLDI beams:

$$\frac{\Delta\rho}{\overline{\rho}} = \frac{\lambda_L}{2\pi K \zeta \overline{\rho}} \sin^{-1}\left(\frac{V}{V_0} - 1\right) \tag{1.13}$$

where $\overline{\rho}$ is the local average density, λ_L is the laser wavelength, K is the aforementioned Gladstone-Dale constant, V is the FLDI photodetector output voltage, V_0 is the center voltage of the infinite fringe (typically corresponding to the middle of

the dynamic range), and ζ is the sensitive length of the FLDI, usually determined by benchtop characterization of the optical setup. Parziale then added a correction coefficient:

$$c(\lambda) = \sin\left(\frac{\pi\Delta x}{\lambda}\right) \tag{1.14}$$

for sinusoidal disturbances of wavelength λ. Given its simple application and relatively early publication in the FLDI literature, this conversion has been used widely in the community (Benitez et al., 2021; Ceruzzi et al., 2020; Hameed and Parziale, 2021).

Schmidt and Shepherd (2015b) used a ray-tracing theoretical model of the FLDI response, with the two FLDI beams modeled as parallel focusing ray bundles, separated by a constant Δx. The origin of the Cartesian coordinate system is set at the midpoint between the two foci as shown in Fig. 2.15. Using the paraxial approximation, each ray in the first beam is paired with a ray in the second beam and propagated through a refractive index field, yielding a phase change between the two beams. $\Delta\Phi$ is then the phase change integrated across the detector:

$$\Delta\Phi(t) = \frac{2\pi}{\lambda_L}\iint_D I_0 \sin\left[\frac{2\pi}{\lambda_L}\left(\int_S^D n\left(\underline{x}_1, t\right) \mathrm{d}s_1 - \int_S^D n\left(\underline{x}_2, t\right) \mathrm{d}s_2\right)\right] \mathrm{d}\xi\mathrm{d}\eta \tag{1.15}$$

where $n\left(x_i, t\right)$ is the refractive index field probed by the i^{th} beam, s_i are the parameterizations of the ray paths, and the source and detector planes, S and D, respectively, have the coordinate system (ξ, η). λ_L is the laser wavelength with normalized intensity distribution $I_0(\xi, \eta)$. Eq. (1.15) can then be linearized using the small-angle approximation, giving:

$$\Delta\Phi(t) = \frac{2\pi}{\lambda_L}\iint_D I_0 \left(\int_S^D n\left(\underline{x}_1, t\right) \mathrm{d}s_1 - \int_S^D n\left(\underline{x}_2, t\right) \mathrm{d}s_2\right) \mathrm{d}\xi\mathrm{d}\eta \tag{1.16}$$

With this ray-tracing approach, Schmidt and Shepherd developed a transfer function for the FLDI response to 1-D sinusoidal disturbances, given by:

$$\begin{aligned} H(k) &= H_s(k) \times H_w(k) \\ &= \frac{2}{k\Delta x}\sin\left(\frac{k\Delta x}{2}\right) \times \exp\left(-\frac{w^2k^2}{8}\right) \end{aligned} \tag{1.18}$$

where w is the Gaussian beam radius at the location of the disturbance, and k is the wavenumber of the sinusoidal disturbance, and $H(k)$ is the overall transfer function. As shown above, $H(k)$ is decomposed into two parts: the effects of the beam separation, $H_s(k)$, and the beam widths, $H_w(k)$. It was shown that the spatial filtering property of FLDI is due to $H_w(k)$, as w increased with z. Settles and Fulghum (2016) independently developed a similar transfer function, albeit with a vastly different approach using the propagation of polarized electric fields. The validity of the transfer function (1.17) and its numerical implementation was confirmed experimentally by Lawson (2021), allowing for an FLDI temporal response to be computed in terms of a phase shift $\Delta\Phi(t)$.

However, this only allowed for simulation of an FLDI signal from a known density disturbance which, while important, is not useful in extracting density information from an FLDI trace. Lawson and Austin (2023a) developed a generalized method to solve the inverse problem: $n(\underline{x}, t) = f^{-1}(\Delta\Phi(t))$. It was shown that for a generalized time-varying plane wave:

$$n(\underline{x}, t) = A\cos(\underline{k}\cdot\underline{x} - \omega t + \varphi) \tag{1.19}$$

where the constants A is the amplitude, $\underline{k}$ is the wavevector, ω is the angular frequency, and φ is the phase, an analytical result could be derived for $\Delta\Phi(t)$:

$$\begin{aligned}\Delta\Phi(t) = \frac{2\pi A}{\lambda_L}\cdot\frac{4\sqrt{2}\pi^{3/2}w_0}{\sqrt{k_x^2+k_y^2}\lambda_L}\cdot\sin\left(\frac{k_x\Delta x}{2}\right)\cdot\sin(\omega t-\varphi)\\ \cdot\exp\left(-\frac{w_0^2}{8}\left[k_x^2+k_y^2+\frac{16\pi^2k_z^2}{\left(k_x^2+k_y^2\right)\lambda_L^2}\right]\right)\\ \cdot\Re\left[\operatorname{erf}\left(\frac{\left(k_x^2+k_y^2\right)L\lambda_L^2+\mathrm{i}\cdot4\pi^2k_zw_0^2}{2\sqrt{2}\pi\sqrt{k_x^2+k_y^2}\lambda_L w_0}\right)\right]\end{aligned} \tag{1.20}$$

where i imaginary unit, $\Re$ is the real part, and erf is the error function. This expression is usually condensed to the form:

$$\Delta\Phi(t) = A\cdot h(\underline{k})\cdot\sin(\omega t-\varphi) \tag{1.21}$$

where the wavenumber-dependent terms are grouped into the term $h(k)$. They demonstrated using spectral inversion, namely Welch's method to calculate power

spectral density (Welch, 1967), that it is possible for all refractive index fields of arbitrary superpositions of sinusoidal plane waves and uniform convecting flows. Using this method, Lawson and Austin (2023b) compared their generalized formulation of Schmidt and Shepherd's various transfer functions to Eq. (1.13) (Parziale et al., 2012) and concluded that it was a specific case that applies only for plane sinusoidal waves propagating in the x-direction. Lawson and Austin also used their method to slightly correct the transfer functions derived in Settles and Fulghum (2016). In the current work, some results are left as the power spectral density of the phase shift, $PSD\{\Delta\Phi(t)\}$, with units of $\text{rad}^2\text{Hz}^{-1}$, but quantifications of density disturbances are calculated using the generalized method outlined in Lawson and Austin (2023a).

1.5 Static Pressure Measurement in High-Enthalpy Facilities

Freestream static pressure is an important freestream quantity to measure in high-enthalpy ground testing facilities. The aforementioned unsteady gasdynamics involved in the operation of such facilities and the sensitivity of model flows to freestream changes highlights the need for high-speed time-resolved static pressure measurement. Additionally, static pressure is key in anchoring the thermodynamic state of the test gas and validating numerical models for accurate nozzle simulation.

Static probes have been implemented in various impulse facilities like the High Enthalpy Shock Tunnel Göttingen (HEG) at the German Aerospace Center (DLR) (Karl, 2011) and the High Enthalpy Shock Tunnel (HIEST) at the Japan Aerospace Exploration Agency (JAXA) (Hashimoto et al., 2009). Flat plate static pressure measurements in carbon dioxide were performed in the T3 Shock Tunnel (Ebrahim and Hornung, 1975). In the T5 Free-Piston Reflected Shock Tunnel, traditional surface-mounted piezoelectric transducers have been used on flat plates (Belanger, 1993) and static pressure probes, but the signal-to-noise ratio was inadequate for use with spectroscopic studies to measure time-resolved species densities in the freestream. Similar structural noise issues were observed in the HEG static pressure measurements, and were alleviated by using piezoresistive transducers with silicone gel and tubing as shielding for the sensor (Martinez Schramm, J., personal communication, Sept 4, 2020).

A static probe design based on Behrens (1963) and Karl (2011) was developed in the present work. In this section, the theory behind the geometry of the probe and the associated correction factors is discussed, along with calculations of the

temporal response. Deployed in T5 with TDLAS to simultaneously characterize the freestream (see Chapter 2), the static probe measurements will be compared to TDLAS-inferred pressure in Chapter 3.

Static Probe Dimensions

The exterior dimensions of the static probe was described in Behrens (1963). Derived from Matthews (1958), the probe had a 20-degree cone tip, with pressure taps 10 tube diameters downstream from the shoulder of the cone. The length of the tube downstream of the pressure taps is at least 20 boundary layer thicknesses (at the location of the tap). The relation for correcting the static pressure data is given for a weak hypersonic viscous interaction by Hayes and Probstein (1958):

$$\frac{p}{p_\infty} - 1 = A\overline{\chi} + B\overline{\chi}^2 \tag{1.22}$$

where A and B are constants and the viscous interaction parameter, $\overline{\chi}$, is defined as

$$\overline{\chi} = \frac{M_\infty^3 C_\infty^{1/2}}{\mathrm{Re}_{x,\infty}^{1/2}} \tag{1.23}$$

and where

$$C_\infty = \left(\frac{\mu_w}{\mu_\infty}\right)\left(\frac{T_\infty}{T_w}\right) \tag{1.24}$$

This relationship has been shown to hold for flat plates and cones (Hayes and Probstein, 1958), and to the first order in $\overline{\chi}$, holds for cone-cylinder bodies as well (Behrens, 1963). Thus the static temperature and Mach number at 10 diameters downstream of the shoulder are essentially equal to the freestream. Based on this model, the ratio of the measured pressure to freestream pressure will be 0.94–0.95 (Behrens, 1963; Karl, 2011).

Static Probe Time Response

Assuming a perfect gas, we calculate the response time of the pressure measurement as a function of the internal geometry of the cavity housing of the transducer. The flow through the cavity is initially choked since the internal cavity pressure is near vacuum and therefore the pressure ratio exceeds the choking criterion. However, as the cavity pressure increases, the pressure ratio becomes proportional to the pressure

difference, and can be used to obtain a function of time. This calculation is presented in detail by Hornung (2004), giving the measured pressure p as a function of time as:

$$\left(\frac{p}{p_e}\right)^{\frac{1}{\gamma}} = \left(\frac{2}{\gamma+1}\right)^{\frac{\gamma+1}{2(\gamma-1)}} a_e \frac{A}{V} t \tag{1.25}$$

where A is the cross sectional area of the pressure taps, V is the total volume of the cavity, p_e is the local pressure, and a_e is the local sound speed. The subscript e in this calculation represents the local boundary layer edge condition just outside the pressure tap. The choked flow assumption no longer holds when

$$p_c > \left(\frac{2}{\gamma+1}\right)^{\frac{\gamma}{\gamma-1}} p_e \tag{1.26}$$

where p_c is the critical pressure. The function $p(t)$ in this post-critical time period can be approximated by relating the flow rate and pressure difference, matching the value and the rate of change of pressure at $p = p_c$, giving

$$\frac{dp}{dt} = C \frac{a_e A}{V} (p_e - p) \tag{1.27}$$

where

$$C = \gamma \frac{(\frac{2}{\gamma+1})^{\frac{3\gamma-1}{2(\gamma-1)}}}{1 - (\frac{2}{\gamma+1})^{\frac{\gamma}{\gamma-1}}} \tag{1.28}$$

To arrive at a function of time we integrate from $p = p_c$ and $t = t_c$ to get

$$\frac{p}{p_e} = 1 - (1 - \frac{p_c}{p_e}) \exp \frac{-C(t - t_c) a_e A}{V}. \tag{1.29}$$

Then, by solving for t_c

$$t_c = \sqrt{\frac{\gamma+1}{2}} \frac{V}{a_e A} \tag{1.30}$$

the two expressions are separated for pressure vs. time. A composite of Equations 1.25 and 1.29 gives a total rise time of $5V/(Aa_e)$ (Hornung, 2004). It is important

to mention that the analytical derivation of the response time does not allow the gas to lose heat to the body of the static probe. At high-enthalpy conditions such as those in T5, heat loss is significant. Therefore, the analytical result underestimates the response time. Nevertheless, the relative response times it gives for the different probe versions is useful for design purposes.

1.6 Driver Gas Contamination in Reflected Shock Tunnels

Monatomic driver gas contamination in reflected shock tunnels is one of the main limiting factors on usable test time, especially in high-enthalpy facilities like T5. The interaction between the reflected shock and the boundary layer on the shock tube wall causes the shock foot to bifurcate. When this bifurcated reflected shock is transmitted through the driver gas, the gas that passes through the bifurcation forms a jet along the wall towards the endwall and contaminates the test gas before the end of the ideal test time (Davies and Wilson, 1969; Mark, 1958; Stalker and Crane, 1978). Since helium and argon are commonly used as the driver gas, the contamination of the air by a monatomic gas leads to changes in gas composition and temperature in the test section, which will influence measurements. In T5, TDLAS experiments were performed on the freestream flow and a decrease in temperature on the order of 1000 K was noticed for a 16 MJ/kg stagnation enthalpy condition while velocity remained constant (Finch et al., 2023b; Girard et al., 2021). More recently, similar trends were noticed in the Sandia Hypersonic Shock Tunnel (Gilvey et al., 2024; Jans et al., 2024), pointing to this expected issue of driver gas contamination.

A simplified model of the flowfield at the end of a shock tube is modeled in various studies (Davies and Wilson, 1969; Mark, 1958; Matsuo et al., 1974). An x-t diagram labeling the various gas states in the reflected shock tube operation is shown in Fig. 1.4, with a schematic of the reflected shock bifurcation reproduced below in Fig. 1.5. Davies and Wilson (1969) also derived an analytical expression for arrival time of driver gas in a reflected shock tube:

$$t = \frac{LU_r}{U_r + u_2}\left(1 - \frac{u_2}{U_1}\right)\left(\frac{1}{U_r} + \frac{1}{U_7^* - U_T}\right) \tag{1.31}$$

where U_1 is the incident shock velocity, u_2 is the flow velocity behind the incident shock, U_r is the reflected shock velocity, U_T is the transmitted shock velocity, U_7^* is the velocity of the flow that has gone through the bifurcated foot of the reflected shock, and L is the length of the channel.

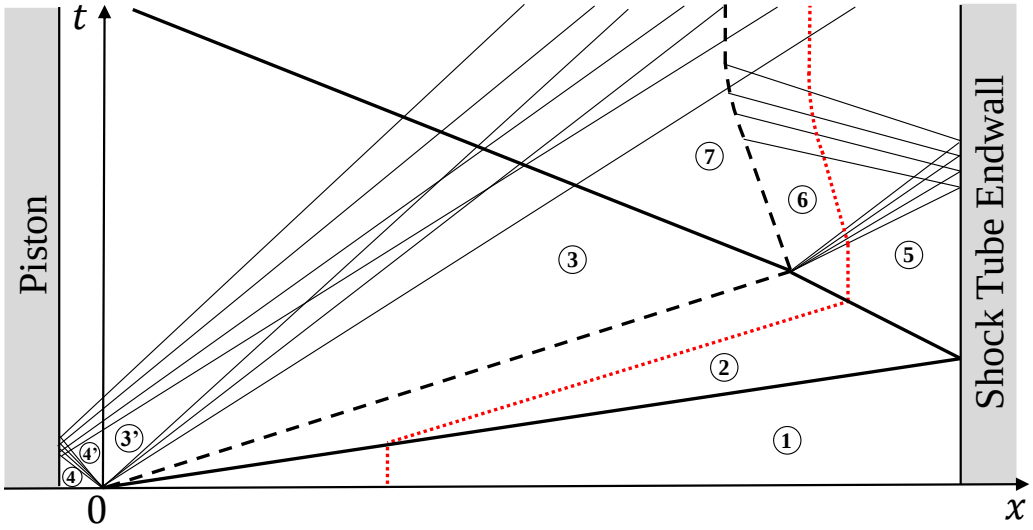

Figure 1.4: *x*-*t* diagram of under-tailored reflected shock tube operation.

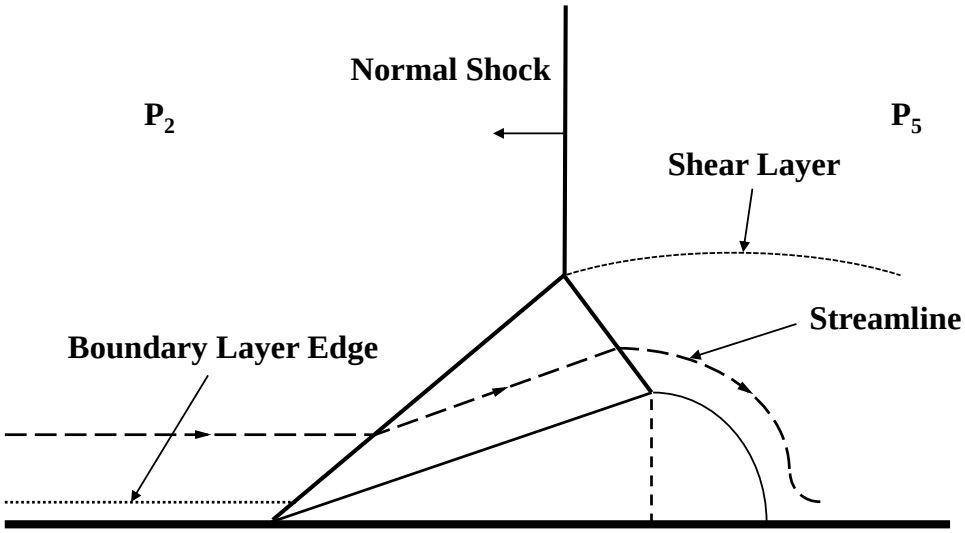

Figure 1.5: Simplified model of shock foot bifurcation of a reflected shock in a shock tube (Davies and Wilson, 1969).

While this phenomena was identified early on, effective methods of quantifying the arrival time and degree of driver gas contamination have been sparse. Stalker (1968) proposed using a probe that operates on the speed of sound difference between test and driver gas. Hornung (1992) observed the onset of driver gas contamination with high-speed images of an oblique shock in T5. A duct/wedge detector was proposed by Paull and King, using the fact that the angle of the shock on the wedge would

increase with the arrival of driver gas, thus choking the duct and causing a sudden increase in pressure (Paull, 1996; Paull and King, 1995).

Building off the work of Paull and King, Sudani and Hornung (1998) were able to measure the onset time of contamination by observing the choking of a duct placed downstream of an oblique shock, caused by the increase of the ratio of specific heats, γ, as monatomic driver gas contaminates the test gas. The device was able to resolve a 5% mole fraction of monatomic gas with high temporal resolution and enabled them to give a usable test period as a function of reservoir enthalpy in T5 (Sudani and Hornung, 1998). Their experimental results matched well with Davies and Wilson's analytical relation. While Sudani and Hornung's detector measured the arrival time of driver gas accurately, the degree of driver gas contamination was limited to discrete mole fractions. The recent spectroscopic work (Finch et al., 2023b; Girard et al., 2021) highlighted the need for high mole fraction resolution for the purposes of chemical modeling to characterize the freestream. The current work builds on the work of Sudani and Hornung, leveraging an opposing-wedge system that can resolve driver gas concentrations on the order of $X_m = 0.01$. This setup will be discussed in Chapter 2 with results presented in Chapter 4.

1.7 Project Scope & Outline

This work has three main goals:

1. Design and characterize static pressure probes in the T5 freestream, then deploy them to measure the time-resolved freestream static and pitot pressure simultaneously with TDLAS and FLDI experiments. Compare the measured static pressure to TDLAS-based pressure-broadening analysis.

2. Temporally characterize the concentration of monatomic driver gas in the T5 freestream and compare to theoretical predictions and previous experiments.

3. Perform off-surface FLDI measurements of a separation shear layer on a 25°–55° double-cone model in T5 with simultaneous freestream FLDI and static pressure measurement. Identify key frequency peaks using power spectral methods, and make scaling arguments for possible Kelvin-Helmholtz instabilities and acoustic disturbances.

The thesis is structured in the following manner: Chapter 2 describes the experimental facility and procedures used in this study, and gives mechanical and design details on all models and instrumentation, as well as flow conditions used in each experimental campaign. Chapter 3 focuses on the static pressure measurement

results, with comparisons to analytical and numerical predictions, as well as absorption spectroscopy-based pressure measurements. Chapter 4 covers the experimental and numerical results from the driver gas contamination study. Chapter 5 focuses on the results from the FLDI experimental campaign probing the separation shear layer and measuring freestream tunnel noise. Finally, Chapter 6 summarizes the thesis, and highlights areas of interest for future work in tunnel characterization and applications of FLDI.

Chapter 2

EXPERIMENTAL FACILITY AND PROCEDURES

This chapter covers information about the experimental facility, test conditions, experimental models, and instrumentation that were used in the various experimental campaigns. Some material in this chapter is adapted and compiled from Yu et al. (2022a, 2022b, 2023, 2024). Detailed test conditions and engineering drawings are provided in Appendices A and E, respectively.

2.1 T5 Free-Piston Reflected Shock Tunnel

The experiments in this study were performed in the T5 Free-Piston Reflected Shock Tunnel at the California Institute of Technology, shown in Fig. 2.1 (Hornung, 1992). It is the fifth shock tunnel in a series of high-enthalpy impulse facilities that generate flight-relevant conditions in which hypervelocity aerodynamics can be studied. It operates using a piston that adiabatically compresses a helium/argon mixture to a high pressure which acts as the driver section to the reflected shock tunnel (Hornung, 1992). The facility has five main sections: the secondary reservoir (2R), compression tube (CT), shock tube (ST), test section (TS), and dump tank (DT). A stainless steel diaphragm initially separates the CT and ST. Based on previous experimental data in the facility, the diaphragm is scored to a precise depth to produce repeatable burst pressures and a predictable petal opening process. The nozzle is located at the other end of the ST and connects to the TS with a sliding seal. A 0.005" Mylar diaphragm is placed at the nozzle throat, separating the ST from the TS and DT.

A piston (120 kg for these experiments) is inserted into the end of the CT while the CT, ST, TS, and DT are evacuated to below 0.04 kPa. The ST is then filled with the test gas, which is usually air, nitrogen, carbon dioxide, or custom mixtures. The CT is filled with a prescribed helium/argon mixture while the 2R is filled with compressed air. The CT and 2R fill pressures are pre-calculated such that the piston strikes the polyurethane buffers at the end of the CT at velocities under 20 m/s to avoid damage. After the facility has been filled to the appropriate pressures, a small amount of high pressure air is released into the space behind the piston, which pushes it slightly downstream. This uncovers the slots between the 2R and CT that the piston previously seals, allowing the compressed air in the 2R to accelerate the piston down

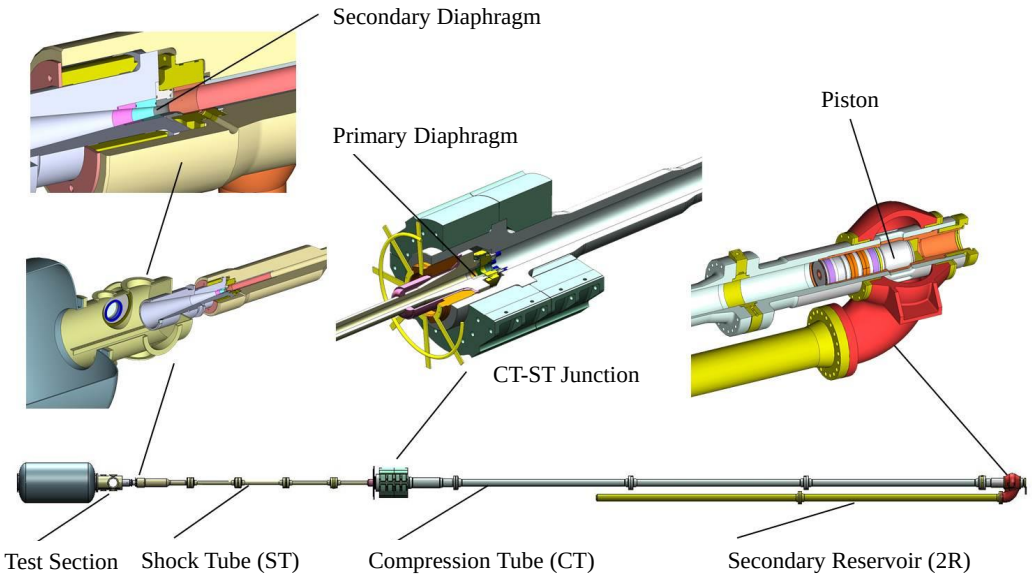

Figure 2.1: Schematic of the T5 Free-Piston Reflected Shock Tunnel.

the CT. The piston adiabatically compresses the helium/argon mixture in the CT and eventually bursts the steel diaphragm at a prescribed pressure, generating a strong incident shock that propagates down the ST. The incident shock reflects off the end wall, forming a stagnant high-temperature/pressure nozzle reservoir. The secondary diaphragm is vaporized by the primary shock and the stagnated gas then expands through the contoured 100:1 area ratio converging-diverging nozzle to the final test condition.

The relevant facility pressures are recorded using vacuum gauges and dynamic pressure transducers (PCB 119M44). Static pressure transducers on the DT, ST, CT, and 2R are used to monitor the pressures during the evacuation and filling processes. Since the gauges are isolated during the shot to avoid damage, the pressures are recorded before the shot. Two dynamic pressure transducers are located immediately upstream of the primary diaphragm to measure the burst pressure for every shot. Four more dynamic transducers are located along the ST to measure the incident shock speed. The last two transducers located at stations 3 and 4 are used to calculate the primary shock speed by cross-correlating the two pressure spikes. The two upstream transducers are not used since shock speed decreases approximately 15% from the speed measured between stations 1 and 2 to stations 3 and 4. Finally, two more pressure transducers are located just upstream of the ST endwall to measure the nozzle reservoir pressure, one of which is used to trigger data collection during a shot. The signals from the eight pressure transducers are

recorded on a Yokogawa 12-bit depth DL850E ScopeCorder oscilloscope at 50 MS/s as well as a National Instruments PXIe-6368 16-bit depth DAQ card at 2 MS/s for redundancy. The measured facility data (tabulated in Appendix A) are used as inputs to numerically calculate the freestream conditions.

2.2 Freestream Conditions

There are three main conditions used in T5 for these experimental campaigns. The first two are 8 MJ/kg stagnation enthalpy conditions used in Knisely's work (Knisely, 2016), one with air and one with nitrogen test gases. They nominally have similar freestream conditions, albeit with differences in temperatures ($T_V - T_R \approx 2000$ K) due to vibrational freezing in the nozzle in the nitrogen case. These two conditions were used by Knisely to explore the effects of oxygen dissociation on the mean flow over double-cone and double-wedge geometries. With good repeatability and relatively "gentle" operation for the facility, these two conditions were ideal for extended freestream characterization campaigns and additional experiments. The air condition was used most frequently across all studies in this thesis, and serves as a anchoring point for the different experimental methods. An additional higher-enthalpy 16 MJ/kg air condition was characterized using absorption spectroscopy and static pressure probe, but was not used for model flow experiments in this study. Variations of this condition were tested to characterize effects of shock tube tailoring.

The freestream conditions for each shot in T5 are simulated by first calculating the nozzle reservoir conditions using the initial ST fill pressure, P_1, the measured primary shock speed, U_s, and the measured reservoir pressure during test time, P_R. Figs. 2.2-2.4 show facility traces from typical T5 operation that are used to measure these values. The post-reflected shock state is calculated with an equilibrium normal shock in Cantera with the Shock and Detonation Toolbox (Browne et al., 2006); the gas is subsequently isentropically expanded to the measured P_R. Once the nozzle reservoir conditions are determined, the steady expansion through the contoured nozzle is simulated using the University of Minnesota Nozzle Code (Candler, 2005), which solves the axisymmetric reacting Navier–Stokes equations with a turbulent nozzle wall boundary layer using the Spalart-Allmaras turbulence model (Spalart and Allmaras, 1992) and Catris and Aupoix compressibility correction (Catris and Aupoix, 2000). The data-parallel line relaxation method, DPLR (Wright et al., 1998) is used for implicit time integration with the inviscid fluxes calculated with Steger-Warming flux splitting (Steger and Warming, 1981) and the van Leer limiter

with second-order space accuracy (Liou and Van Leer, 1988). The structured grid of the nozzle geometry has 492 axial cells and 219 radial cells. The Bose-Candler nitric oxide reaction rates are used (Bose and Candler, 1996, 1997). Representative calculated freestream properties for the three conditions used in this study are tabulated in Table 2.1, and detailed conditions for each shot are tabulated in Appendix A.

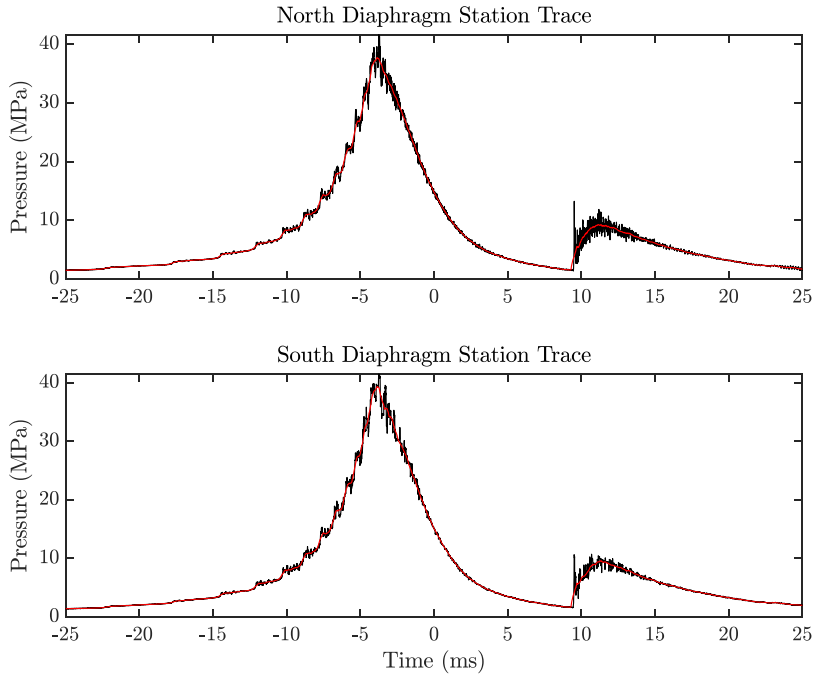

Figure 2.2: Diaphragm station pressure traces during Shot 3050. Moving-average trace shown in red.

Table 2.1: T5 Test Conditions

Condition	h_0 (MJ/kg)	M_∞	U_∞ (m/s)	P_∞ (kPa)	T_∞ (K)	$T_{v,\infty}$ (K)
H8-Re2-Air	8.03	5.46	3639	7.20	1084	1091
H8-Re2-N2	8.57	6.63	3835	4.55	802	3075
H18-Air	16.3	4.92	4948	27.1	2315	2315

2.3 Static Pressure Probes

A series of three static probes were designed and fabricated for use in T5. This section covers the design, mounting, and instrumentation of the three probes in the T5 test section.

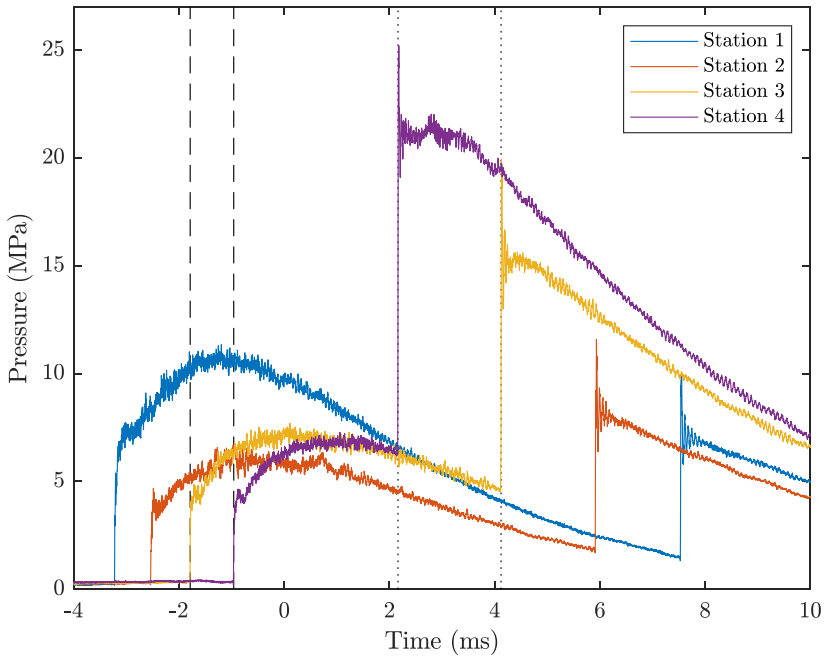

Figure 2.3: Shock station traces during Shot 3050. Dashed line indicates passage of incident shock, dotted lines indicate passage of reflected shock.

Static Probe V1

The static probe design closely adhered to the relative dimensions presented in Behrens (1963), albeit significantly scaled up by a factor of four. A schematic of the static probe used in T5 is shown in Fig. 2.5. The main structure of the probe is machined from 316 stainless steel, while the removable tip is fabricated from molybdenum to withstand the repeated high-temperature conditions during the experiments. The entire assembly is mounted in a clamp, which is tightened between two vertical plates that are bolted to the test section wall. The sting is further secured with a stainless steel rod that prevents any streamwise motion during the shot. This assembly is positioned such that during a shot, the streamwise position of the nozzle exit plane aligns with the position of pressure taps. The vertical and horizontal positions are also adjusted so that the centerlines of the probe and nozzle coincide as well.

The transducer cavity in this probe was initially designed to house a PCB113B26 transducer and included no mechanism for mechanical damping of vibrational noise. After two initial tests which had inadequate signal-to-noise ratio, Kulite XCS-062-

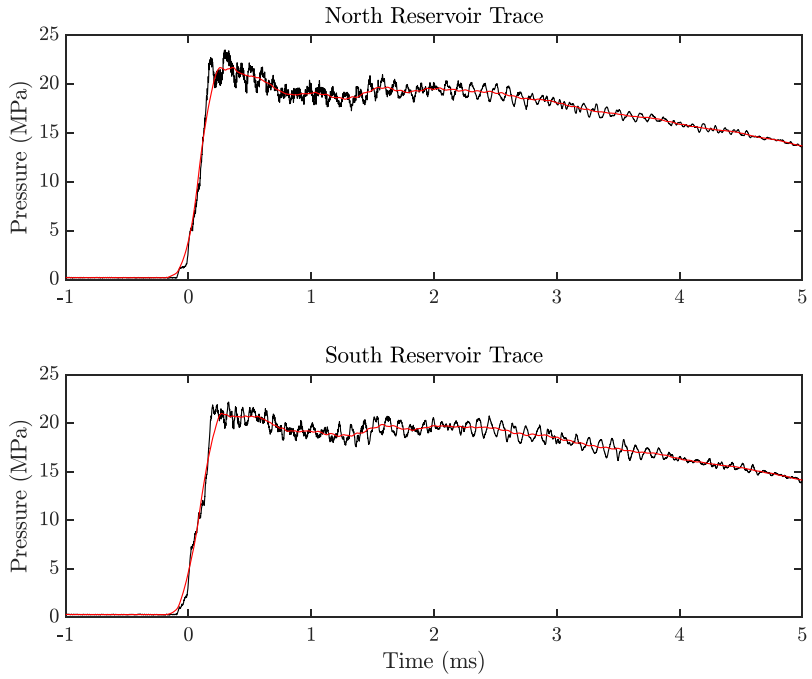

Figure 2.4: Nozzle reservoir traces during Shot 3050. Moving-average trace shown in red.

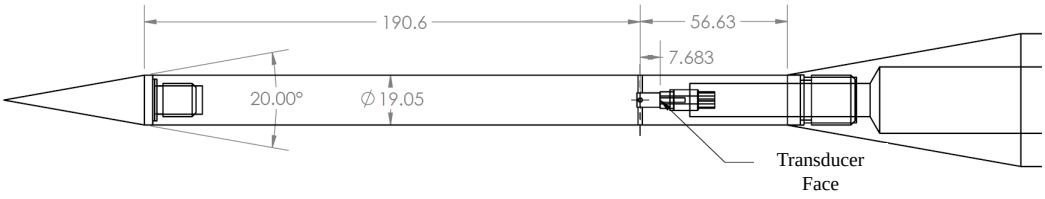

Figure 2.5: Schematic of the large scale static probe (V1) used in T5 for these studies (dimensions in mm).

5A transducers were used instead, and, as suggested by HEG researchers (Martinez Schramm, J., personal communication, Sept 4, 2020), the transducer was coated with RTV, and inserted into a silicone tubing. The silicone tubing was then also coated in RTV, and placed inside a stainless steel insert to fit into the cavity. The signal from the Kulite was amplified using a Vishay 2310B signal conditioner with a 10-volt excitation and a gain of 100. The pressure transducer was calibrated during the tunnel evacuation process and the Wheatstone bridge was balanced at the expected freestream static pressure of each shot. The main source of error in the experiment

comes from this process, since the resolution of the gauge used to calibrate the Kulites limited the calibration to 2.5% uncertainty in the 7 kPa freestream case. The instrumentation was triggered using the initial rise in the reservoir pressure, and $t = 0$ in all plots corresponds to this initial rise time. All facility measurements are collected at a 50 MHz sampling rate on the same Yokogawa DL850E ScopeCorder oscilloscope. Signal conditioning and data collection methods were kept consistent for the subsequent V2 and V3 probes.

Static Probe V2

The V1 static probe design demonstrated the geometry and transducer housing was capable of static pressure measurement in T5. In order to have a pitot and static pressure measurements in conjunction with any model testing, a smaller version of this probe mounted to the vertical support plates was needed. A schematic of this smaller probe is shown in Fig. 2.6. In this design, the transducer face sits further back from the pressure taps, so the initial rise time was longer than observed in the larger probe. However, it was calculated in both cases that the initial rise time was around 360 µs, which is acceptable given the typical 1–2 ms test times in the T5 facility. This probe used the same Kulite transducer as the large probe, and was complemented by a pitot probe with the same dimensions using a straight section of tubing for the main structure with the molybdenum tip removed. This pitot probe used a PCB 113B26 pressure transducer as the sensing element. The two probes are 3 inches below the large probe and offset by 2.25 inches horizontally in both spanwise directions. As will be discussed in Chapter 3, the numerical simulations of the flow showed that the shocks generated by these probes do not interfere with each other, and thus could be installed in parallel.

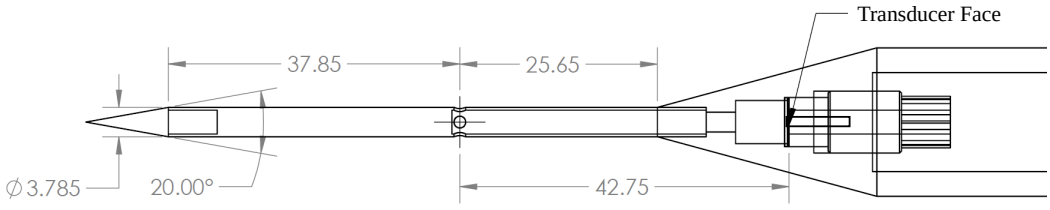

Figure 2.6: Schematic of the smaller scale scale static probe (V2) (dimensions in mm).

Static Probe V3

While the external geometry of static probe V3 (Fig. 2.7) is essentially unchanged compared to V2, the diameter of the hypodermic tubing is 0.017" larger to accommodate the Kulite XCS-062-5A transducer and silicone tubing. With this minor change, the transducer could now sit just downstream of the pressure taps instead of in the shoulder of the probe. As shown in Fig. 2.8, this change in position of the transducer reduces the response time by a factor of ten. As before, the transducer is coated with RTV, and inserted into a silicone tubing. The silicone tubing is then also coated in RTV, and placed inside the hypodermic tubing of the static probe. This final version of the static probe was the design used in the FLDI to measure the usable test time for each shot.

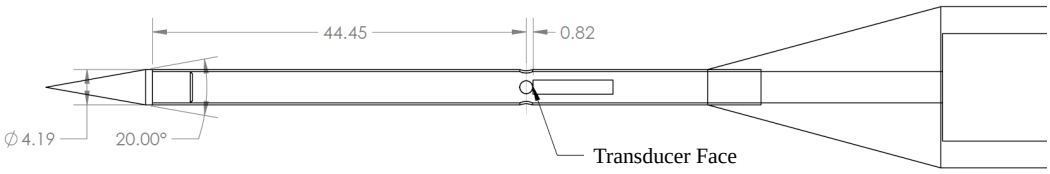

Figure 2.7: Schematic of final static probe V3 design (dimensions in mm).

2.4 TDLAS Experimental Setup

As part of a collaboration with the Hanson group at Stanford University that spanned five experimental campaigns, tunable diode laser absorption spectroscopy (TDLAS) was used to characterize the aforementioned freestream conditions in T5 by measuring freestream temperature, velocity, and number density of species of interest. Additionally, TDLAS was used to probe regions with high levels of nonequilibrium on cylinder and wedge flows for purposes of validating computational thermochemical models. The TDLAS measurements relevant to the work in this thesis focus on freestream characterization, specifically the use of pressure broadening to infer static pressure from the TDLAS lineshape. To avoid repetition, the details of the theory and experimental setups are deliberately kept brief in this section. For more in-depth explanation of the TDLAS designs for use in T5, see Girard et al. (2021) and Finch et al. (2023b).

As is common practice for laser-based absorption measurements, the measured absorbance was related to the freestream temperature and nitric oxide (NO) number density using the Beer-Lambert relation for monochromatic light (Hanson et al.,

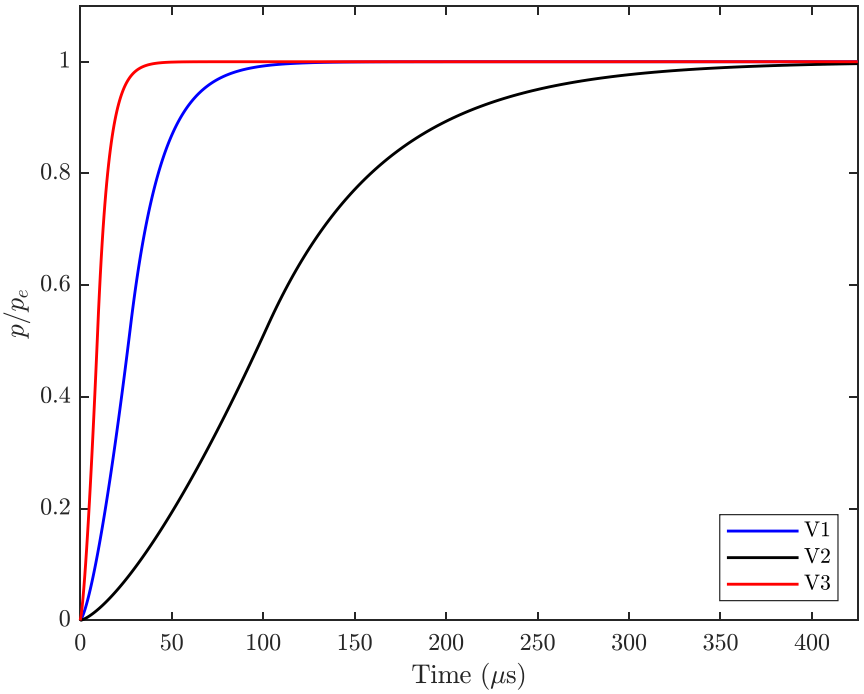

Figure 2.8: Analytical response time comparison of the three static probe designs.

2016). This specific formulation of the Beer-Lambert relation, shown in Equation 2.1, expresses the frequency-integrated absorbance, A_i, for each transition, i, of the absorbing species, j, as a function of the absorbing path length, L, absorber partial pressure, P_j, temperature-dependent linestrength $S_i(T)$, and lineshape function $\Phi_i(T, P, \nu)$:

$$A_i = \int_{-\infty}^{\infty} P_j L S_i(T) \Phi_i(T, P, \nu)\, d\nu = P_j L S_i(T). \tag{2.1}$$

By tuning the laser frequency across the absorbing linewidth to remove the dependence on $\Phi_i(T, P, \nu)$, the relation simplifies to the linear product in Equation 2.1, which can be adapted to the two-temperature model ($T = T_R \neq T_V$) for use in cases where thermal equilibrium cannot be assumed. The two-temperature formulation is detailed in Girard et al. (2021) along with the data reduction methods used to extract T_R, T_V, and P_{NO} from TDLAS measurements in the T5 freestream. The partial pressure of NO can be converted to a mole fraction given an accurate and time-resolved measurement of static pressure in the freestream. Historically, the static pressure in

T5 was reported as a steady-state output from a numerical simulation of the nozzle flow, yielding large uncertainties in the NO mole fraction calculation (Girard et al., 2021) given the temporal variations in the freestream static pressure. This pointed to a need for simultaneous static pressure measurements with TDLAS to properly anchor the spectroscopic measurements in time.

TDLAS-based pressure measurements were collected using lineshape analysis from up to 13 NO rovibrational quantum transitions at wavelengths near 5 µm. These transitions are tabulated in Finch et al. (2023b). Three NO-targeting Quantum Cascade Lasers (QCLs) were aligned perpendicular to the T5 freestream flow, passing through a pair of optical arms that extend through the nozzle shear layer and allow the beams to probe the T5 core flow. NO measurements were obtained by spectrally modulating the monochromatic QCLs, scanning the laser wavelength across several neighboring quantum transitions in a periodic manner. In this study, the modulation rate was 25 kHz, allowing for a 50 kHz measurement rate, or two measurements per period (Finch et al., 2023b). A Fabry-Pérot étalon was used to measure the relative output wavelength of the laser as a function of time. The spectral absorbance distribution for a given transition, or lineshape, is well-modeled in this work using a pair of mutually-constrained Voigt profiles. The Voigt profile is a convolution of two modes: a Gaussian function, caused by the Doppler effect of a gas following a Maxwellian velocity distribution; and a Lorentzian function, primarily caused by the action of molecular collisions, and thus sensitive to pressure (Almodovar et al., 2019). This latter effect is leveraged to infer static pressure. NO absorption transitions were fit with a floated Lorentzian mode and the Gaussian mode constrained based on inferred temperature from the ratios of absorption integrated areas between the different NO transitions. It was possible to infer pressure from TDLAS data for approximately 3 ms, coinciding with the interval of sufficient NO concentration in the T5 freestream and fully encapsulating the usable test time. The Doppler and collisional broadening full-width half-maximums (FWHMs) are defined by the following equations:

$$\Delta\nu_D = \nu_0 \left(\frac{8kT \ln 2}{mc^2} \right)^{1/2} \tag{2.2}$$

$$\Delta\nu_C = P \sum_A X_A 2\gamma_{B-A}(T) = P \sum_A X_A 2\gamma_{B-A}(T_0) \left(\frac{T_0}{T} \right)^{n_{B-A}} \tag{2.3}$$

In Eq. (2.2), ν_0 is the linecenter wavenumber for the transition, T is the translational temperature, and m is the molecular mass of the absorber. In Eq. (2.3), $2\gamma_{B-A}$ is the collisional broadening parameter of absorber 'B' with collision partner 'A' at a reference temperature T_0, X_A is the species mole fraction, and P is the pressure in atm.

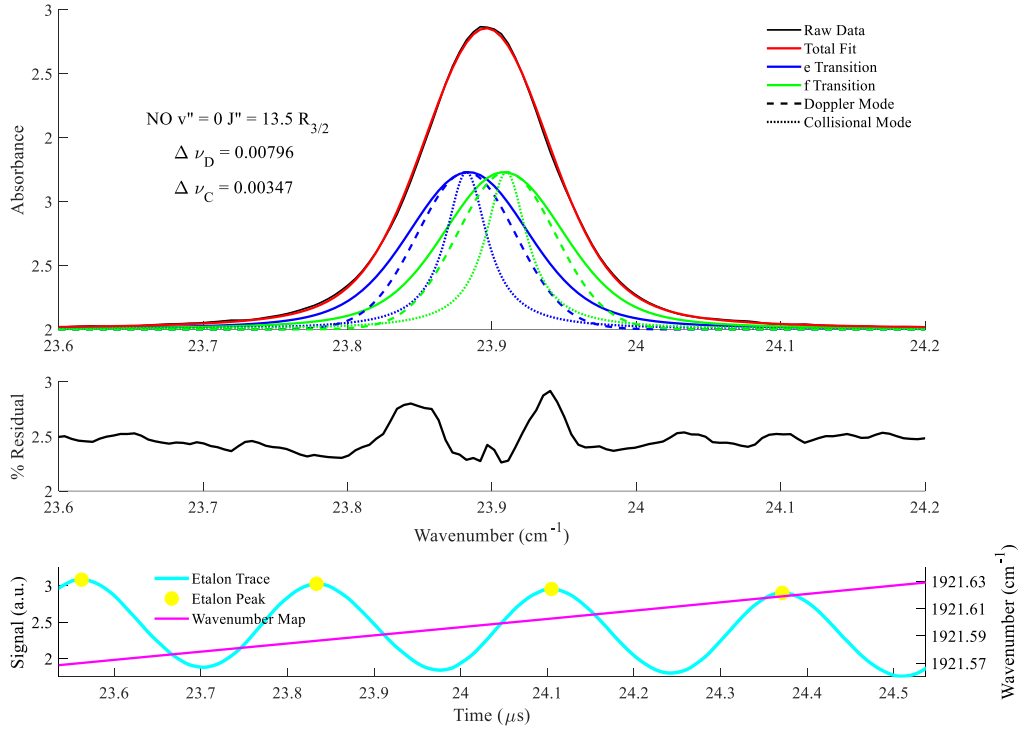

Figure 2.9: (Top) Example Voigt lineshape fit for an NO transition used to infer pressure, including Doppler and Collisional modes and Λ-type doubling; (Middle) Voigt fit residual; (Bottom) Etalon trace and map from time to spectral frequency.

An example Voigt profile fit is shown in Fig. 2.9, taken during test time in the 8 MJ/kg condition. This particular NO transition is v" = 0, J" = 13.5 $R_{3/2}$ at approximately 1921.6 cm^{-1}. The best-fit Voigt lineshape is shown in red, with the raw data trace in black. In reality, each NO transition is actually a composite of multiple lines due to the hyperfine structure of NO. The most ubiquitous hyperfine structure is known as Λ-type doubling, which breaks the degeneracy of each rovibrational level into two according to the possible orientations of the electron angular momentum projection; these two levels are labeled by their rotationless parity using the labels e and f. The temperature and pressure conditions in the T5 freestream cause all of the observed NO transitions to broaden to the extent that the Λ doubled lines are

blended, usually appearing as a single feature. For the transition shown in Fig. 2.9, the Doppler and collisional FWHMs were found to be 0.00796 and 0.00347 cm^{-1}, respectively. Both broadening modes are of the same order, but the Doppler mode is dominant. The relative contributions of the two modes are shown with dashed and dotted lines. Additional details regarding the theory of pressure broadening and TDLAS experimental setups in T5 can be found in Almodovar et al. (2019), Girard et al. (2021), Finch et al. (2023b).

2.5 Driver Gas Contamination Detector

To address the issue of driver gas contamination and improve the sensitivity to mole fraction change in the freestream, a new detector was designed for use in T5. The flow model in these experiments is a pair of opposing symmetric 38° wedges, shown in Fig. 2.10. The opposing-wedge flow generates a system of shock reflections that can either be regular or Mach reflections, determined by the wedge gap size if the wedge angle is constant (Mouton, 2007). Thus, the opposing-wedge can be configured with a gap size such that a Mach reflection forms for a range of γ, and as driver gas contamination increases and the γ threshold is reached, the flow chokes. This then generates a gap size vs. driver gas mole fraction parameter space that can be used to determine freestream driver gas concentration with high resolution. Calculations of this parameter space are detailed in Chapter 4.

The wedges are constructed from A2 tool steel, with size W = 36.25 mm and span L = 158.75 mm. The wedges are mounted on a flat support plate with square locating features, which are then mounted to a vertical wedge with additional locating features to maintain the relative roll, pitch, and yaw of the wedges. In addition, the vertical wedge also serves as a flow relief mechanism to prevent the flow from unstarting, and also allows for precise shimming of the support plates to change the gap size, G, at 0.1 mm increments. The entire assembly is sting-mounted to the support structure in the T5 test section.

Initially, the model design was informed by 2-D simulations in Eilmer4 of opposing-wedges without an expansion corner, which showed a separation bubble forming just downstream of the expansion fan, as shown in Fig. 2.11. A symmetric expansion corner was added partly to eliminate this effect but also to explore the nonequilibrium temperature effects in the expansion fan spectroscopically in a single wedge configuration. The final geometry was determined using results from further 3-D simulations showing a stable Mach stem during test time freestream conditions while

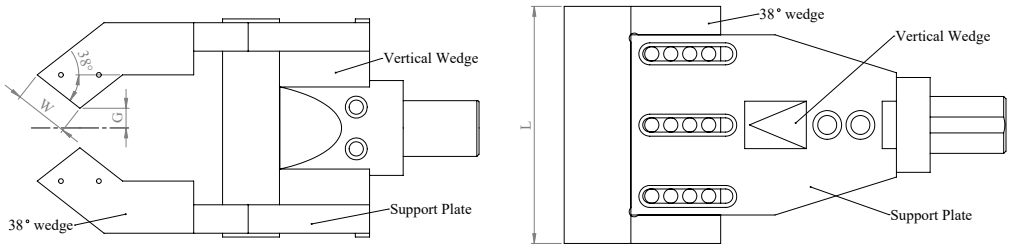

Figure 2.10: Schematic of the opposing-wedge model. Note: the gap size G is defined as half the distance between the expansion corners of the two wedges.

being sensitive enough to detect small amounts of monatomic gas contamination. These simulation methods and results are detailed in Chapter 4.

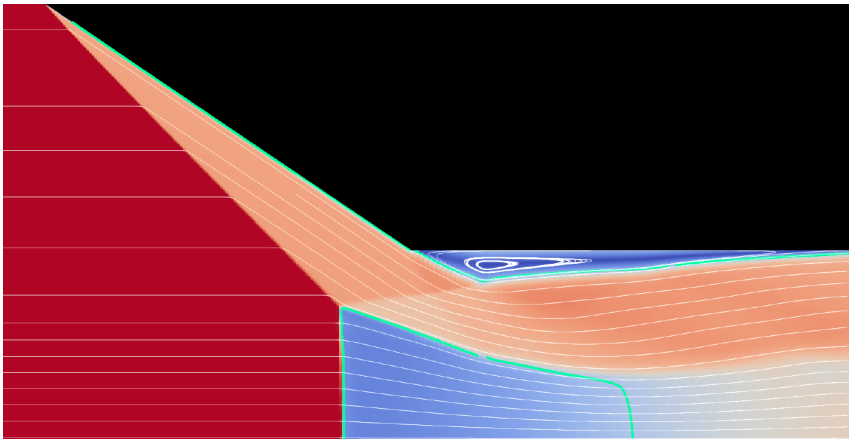

Figure 2.11: Results of an exploratory 2-D simulation of the opposing-wedge geometry without an expansion corner. Note: the separation bubble downstream of the expansion fan. Streamlines are in white, and the sonic line is shown in turquoise.

2.6 High-Speed Imaging

High-speed schlieren/shadowgraph images of the opposing-wedge model flow were taken in T5 using a Shimadzu HPV-X2 camera with a Z-type setup, shown in Fig. 2.12. The images were captured at 400x256 pixel resolution at 100 kHz and 75 kHz frame rates with an exposure time of 200 ns. The 100 kHz frame rate is used to record 2.56 ms of footage to capture details of the nozzle startup process and temporal behavior of the Mach stem. The 75 kHz frame rate is used to record 3.41 ms of footage to capture flow after test time with higher amounts of helium contamination. Due to the freestream and shock layer luminescence in T5 test conditions and high

flow velocities, a traditional continuous white light source is not sufficient to capture crisp "temporally-frozen" images. A Sony SLD1332V laser diode is used with a PicoLAS LDP-V 03-100 UF3 driver to emit light at 670 nm (Parziale et al., 2015a) with a pulse length of 80 ns. The light from the diode is collimated with a 6.24 mm aspheric lens and expanded using a 100 mm plano-concave lens, then collimated into the test section with 203.2 mm diameter, f/15 collimation mirrors and planar turning mirrors. A 200 mm focal length spherical lens is used to focus the image into the camera. To block shock layer luminescence, an aperture is placed near the focus to block rays that are not parallel to the collimated beam. Additionally, a 670 nm bandpass filter is placed in front of the camera to decrease the contribution of broadband luminescence and a baffle system is used to reduce stray light entering the camera.

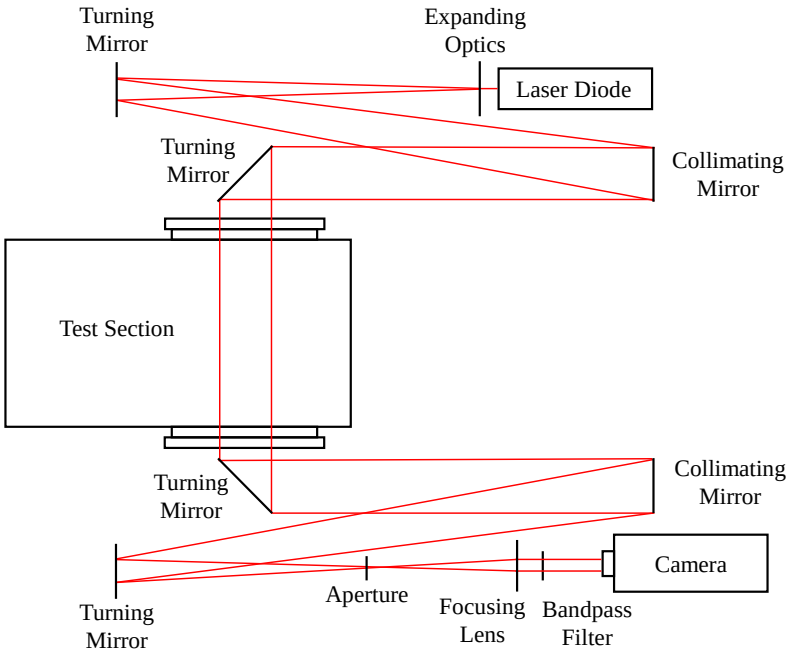

Figure 2.12: Schlieren/shadowgraph optical setup in T5.

2.7 Double-Cone Model

The double-cone geometry used in this study had the same dimensions as the model in Knisely (2016), with a fore half-angle of 25 degrees and aft half-angle of 55 degrees, based the design of Nompelis et al. (2003). The double-cone model was machined from A2 tool steel, with a fore base diameter of 48.2 mm and an aft base diameter of 122.3 mm, shown in Fig. 2.13. An array of 64 thermocouples are

installed to allow for heat flux measurements. The tip is made from molybdenum to withstand the high heat flux at the tip, but also allows for replacement in case of severe damage. The double-cone model is installed inline with the nozzle centerline axis and with a measured pitch and yaw of less than 0.1 degrees. A schematic of the 25°–55° double-cone model is shown in Fig. 2.14.

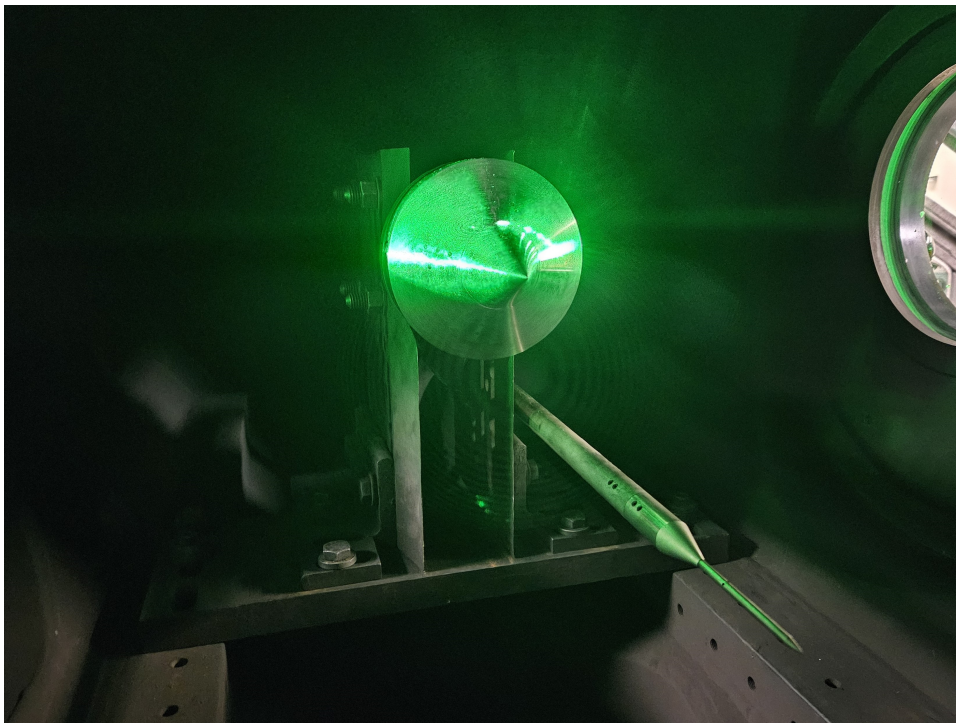

Figure 2.13: 25°–55° double-cone model with the V3 static probe in the T5 test section.

Surface heat flux measurements were obtained using fast-response coaxial thermocouples. The Type-E (constantan-chromel) thermocouples were developed by Sanderson for use in T5 (Sanderson and Sturtevant, 2002). The thermocouples were consistently flush mounted to the surface of the model using a 3-D printed positioning block, then sanded down using fine grit sanding stones to match the contour of the double-cone. The thermocouples were assembled from two components with the outer chromel electrode having a diameter of 2.4 mm and the inner constantan electrode having a diameter of 0.635 mm. The contact area between the two electrodes over which the measurement is made has a diameter of 0.787 mm, with an effective response time on the order of 1 µs. 64 thermocouples were installed into the T5 25°–55° double-cone model at uniform streamwise locations. The thermocouples are arranged radially in groups of 16 at four azimuthal angles,

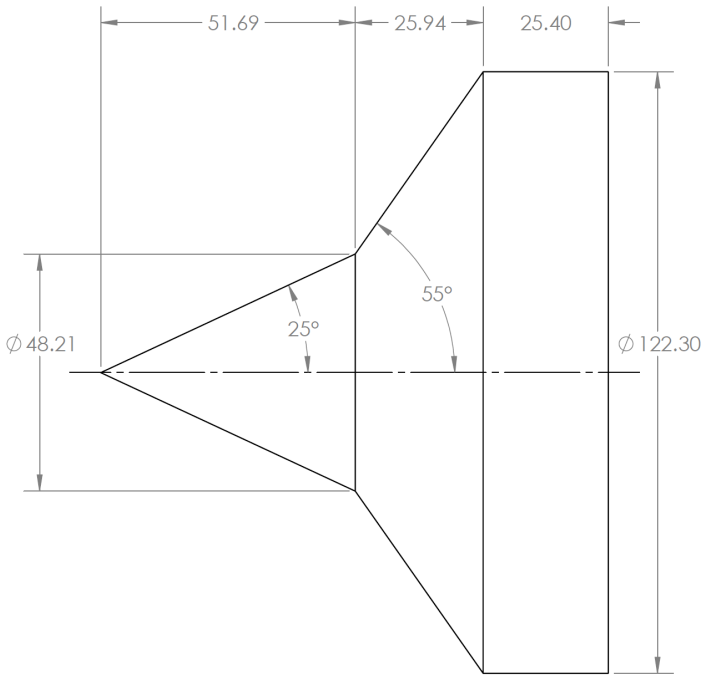

Figure 2.14: Schematic of the 25°-55° double-cone model used in this study.

and within each group are staggered along two azimuthal angles separated by 15 degrees to densely pack more thermocouples in the streamwise direction. Detailed machine drawings of the model with thermocouple locations are given in Knisely (2016).

The signals from the thermocouples are routed out of the T5 test section through a D-sub connector plate, then passed through a signal conditioner with a nominal amplification factor of 100. These signals are then recorded on the National Instruments DAQ system at 2 MHz. The temperature is then determined from the voltage using the standard NIST tables, which in turn is used to calculate the heat flux using the spectral decomposition method detailed by Sanderson and Sturtevant (2002) and Davis (1999).

The heat flux is measured at specific points throughout the thermocouple response during useful test time. As with most thermocouple measurements, they are governed by the one-dimensional heat flux equation with the given boundary conditions:

$$\begin{aligned} \frac{\partial^2 T}{\partial x^2} &= \frac{1}{\alpha}\frac{\partial T}{\partial t} \\ T(x,0) &= T_i \\ T(0,t) &= T_i + \Delta T(t) \\ \left.\frac{\partial T(x,t)}{\partial x}\right|_{x\to\infty} &= 0 \\ \left.\frac{\partial T(x,t)}{\partial x}\right|_{x\to 0} &= \dot{q}(t) \end{aligned} \tag{2.5}$$

where T is the temperature, x is the spatial coordinate normal to the surface, α is the thermal diffusivity, t is time, and $\dot{q}$ is the heat flux. In this case, $\alpha = k/\rho c$ is the thermal conductivity, ρ is density, and c is the specific heat of the material. A solution to the equation is then:

$$\Delta T(x,t) = \int_0^t g(x, t-\tau)\dot{q}\, d\tau \tag{2.6}$$

where T is the change in temperature and $g(x,t)$ is an impulse function

$$g(x,t) = \sqrt{\frac{\alpha}{\pi k^2 t}} \exp\left(\frac{-x^2}{4\alpha t}\right) \tag{2.7}$$

for $t > 0$, where x is the junction thickness. Then, the discrete Fourier transform is taken of this solution to extract the heat flux component. The heat flux solution is then found by taking the inverse Fourier transform:

$$\dot{q} = FFT^{-1}\left[\frac{\Phi Z}{G}\right] \tag{2.8}$$

where Φ is the filtering function, Z is the Fourier transform of the noisy temperature time sequence, and G is the Fourier transform of the impulse function, $g(x,t)$. A lowpass Butterworth filter with a cutoff of 20 kHz was used, since the literature has shown that most of the heat flux information is contained below this frequency.

The physical properties of the thermocouple and the junction depth have been measured by Sanderson and Davis, who showed it is sufficient to use the average properties of the thermocouples calculated from data from Sundqvist (1992). A junction depth of 1 µm is used for these calculations, based on measurements performed by Davis (1999). Uncertainty in the mean heat flux is due to errors in

the NIST thermocouple conversion tables, uncertainty in material properties, and uncertainty due to fluctuations in the freestream during a shot. According to Davis (1999), the material properties have an uncertainty of 8% and the NIST tables have an uncertainty of 1.7%. Uncertainty due the freestream fluctuations is addressed by using the 95% confidence interval for the mean heat flux measured by each thermocouple (Flaherty, 2010). The sources of uncertainty are combined as error bars in the mean heat flux plots. It is important to note that this heat flux calculation method is specific to the thermocouples designed by Sanderson and Sturtevant (2002) and not a general solution for standard thermocouples. The heat flux results are plotted in Appendix B.

2.8 Focused Laser Differential Interferometry

Optical Design

As with most FLDI setups in the literature, the optical design procedure for the DFLDI diagnostics in this study was an optimization process to minimize w_0 with physical constraints such as optical table dimensions and readily available commercial optical components. As discussed in the literature review of FLDI in the previous chapter, the base FLDI setup consists of a CW laser, diverging lens, quarter-wave plate, a pair of Wollaston prisms, a pair of converging lenses, a linear polarizer, and a high-frequency photodetector. A schematic of this standard FLDI configuration is shown in Fig. 2.15.

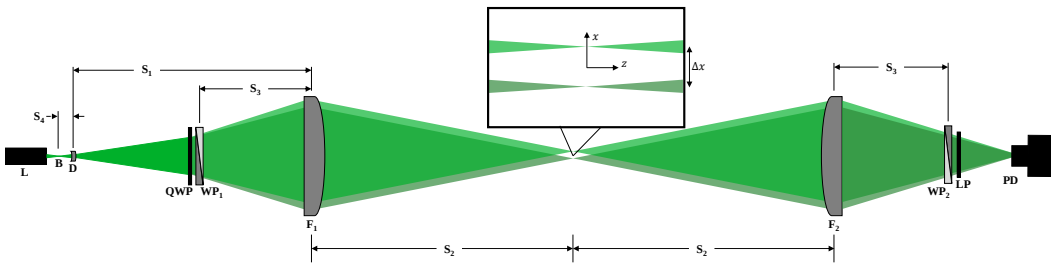

Figure 2.15: Schematic of a standard FLDI setup.

Using ray transfer matrix analysis and Gaussian optics (Milonni and Eberly, 2010), a simple model of the pitch-side of the setup can be constructed. This method was clearly described in Lawson (2021), but will be repeated here for clarity and consistency of terminology. With this method, a complex beam parameter $q(z_n)$ is modified using a series of transfer matrices that represent the lenses in the FLDI setup. The term z_n is the axial distance measured from the natural beam waist along

the z-axis. The fixed value, q_n, at the natural waist is related to the test section focus, q_f, by:

$$q_f = \frac{Aq_n + B}{Cq_n + D} \tag{2.9}$$

A, B, C, and D are the elements of the total transfer matrix M, here composed from five elementary matrices representing three propagations and two thin lenses:

$$\begin{aligned} \mathbf{M} &= \mathbf{M_5 M_4 M_3 M_2 M_1} \\ &= \begin{bmatrix} 1 & S_2 \\ 0 & 1 \end{bmatrix} \begin{bmatrix} 1 & 0 \\ -1/f_2 & 1 \end{bmatrix} \begin{bmatrix} 1 & S_1 \\ 0 & 1 \end{bmatrix} \begin{bmatrix} 1 & 0 \\ -1/f_1 & 1 \end{bmatrix} \begin{bmatrix} 1 & S_4 \\ 0 & 1 \end{bmatrix} \\ &= \begin{bmatrix} A & B \\ C & D \end{bmatrix} \end{aligned} \tag{2.10}$$

S_1, S_2, and S_4 are the z-axis dimensions labeled in Fig. 2.15, while f_1 and f_2 are the focal lengths of the diverging and focusing lenses, respectively. The beam parameter is given by:

$$q(z_n) = \left[\frac{1}{R(z_n)} + \frac{i\lambda_L}{\pi w^2(z_n)} \right]^{-1} \tag{2.11}$$

The wavefront curvature R must be zero at a waist, and the test section focus is by definition another beam waist. With this requirement that the real part of q_f is zero, then $qf \equiv q(z_n = S_1 + S_2 + S_4)$. Thus, the radius at the focus w_0 can be isolated from the imaginary part of q_f. Since the typical splitting angles of the Wollaston prisms used in FLDI are small, they do not affect the calculation of the location and size of the focus in this context. For a pair of beam centerlines to run parallel in the test section, the Wollaston prism WP1 must be located at the focal point of the first focusing lens, such that $S_3 = f_2$. Then, through the small-angle approximation, it can be shown that the beam spacing is:

$$\Delta x = 2S_3 \tan\left(\frac{\theta}{2}\right) \approx S_3\theta \tag{2.12}$$

where θ is the Wollaston prism splitting angle. Due to the finite thickness of actual optics, measuring the length of S_3 is difficult in reality. In order to properly locate the focal length of F_1, some characterization with a beam profiler after each optical alignment is recommended to check Δx and the foci diameters.

In order to expand the FLDI system to DFLDI, various techniques have been used and were discussed in Chapter 1. The two methods considered were a second Wollaston prism/converging lens (Lawson, 2021) or diffractive optics (Hameed et al., 2022). While both techniques effectively yield the same result in regards to beam diameter and parallelism, the diffractive optics were selected due to space constraints outside of the T5 test section as well as beam spacing requirements and the possibility for increased density of beam-pairs. From a ray transfer matrix analysis perspective, the diffractive optic can be represented as a splitting element in the same manner as the Wollaston prism. As the Wollaston prism is at the focus of the converging lens in order to keep the beams parallel, it is physically impossible to place the diffractive optic in a location that keeps the beam-pairs parallel with respect to each other. To alleviate this problem, a second converging lens is added just after the diffractive optic such that the beam centers of the two primary beams interact with the Wollaston prism at the same location. Using the same optimization process above but adapted for an additional splitting element and converging lens (Lawson, 2021), with the added constraint of the optical table dimensions and the parallelism of the beam-pairs, a base linear setup of the DFLDI was developed and shown in Fig. 2.16.

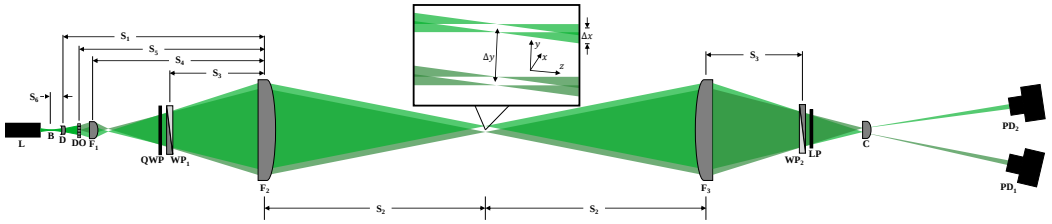

Figure 2.16: Schematic of a standard DFLDI setup using a diffractive optic as a secondary splitting element.

The final DFLDI setup used in these experiments is shown in Fig. 2.17, with the optical components listed in Table 2.2. To accommodate space, various turning mirrors are used to turn the beams before the quarter-wave plate on the pitch side and an aspheric condenser lens is used to separate the beams on the catch side. It is important to note that these additional optics are added outside the region where interference occurs (from quarter-wave plate to linear polarizer), so it has no effect on the behavior of the interferometer itself. The beam spacing is 145 µm, with the beam-pairs vertically spaced by 5.18 mm. The FLDI photodetector signals are recorded on a Yokogawa DL850E oscilloscope at 100 MHz.

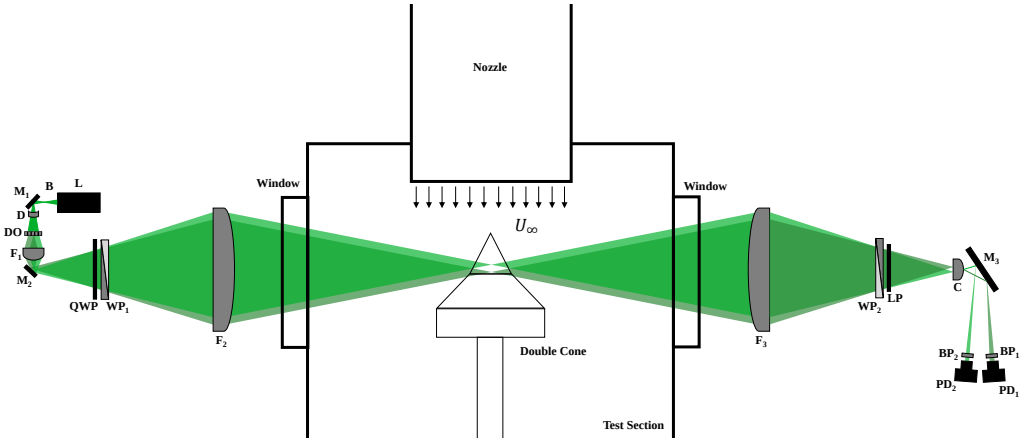

Figure 2.17: Schematic of a DFLDI setup mounted on the T5 test section.

It is important to note, initial experiments (Shots 3041–3042) were performed on the 25°-55° double-cone model separation shear layer using an 200 mW Excelsior 532nm CW laser instead of the Cobolt 05-01. These shots were used to explore the effect of the resting DC voltage of the instrument on the signal noise floor. The results of this study are covered in Appendix D.

Table 2.2: FLDI Optical Parts List

Optic	**Abbreviation**	**Part Name**
Laser	L	Cobolt 05-01 Samba 1500 mW 532nm CW laser
Turning Mirror	M_1	Thorlabs NB1-K12 25.4mm Nd:YAG Mirror
Diverging Lens	D	Thorlabs LC2067-A 9mm Plano-Concave Lens, f = -9.0mm
Diffractive Optic	DO	HOLO-OR DS-278-Q-Y-A Fused Silica Diffractive Optic, $\theta = 2.95°$
Focusing Lens	F_1	Thorlabs AC508-075-A 50.8mm Achromatic Doublet Lens, f = 75mm
Turning Mirror x2	M_2, M_3	Thorlabs PF20-03-P01 50.8mm Protected Silver Mirror
Quarter-Wave Plate	QWP	Thorlabs WPQ20ME-532 50.8mm Mounted Polymer Zero-Order Quarter-Wave Plate
Wollaston Prism x2	WP_1, WP_2	United Crystals Inc. Quarts Wollaston Prism, 50x50mm, 2 arc-min splitting angle
Focusing Lens x2	F_2, F_3	Newport PAC095AR.14 76.2mm Achromatic Doublet Lens, f = 250mm
Linear Polarizer	LP	Thorlabs LPVIS100-MP 25mm Mounted Linear Polarizer
Condenser Lens	C	Thorlabs ACL12708U-A 12.7mm Aspheric Condenser Lens, f = 8mm
Bandpass Filter x2	BP_1, BP_2	Thorlabs FLH532-10 25mm Hard-Coated Bandpass Filter, FWHM = 10nm
Photodetector x2	PD_1, PD_2	Thorlabs PDA36A2 Si Switchable Gain Detector

Optical Alignment and Calibration

The DFLDI system is aligned by first setting a target on the catch side of the test section at the height of the laser head. This height corresponds to the centroid of the four beams in the final setup shown in Fig. 2.18. This centroid is calculated relative to the model surface, and positioned using a 3-D printed alignment tool. After the necessary turning mirrors are in place, the beam height is confirmed to be constant along the z-axis before continuing. The three focusing lenses are then aligned by aiming at the target and checking back-reflections in sequence starting with the most downstream lens in the z-axis. The pitch-side Wollaston prism and quarter-wave plate are then added in and aligned using back-reflections, followed by the diverging lens. At this point in the alignment process, the pitch-side optics should be functioning as a roughly-aligned standard single FLDI system. This is confirmed visually using laser burn paper.

To aid in the precise alignment process of the DFLDI, a Thorlabs BP209-VIS beam profiler was used to measure the beam spacing (Δx), beam-pair spacing (Δy), the beam inclination (α), as well as the Gaussian beam diameter at the focus (d_0). Since the beam profiler is unable to fit near the surface of the model, the optics are translated upwards vertically in the y-axis to accommodate the beam profiler and realigned using back-reflections to measure these beam parameters. While the aforementioned rough placement of the optics was done by hand measurement, final positions were all verified using the calculated beam spacings Δx and Δy. As these beam spacings are directly coupled to the lens and Wollaston prism placement, and the beam profiler is capable of measuring beam parameters with ± 2 µm precision, the z-position of D, F_1, and WP_1 can be adjusted using a micrometer stage to maintain beam parallelism.

Once Δx, Δy, α, and d_0 are measured, the optics are locked and returned to their original y-position. Before aligning the catch-side optics, precise beam locations relative to the model are measured using a laser burn paper on an aluminum plate shaped into the negative of the model geometry. The laser burn marks are then measured under a microscope to check the beam spacing and rotation. This method gave repeatable beam orientation and position measurements, and also served as a confirmation for the beam profiler measurements. At this stage, the catch-side Wollaston prism and linear polarizer are positioned using a micrometer stage such that an infinite-fringe configuration is achieved (Lawson, 2021). The final step before calibration is focusing the two beams onto two photodetectors; any optical method

can be used at this stage as the interference is complete (as long as polarization and phase are not disturbed). In the current work, a condenser lens is used to separate the beams.

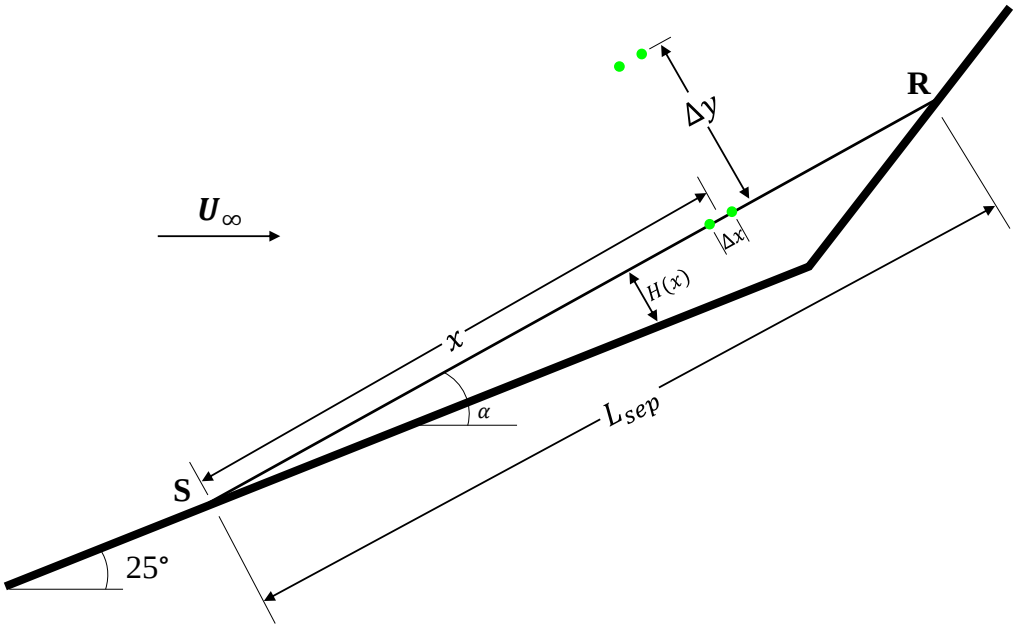

Figure 2.18: Simplified illustration of shear layer region on the double-cone with representative FLDI beams. For clarity, drawing is not to scale.

The calibration process of the DFLDI is the same as described in Lawson (2021), where a relationship between the raw photodetector voltage and $\Delta\Phi$ is established (Schmidt and Shepherd, 2015b). This function is given by:

$$V = A\sin(\Delta\Phi - \Delta\Phi_0) + D \tag{2.13}$$

As performed in Lawson (2021), the Wollaston prism is positioned where the resting photodetector voltage, V_0, is at the middle of the dynamic range. Using a Thorlabs Z812B mechanical stage controlled by a KDC101 controller, it is then translated at a small velocity through the entirety of the infinite fringe, effectively causing a constant change in $\Delta\Phi_0$. This process generates a smooth sinusoid that has an amplitude equal to that of the dynamic range of the interferometer, and curve-fitting tools can be used to fit a full period of the sine wave to calculate the constant values of A, D, and $\Delta\Phi_0$. This process is also used to check the two FLDI beam-pairs have the same dynamic range and are "in phase" with each other, allowing quantitative comparisons between the two beam positions for multi-point measurements.

Effort was taken to characterize the frequency response of the two beams using an ultrasonic acoustic generator. As the background noise and frequency response are affected by the resting voltage, care was taken to set the dynamic range and resting voltage of the two beam-pairs to match each other. It was shown that the resting voltage could only be synchronized while maintaining beam parallelism if the beams were split in the vertical direction in the current configuration, thus hitting the same splitting plane of the Wollaston prism. More on this process is detailed in Appendix D.

Chapter 3

RESULTS: STATIC PRESSURE MEASUREMENTS

The numerical modeling of external and internal flows of the various static probe designs is detailed in this chapter, as well as comparisons between the theory, simulations, and experimental data, with additional comparisons to simultaneous freestream TDLAS-based pressure inferences. The shots included in this study are Shots 2943–2946 (Static Probe V1), Shots 2972, 2973, and 2977–2979 (Static Probe V2), and Shots 3029–3031 (Static Probe V3). The material in this chapter is primarily combined from two publications: Yu et al. (2022a) and Yu et al. (2024). The work presented in Sections 3.1–3.2 is from Yu et al. (2022a), addressing most of the modeling and characterization of Static Probes V1 and V2. Sections 3.3–3.4 are from Yu et al. (2024) and cover the improvements to the response time of the static probe design (V3) and comparisons with TDLAS-based pressure inferences. As part of a larger research initiative exploring nonequilibrium flows, TDLAS was deployed in T5 over five experimental campaigns, the results of which are published in Girard et al. (2021), Finch et al. (2023b), and Finch et al. (2023a). Although most of the material in these publications will not be discussed in this thesis, the facility data and freestream conditions are tabulated in the Appendix A for completeness. The TDLAS pressure-broadening data are kindly provided by Dr. Peter Finch and reproduced here with permission.

3.1 Numerical Simulations of External Flow and Transducer Cavity

The flow over both the V1 and V2 static probes were simulated using Eilmer4, an open source Navier–Stokes solver developed by Rowan Gollan and Peter Jacobs, which has been verified and validated for the simulation of transient, compressible, viscous, and reacting 2-D and 3-D flows (Gollan and Jacobs, 2013; Jacobs, 1991). The freestream conditions chosen for this simulation was representative of the low pressure shots, with $p_\infty = 10$ kPa, $T_\infty = 1100$ K, and $U_\infty = 3600$ m/s. Since the test section is at room temperature before a shot, the surface temperature of the static probe was set to 300 K. A 280x100 cell grid with high resolution near the wall was used to achieve a detailed simulation of the boundary layer. The simulation assumes viscous, axisymmetric flow in the five-species air kinetic model of Gupta et al. (1990). The static pressure and temperature distribution can be seen in Figs.

3.1 and 3.2. The numerical results are used with permission to compare with experimental data (Hornung, H., personal communication, 2021).

It is important to note that the measured static pressure is not exactly the freestream pressure, as shown in Figs. 3.1 and 3.2. The flow at the point of measurement has passed through a weak shock and expansion at the tip and shoulder of the probe, respectively. Multiple simulations have shown that a correction factor of 0.94 (ratio of measured to free-stream pressure) must be applied to the measured pressure, which matches with Behrens' calculation (Behrens, 1963) and Karl's calculation (Karl, 2011) for Re above 1.4×10^6 m^{-1} . Additionally, the boundary layer profiles are shown in Fig. 3.3. The boundary layer is thicker by a factor of $\sqrt{5}$ on the larger probe, which is expected for the scaling between the two sizes.

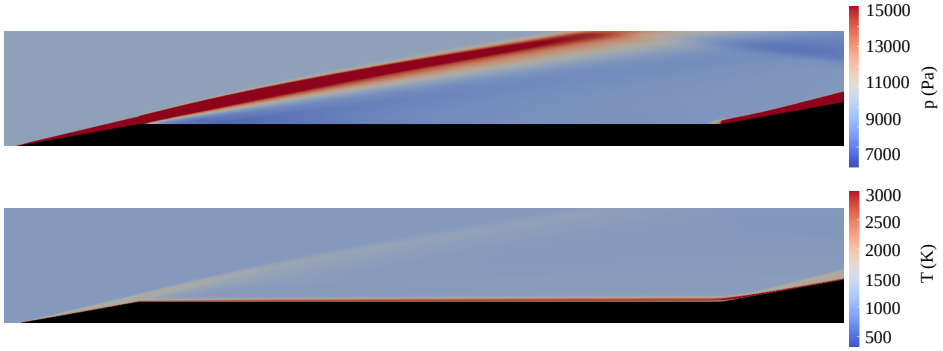

Figure 3.1: Pressure (top) and temperature (bottom) contours at steady state for the large static probe simulated in Eilmer4.

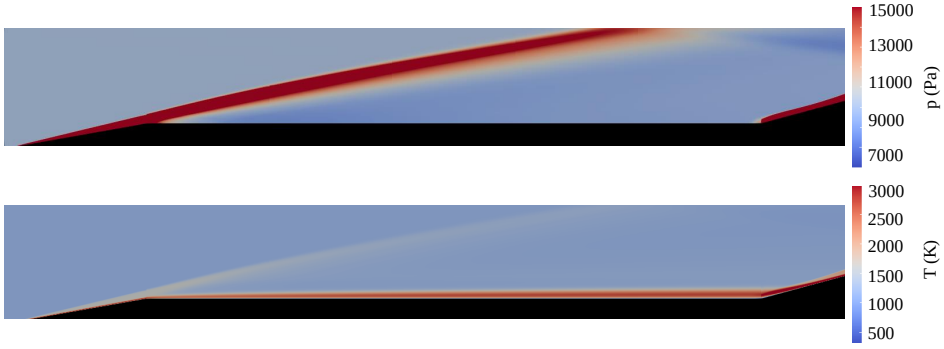

Figure 3.2: Pressure (top) and temperature (bottom) contours at steady state for the small static probe simulated in Eilmer4.

Additional two-temperature simulations were performed to model the flow in the pressure taps and the probe cavity to further understand the response time of the

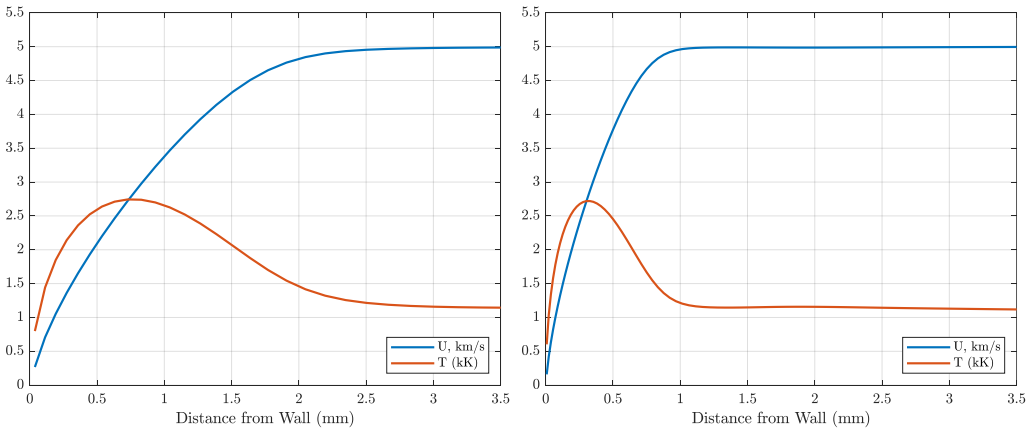

Figure 3.3: Computed boundary layer velocity and temperature profiles at steady state at the pressure tap location for the large **(left)** and small **(right)** probe.

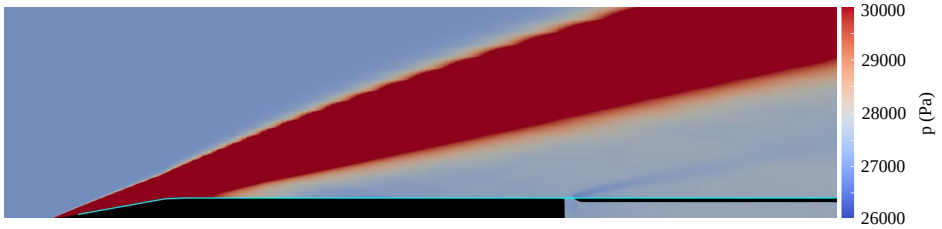

Figure 3.4: Simulated pressure distribution at steady state for the small static probe in the 16 MJ/kg condition. Sonic line in the boundary layer is shown in turquoise.

probe and possible sources of noise from acoustic ringing. Fig. 3.4 shows the pressure distribution of the small probe in the 16 MJ/kg case (27–30 kPa), including the cavity housing the Kulite transducer. Fig. 3.5 shows an enlargement of the the cavity of the large probe showing sound speed. In both probes, the sonic line is shown in turquoise. The geometry of this equivalent axisymmetric configuration has the slit width with the same hydraulic diameter as the four probe holes. Since the axisymmetric geometry increases the total internal volume of the probe, the volume of the transducer cavity is correspondingly reduced to match the physical geometry. The same geometry was used in the simulations for both probe sizes and the pressure responses are compared to the theoretical and experimental traces in the following section.

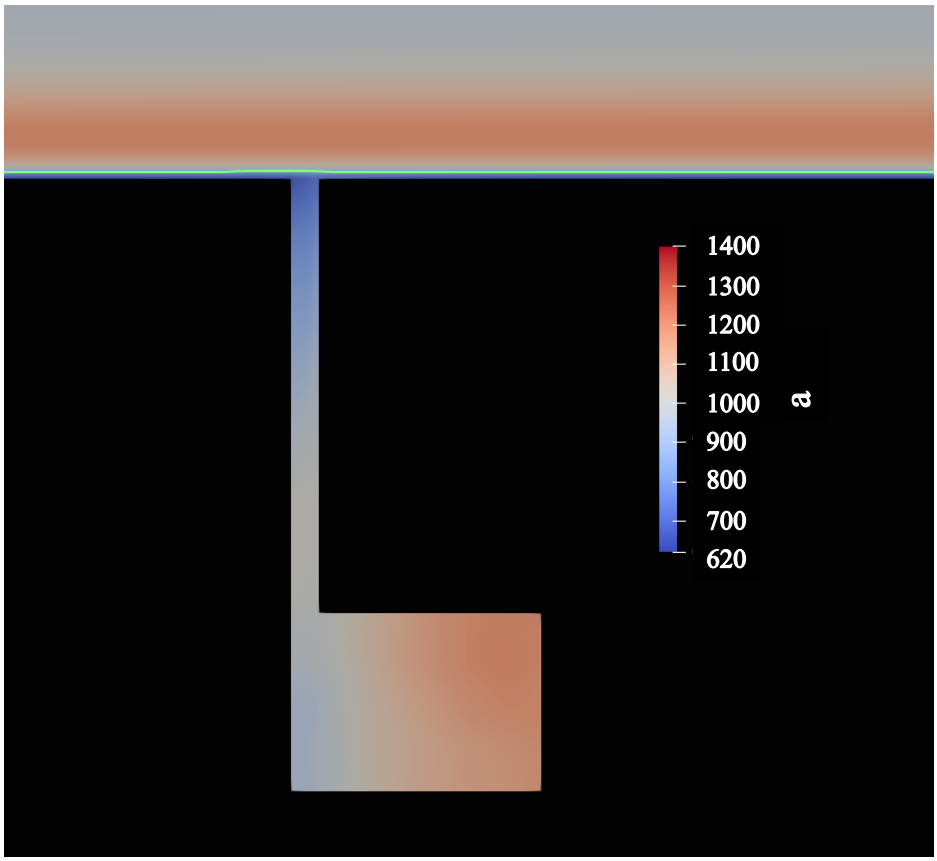

Figure 3.5: Simulation of the sound speed outside and inside the transducer cavity at steady state for the large probe. Sonic line is again shown in turquoise.

3.2 Static Probes V1 and V2 Results

The six shots used in this part of the study are at two of the aforementioned conditions used in various research campaigns in T5: H8-Re2-Air and H18-Air. The two conditions were ideal candidates since measurements of freestream temperature and velocity have recently been obtained (Finch et al., 2023b; Girard et al., 2021). Both conditions were repeated twice in this study, and the static pressure traces agree well with each other, as well as with the simulated static pressure, as seen in Fig. 3.6. We can also see the condition dependent ~200–250 µs nozzle startup process shown by the time shift between the reservoir pressure and the static pressure rises. For consistency, $t = 0$ is always determined by the pressure rise in the nozzle reservoir due to the arrival of the incident shock. Shots 2943 to 2946 were performed with just the large static probe installed, and Shots 2972 and 2973 were performed with small probe and pitot probe mounted in parallel with the large probe. The three probes were mounted such that the pressure taps were at the same streamwise location inside

the test rhombus, so the freestream conditions are the same between the probes.

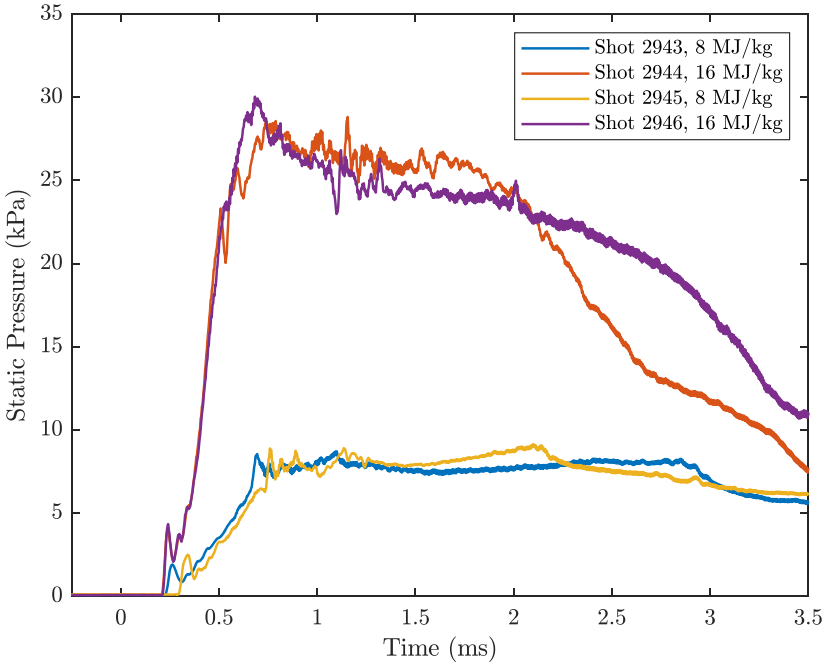

Figure 3.6: Static pressure traces for the four tabulated shots (2943–2946) in Table A.1 using the large probe, includes one repeat shot for each condition to show repeatability and shot to shot variation.

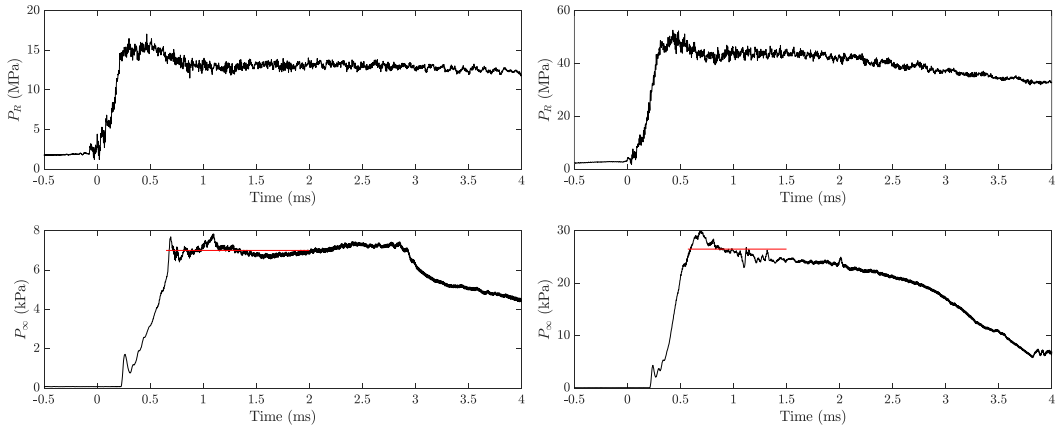

Figure 3.7: Nozzle reservoir pressure and static pressure traces for Shot 2943, 8 MJ/kg case **(left)** and Shot 2946, 16 MJ/kg case **(right)**. The red lines indicate the Nozzle Code-predicted freestream static pressure during the nominal test time.

An important result that can be extracted from the static pressure trace is the end of test time. The static pressure traces are plotted next to the nozzle reservoir pressure traces in Fig 3.7. Traditionally, the test time is determined by visually inspecting the reservoir pressure trace and using the decrease in pressure to demarcate the end of test time. However, this method is not accurate, as the reservoir pressure decreases gradually. In the static pressure trace, however, the arrival of driver gas is realized clearly with a sharp decrease in static pressure (Sudani and Hornung, 1998). In the 8 MJ/kg total enthalpy condition, the test time is nearly 2 ms, while the 16 MJ/kg total enthalpy condition has just under 1 ms of test time, which agrees well with Sudani and Hornung (1998). The beginning of test time is also shown by the pitot trace plotted in parallel with the static pressure and reservoir pressure as shown in Figs. 3.8 and 3.9. The relatively constant value of P_∞/P_R during test time is a good indicator of steady freestream velocity. The shot-to-shot comparison shows good repeatability and agreement between the absolute pressure measurement of the two probes. It is clear the slower response time of the smaller probe does filter flow features that are evident in the large probe signal. Initial tests with the pitot probe showed thermalization effects causing the voltage to drop during test time, thus preventing the end of test time from being clearly identified. This issue was mitigated by placing loose steel wool in the pitot probe upstream of the transducer and covering the transducer face with a thin film of silicone, effectively protecting the transducer from thermal effects during the shot. Note the ~4 kHz oscillation in the pitot trace, which corresponds to the "organ pipe" acoustic ringing inside the pitot tube, with frequency scaling with the local sound speed and tube length. This can be mitigated by using a smaller diameter and shorter length tube in future pitot probe designs.

The final comparison is between the theoretical, simulated, and measured response time of the two static probes. Initial theoretical calculations assuming freestream sound speed yielded a factor of two faster response time compared to the simulation. As seen in Fig. 3.5, the sound speed in the tube leading to the cavity is much lower than in the freestream, so the theoretical response time was recalculated with a cold wall sound speed, and agreed well with the simulated time response. These two pressure response curves for the 16 MJ/kg case are shown in Figs. 3.10 and 3.11, overlaid with the Shot 2972 experimental pressure response for the corresponding probe. Since the simulation and theory do not account for the aforementioned nozzle startup process, the theoretical and simulated responses are time shifted by 200 μs to match the experiment time. In both probes, the experimental responses reach test

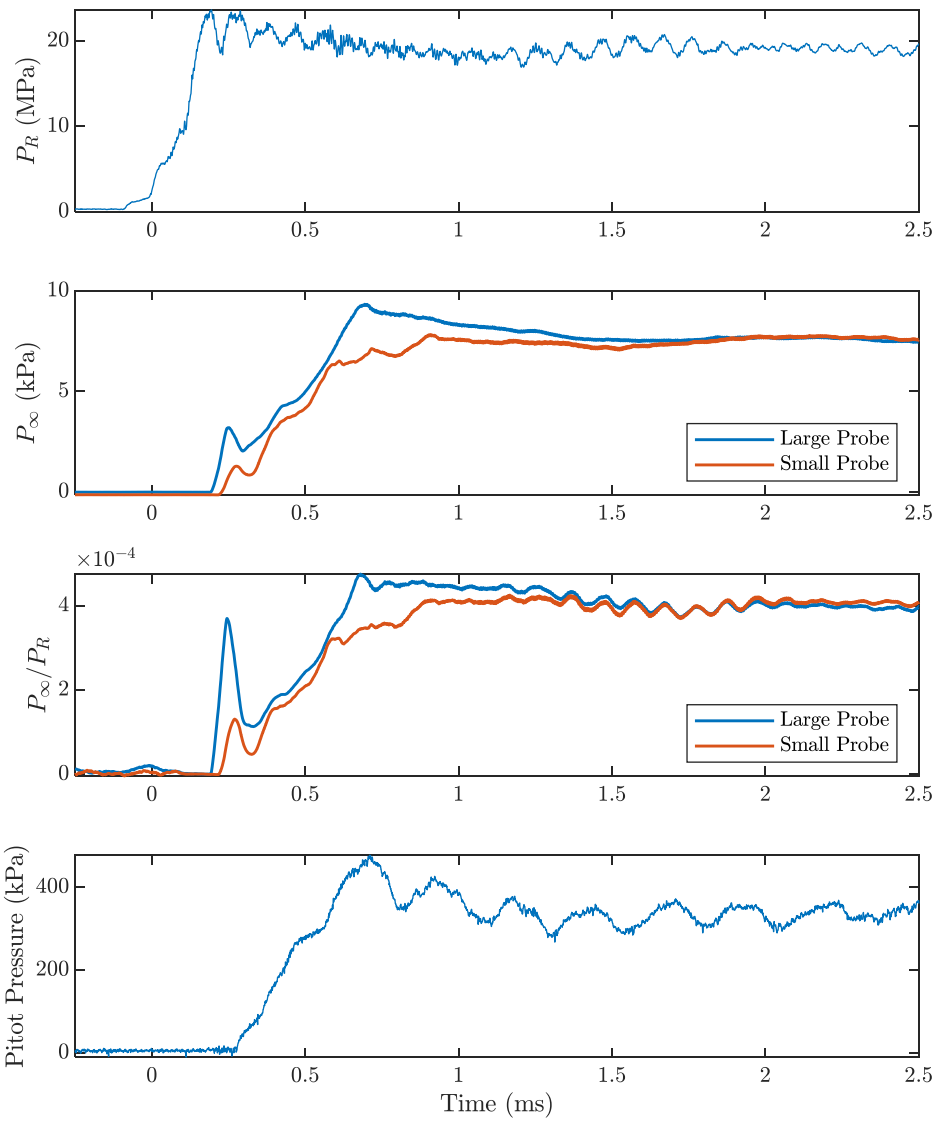

Figure 3.8: Nozzle reservoir (top) and static pressure comparison between the two static probes (middle), and the pitot probe (bottom) traces for Shot 2973, 8 MJ/kg case.

time steady state at comparable times to those of the theory and simulation. While non-ideal features from the startup can be seen in the experiment, the overall shape of the response matches as well. For the large probe (V1), the theory, simulation, and experiment agree well in magnitude and temporal behavior. However, for the small probe (V2), the complex internal geometry caused the simulations to diverge from the theoretical prediction, and poor agreement is observed in the startup when compared to the experiment. While the magnitude agrees well when steady state is reached, it is clear that modeling the internal geometry requires higher resolution

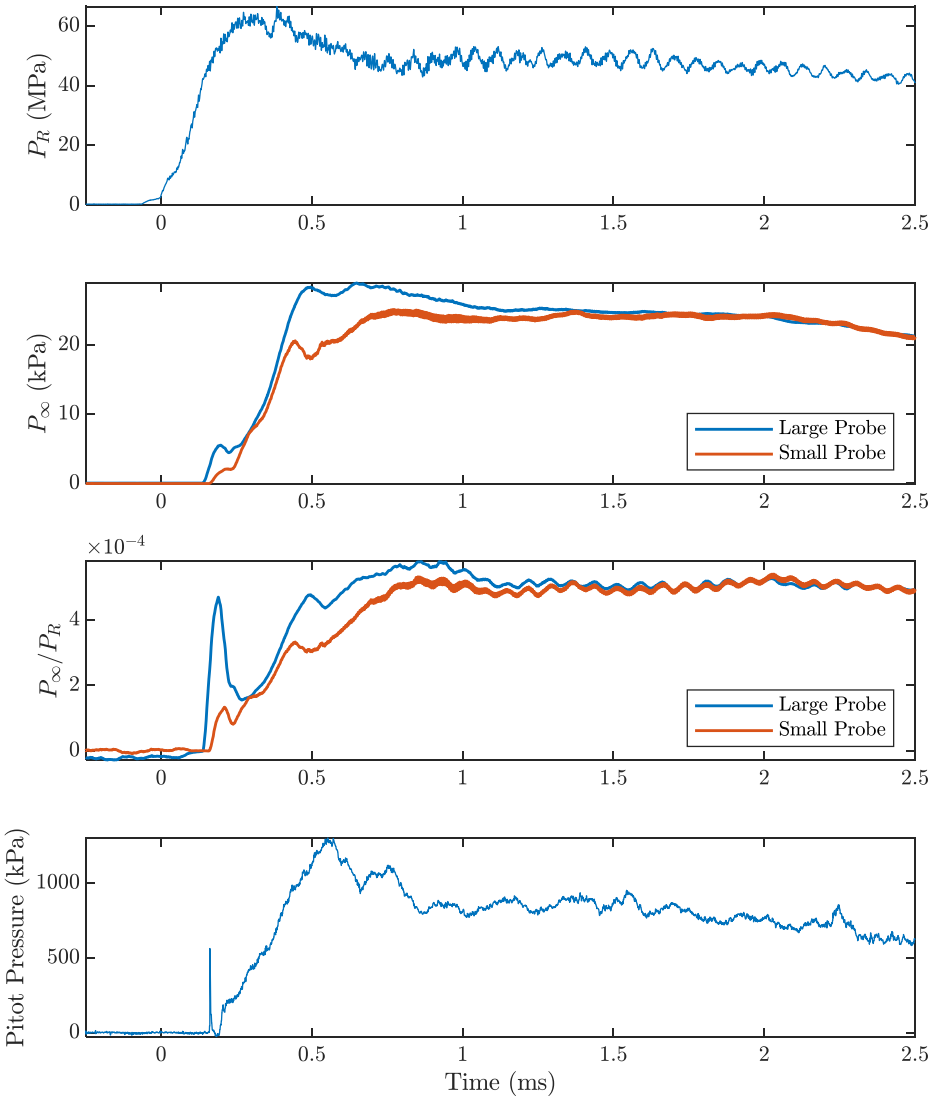

Figure 3.9: Nozzle reservoir (top) and static pressure comparison between the two static probes (middle), and the pitot probe (bottom) traces for Shot 2972, 16 MJ/kg case.

3-D simulations. At this stage, effort was placed in designing the V3 probe with a smaller and simpler internal cavity.

3.3 Comparison to TDLAS-Inferred Pressure

As shown above, the static pressure in the freestream of both conditions has been measured using static probe V1 and shows good repeatability and agreement with the nozzle-code-simulated static pressure. In the same study, the smaller static probe V2 was tested in the same conditions and agreed well with V1, albeit with

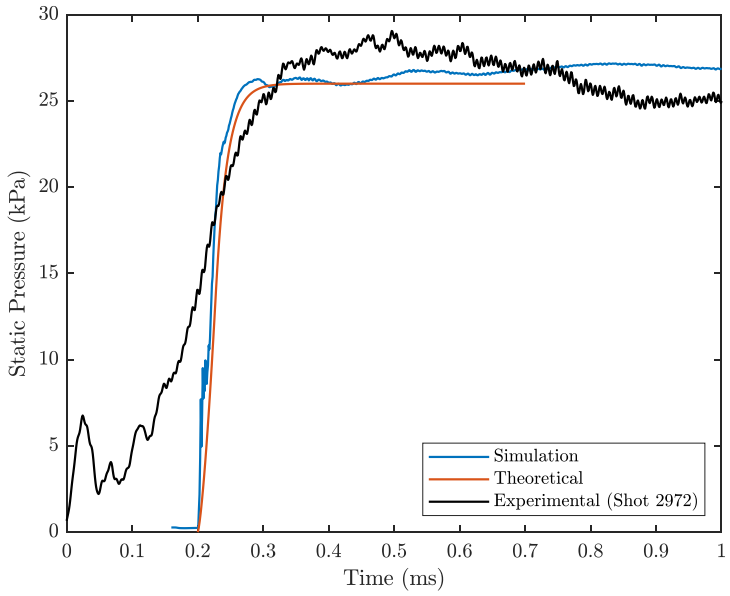

Figure 3.10: Comparison of large static probe response time between theoretical, viscous CFD simulation, and experimental data for Shot 2972. The theory and simulation responses are shifted by 200 µs to account for the nozzle startup time.

a slower response time due to the recessed position of the transducer. In the current work, V2 was used to measure static pressure simultaneously with TDLAS in the 8 MJ/kg condition. The V1 static probe data were used to compare with TDLAS measurements for the 16 MJ/kg case using repeat shots. The measurement uncertainties for each measurement technique are represented by shaded bands in Figs. 3.16-3.18. For all three static probes, the main source of the 2.5% measurement uncertainty is the pressure calibration process, which involves evacuating the test section in stages, recording the pressure at discrete points, and fitting a linear regression. With a new pressure gauge recently installed, this uncertainty can be reduced even further in future experiments by recording the pressure continuously over the entire evacuation process.

The pressure traces from the two measurement techniques in the 8 MJ/kg case are plotted in Figs. 3.12-3.14 along with the nominal nozzle-code-predicted freestream pressure during test time. The static probe measurement magnitude and TDLAS measurement agree well with the nozzle-code-predicted freestream pressure for most of test time. However, it is evident that earlier in test time and in the nozzle startup, the more transient pressure changes in the TDLAS pressure are not seen

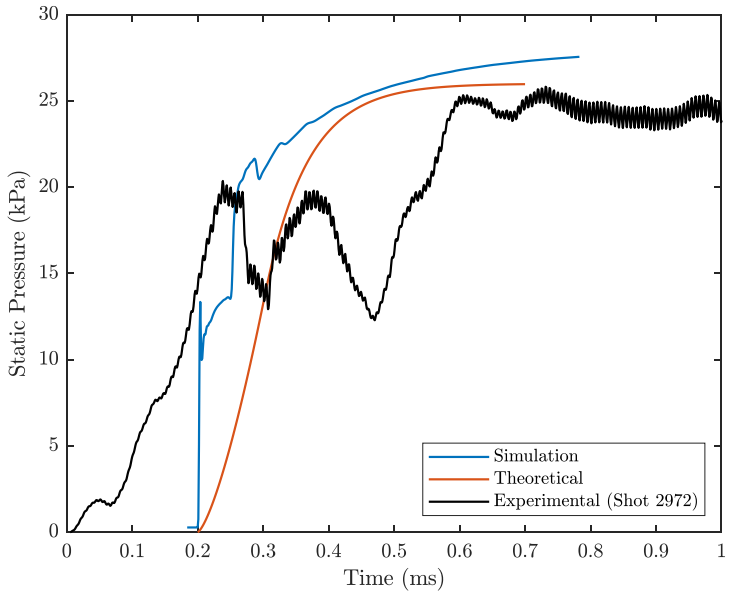

Figure 3.11: Comparison of small static probe response time between theoretical, viscous CFD simulation, and experimental data for Shot 2972. The theory and simulation responses are shifted by 200 µs to account for the nozzle startup time.

in the static probe measurement. Unsteady flow features during the nozzle startup process before test time cause larger uncertainties in both measurement techniques. The slower response time of the static probe does not capture the pressure overshoot seen in the reservoir pressure and TDLAS measurement, thus the measured value is below the Nozzle Code prediction in the early test time. The faster response of the TDLAS measurement resolves the transient nozzle startup and then converges with the static probe measurement onto the nozzle-code-predicted freestream pressure.

The discrepancy between the two techniques is more noticeable in the 16 MJ/kg condition, where test time is 40% shorter and freestream velocity is 30% higher. Additionally, the uncertainties in the spectroscopic constants used to infer static pressure at T>2000 K (Almodovar et al., 2019) in the 16 MJ/kg condition may exacerbate the difference in the two pressure measurements. As seen in Fig. 3.15, the overall behavior is similar to the 8 MJ/kg condition as the TDLAS pressure overshoots the nozzle-code-predicted value and settles back to the value during test time. However, in the 16 MJ/kg condition, the static probe and TDLAS measurements do not agree within their respective measurement uncertainty bounds. While the simultaneous measurements show the static pressure can be accurately measured

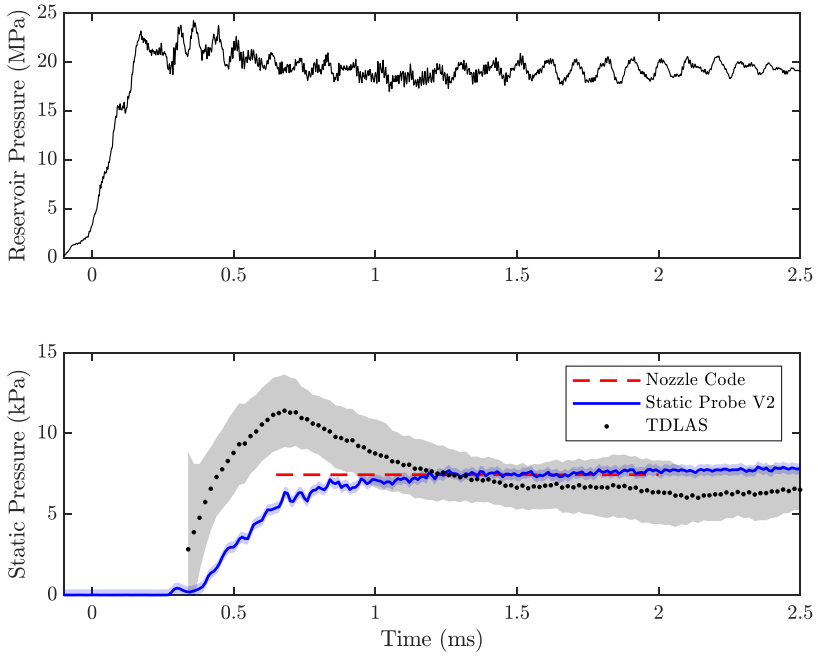

Figure 3.12: Comparison of static probe and TDLAS pressure measurements for Shot 2977.

in T5, additional improvements to the static probe design are needed to reduce the response time. Since the response rate of the Kulite transducer is around 30 kHz (Hurst et al., 2014), the internal cavity geometry of the static probe needs to be small enough to match the physical and electrical response time of the sensor. This is possible with some slight adjustments to the probe diameter so the transducer can be placed just downstream of the pressure taps similar to the V1 design.

3.4 Improvements to Response Time: Static Probe V3

In an effort to improve the response time of the in-situ static pressure measurements, another version of the small static probe was designed (V3). Although the external geometry is essentially unchanged, the slightly larger tube diameter allows the placement of the pressure transducer just downstream of the pressure taps, whereas the transducer in V2 was located near the shoulder of the probe. This reduction of internal volume shortens the response time of the static probe by a factor of 10. With an effective response rate of 30 kHz, the probe can resolve the transients exhibited during the nozzle startup.

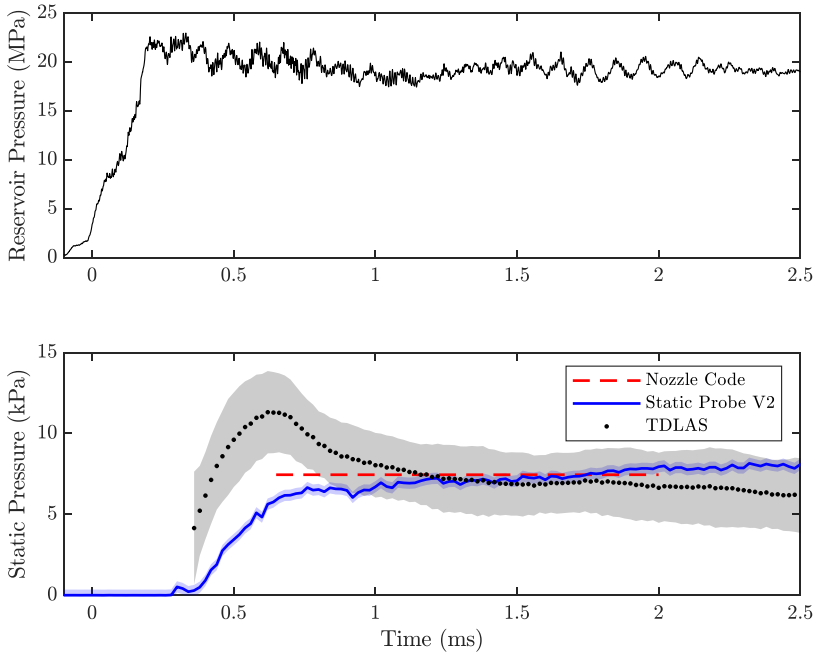

Figure 3.13: Comparison of static probe and TDLAS pressure measurements for Shot 2978.

For the 8 MJ/kg condition (Shots 2977 and 3029), the newly designed static probe V3 was used in Shot 3029 to compare with the simultaneous TDLAS and V2 measurements from Shot 2977. In Fig. 3.16, both static pressure traces from V2 and V3 are plotted with the TDLAS measurement along with the Nozzle Code-predicted freestream static pressure. Note that the condition dependent ~200–250µs startup process can be observed in the time shift between the reservoir pressure and the static pressure rise. The TDLAS-inferred pressure overshoots the Nozzle Code-predicted pressure, then monotonically decreases to the steady-state pressure during test time, intersecting the pressure trace of static probe V2. This discrepancy was due to the significantly slower response time of static probe V2, motivating the design of the V3 probe. The quicker response time of V3 compared to V2 is immediately observable in the sharp spike during the arrival of the transmitted and nozzle startup shocks at $t \approx 250\mu s$. Additionally, the temporal behavior during the pressure rise and downward slope in test time matches well with TDLAS-inferred pressure. As expected, it is clear that the faster response time brings the two

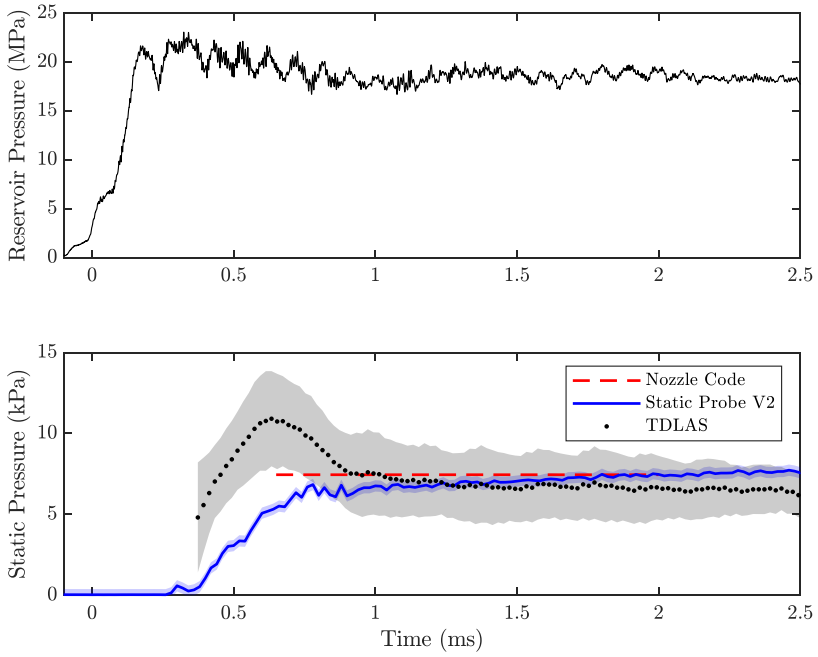

Figure 3.14: Comparison of static probe and TDLAS pressure measurements for Shot 2979.

pressure measurement techniques closer in absolute value and temporal behavior. The TDLAS sample rate of 50 kHz is still higher than the 30 kHz static probe response rate, which is physically limited by the pressure tap size and the rise time of the transducer. Thus, the static probe V3 temporal response still lags behind the TDLAS, and does not reach the same peak pressure before test time.

Simultaneous static pressure and TDLAS measurements for the 16 MJ/kg were not obtained, so two repeat shots are used to compare the two techniques (Shots 2919 and 2946). TDLAS was used to measure static pressure in Shot 2919 and the V1 static probe was used in Shot 2946. As seen in Fig. 3.17, the two measurements exhibit the same behaviors as seen in the 8 MJ/kg case, but the temporal discrepancy is larger due to the response time of the probe and the higher velocity and shorter test time in the 16 MJ/kg condition. These effects contribute to pushing the disagreement outside of the measurement error bounds. The V3 probe was tested in the same condition and the magnitude and temporal agreement is significantly improved. As seen in Fig. 3.17, static probe V3 resolves the nozzle startup process more accurately

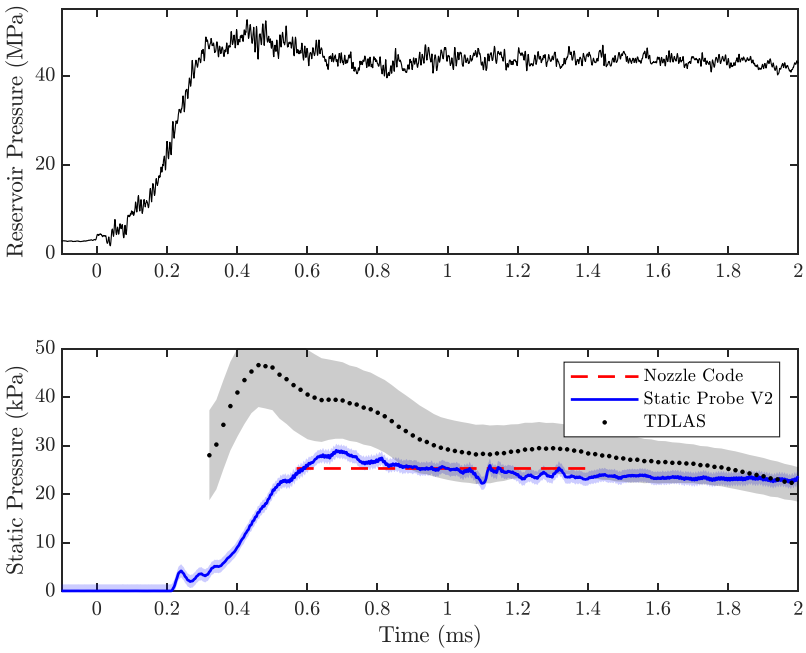

Figure 3.15: Comparison of static probe and TDLAS pressure measurements for Shots 2919 and 2946.

than static probe V1, and the slope of the pressure trace both before and during test time matches closely with the TDLAS-inferred pressure. Unlike the response of static probe V1, the V3 trace is within the measurement error of the TDLAS for the duration of test time, which increases the confidence in both measurement techniques for this higher enthalpy condition. Spectroscopic constants used to infer static pressure become increasingly uncertain at the higher temperatures (>2000 K) of the 16 MJ/kg condition, but this improved agreement does indicate the viability of broadening-based pressure measurements in these high-temperature environments. Additional comparisons of the static probe and TDLAS signals to time-resolved nozzle computations in Eilmer4 are discussed briefly in Appendix C.

Another test of the static probe V3 capability is the sensitivity to facility tailoring. Tailoring refers to the fine-tuning of the acoustic impedance between the test gas and driver gas, which determines the nature of the reflected wave when the main reflected shock interacts with the contact surface (Gaydon and Hurle, 1963). T5 is generally operated at slightly under-tailored conditions to delay the arrival of

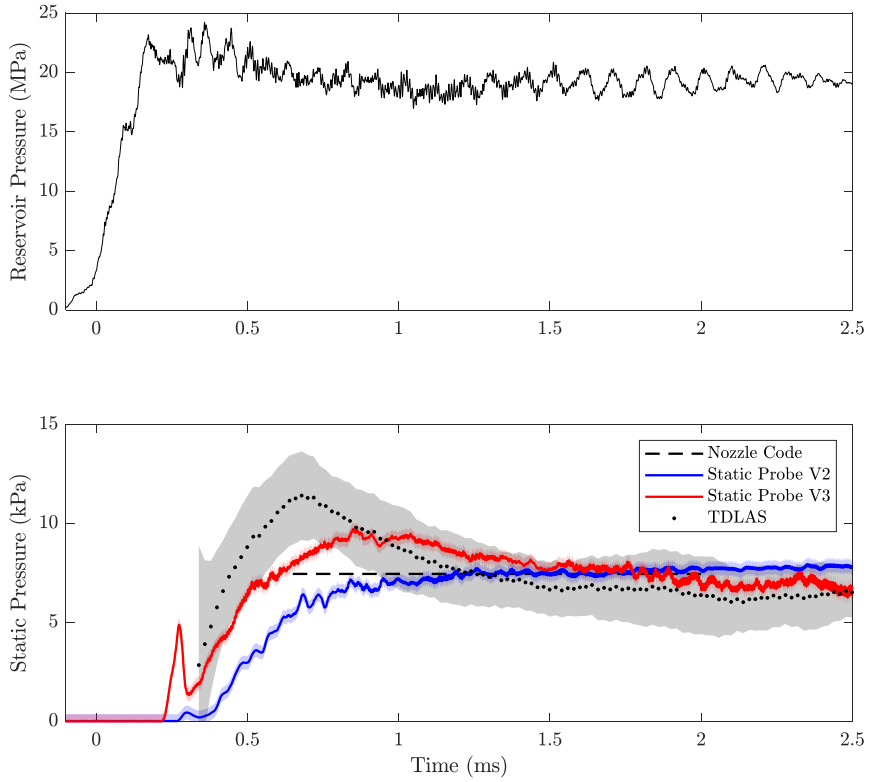

Figure 3.16: Static pressure traces for the 8 MJ/kg condition (Shots 2977 and 3029) using static probes V2 and V3 and TDLAS. The shaded bands are the associated uncertainty for each measurement. The length of the dotted line represents the nominal test time.

driver gas and maximize the length of usable test time (Sudani and Hornung, 1998). For previous spectroscopic studies (Finch et al., 2023b; Girard et al., 2021), the tailoring of the facility was determined by qualitative inspection of the nozzle reservoir trace. While the reservoir pressure measurement is generally a sufficient metric for facility operation, it is not a quantifiable freestream property that can be used to anchor spectroscopic measurements. Static probes V1 and V2 were able to resolve the general decrease in pressure during test time for the 16 MJ/kg condition, which is expected from a slightly under-tailored condition. However, the slower response times of the earlier probes could not measure the subtle differences between differently tailored versions of the same condition. The minimized time response of static probe V3 was tested in a better-tailored version of the 16 MJ/kg condition that would yield a more constant pressure trace in the latter half of test time (Shot 3031). In Fig. 3.18, Shot 3031 is plotted with Shot 3030 as a comparison. The

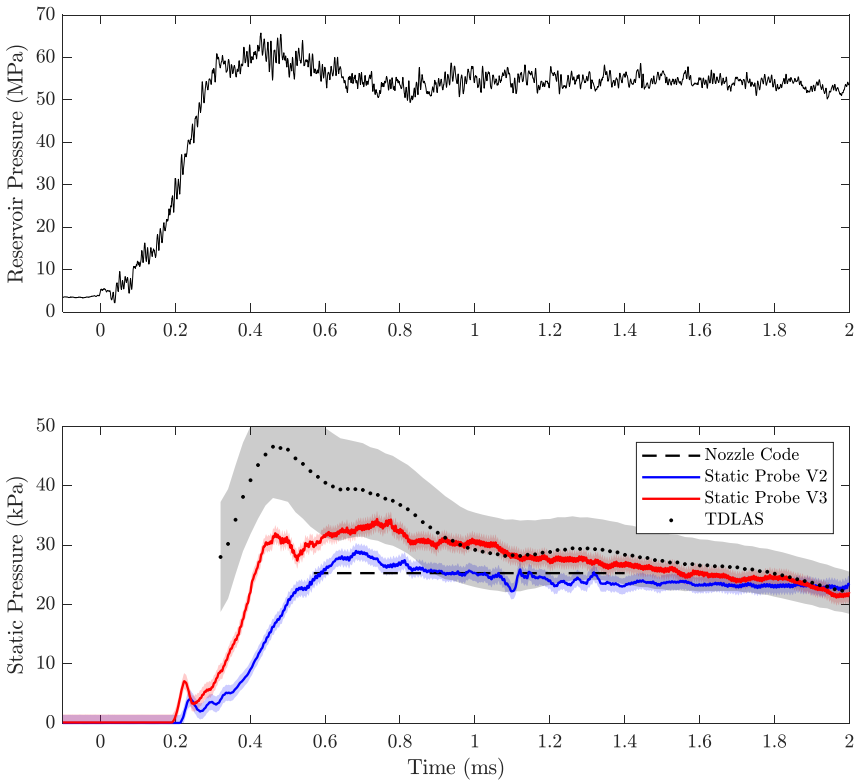

Figure 3.17: Static pressure traces for the 16 MJ/kg condition (Shots 2919, 2946, and 2977) using TDLAS, static probe V1, and static probe V3, respectively. The shaded bands are the associated uncertainty for each measurement. The length of the dotted line represents the nominal test time.

reservoir pressure exhibits the expected behavior of decreasing earlier in test time and rising to the steady state for the second half of test time, which is a characteristic of a better-tailored condition. The static pressure trace follows this trend and decreases quickly in the first half of test time before flattening out for the second half instead of slowly decreasing for the entirety of test time. Having this capability to measure slight changes in freestream temporal behavior simultaneously with test models is valuable, as it allows for better shot-to-shot comparison and makes fine-tuning of new conditions much easier. This final version of the static probe will be a permanent fixture for future experiments that allows installation of parallel instrumentation.

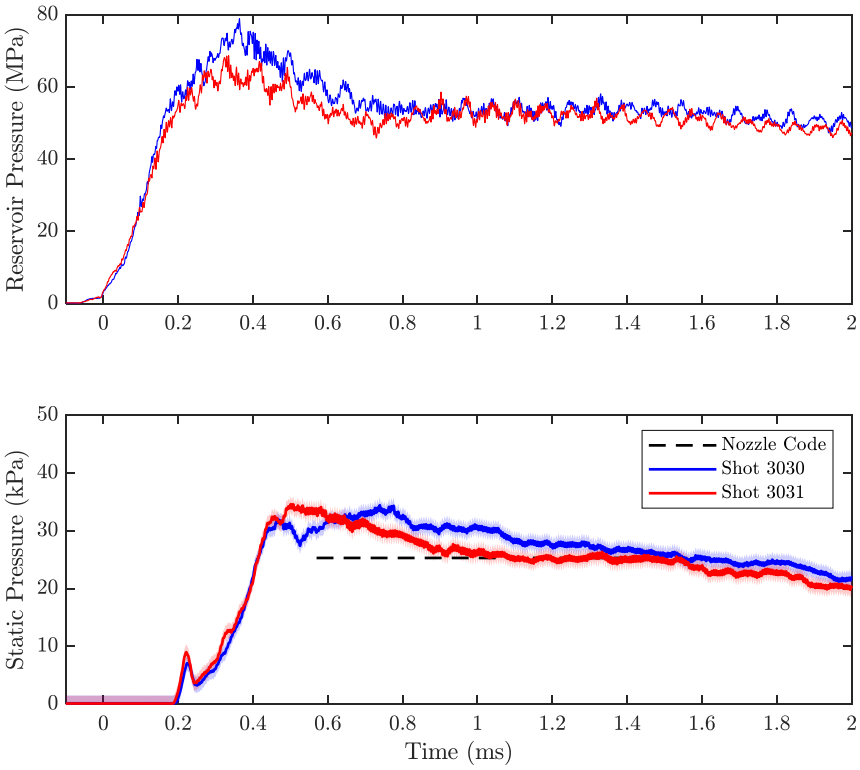

Figure 3.18: Static pressure traces for the 16 MJ/kg condition (Shots 3030 and 3031) using static probe V3. With the quick response time of the V3 probe, small temporal differences can be observed in the freestream caused by slight condition tailoring.

Chapter 4

RESULTS: DRIVER GAS DETECTION

The results in this chapter include 3-D numerical simulations of canonical opposing-wedge flow, with monatomic driver gas added as a non-reacting contaminant to determine the sensitivity bounds of the opposing-wedge geometry to freestream driver gas contamination levels. The simulation results are then compared with high-speed schlieren and shadowgraph images of the the opposing-wedge flow in T5 and results from Sudani and Hornung (1998). The material presented is mostly reproduced from, but with additional quantitative analyses of the high-speed images.

4.1 Numerical Simulations of Opposing-Wedge Flow

The flow over the opposing-wedge model is simulated in 3-D using Eilmer4 (Gollan and Jacobs, 2013; Jacobs, 1991). The freestream conditions chosen for this simulation are representative of the H8-Re2-Air condition shown in Table 2.1, with p_∞ = 7.46 kPa, T_∞ = 1067 K, and U_∞ = 3.619 km/s. Since the test section is at room temperature before a shot, the surface temperature of the model is set to 300 K. The simulation assumes unsteady, reacting, viscous flow with vibrational and chemical nonequilibrium in the five-species air kinetic model of Gupta et al. (1990). The inflow boundary condition is set to the freestream condition, with a reflecting boundary condition at the symmetry plane. The 3-D computations are run with a coarse grid of 1000 cells per block with 32 blocks for 50 flow times (flow time = W/U_∞), followed by a run with a finer grid of 8000 cells per block for five flow times, and then by a run with the finest grid of 64000 cells per block for one flow time. During the run with the coarse grid, the flow reaches steady state, then each refinement uses the last condition of the previous run as the initial state. The numerical results are used with permission to compare with experimental data (Hornung, H., personal communication, 2022).

Initial simulations with pure air test gas showed that the flow chokes at G = 14.4 mm, providing a lower bound for the gap size. A new gas model was added by Rowan Gollan in 2022, allowing helium to be seeded as a passive contaminant in reacting two-temperature air. This was used to vary the degree of helium contamination by mole fraction, X_m, for a range of values of G, and the choking threshold was determined for each gap size. The thresholds were used to generate an empirical

curve separating the choked and unchoked regimes in the X_m vs. G space. This curve-fit is shown with all the simulated contamination levels and normalized gap sizes in Fig. 4.1. To compare the different data sets, the three gap sizes of the experiments are overlaid as vertical dashed lines onto the plot of X_m vs. normalized gap size G/W, while the contamination levels measured by Sudani and Hornung are overlaid as horizontal dotted lines to relate X_m to instances in time.

An important behavior shown in the simulations is the rate at which choking occurs. For instance, the case with G = 14.7 mm and X_m = 0.067 takes 0.5 ms to fully choke as shown in Fig. 4.2. Given that the test time for this condition is 1.5 ms, and the helium contamination in the freestream changes with time, the response time is a complicating factor. Thus, some additional 3-D simulations were performed with a smaller wedge with the same span (W = 10 mm, G = 5.4 mm). The location of the Mach stem for the two model sizes is tracked relative to the expansion corner of the wedge over time and plotted in Figs. 4.3 and 4.4. The shorter wedge length and increased two-dimensionality of the smaller model quickens the response from 0.5 ms to 0.1 ms, an acceptable delay for this condition. The experimental results presented in the following section focus on the larger model as a proof of concept in detecting driver gas in the freestream and a comparison to Sudani and Hornung's results.

4.2 Experimental Results

This section discusses the findings from the time-resolved high-speed images of four shots performed using the larger opposing-wedge model. Three gap sizes were used (14.7 mm, 16.5 mm, and 15.8 mm), with the 15.8 mm case repeated using air test gas seeded with a helium/argon mixture. For consistency, t = 0 will refer to the time of the pressure rise in the reservoir, P_R (threshold of P_R = 1 MPa), and the time of the first upstream motion of the Mach stem is defined as t_c.

The schlieren images taken during Shot 3012 with G = 14.7 mm (G/W = 0.400) are shown in Fig. 4.5, where the flow began choking 0.1 ms after test time begins at t = 0.56ms. The three images show the progression of the Mach stem from t_c = 0.66 ms to being fully choked by t = 1.1 ms. This agrees well with the predicted 0.5 ms choking time from the simulations, and the size of the Mach stem in early test time suggests the contamination level is close to the choking threshold for this gap size. As seen in Fig. 4.1, this corresponds to a 2% monatomic gas mole fraction in the freestream, which is possible for this condition since the reflected shock in the

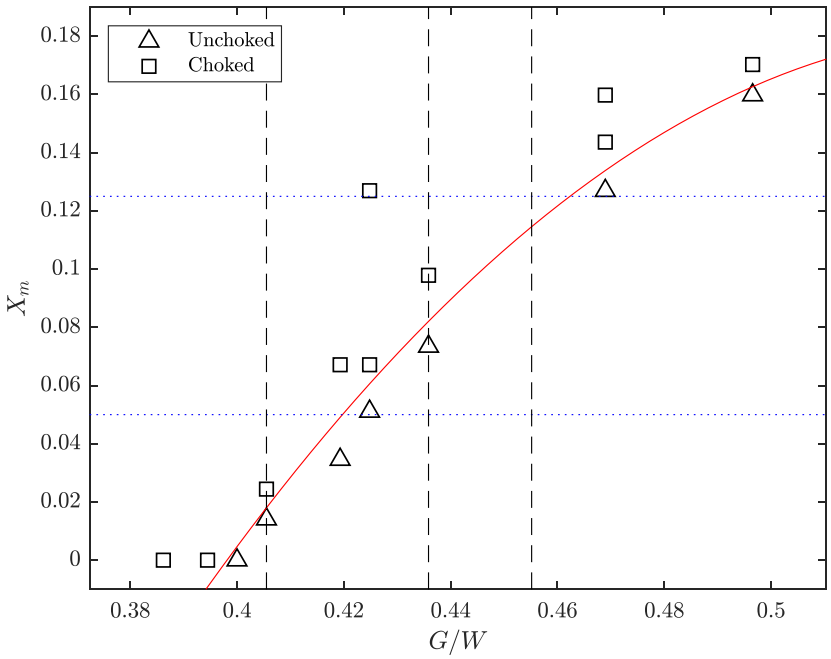

Figure 4.1: Plot relating the mole fraction of monatomic gas, X_m, and the normalized gap size, G/W. The experimental gap sizes used in the four shots are shown as vertical dashed lines, while the dotted lines demarcate the cutoff mole fractions from Sudani and Hornung's gas detector study.

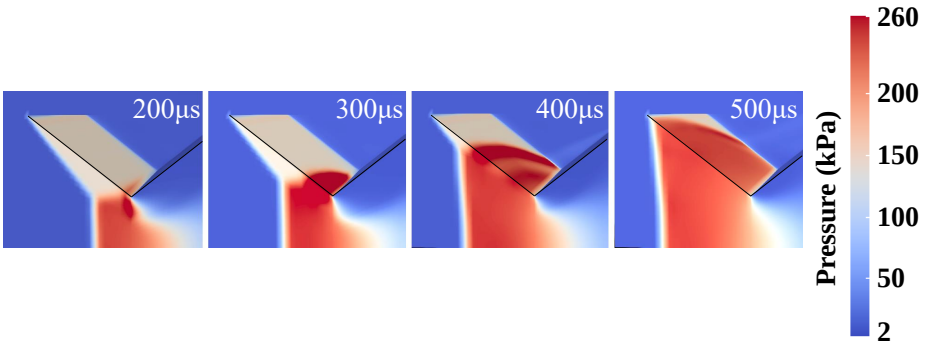

Figure 4.2: Development of the impingement region with time in a 3-D pressure distribution for the case G = 14.7 mm and 1% helium mass fraction at 200, 300, 400, and 500 µs from flow start, simulated in Eilmer4. The black lines delineate the model edge for clarity.

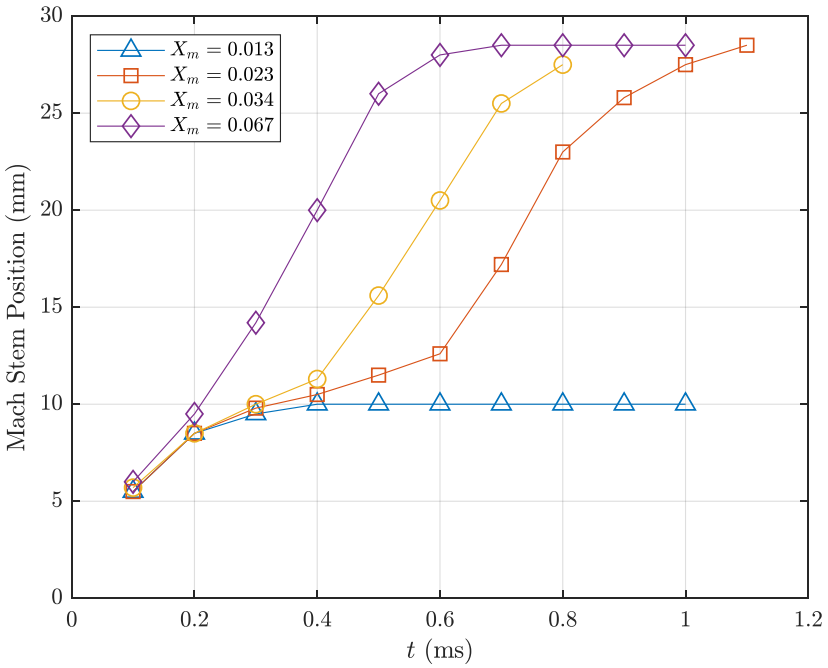

Figure 4.3: Simulated Mach stem location, s, of the Mach stem upstream of the expansion corner of the large W = 36.25 mm, G = 14.7 mm opposing-wedges over time at various values of X_m in the freestream.

shock tube will interact with the contact surface within 0.5 ms after reflecting off the shock tube end wall. However, this gap size was clearly too sensitive since the reflected shock is impinging on the expansion corner, so other factors in the flow can cause the flow to unstart. Additionally, it was clear from these images that the diffraction artifacts from the knife-edge and high contrast affected the clarity of the flow features, so subsequent shots used a shadowgraph setup instead.

In Fig. 4.6, the shadowgraph images of the G = 16.5 mm (G/W = 0.455) wedge configuration from Shot 3013 are shown. According to the curve-fit in Fig. 4.1, this configuration is expected to choke at 11.5% monatomic gas contamination. The experiment agrees with this prediction and Sudani and Hornung's measurement as the Mach stem is stable until there is slight upstream motion at t = 2.25 ms. This is in the same time period (t = 2.25–5 ms) in which Sudani and Hornung measured $\leq$12.5% contamination in the freestream of the 14 MJ/kg test condition. It can be concluded that the helium contamination level in the 8 MJ/kg condition is well

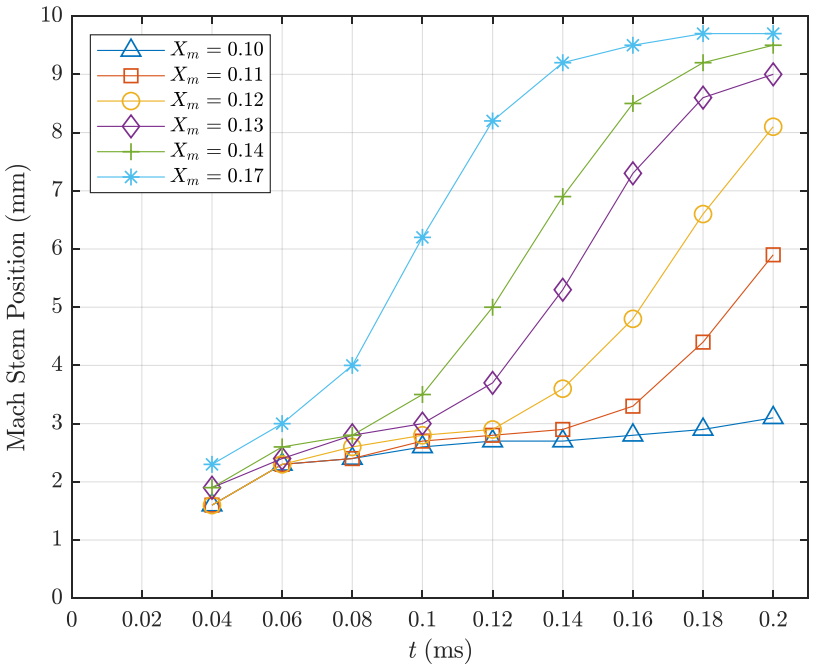

Figure 4.4: Simulated Mach stem location, s, of the Mach stem upstream of the expansion corner of the small W = 10 mm, G = 5.4 mm opposing-wedges over time at various values of X_m in the freestream.

below the 11.5% threshold given by the curve-fit before t = 2.56 ms. However, this wedge configuration is not sensitive enough to bound the contamination level in time more accurately than Sudani and Hornung.

The 100 kHz frame rate limited the collection time to 2.56 ms for Shots 3012 and 3013, so the footage of the flow fully choking was not captured. The frame rate was adjusted to 75 kHz in the subsequent two shots to capture 3.41 ms of footage. The G = 15.8 mm (G/W = 0.436) configuration is shown in Fig. 4.7. The Mach stem exhibits the same slight upstream motion observed in the previous shot, and the flow begins to choke at t_c = 3.25 ms, signifying a contamination level ≤8% from t = 0.56–3.25 ms, bracketing the measurable contamination levels between 2.5% and 8% mole fraction for the duration of test time of the 8 MJ/kg condition. Based on Sudani and Hornung's measurements and the observed steady behavior of the Mach stem at $t \leq$ 2.25 ms, it is likely that X_m is closer to 2% for the duration of test time (t = 0.56–2.25 ms) and grows to 8% from t = 2.25–3.25 ms.

To check the sensitivity of this gap size, Shot 3015 was performed with the air test gas mixed with 7.5% mole fraction of monatomic gas. Since the driver gas for this condition is 85% helium and 15% argon, the ratio was adjusted to match this mixture. The expectation was that adding 7.5% monatomic gas to the 2.5% contamination present in early test time would cause the flow over the 15.8 mm gap model to choke at a similar time as the 14.7 mm model in Shot 3012. As seen in Fig. 4.8, the flow did choke earlier at t_c = 2.88 ms, but it was still much later than the t_c = 0.66 ms from Shot 3012. While this shows the model is sensitive to an increase in driver gas contamination, the process can be improved with a better gas mixing process and a smaller wedge with a quicker response time.

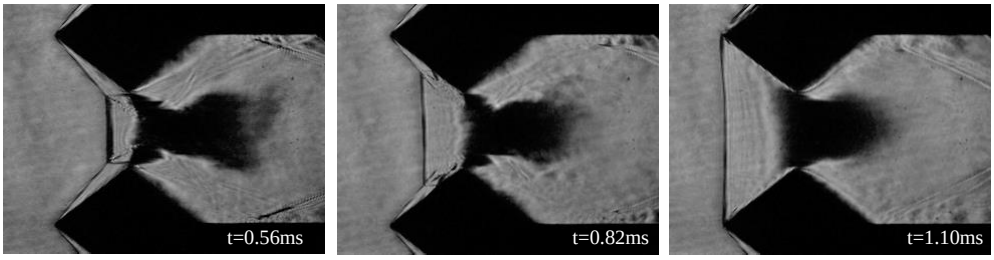

Figure 4.5: Schlieren images of the 38° opposing-wedge with G=14.7 mm in air test gas (Shot 3012).

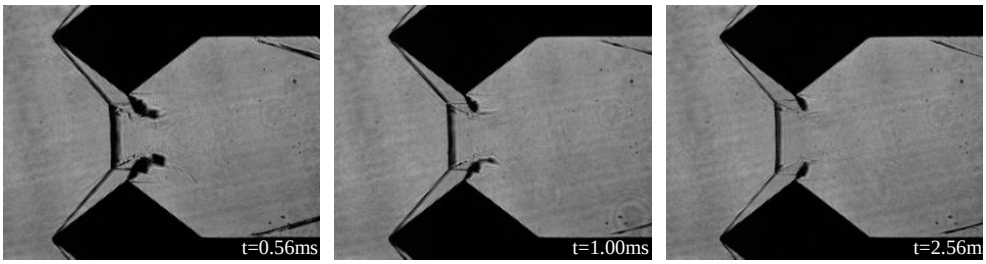

Figure 4.6: Shadowgraph images of the 38° opposing-wedge with G=16.5 mm in air test gas (Shot 3013).

4.3 Mach Stem Edge Tracking

While qualitatively inspecting the high-speed images was useful to bound the driver gas mole fraction, the 500 µs response time of the large opposing-wedge model caused difficulty in tracking the exact temporal behavior of the Mach stem. In order to more quantitatively measure the movement of the Mach stem, Canny edge detection (Canny, 1986) was used in the edge function in MATLAB to track the

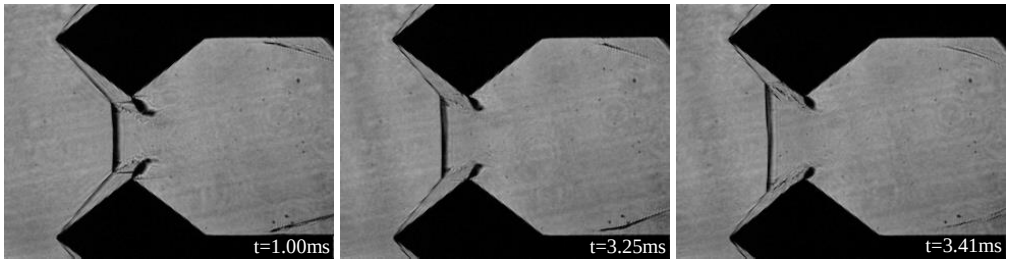

Figure 4.7: Shadowgraph images of the 38° opposing-wedge with G=15.8 mm in air test gas (Shot 3014).

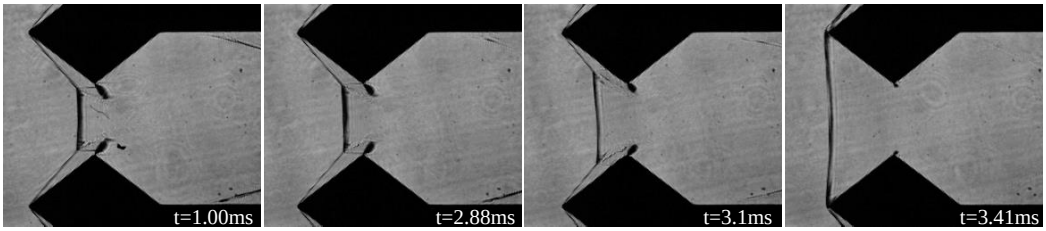

Figure 4.8: Shadowgraph images of the 38° opposing-wedge with G=15.8 mm in air test gas mixture with 7.5% (85% He and 15% Ar) mole fraction of monatomic gas (Shot 3015).

motion of the Mach stem. An example of this process is shown in Fig. 4.9, where a segment of the Mach stem (in blue) is tracked over a streamwise region of interest (in red). The positions of the Mach stems during the four shots are plotted in Figs. 4.10 and 4.11.

With the positions for Shots 3012 and 3013 plotted together in Fig. 4.10, it is easy to see the consistency of the nozzle startup process in the behavior of the Mach stem. From 0.3 to 0.7 ms, the two traces match well in position and temporal behavior. However, the smaller gap size of Shot 3012 causes the Mach stem to quickly move upstream and choke the flow. In Fig. 4.11, Shots 3014 and 3015 are plotted together to demonstrate the effect of seeding helium/argon into the test gas. Since the gap size is kept constant between the two shots, the Mach stem position and temporal behavior match well during startup and test time. The traces diverge late after test time at 3 ms, where the additional "driver gas" causes the Mach stem to move upstream earlier in Shot 3015.

From the edge tracking results, it can be shown that the measured contamination levels are within the 5% at t = 1.9 ms and 12.5% at t = 2.25 ms bounds reported in

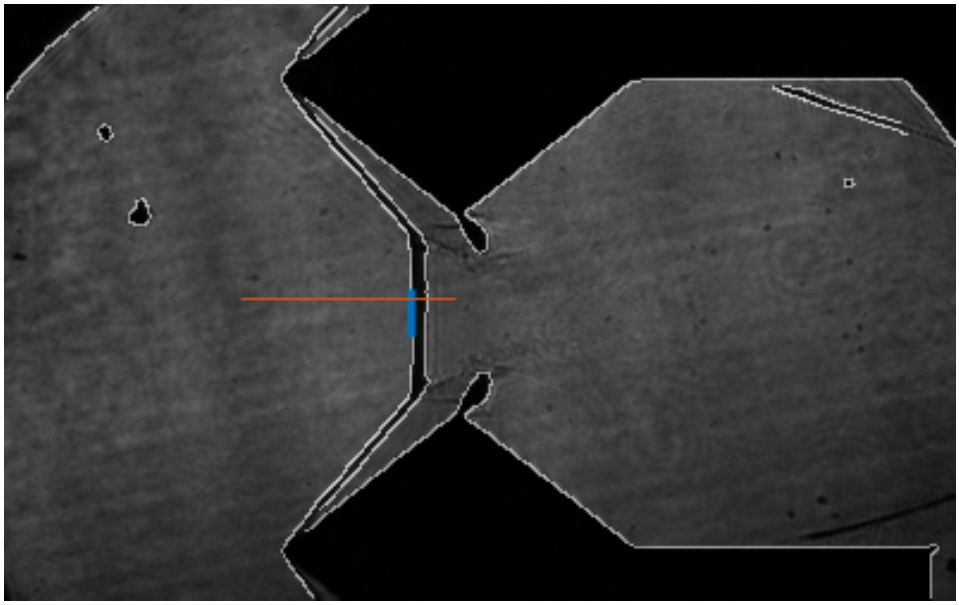

Figure 4.9: Example of Canny edge detection on a high-speed shadowgraph image from Shot 3013.

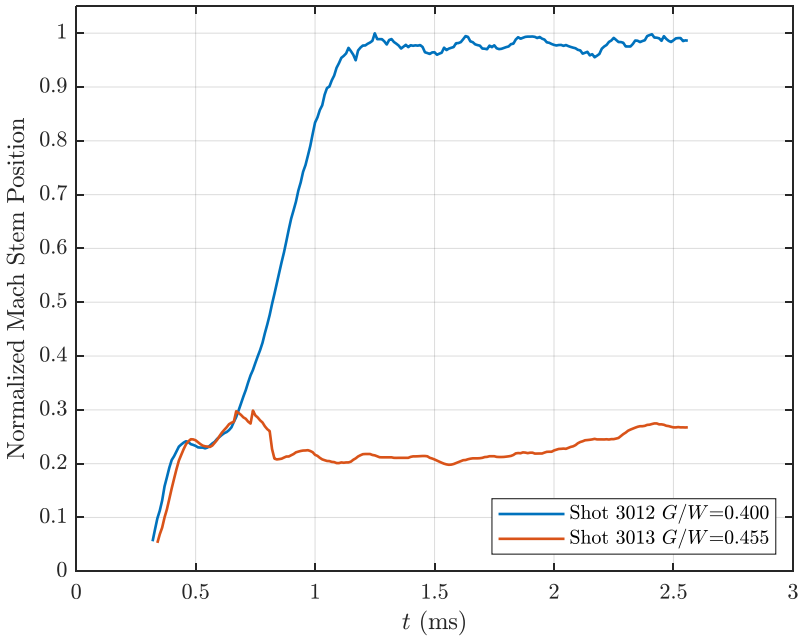

Figure 4.10: Normalized Mach stem position vs. time for Shots 3012 and 3013.

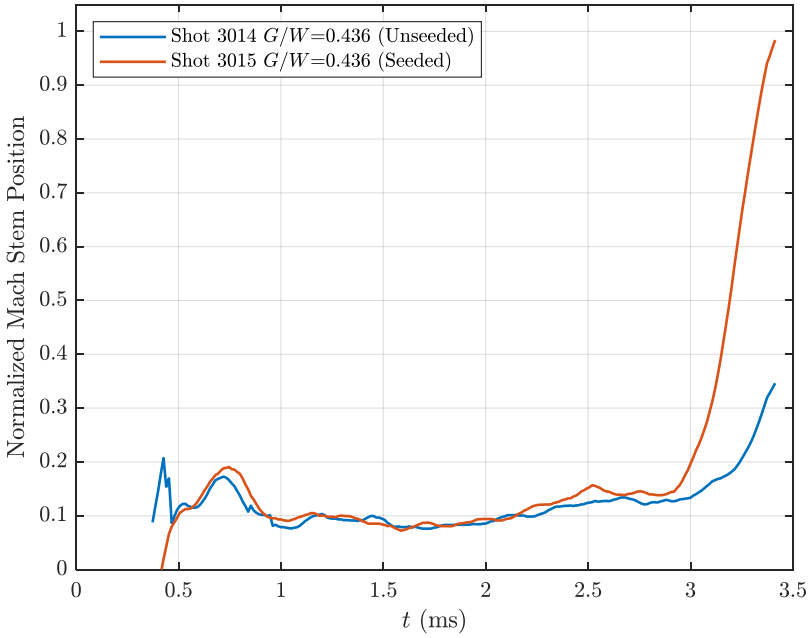

Figure 4.11: Normalized Mach stem position vs. time for Shots 3014 and 3015.

Sudani and Hornung (1998). Using the higher X_m sensitivity of the opposing-wedge model, it can be concluded that the contamination is closer to ~2% for the duration of test time and grows to 8% in the millisecond afterwards. While essentially reaching the same conclusion as the previous section, it shows the Canny edge detection is an effective method for analyzing the Mach stem behavior in future driver gas detection experiments. It is clear that the response time of this large opposing-wedge configuration hinders the temporal resolution of the detector, so combining this analysis process with smaller wedges with the same span will be beneficial to characterizing the driver gas content in the T5 freestream. An additional method that can be explored is a toroidal opposing-wedge geometry with an adjustable sting at the centerline that acts as a "spike" (akin to engine inlets). This would allow precise gap size changes and an even quicker response time with a smaller form factor. This installation would require a static pressure measurement just downstream of the oblique shock to track the choking time corresponding to the arrival of a prescribed amount of driver gas, but would allow for simultaneous measurement like the static pressure probes in Chapter 3.

Chapter 5

RESULTS: DFLDI EXPERIMENTS ON DOUBLE-CONE

This chapter discusses the results of the T5 experimental campaign using DFLDI to simultaneously probe the separation shear layer and freestream. As described in Chapter 2, the DFLDI configuration had the parameters: $d_0 = 8 \pm 2$ µm, $\Delta x = 145 \pm 2$ µm, $\alpha = 31°$, and $\Delta y = 5.18 \pm 0.01$ mm. The campaign consisted of 15 shots (3042–3051, 3052–3057), all of which are tabulated in Tables A.1 (measured facility data) and A.2 (calculated freestream conditions). The measurements are compared to simulated FLDI signals and also analyzed spectrally. In the context of the discussion in Chapter 1, the extracted low-frequency content (<100 kHz) is compared with scaling arguments for Kelvin-Helmholtz and streamwise acoustic instabilities, while the medium-frequency content (300–500 kHz) is discussed in terms of acoustic disturbances scaled with the separation region height $H(x)$, and high-frequency content (>1 MHz) is briefly reviewed in regards to second-mode instabilities. Concurrent heat flux and static pressure measurements during these experiments are plotted in Appendix B.

To give physical context for the dataset, the array of beam locations that are probed in this experimental campaign are illustrated in Figs. 5.1 and 5.2 for the H8-Re2-N2 and H8-Re2-Air conditions, respectively. The green dots corresponding to locations A-F along the shear layer are overlaid on high-speed shadowgraph images of each condition of the 25°–55° double-cone model, captured by Andrew Knisely and used here with permission. The corresponding freestream FLDI beam location is included as well. Additionally, red dots mark the streamwise locations of thermocouples instrumented on the model surface. Note: one experiment (Shot 3057) was performed with the FLDI beams oriented parallel to the freestream at location A to test dependence of the signal strength on α, but no statistically significant differences were observed, so the results are included as part of the same dataset.

5.1 FLDI Signal Processing

The general structure of the raw FLDI signal in T5 is consistent shot to shot, so representative signals for both the shear layer and freestream beam-pairs are shown in Fig. 5.3. The useful traces to compare with the FLDI are the nozzle reservoir

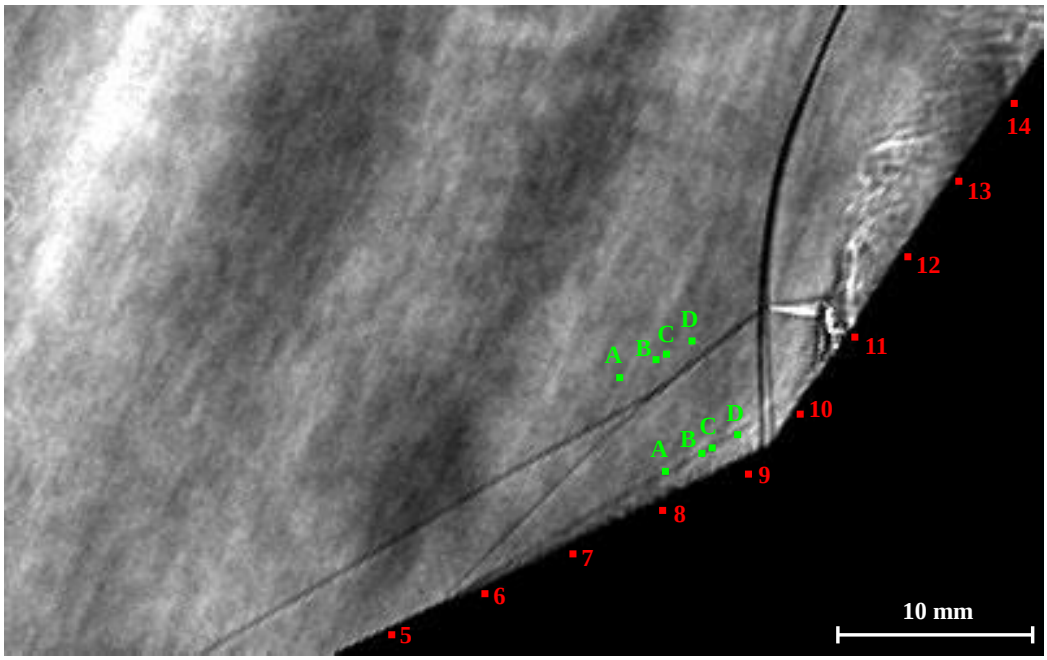

Figure 5.1: FLDI Beam Locations for the H8-Re2-N2 Condition (Shadowgraph image from Shot 2856, (Knisely, 2016)

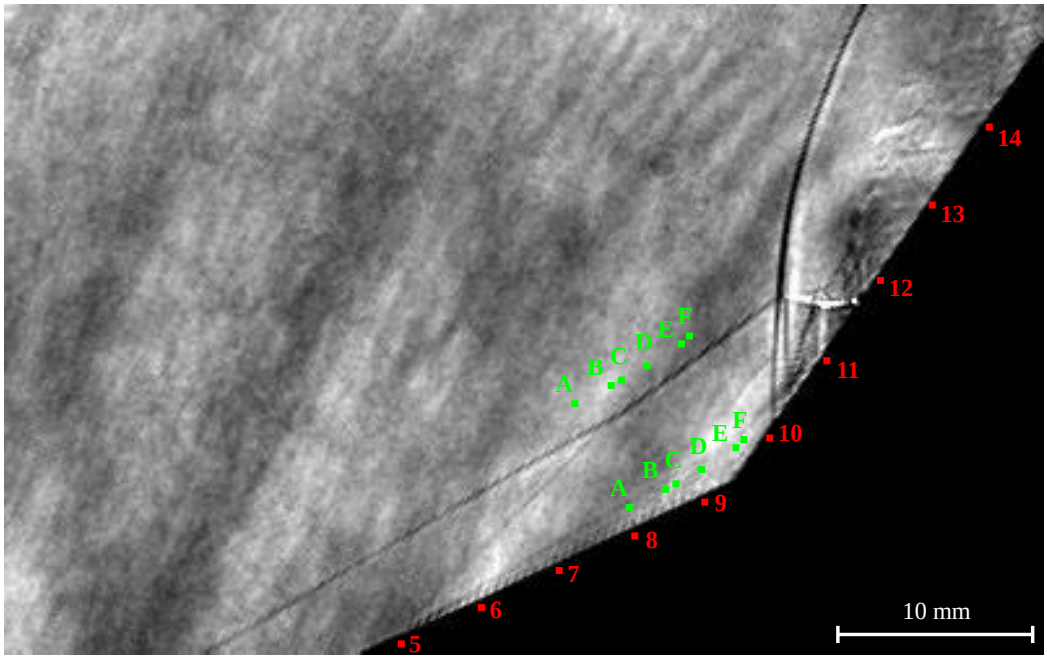

Figure 5.2: FLDI Beam Locations for the H8-Re2-Air Condition (Shadowgraph image from Shot 2858, (Knisely, 2016)

and static pressure traces (Fig. 5.4), as they provide a time history of the facility

for each shot at two locations. Comparing to the standard reflected shock tube x-t diagram (Fig. 1.4), the associated startup waves can be identified in the traces. The nozzle startup shock can be seen as a sharp spike in both the static pressure and FLDI, but due to the MHz range response time of the FLDI, the spike is significantly sharper than the one observed in the static pressure trace. Also important to note is the time lag between the reservoir pressure, static pressure, and FLDI traces. As explained in Chapter 3, the ~200–250 µs condition dependent delay between the reservoir and static pressure traces is expected. Additionally, the static probe taps sit roughly 160 mm upstream of the FLDI beam locations, so the ~30 µs lag between the static pressure and FLDI traces also aligns with the expected startup process. The initial State 5 behind the reflected shock is observed in the reservoir and static pressure peaks, as well as the larger amplitude noise around 0.5 ms in the FLDI signal. Then, the arrival of the reflected expansion fan at ~0.65 ms, just before the more constant State 6, can be seen in the freestream FLDI signal. The time period between 0.65–2.00 ms is usually considered usable test time before significant driver gas contamination occurs, as discussed in Chapter 4 and shown by Sudani and Hornung (1998). The freestream beam-pair not only serves as a simultaneous background signal for each shear layer measurement, but also allows for facility noise characterization and condition troubleshooting. Additionally, the FLDI signal before $t = 0$ can be used as a noise floor, which will be revisited in the discussion of background noise subtraction in the Section 5.2. As in the previous Chapters, $t = 0$ is determined from the pressure rise in the nozzle reservoir due to the arrival of the incident shock.

The theory and method describing the FLDI calibration and conversion process of the raw voltage signal into a $\Delta\Phi$ signal is detailed in Chapter 2. However, for completeness, an example calibration sweep done prior to Shot 3050 is shown in Fig. 5.5 to illustrate the FLDI post-processing procedure. Based on the calibration data, a conversion from raw photodetector voltage, V, to phase shift, $\Delta\Phi$, is obtained and plotted for t=1–1.75 ms in Fig. 5.6. Qualitatively, it is immediately noticeable that the magnitude of the phase shift in the shear layer is significantly larger than the freestream. This demonstrates that the signal in the shear layer beam-pair is unique to that region, as only the startup shock and subsequent waves are observed in the freestream signal until the beginning of test time. As will be demonstrated in the next section, the differences between the shear layer and freestream frequency content are repeatable and quantifiable when the signals are analyzed spectrally.

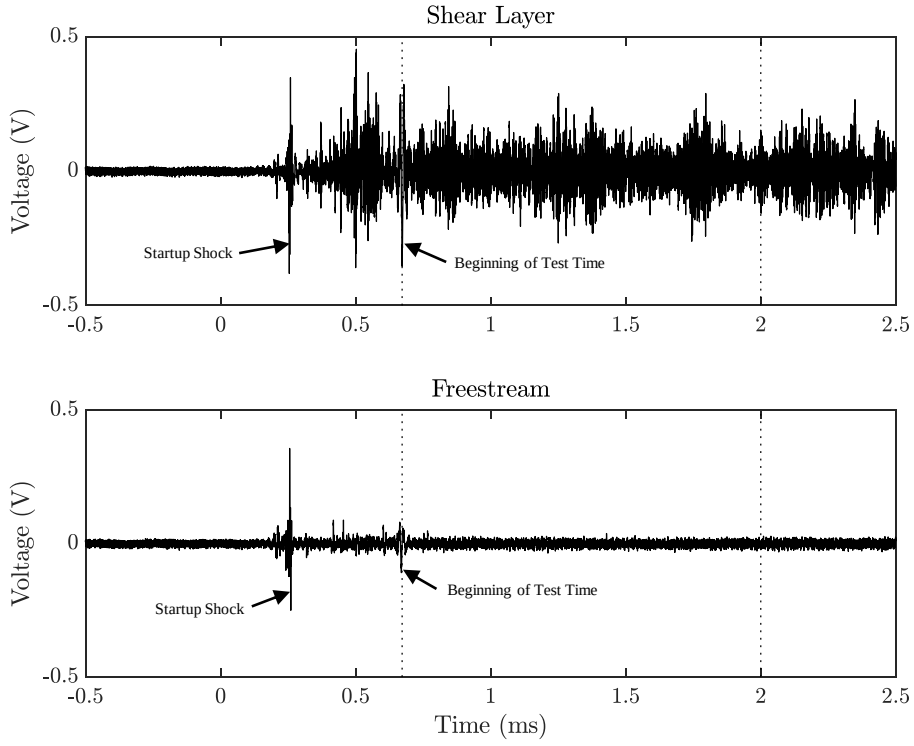

Figure 5.3: FLDI photodetector signals in the freestream and shear layer. Dotted lines indicate nominal test time.

5.2 FLDI Spectral Analysis

Power Spectral Method

While inspection of the measured $\Delta\Phi$ is useful in qualitatively comparing signals and analyzing low-frequency structures (as will be discussed in Section 5.4), frequency content above 100 kHz is difficult to quantify without power spectral methods, as the different frequencies are usually superimposed in the raw signal. As discussed in Section 1.4, the power spectral density is required to invert the signal from $\Delta\Phi$ to n, from which quantitative density fluctuations can also be analyzed. The PSD is defined as:

$$PSD\{g(t)\} = \lim_{T\to\infty} \frac{1}{T} |\hat{g}_T(f)|^2 \tag{5.1}$$

where the windowed function $g_T(t)$ is:

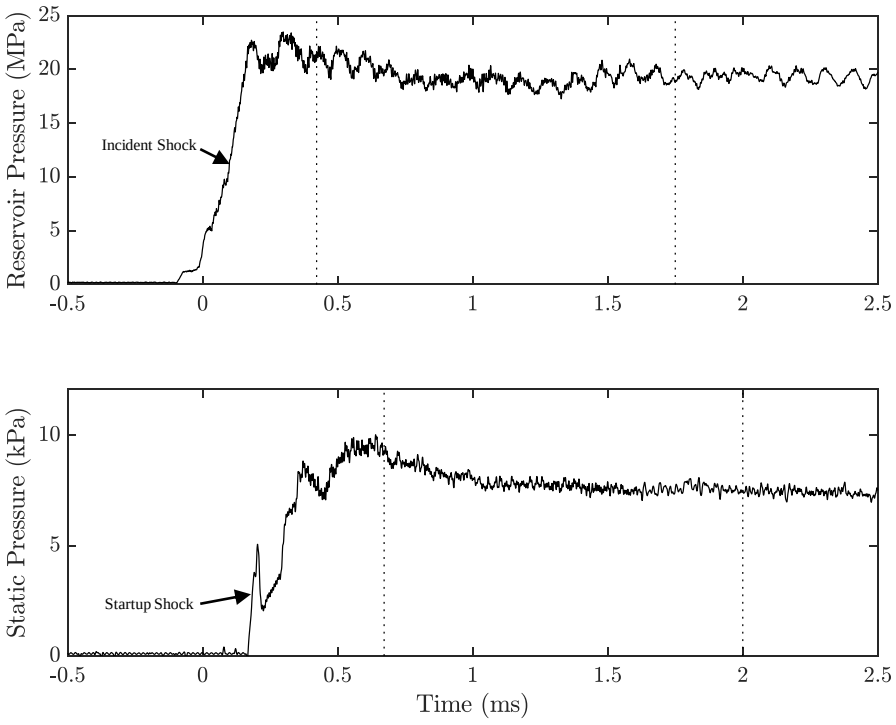

Figure 5.4: Shot 3050 reservoir and static pressure trace. Dotted lines indicate nominal test time.

$$g_T(t) = \begin{cases} g(t) & -\frac{T}{2} \leq t < \frac{T}{2} \\ 0 & \text{otherwise} \end{cases} \tag{5.2}$$

with units of generalized power per unit frequency: $\text{rad}^2\ \text{Hz}^{-1}$ (Goodman, 2015). Given a finite-length discrete signal (from an experiment), one can only estimate the power spectral density. Welch's method (Welch, 1967) has been commonly used for this application (Lawson, 2021), which takes an evenly spaced time-series spaced by $\Delta t = 1/f_s$, where f_s is the sampling frequency, and returns a spectrum at discrete frequencies from $\Delta f = f_s/n_{ps}$, where n_{ps} is the number of samples per segment. The implementation used in this study is the `pwelch` function in MATLAB, with a Hann window (50% overlap, $\Delta f = 10.66$ kHz).

While the onset of test time is easy to identify from the reservoir and static pressure traces and the sharp spikes in the FLDI signal, determining the useful test time period for the shear layer region requires preliminary spectral analysis and comparison to

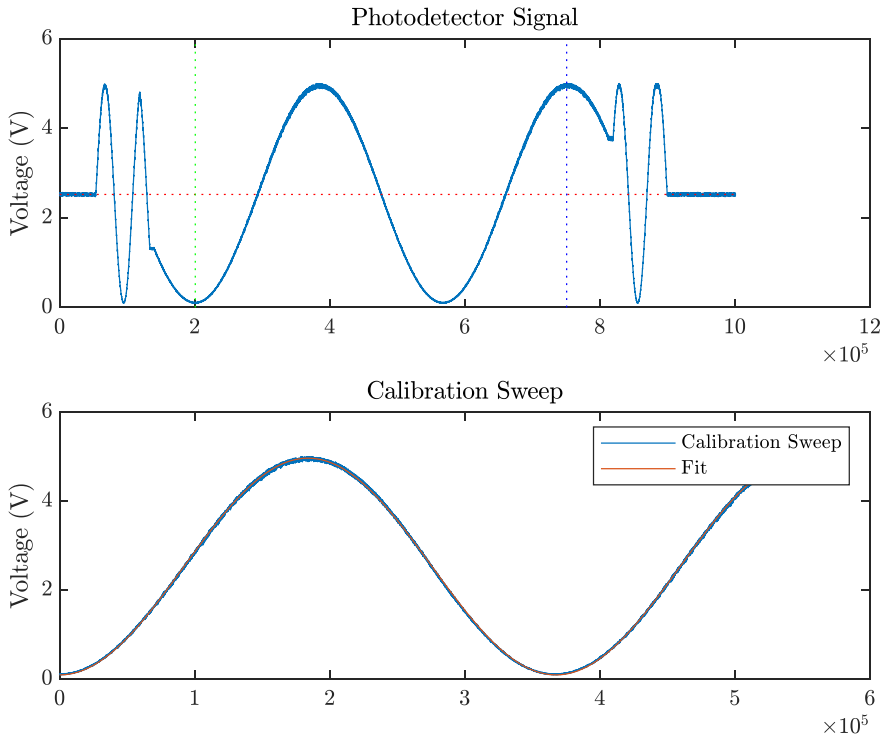

Figure 5.5: FLDI Calibration Sweep. Vertical dotted lines indicate the segment used for curve-fitting, the horizontal dotted line is V_0.

the static and reservoir pressure traces. To aid in the extraction of test time and as a first pass for identifying anomalous signals, spectrograms are used to visualize the shear layer and freestream FLDI signals, as shown in Figs. 5.7 and 5.8. The spectrograms are generated by estimating the PSD at short time intervals using `pwelch` and plotting the PSD's with respect to time, roughly showing the temporal evolution of frequency content. Just by qualitative inspection, a clear frequency band is evident in the shear layer spectrogram with temporal behavior correlating to the reservoir and static pressure traces. There is a period of constant reservoir and static pressure from 1.00–1.75 ms corresponding to a plateau in frequency band of shear layer FLDI signal. This also matched well with the flowfield establishment time on the double-cone as seen in the high-speed images in Knisely (2016) and falls well within the driver gas contamination bounds discussed in Chapter 4. Thus, further spectral analysis of the FLDI signal in this study was limited to this time period.

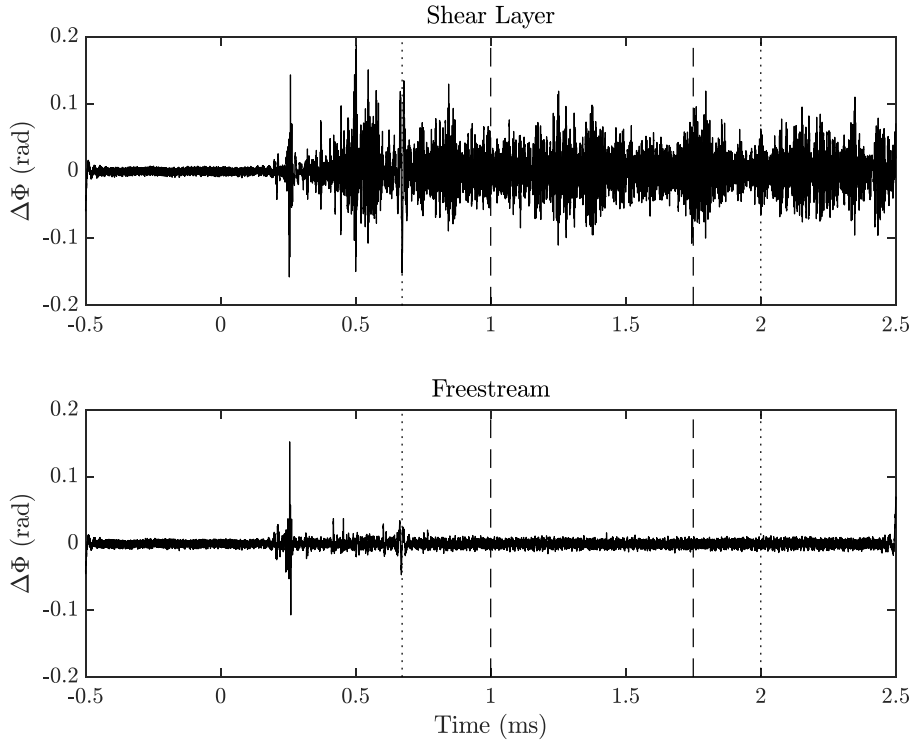

Figure 5.6: FLDI $\Delta\Phi$ signal after applying calibration constants. Dotted lines indicate nominal test time, dashed lines mark the time-segment used for further spectral analysis.

The two FLDI signal time segments (shown in Fig. 5.9) are then used to compute $PSD\{\Delta\Phi\}$ using Welch's method and the background noise of the each FLDI beam-pair is then subtracted using the method outlined in Lawson (2021), where the background-subtracted FLDI signal, $\widetilde{\Delta\Phi}(t)$, is expressed as:

$$PSD\{\widetilde{\Delta\Phi}(t)\} \approx \left|\frac{1}{a_1}\right|^2 \left(PSD\left\{\log\left[V^*(t)\right]\right\} - PSD\{\log[\alpha(t)]\}\right) \tag{5.3}$$

where $V^*(t)$ is the measured photodetector voltage, $\alpha(t)$ is the background noise signal (taken in the quiescent flow before shock arrival), and $a_1 = f(A, B, \Delta\Phi_0)$ is found from the calibration process outlined in Chapter 2. The background-subtracted PSD's are used for further analysis in the rest of the chapter, and examples of the shear layer and freestream PSD's for Shot 3050 are plotted in Fig. 5.10. There is a clear broadband peak in the 300–500 kHz range that is up to 3 orders of magnitude

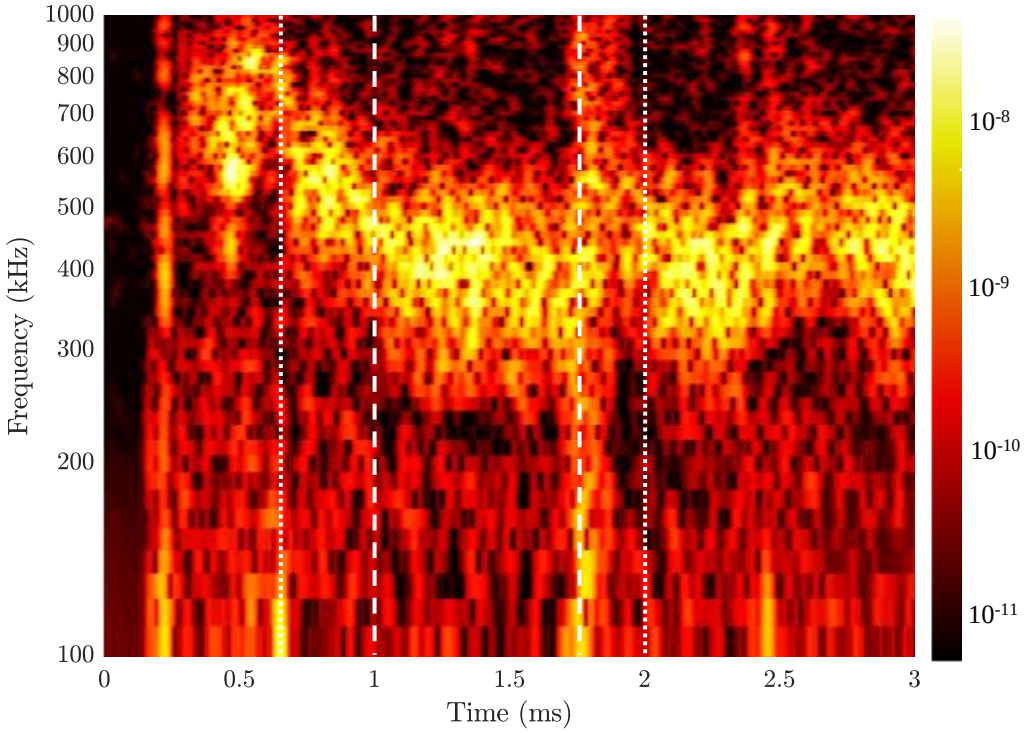

Figure 5.7: Spectrogram of shear layer FLDI signal. Dotted lines indicate nominal test time, dashed lines mark the time-segment used for further spectral analysis.

higher than the freestream measured frequency content. To show the repeatability of the strength of these density fluctuations and the shot-to-shot signal variation, all of the background-subtracted PSD's from the experimental campaign are plotted in Fig. 5.11 (Δf = 21.33 kHz for clarity). The repeatability of the strong broadband peak in the shear layer is evident across the shot matrix, showing the robustness of the measured flow feature.

Freestream Density Disturbances

As discussed in Section 1.4, the ability to extract density disturbance information from $\Delta\Phi$ is an important capability for tunnel noise characterization (Lawson, 2021; Parziale et al., 2012). Various methods were outlined, including the analytical relation by Parziale et al. (2012) and the transfer function approach by Schmidt and Shepherd (2015b) for sinusoidal plane waves, which was later generalized by Lawson and Austin (2023a). To frame the work of Lawson and Austin back in the context of the T5 freestream disturbances, the spectral inversion method to calculate

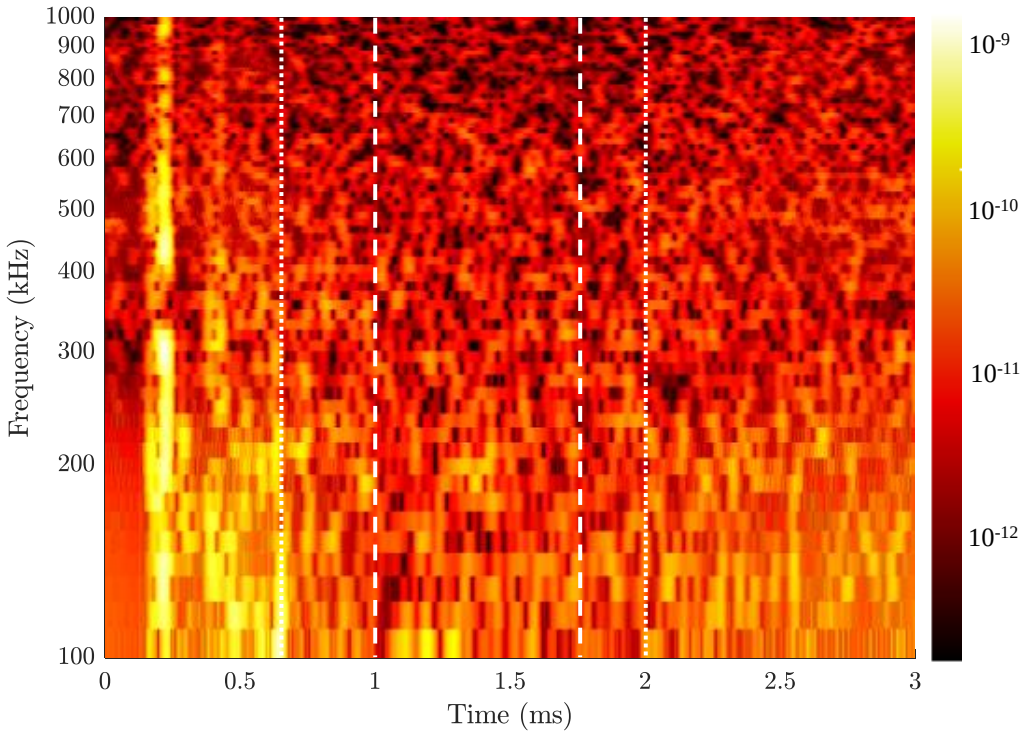

Figure 5.8: Spectrogram of freestream FLDI signal. Dotted lines indicate nominal test time, dashed lines mark the time-segment used for further spectral analysis.

$PSD\{\rho'/\overline{\rho}\}$ is compared to Parziale's analytical relation, repeated here:

$$\frac{\Delta\rho}{\overline{\rho}} = \frac{\lambda_L}{2\pi K\zeta\overline{\rho}} \sin^{-1}\left(\frac{V}{V_0} - 1\right) \tag{5.4}$$

with the correction coefficient:

$$c(\lambda) = \sin\left(\frac{\pi\Delta x}{\lambda}\right) \tag{5.5}$$

for sinusoidal disturbances of wavelength λ. In this case, the freestream velocity is used to convert the measured frequency to λ with units of m.

Using the spectral inversion approach, the PSD of the index of refraction is calculated using:

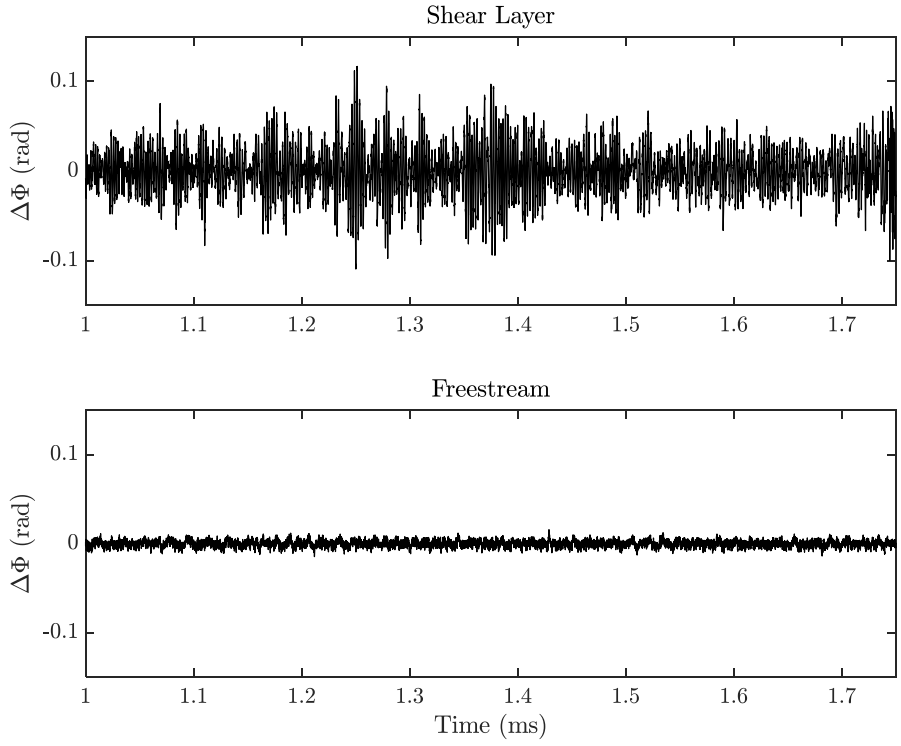

Figure 5.9: FLDI signal during test time.

$$PSD\{n'\} = \frac{PSD\{\Delta\Phi\}}{h_{xy}^2(f)} \tag{5.6}$$

where $h_{xy}(f)$ is as defined in Eqns.(1.20) and (1.21), but in terms of the frequency instead of wavenumber. This requires knowledge of the freestream Mach number and sound speed, which is calculated using the Nozzle Code. Note: the disturbance is assumed to propagate in the x-direction in the lab frame, but since the beam-pairs in this study are at an inclination of 31°, the directional contributions of the disturbance are split into x- and y-components. The conversion from index of refraction to density (Lawson, 2021) is then given by:

$$PSD\{n'\} = \frac{1}{K^2} \times PSD\{\rho'\} \tag{5.7}$$

Thus, there are now two ways to solve the inverse problem of $PSD\{\Delta\Phi\} \rightarrow PSD\{\rho'/\overline{\rho}\}$. A plot of $PSD\{\rho'/\overline{\rho}\}$ for both methods is shown in Fig. 5.12 for

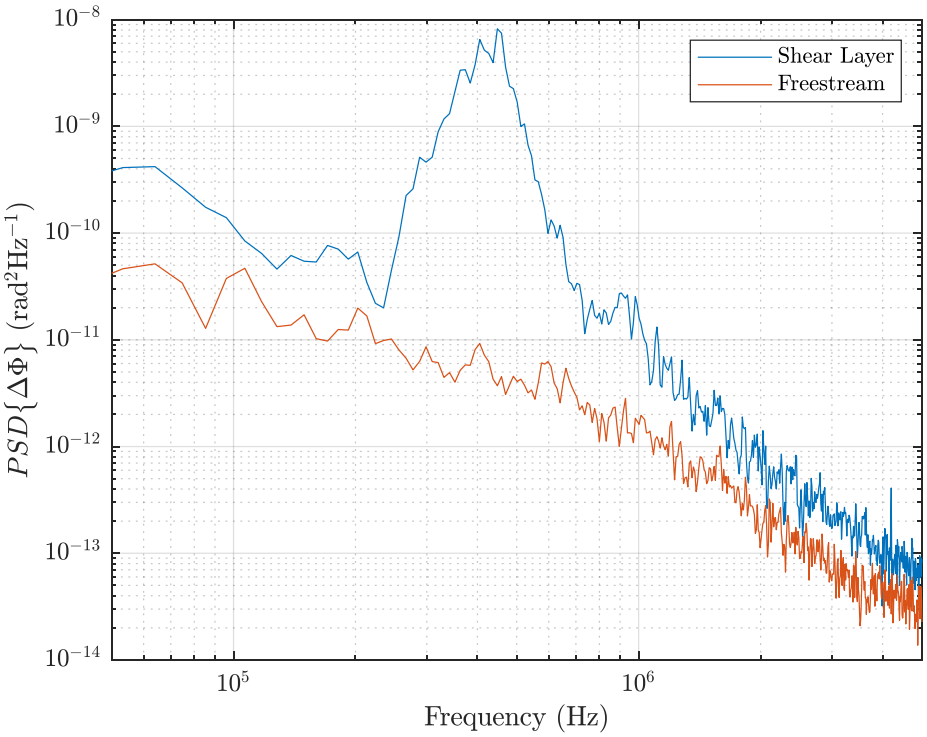

Figure 5.10: Comparison of shear layer and freestream PSD's of respective FLDI signals.

Shot 3050, compared to the corresponding T5 tunnel noise PSD's from Parziale (2013), reproduced here with permission. The structure of $PSD\{\rho'/\overline{\rho}\}$ agrees well with Parziale (2013), albeit with slightly lower magnitude, as the conditions used in this study have a nozzle reservoir pressure roughly a third of those used in Parziale (2013). As observed by Lawson and Austin (2023b), Parziale's analytical method generally under-predicts the density disturbance slightly, which is observed here when compared with the spectral inversion method. The slight difference between the two methods matches well with the findings of Lawson and Austin. The same sinusoidal plane wave assumption cannot be made for the shear layer as the region has highly complex three-dimensional flows, so this analysis is currently limited to the freestream flow. As the frequency content of the shear layer is more relevant to this study, the results will be left as $PSD\{\Delta\Phi\}$.

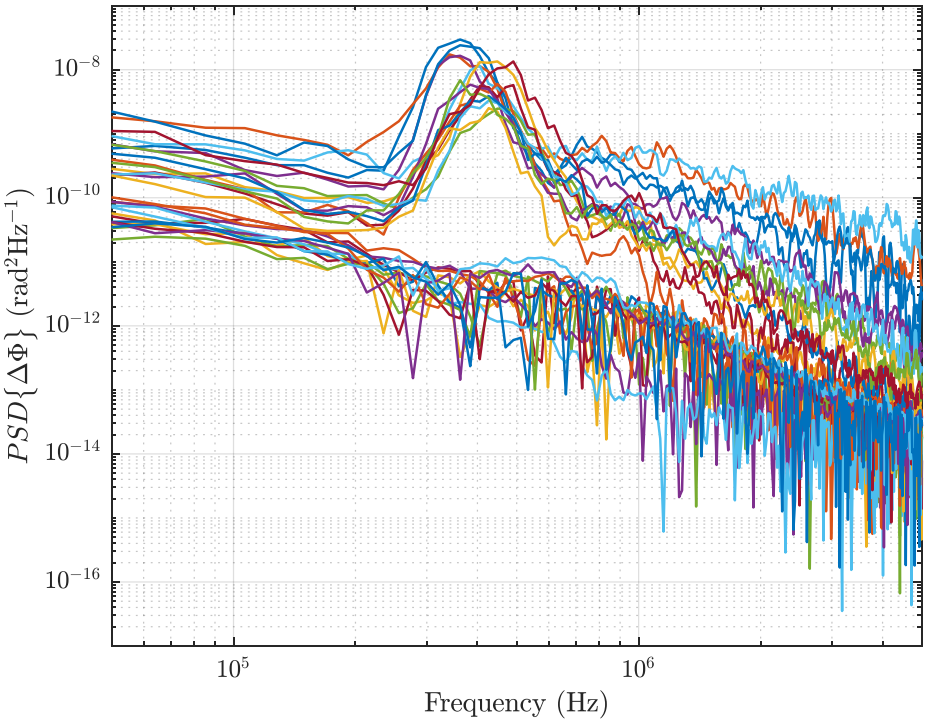

Figure 5.11: Compilation of all FLDI signal PSD's across shot matrix.

5.3 Simulations of Mean Flow and FLDI Response

To properly inform the FLDI measurements, certain information about the freestream and local flow conditions on the model are necessary. The average freestream conditions are provided by the Nozzle Code. This section describes the axisymmetric numerical simulations of the mean flow over the 25°–55° double-cone that inform 2-D numerical simulations of canonical Kelvin-Helmholtz instabilities for use with an analytical FLDI ray-tracing model (Lawson, 2021; Schmidt and Shepherd, 2015b).

Double-Cone Mean Flow Simulation

The mean flow over the 25°–55° double-cone model is numerically simulated in Eilmer4 in the H8-Re2-Air and H8-Re2-N2 freestream conditions (Table 2.1). The simulation assumes axisymmetric, unsteady, reacting, viscous flow with vibrational and chemical nonequilibrium in the five-species air kinetic model of Gupta et al. (1990). The inflow boundary condition is set to the freestream condition in T5, with a cold wall set to 300 K. A schematic with the boundary conditions is shown in

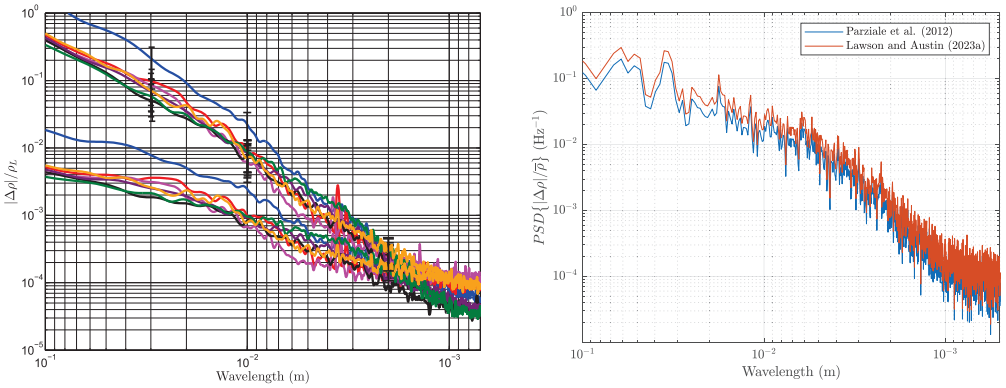

Figure 5.12: PSD's of density fluctuations, $PSD\{|\Delta\rho|/\overline{\rho}\}$, in the T5 freestream. **(Left)** Wavelength spectrum of T5 freestream tunnel noise for conditions with P_R = 40–50 MPa at h_0 = 5–18 MJ/kg (Parziale, 2013). Note: the higher magnitude data has been corrected using $c(\lambda)$. **(Right)** Wavelength spectrum of T5 freestream tunnel noise in the 8 MJ/kg air condition (P_R = 18 MPa). The analytical (Parziale, 2013) and spectral inversion (Lawson, 2021) methods of density fluctuation calculation are also compared in this case. Note: the y-axes labels have slightly different notation, but the plotted values are the same.

Fig. 5.13. The computations are run with a coarse grid to establish the flowfield and the grid resolution is increased in three stages. Table 5.1 details the respective resolutions and flow times for each case. Grid resolution is increased near the walls and compression corner to resolve the separation region and boundary layer. As shown in Fig. 5.16, reasonable grid-independence is demonstrated in the fine mesh case by plotting vertical velocity cross-sections through the shear layer, Region 2, and the freestream.

Table 5.1: 25°–55° Double-Cone Simulation Grid Parameters

Resolution	x-cells	y-cells	Flow Times (L_1/U_∞)
Coarse	800	40	5
Medium	1600	80	5
Fine	3200	160	25
Finest	4800	240	5

To give physical context to the simulation, a full-field image of the Mach number contour plot from the finest grid resolution case is shown in Fig. 5.14. The main shock structures and interactions are resolved, along with the separation and post-reattachment regions. Since the focus of this study is on the separation shear layer, a more zoomed-in view of the region is shown in Fig. 5.15, represented as a synthetic schlieren image to highlight important structures. Even at the finest grid resolution,

the shear layer spans only one to two cells (Fig. 5.17), meaning flow structures like vortices and vortex amalgamations may not be resolved correctly. Further increasing the resolution would require significantly more time and computational resources. Thus, only mean flow properties in the flowfield can be extracted for scaling arguments.

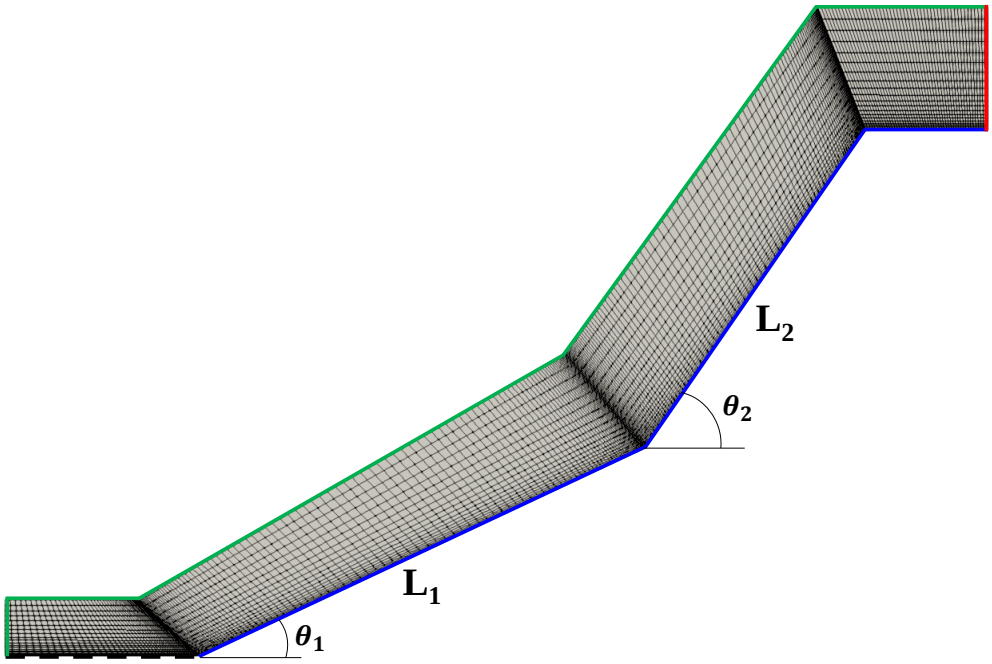

Figure 5.13: Schematic of the axisymmetric simulation of 25°-55° double-cone geometry in Eilmer4. L_1 = 57.02 mm, L_2 = 45.23 mm, $\theta_1 = 25°$, $\theta_2 = 55°$. Green boundaries are inflows, red boundaries are outflows, blue boundaries are no-slip cold walls, the dotted boundary is the axis. The coarse mesh is overlaid to show the grid structure.

Canonical Kelvin-Helmholtz Instability Simulation

A canonical 2-D Kelvin-Helmholtz instability is simulated in Eilmer4 using the local conditions near the shear layer calculated from the mean flow double-cone simulations. The simulation is adapted from the `kelvin-helmholtz` example in Eilmer4, inviscid with ideal air using a 512-by-256 uniform grid, with periodic inflow and outflow conditions open sidewalls. U_1 and ρ_1 are set to the the conditions just outside of the separation region, while U_2 and ρ_2 are set to the conditions just inside the separation region. The y-velocity is given a small perturbation at the first time-step to initiate the instability. The simulation is run such that one vortex has enough time to convect across the length of the domain, making the

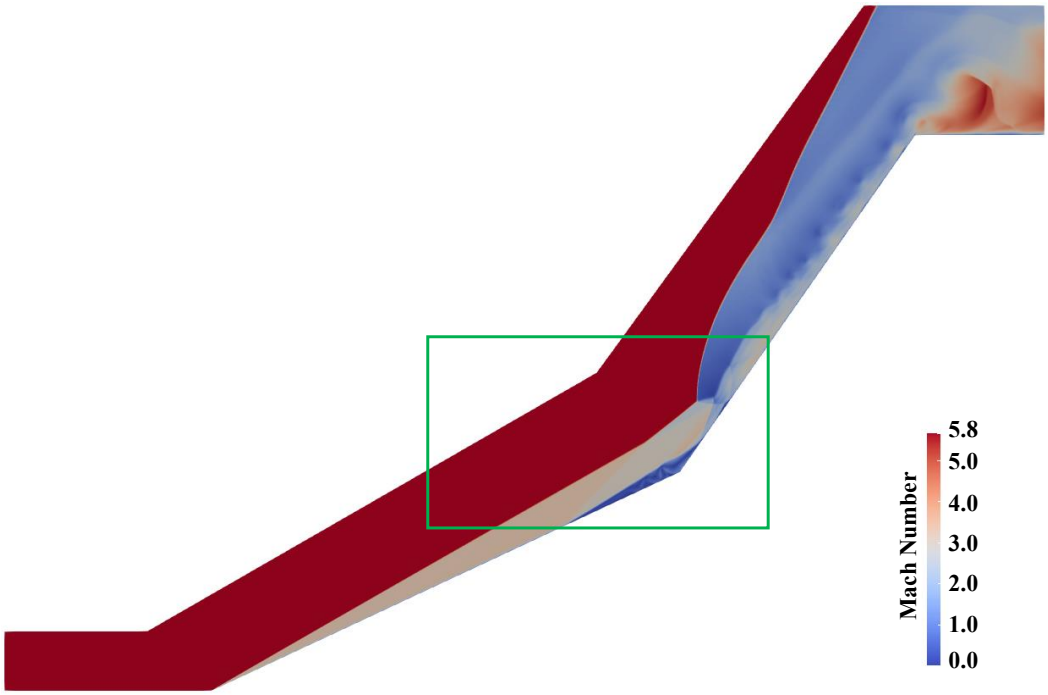

Figure 5.14: Contour plot of Mach number at steady state from simulation of 25°–55° double-cone geometry in Eilmer4. The green box indicates the region shown in Fig. 5.15.

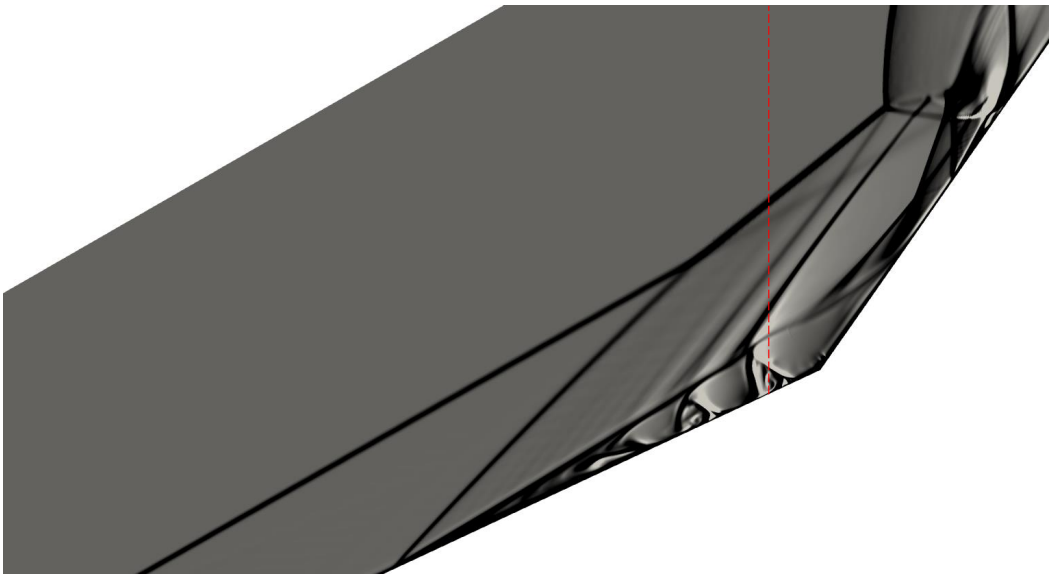

Figure 5.15: Synthetic schlieren of the separation region at steady state on 25°–55° double-cone geometry in Eilmer4. Dotted red line marks the vertical velocity cross-section used for grid-independence tests shown in Fig. 5.16.

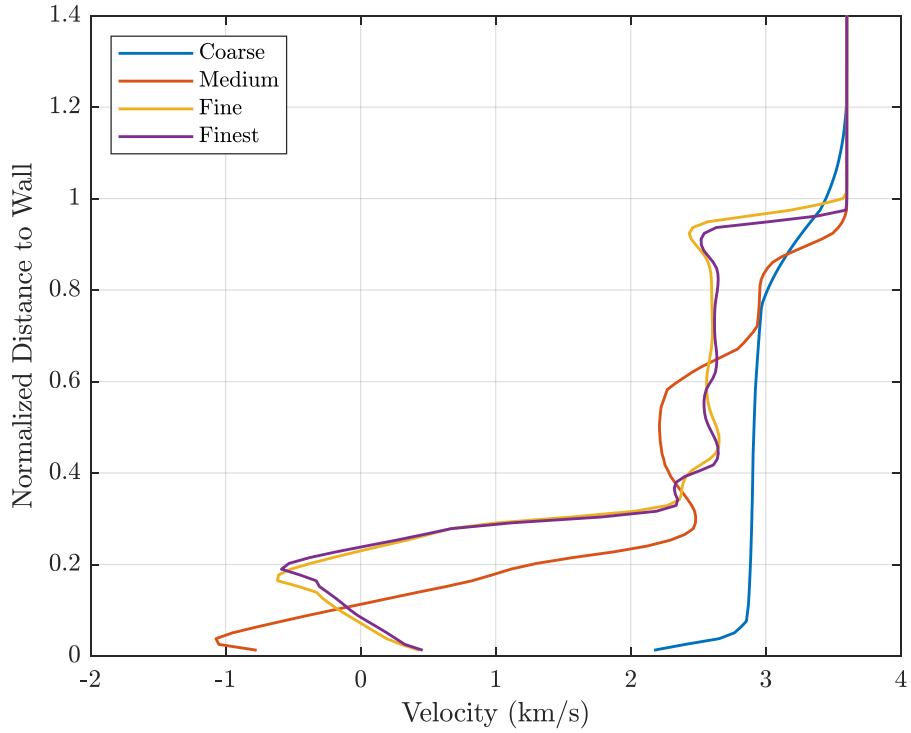

Figure 5.16: Plot of double-cone velocity cross-sections at steady state shown by dotted red line in Fig. 5.15 at the four grid resolutions.

Figure 5.17: Finest mesh case (4800x240) overlaid on synthetic schlieren on 25°–55° double-cone in Eilmer4.

eventual looping in implementation with the ray-tracing model simpler. Fig. 5.18 shows six stages, (a)–(f), of the simulation that correspond to different degrees of vortex roll-up of the Kelvin-Helmholtz instabilities. This in effect represents different streamwise positions along a shear layer, allowing for the exploration of any frequency dependence on streamwise position. Note: case (a) is simply the initial state of the simulation, and is not used in the analysis.

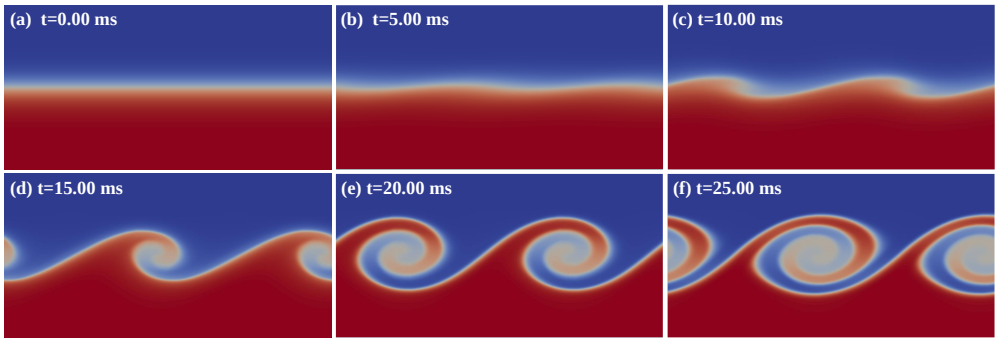

Figure 5.18: Contour plots of density from numerical simulation in Eilmer4 of canonical Kelvin-Helmholtz instability for use with FLDI ray-tracing model.

Applying FLDI Ray-Tracing Model

As discussed in Chapter 1, Schmidt and Shepherd (2015b) developed a ray-tracing model of the FLDI response and a numerical scheme to simulate the FLDI optical path between the two focusing lenses. The beams are discretized into circular slices with a non-dimensional radius, $\tilde{r}$, normalized to the local Gaussian beam radius. A ray in the FLDI beam is then simply the locus with a constant $\tilde{r}$ and θ. This allows Eq. (1.16) to be rewritten as:

$$\Delta\Phi = \frac{2\pi}{\lambda_L}\int_0^{2\pi}\int_0^{\infty}\tilde{I}_0(\tilde{r})\left(\int_{z_a}^{z_b} n_1\,\mathrm{d}z - \int_{z_a}^{z_b} n_2\,\mathrm{d}z\right)\tilde{r}\,\mathrm{d}\tilde{r}\,\mathrm{d}\theta \tag{5.8}$$

This discretization scheme was implemented in Python by Lawson (2021). This model was then adapted for use with the current beam geometry, and modified to accept flow solutions from Eilmer as inputs. To easily interact with simulated Cartesian flowfields in the Cartesian, the beams are transformed into the Cartesian coordinate system and integrated using Eq. (1.16). A grid with 311 cells in r, 256 cells in θ, and a 250 µm z-spacing was used, with a finer 50 µm z-spacing at the foci ±20 mm, giving a final 3-D mesh of $(n_r, n_\theta, n_z) = (311, 256, 5893)$ per beam.

More details on the Python code structure, grid resolution study, and validation of this code are given in Lawson (2021).

The flowfield from the canonical Kelvin-Helmholtz simulation discussed above is used as an input into the ray-tracing model to simulate the response of FLDI to vortices passing through the beam-pair at various stages of roll-up. The interaction of the two models makes a few assumptions. Firstly, as the Kelvin-Helmholtz simulation is 2-D, it must be extruded in the z-axis to represent a 3-D flowfield, in this case ±20 mm to roughly represent the flowfield along the surface of the double-cone. This arrangement is illustrated in Fig. 5.19. As the actual flow is axisymmetric, this is not an accurate representation of the real flowfield. However, for the sake of understanding the interaction and minimizing computational costs, this approach is used. To additionally reduce computation time, the regions of the simulated Kelvin-Helmholtz instability that do not interact with the beams do not need to be integrated. To illustrate the temporal behavior of the density field, the average densities at the location of the beam foci and associated $\Delta\Phi$ response of the simulated FLDI are plotted in Fig. 5.20 for cases (b)–(f) in Fig. 5.18. The simulated response shows the frequency dependence on the roll-up stage of the vortices, with case (f) exhibiting similar signal structure to the raw signal shown and discussed later in Section 5.4.

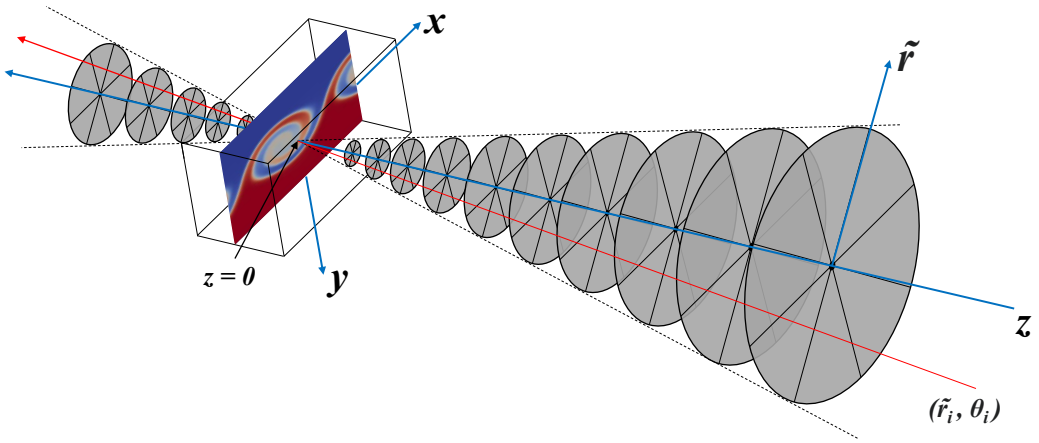

Figure 5.19: Schematic of the numerical FLDI ray-tracing model with the extruded 2-D Kelvin-Helmholtz simulation as a propagating density disturbance field.

5.4 Low-Frequency Instabilities

Upon inspection of the FLDI signal, significant low-frequency wave packets were noticed in the shear layer across all shots. An example from Shot 3050 is shown

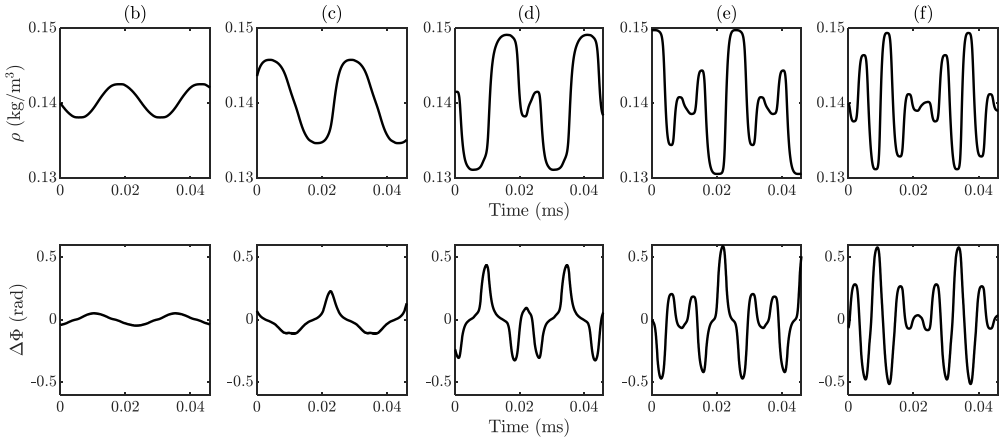

Figure 5.20: Local $\rho(t)$ and associated simulated $\Delta\Phi(t)$ at each stage (b)–(f) in the Kelvin-Helmholtz instability simulation in Eilmer4.

in Fig. 5.21. As mentioned in Section 5.2, the low-frequency fluctuations in the shear layer can be characterized by direct analysis of the $\Delta\Phi$ signal. In fact, it can actually be difficult to analyze spectrally given the irregular length and spacing of the features and the limited number of samples taken during test time. When estimating the PSD of such signals, Δf is on the order of 10–20 kHz, making it challenging to resolve low frequency disturbances. Thus, it is helpful to envelope the signal to aid in extracting the wavelength distributions of the disturbances. This section discusses this process, and compares the results to scaling arguments both for Kelvin-Helmholtz instabilities and streamwise acoustic disturbances along the shear layer. Since the convective velocity is not known *a priori* in the context of a time-resolved measurement, the wavelength, λ, is presented in this section as a period, τ, in units of ms.

Wave Packet Distributions

As shown in Fig. 5.21, the envelope of $\Delta\Phi$ is taken to bound the signal, essentially tracing the lower and upper peaks for a given time period. The distance between the upper and lower envelopes are then calculated, and a threshold of 20% peak magnitude was set to demarcate the beginning and end of an envelope. This was determined by trial-and-error visually as a higher threshold would be overly sensitive while a lower threshold would "filter" out less-pronounced packets. The periods of the fluctuations are then compiled for each shot and a histogram is generated to analyze the distribution, shown in Fig. 5.22. The distributions are generally lognormal, so a Gaussian fit is performed on the $\log(\tau)$. To test the goodness-of-

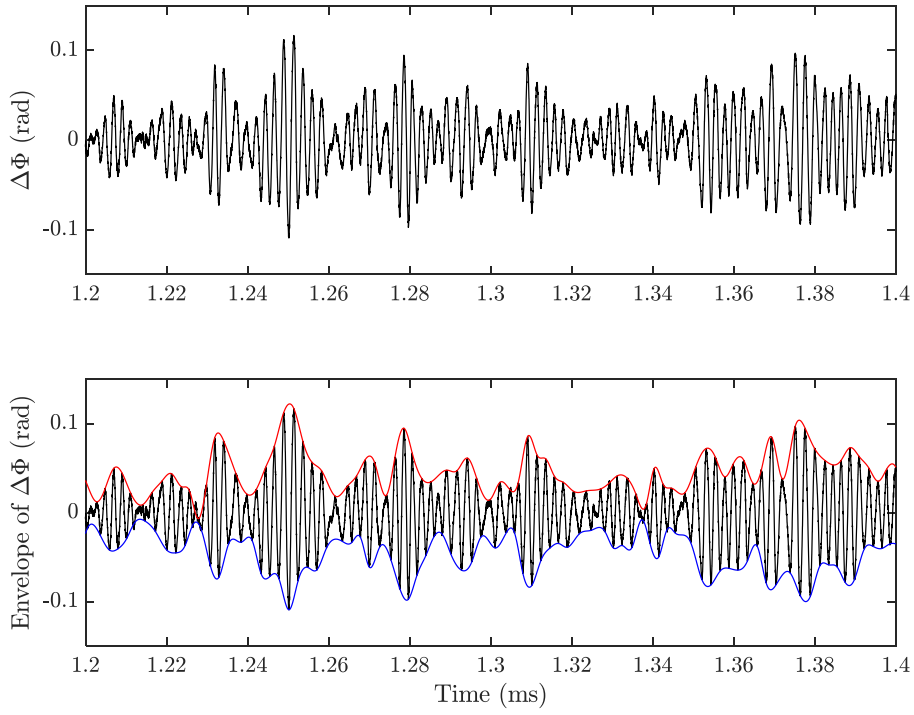

Figure 5.21: Low-frequency "packets" in the FLDI signal, shown with envelope.

fit, a visual quantile-quantile plot is used (Fig. 5.23) to compare the dataset to a standard normal distribution. Additionally, the Shapiro-Wilk test (Royston, 1992; Shapiro and Wilk, 1965) with an α for the p-value threshold of 0.05 to quantify the goodness-of-fit for each shot. The fits for all shots are plotted in Fig. 5.24 with their associated p-values.

The mean frequency is taken from each distribution and plotted versus x/L_{sep} with 1-σ error bars in Fig. 5.25. The horizontal error bars in this plot and all subsequent plots in this chapter are determined from the 0.1 mm measurement error in the FLDI beam locations during the optical alignment process. The mean period appears to be constant within error along the length of the shear layer for the measured locations, suggesting the streamwise instabilities are independent of the position along the shear layer. To non-dimensionalize the measured periods, the Strouhal number is calculated using the local edge velocity outside the separation region in Region 2 and plotted in Fig. 5.26. The Strouhal number also collapses to a constant value over the different streamwise locations, with slight differences between the air and nitrogen

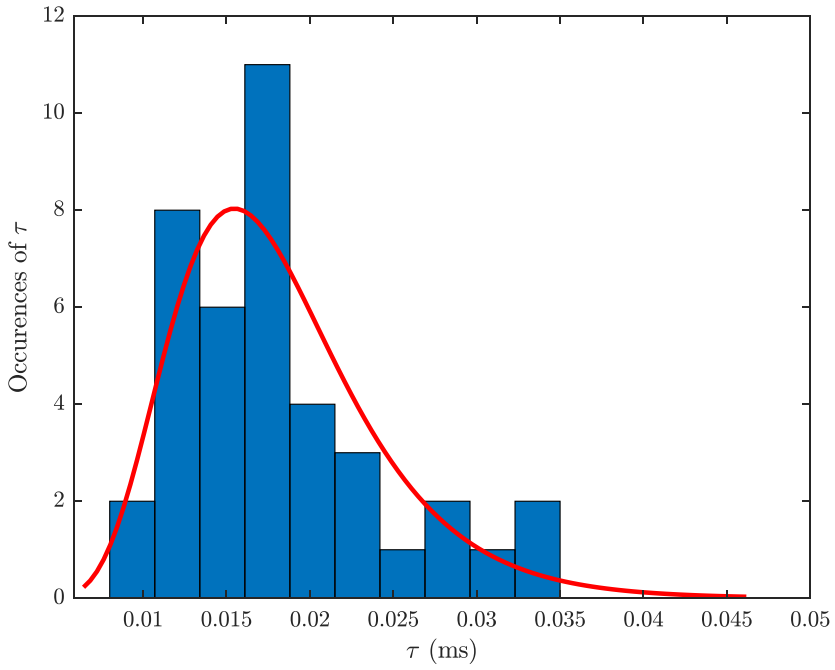

Figure 5.22: Histogram of τ with lognormal fit, p-value = 0.43.

cases due to the shorter separation length in the nitrogen condition. However, data for both air and nitrogen agree well within the uncertainty bounds.

Kelvin-Helmholtz Instability Scaling

Revisiting the scaling arguments presented in Chapter 1, the important parameters for characterizing the Kelvin-Helmholtz instabilities in a compressible shear layer are the growth rate, δ', and the convective Mach number, M_{c_1}. Papamoschou and Roshko (1988) showed that δ' decreases with increasing M_{c_1}. For this case, with U_1 = 3100 m/s, the convective velocity is roughly 1600 m/s, giving a convective Mach number of approximately 1.4. Using the associated growth rate $\delta' = 0.02$, the expected vortex size ranges from 0.05 to 0.2 mm. Assuming an Eulerian frame of reference (representative of an FLDI beam-pair), the frequency of passage is in the 8–32 kHz range, (St = 0.05–0.21 when scaled with the separation length). This is significantly lower than the measured mean frequencies and Strouhal numbers, but the order of magnitude of these disturbances match well. The relatively constant passage frequency, and subsequent M_{c_1}, in the region of measurement is consistent with the observations in Brown and Roshko (1974) and Papamoschou and Roshko

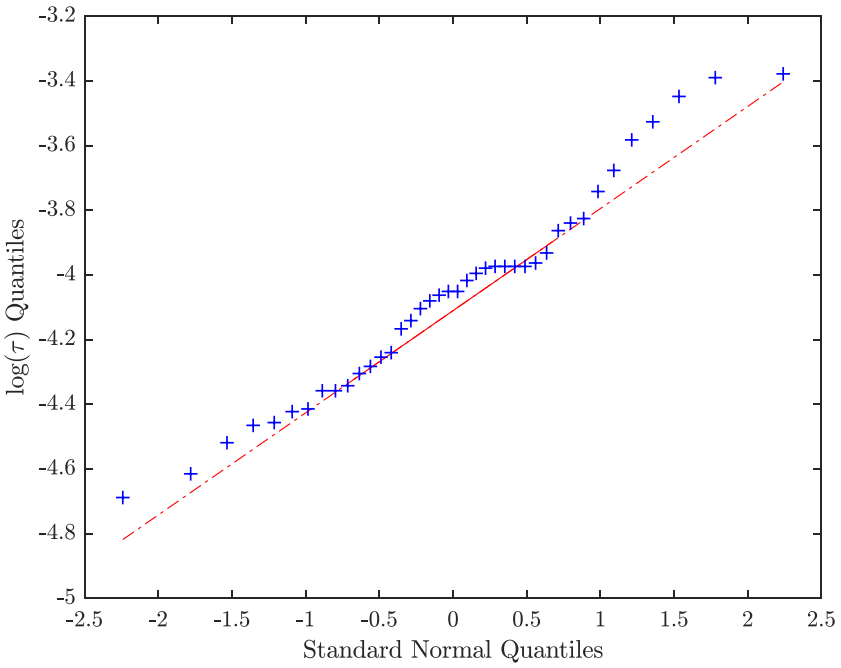

Figure 5.23: Quantile-Quantile plot of $\log(\tau)$.

(1988). However, as the mean periods in Fig. 5.25 obtained from enveloping the FLDI are essentially time-averaged, important information about the distributions of the vortical structures is not apparent. Thus, the standard deviations of the lognormal distributions must be considered.

In Bernal (1988), the statistical framework developed to analyze vortex amalgamation processes is presented. It is considered here in the context of the standard deviation, σ, of the lognormal fits to the measured periods. Bernal showed that σ ranges from 0.162 (tearing) to 0.276 (pairing), to 0.436 (tripling). Bernal concluded that 80% of the amalgamation processes are attributed to pairing, so $\sigma = 0.276$ was generally a descriptive metric to characterize vortex amalgamation in shear layers. The standard deviations from the current work are plotted versus streamwise position in Fig. 5.27, showing a general increase from 0.35 to 0.45 along the shear layer, albeit with a significant amount of scatter. This results suggests the separation shear layer is more dominated by vortex tripling and pairing than tearing. In the context of compressibility effects as discussed in Chapter 1, Papamoschou and Roshko (1988) and subsequent works showed the stabilizing effect of compressibility on shear layers, reducing the growth rate and inhibiting mixing. The loose trend of increasing

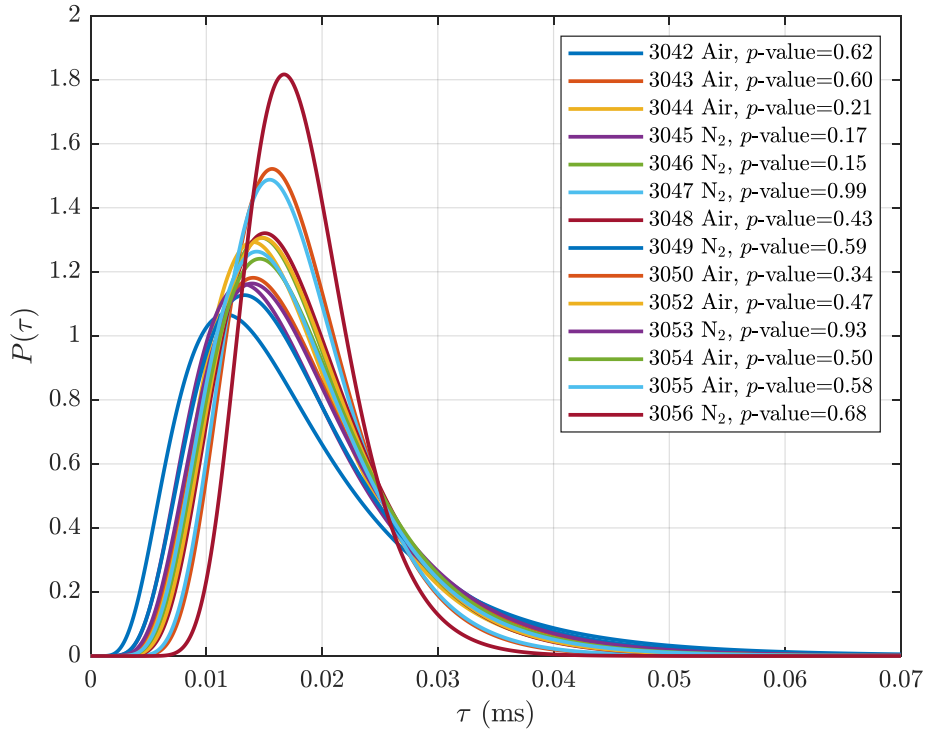

Figure 5.24: Lognormal distributions of wave packet period, τ.

standard deviation with streamwise position correlates with this observation as the likelihood of vortex tearing decreases.

Streamwise Acoustic Disturbance Scaling

The scaling presented in Schmidt and Shepherd (2015a) attributes the oscillations in the cylinder wake shear layer to streamwise acoustic communication in the subsonic region inside the separation. The acoustic frequencies, as mentioned in Chapter 1, scale with the local sound speed and separation length:

$$f_{SW} = \frac{a}{2L_{sep}} \tag{5.9}$$

With this scaling, the expected frequencies range from 28 to 31 kHz, which correspond to $St = 0.16$–0.17. This, of course, overlaps with the Kelvin-Helmholtz associated frequencies and Strouhal numbers significantly. Much like the scaling argument of the Kelvin-Helmholtz instabilities, the measured frequencies and

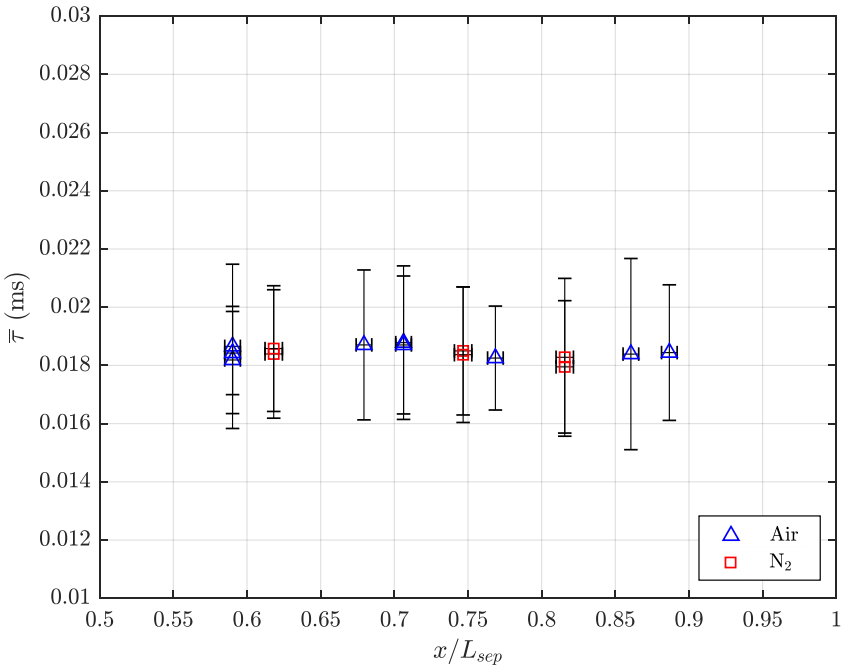

Figure 5.25: Plot of $\overline{\tau}$ vs. L_{sep}.

Strouhal number are higher than (outside of uncertainty bounds) the predicted values. As both streamwise acoustic disturbances and Kelvin-Helmholtz instabilities are present in the flow, the FLDI signal is likely a superposition of the two response. Without simultaneous high-resolution time-resolved images and simulations, it is difficult to decouple the two phenomena. From the ray-tracing analysis, the signal resembles the Kelvin-Helmholtz vortex passage structure more so than a sinusoidal acoustic wave. However, it is likely that the physical interpretation of the signal requires characterization of both types of instabilities in the context of $h(\underline{k})$ (as defined in Chapter 1) to extract a definitive conclusion.

5.5 Medium-Frequency Instabilities

The strong 300–500 kHz peaks in the PSD's in Section 5.2 can be seen visually as the medium-frequency oscillations superposed on the low-frequency oscillations in Fig. 5.21. The fitting process to the broadband peak in the PSD is discussed here, followed by scaling arguments in relation to incoming acoustic disturbances from the boundary layer and the separation region height, $H(x)$.

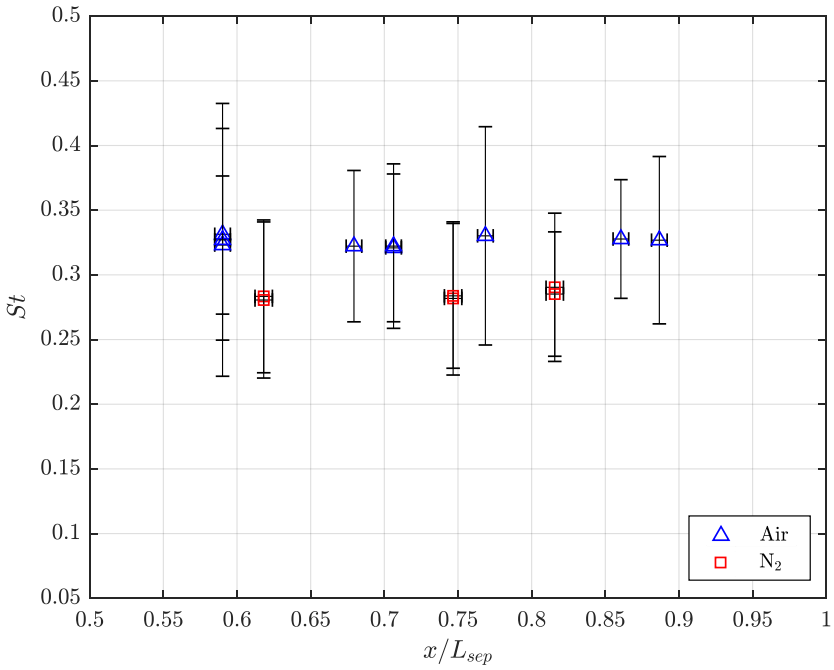

Figure 5.26: Plot of Strouhal Number vs. L_{sep}.

Fit to PSD Peak

As the broadband peaks in the PSD's (Fig. 5.11) appear to have a Gaussian profile on a log scale, a similar fitting process as before is used to characterize the mean frequency of the peak. A normal distribution is fit to $\log(f)$ as shown in Fig. 5.28. The fits for all shots are plotted in Fig. 5.29, again with the associated p-values from the Shapiro-Wilk test. The fits are then plotted versus the normalized $f/\overline{f}$ for easier comparison of peak magnitude.

Separation Region Height Scaling

When plotting the mean frequency versus x/L_{sep} (Fig. 5.30), the mean frequency has a clear dependence on the streamwise position. The decrease in frequency is significant outside of the 1-σ uncertainty bounds of the mean frequency. There is no discernible difference in the trends of the air and nitrogen cases. Since the frequency of this broadband peak is too high for streamwise acoustic disturbances or Kelvin-Helmholtz instabilities, another length scale must be considered. The significantly decreasing frequency with streamwise position suggests a changing length scale.

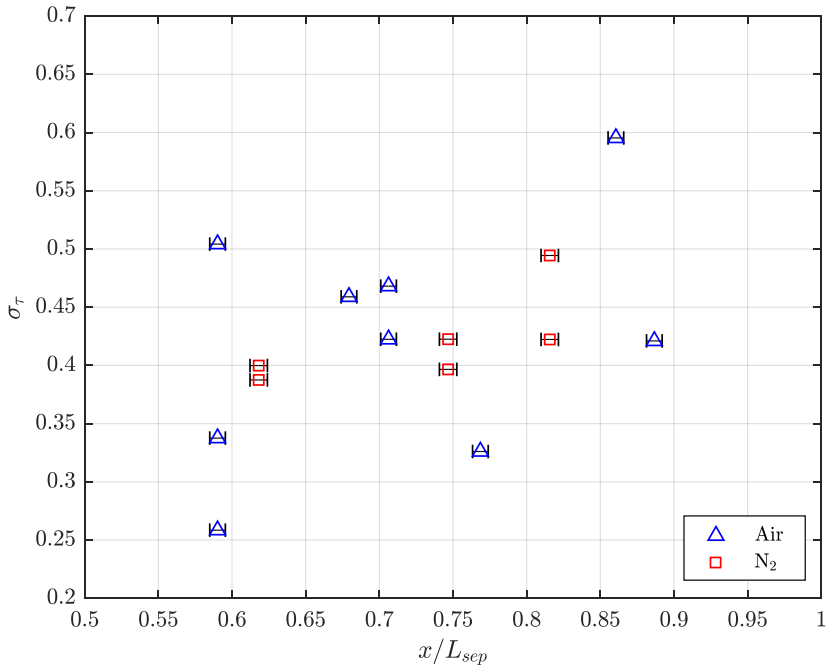

Figure 5.27: Plot of σ vs. L_{sep}.

In this case, a possible candidate for a length scale is the wall-normal distance to the shear layer, defined as $H(x)$ in Chapter 1, which increases with streamwise position. Considering acoustic disturbances, the frequency can be scaled as:

$$f_H = \frac{a}{2H(x)} \tag{5.10}$$

where a is the local sound speed in the separation region and $H(x)$ is the wall-normal distance to the shear layer, which is a linear function of x. With this scaling, the predicted frequencies range from 450 kHz at the most upstream measurement location and 370 kHz at the most downstream measurement location before the corner, which agrees remarkably well with the mean frequencies at those locations. When the Strouhal number is calculated using this length scale and the edge velocity in Region 2, it collapses around 0.5 for most of the measurement locations, as shown in Fig. 5.31. The only exception are the two measurement locations downstream of the corner, where the wall-normal distance decreases dramatically, causing the Strouhal number to decrease significantly. If the instability scaled purely with $H(x)$, the frequency would be expected to respond to the change of slope in $H(x)$ after the

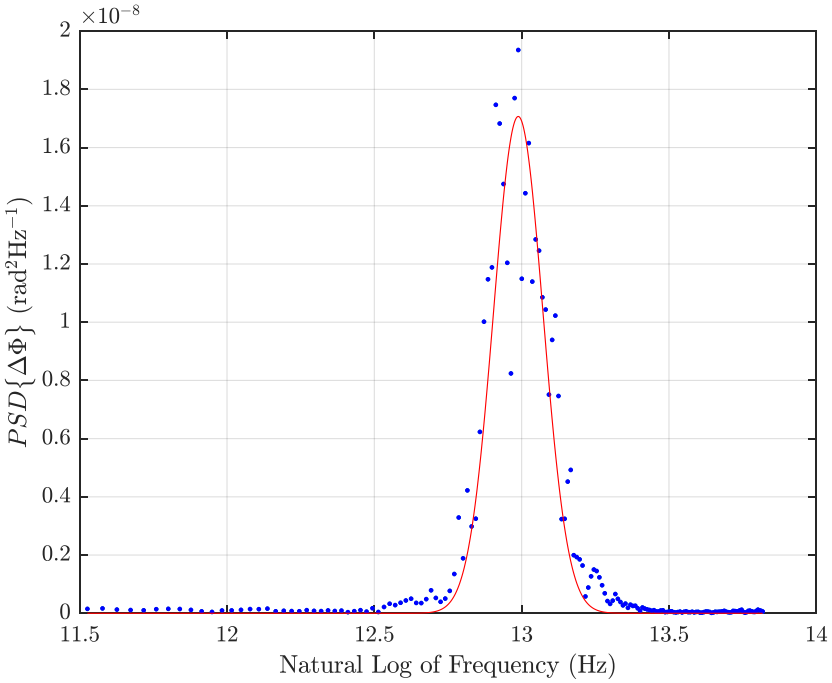

Figure 5.28: Gaussian fit to a PSD of the FLDI signal from Shot 3046 using the natural log of the measured frequency (lognormal fit).

corner, but it is clear from Fig. 5.31 that the scaling fails after the corner. Thus, additional length and velocity scales are explored, namely the shear layer thickness based on the scalings from Papamoschou and Roshko. Using the edge velocity in Region 2 and the simulated shear layer convective velocity, two Strouhal numbers are calculated to be 0.04 and 0.08, respectively. As shown in Fig. 5.32, these Strouhal numbers collapse well for all the cases, as the length scale does not have an abrupt change in slope with streamwise position. However, the value of St is lower than typically observed in literature for compressible shear layers (Butler and Laurence, 2021; Schmidt and Shepherd, 2015a).

Comparing these findings to the results of Pandey et al. (2022), Butler and Laurence (2021), and Benitez et al. (2020), they observed frequency content in the 15–60 kHz, 60–90 kHz, and 50–170 kHz ranges, respectively, which agree well with the proposed scaling in Eqn. (5.10) for their corresponding sound speeds and separation region heights. Butler and Laurence and Benitez et al. both concluded that these shear layer instabilities are independent of the second-mode. Pandey et al. (2022) also observed the frequency decreasing along the length of the shear layer and

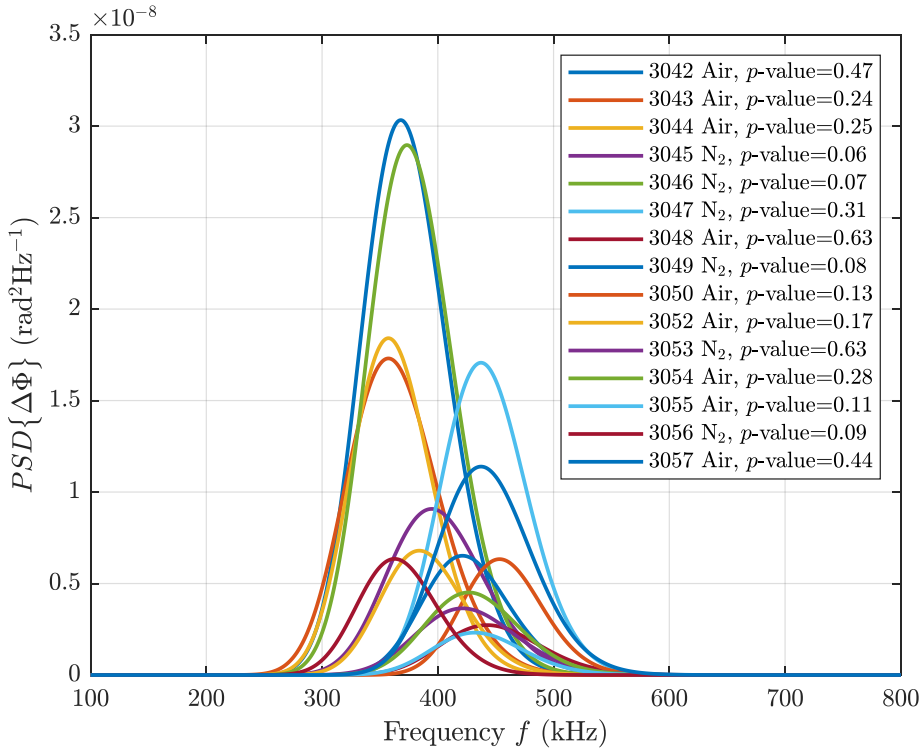

Figure 5.29: Comparison of the lognormal fits to the FLDI signal PSD from all shots.

attributed the change to the increasing distance between the shear layer and model surface, matching the observation in the current work. It is important to note, as to not conflate the different frequency ranges observed in the studies, the medium-frequency content in the current work is significantly higher frequency than the second-mode instabilities observed in the three cold-flow experiments, as the sound speed in T5 is roughly higher by a factor of five. This effectively scales up the second-mode dominant frequency bands to the MHz range (Bitter, 2015; Parziale et al., 2012), and likewise shifts these lower-frequency features up to the 370–450 kHz range.

The agreement between the experiment and scaling argument in the region upstream of the corner suggests a significant correlation between the measured broadband peak and the local distance of the shear layer to the wall. Since the frequency range is too low for second-mode instabilities inside the boundary layer or shear layer at these freestream velocities, these measured disturbances are likely a result of the

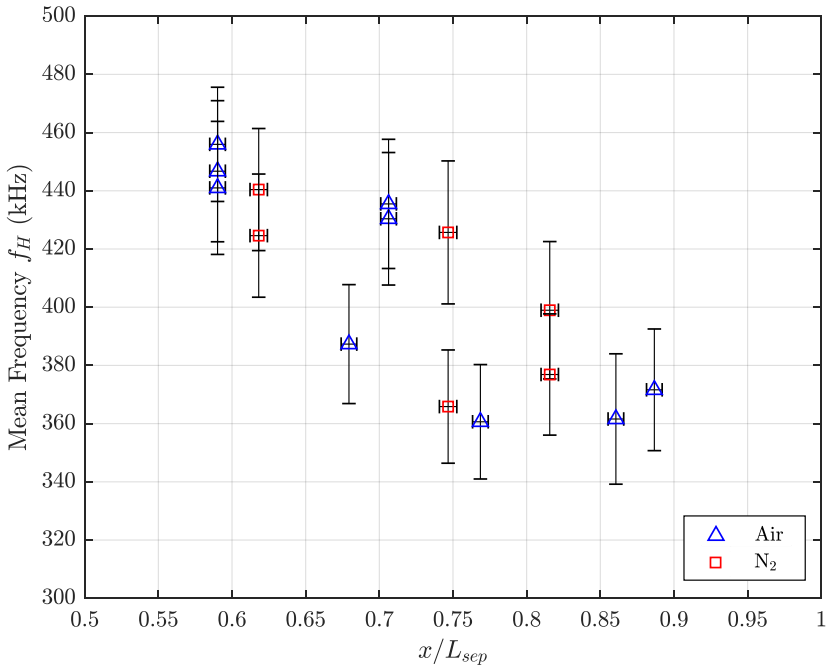

Figure 5.30: Mean frequency vs. normalized position along separation shear layer.

communication between the shear layer and the model surface through the subsonic separation region. When considering the mean frequency, the measurement points downstream of the corner do not deviate from the trend. It is only when considering Strouhal number that the downstream points do not collapse, suggesting that the acoustic disturbances do not react to the wall angle change. This is possible considering the small supersonic region inside the separation near the corner. This deviation will be a significant topic of future experimental work and simulations. While the general trend of decreasing frequency upstream of the corner is promising in considering $H(x)$ as a possible universal length scale, scatter in the data makes it difficult to conclusively collapse the measurements on a constant Strouhal number. While similar trends are noticed in other cold-flow experiments on flared cones and cone-slice-ramps, FLDI measurements both upstream and downstream of the current beam positions combined with high-resolution schlieren imaging focused on the double-cone shear layer would help characterize this frequency band. Given the prevalence of these shear layer instabilities in experiments without strong conclusive scaling arguments, high-resolution schlieren imaging and high-fidelity simulations of the separation shear layer and stability analysis could be useful in determine the

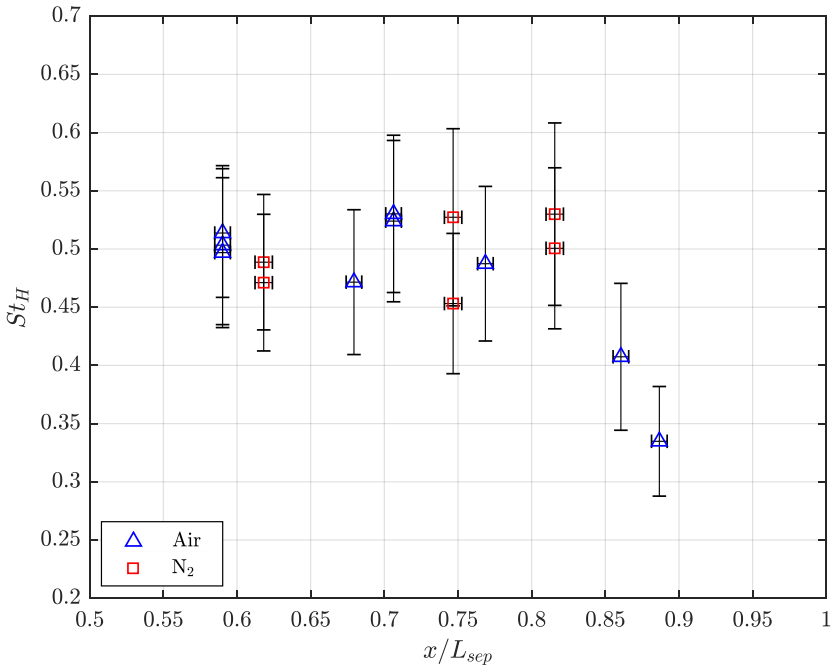

Figure 5.31: Strouhal number ($H(x)$ length scale) vs. normalized position along separation shear layer.

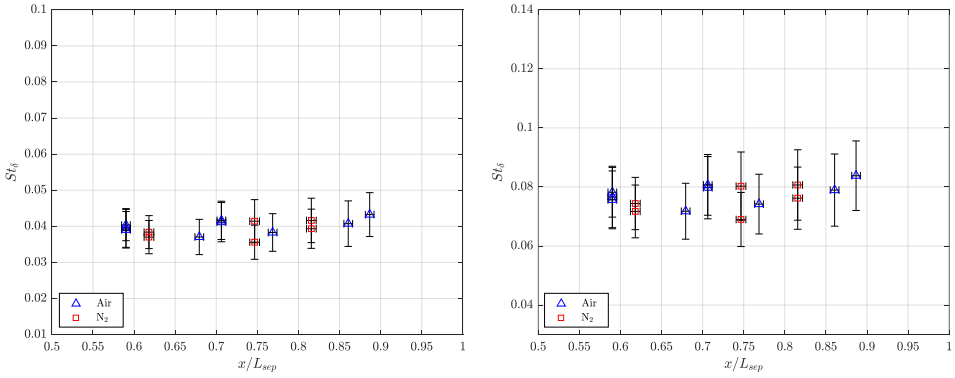

Figure 5.32: Strouhal number ($\delta(x)$ length scale) vs. normalized position along separation shear layer. Two characteristic velocities are used: edge velocity above the shear layer **(left)** and convective velocity **(right)**.

nature of these disturbances.

5.6 High-Frequency Instabilities

Additional higher-frequency content in the MHz range was observed in some shots during the campaign. As these frequencies are too high for streamwise acoustic disturbances or Kelvin-Helmholtz instabilities along the shear layer, or transverse acoustic instabilities in the separation region, the likely candidate for these features are second-mode instabilities originating in the incoming boundary layer. Pandey et al. (2022), Benitez et al. (2020), and Butler and Laurence (2021) observed second-mode instabilities in the separation shear layer that originated from the incoming boundary layer on a cone-slice-ramp geometry. The expected frequency scaling for these instabilities is:

$$f_M = \frac{KU_E}{2\delta} \tag{5.11}$$

as defined in Chapter 1. In the freestream conditions of T5, the expected frequency range is 1–5 MHz depending on whether the incoming boundary layer or the shear layer thickness is used as the length scale, respectively (Bitter, 2015; Parziale et al., 2012). Examples of such frequency features are shown in the context of the $PSD\{\Delta\Phi\}$ for Shots 3047–3050 in fig. 5.33. These shots were chosen as they were repeats in air and N_2 at the same FLDI beam positions. A peak near 1 MHz was observed for three of the experiments, but was absent in Shot 3048. Similarly transient presence of the peak was noticed in other shots, with lesser prominence in the peak magnitude. This suggests the confinement of any second-mode instabilities to within the shear layer, making detectability using the FLDI sensitive to bulk shear layer movement. Both Pandey et al. (2022) and Butler and Laurence (2021) showed the lift-off of the second-mode waves from the incoming boundary layer propagating into the shear layer, noticing the drop in second-mode signal magnitude in the separation region. The transient nature of the high-frequency peak suggests a localized propagation of the second-mode disturbances through the shear layer, while the much more repeatable and larger magnitude medium-frequency content implies a more global interaction in the separation region.

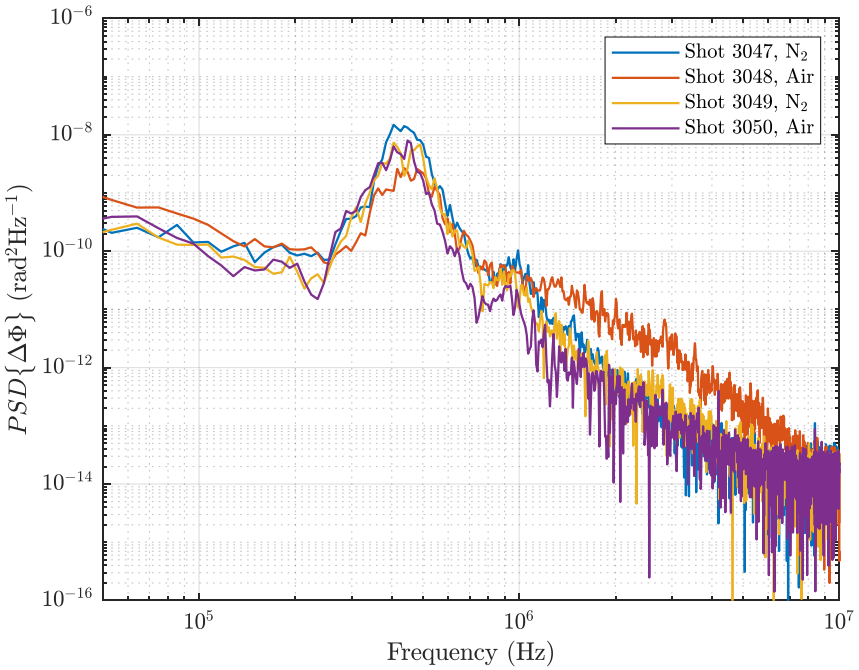

Figure 5.33: PSD's of shear layer FLDI signal for Shots 3047–3050.

Chapter 6

CONCLUSIONS & FUTURE WORK

This closing chapter summarizes the contributions of this work, which is grouped into two main areas: advancements in freestream characterization of high-enthalpy shock tunnels and applications of FLDI to measure instability modes in high-enthalpy shear layers. The conclusions are followed by recommendations for future directions of research in freestream characterization and FLDI implementation and validation in detecting shear layer instabilities.

6.1 Conclusions

Contributions to High-Enthalpy Static Pressure Measurement

A series of three static pressure probes based on Behrens (1963) and Karl (2011) were designed and deployed in the T5 Free-Piston Reflected Shock Tunnel in two test conditions at 8 MJ/kg and 16 MJ/kg stagnation enthalpies. TDLAS was also used to infer static pressure in both conditions with simultaneous measurements using the V2 static probe in the 8 MJ/kg condition. In addition to good agreement with theory and predicted values from the UMNAEM Nozzle Code, the static pressure measured by the first two static probes agreed well with each other and the TDLAS measurements in magnitude, but the V1 and V2 static probes had significantly longer response times and thus could not resolve the transient pressure changes in the nozzle startup and test time. Axisymmetric numerical simulations of the static probe responses were performed in Eilmer4, with good agreement in magnitude with the experiment. However, the overly complex internal transducer cavity of the V2 probe proved difficult to simulate accurately, so the temporal response of the probes did not match with simulation.

These discrepancies motivated the design of a static probe with a quicker response time comparable to the TDLAS measurement rate of 50 kHz. The V3 static probe was developed such that the pressure transducer location was much closer to the pressure taps, minimizing the internal cavity size and simplifying the internal geometry, increasing the response rate to 30 kHz from the 3 kHz response of the V2 static probe. The V3 probe was deployed in T5 at the 8 MJ/kg and 16 MJ/kg conditions and the temporal response and magnitude had much better agreement with the TDLAS measurement. Additionally, the V3 probe was tested in a better-

tailored version of the 16 MJ/kg condition and was able to resolve slight temporal differences between the conditions that the previous probes could not measure. With low measurement uncertainty and good repeatability, this new capability will allow for easier condition design and shot-to-shot comparison. This study has shown that the updated static probe design can be used as a permanent fixture to consistently measure static pressure with high temporal resolution for future experiments in the facility.

Contributions to Driver Gas Contamination Measurement

In this study, high-speed time-resolved schlieren/shadowgraph images were captured of a 38° symmetric opposing-wedge model in a Mach 5.5, 3.5 km/s, 8 MJ/kg stagnation enthalpy condition in T5 to quantify driver gas contamination mole fraction and arrival time. By changing the gap size between the opposing-wedges, the flow choked at varying times corresponding to different mole fractions of monatomic driver gas present in the freestream. A boundary between the choked and unchoked regimes was calculated through numerical simulations in Eilmer4 for a wide range of gap sizes and mole fractions, and then confirmed by the experiments. The measured contamination levels are within the 5% at t = 1.9 ms and 12.5% at t = 2.25 ms bounds reported in Sudani and Hornung (1998). With the higher sensitivity of the opposing-wedge model, it can be concluded that the contamination is closer to ~2% for the duration of test time and grows to 8% in the millisecond afterwards. However, the temporal resolution in study was limited by the long 500 µs response time of the large opposing-wedge model.

Contributions to FLDI Applications in Hypervelocity Shear Layers

To the author's knowledge, this is the first application of FLDI to characterize shear layer instabilities in hypervelocity conditions. While numerous studies have used FLDI in high-enthalpy freestream and boundary layers (Hameed et al., 2022; Lawson, 2021; Parziale et al., 2012), investigations of shear layers have been limited to cold-flow conditions (Benitez et al., 2020; Butler and Laurence, 2021; Pandey et al., 2022). This portion of the thesis demonstrates the feasibility of using FLDI to probe near-surface features such as the separation shear layer on the canonical 25°-55° double-cone geometry. A comprehensive FLDI dataset was collected in the streamwise direction along the shear layer in both air and N_2 test conditions, along with a simultaneous FLDI measurement in the freestream and time-resolved static pressure for each shot.

Axisymmetric numerical simulations of the 25°–55° double-cone flow were performed in Eilmer4 to calculate mean flow properties near the separation region and shear layer. The calculated velocity and density were used as inputs for a 2-D simulation of a canonical Kelvin-Helmholtz instability, also in Eilmer4. The calculated density contour was then used as a convecting disturbance in the FLDI ray-tracing model developed by Schmidt and Shepherd (2015b) and Lawson (2021) to simulate the FLDI response to various Kelvin-Helmholtz instabilities. Low-frequency (~50 kHz) wave packets of similar structure were identified in the experiment by enveloping the raw FLDI signal and measuring the periods of the envelopes, then lognormal profiles were fit to the period distributions to calculate mean frequency. The measured disturbances agree in order of magnitude with proposed scalings for Kelvin-Helmholtz instabilities (Papamoschou and Roshko, 1988) and streamwise communication between the separation and reattachment along the length of the shear layer (Schmidt and Shepherd, 2015a). Overall, the Strouhal numbers are roughly twice as large as the expected values for these modes.

The PSD's of the FLDI signal were calculated for each shot. Broadband medium-frequency peaks (~370–450 kHz) three orders of magnitude higher than the freestream were observed in all shots during this experimental campaign. Lognormal distributions were fit to the broadband peaks to determine mean frequency, which decreases with streamwise position along the shear layer. When the proposed length scale of the separation height, $H(x)$, is used to calculate Strouhal number, the data collapses to a value of 0.5 ± 0.05 for all data points upstream of the corner. When considering the same scaling using $H(x)$, similar frequency ranges are observed in cone-slice-ramp separation regions (Pandey et al., 2022) with the same decreasing frequency along the shear layer, and shear layer instabilities on flared cones (Benitez et al., 2020; Butler and Laurence, 2021). This suggests the instabilities within the shear layer are driven by communication between the shear layer and the wall. Higher-frequency peaks were also observed in some of the PSD's, which are likely due to Mack (second-mode) disturbances propagating from the boundary layer into the shear layer, as observed in multiple studies Benitez et al. (2020), Butler and Laurence (2021), and Pandey et al. (2022).

6.2 Recommendations for Future Work

Further Characterization of Static Probe Step Response

While the time-response improvements of the static probe designs were qualitatively observed, the nozzle startup process of a reflected shock tunnel is complex, so a

cleaner, more repeatable wave structure would be easier to model and characterize. A more rigorous study using a simple reflected shock tube or Ludwieg tube would be beneficial to characterizing and validating current and future static probe designs.

Fast Time-Response Driver Gas Detector

Additional work is needed to better characterize the time history of the driver gas contamination in the freestream. A smaller wedge model with the same span would have a response time on the order of 100 µs and allow the installation of a staggered "rake" of up to five pairs of opposing-wedges with different gap sizes, giving better time resolution and sensitivity to small amounts of driver gas contamination. Time-resolved shadowgraphy would be able to capture the changing monatomic gas concentration during and after test time, fully utilizing the temporal resolution in the current high-speed imaging capabilities. With the smaller wedge model, the driver gas contamination in the high enthalpy 16 MJ/kg condition with a much shorter test time could be characterized. A different option to explore is a toroidal opposing-wedge geometry with an adjustable centerline spike instrumented with a static pressure transducer to precisely track the driver gas arrival time simultaneously with flow-model experiments.

Improvements to Multi-FLDI Instrumentation

To ensure beam parallelism, the DFLDI setup used in this study consisted of two flow-oriented beam-pairs split perpendicular to the shear layer angle. This allowed for simultaneous measurements in the shear layer and the T5 freestream, which gave confidence in the measurements, as any tunnel noise could be subtracted. However, additional simultaneous beam-pairs in the streamwise direction would be useful in characterizing the convective velocity of the vortices in the shear layer. This would require additional optics, or diffractive optics capable of splitting in orthogonal directions. Further optical design and benchtop validation of this setup for future experiments could simplify the experiment and eliminate shot-to-shot variability. Additional constraints on optical placement need to be explored in order to ensure all streamwise-split FLDI channels are in phase and have the same dynamic range. Another avenue to explore would be a higher density vertical splitting angle, generating six or eight tightly spaced beam-pairs split in the y-axis. This would allow for measurements at different regions of the shear layer in the same streamwise position, which would be useful in quantifying the growth rate.

Simultaneous high-speed schlieren with multi-FLDI would be a useful tool in char-

acterizing temporal behaviors during an experiment, and also reducing uncertainty due to shot-to-shot variations. It would also allow for accurate measurement of FLDI beam locations relative to flow features of interest, allowing for precise probing of different y-positions of the shear layer. This can be achieved by placing beamsplitters between the focusing lenses and routing a schlieren optical setup at a different laser wavelength through the same location as the FLDI beams. Non-ideal effects from the beamsplitters on the FLDI beams need to be characterized before this technique can be deployed.

Additional Shear Layer Characterization in Hypervelocity Flows

The conclusions presented in this study are based largely on scaling arguments of characteristic flow features proposed in the literature for compressible shear layers, which have been shown to interact with each other. There is still a need to understand the interaction between the flowfield on the double-cone and the FLDI beams. This would require a more detailed knowledge of the full region of the flow that the beams pass through, from the foci at the shear layer to the expanded beams in Region 2. To do this, higher-resolution numerical simulations and stability analysis are needed to resolve the flow structures on the shear layer so the density field can be used with the ray-tracing model to simulate an associated $\Delta\Phi$. This can be aided by additional multi-FLDI experiments that target different regions of the flow to more quantitatively map the locations of the measured instabilities. Further experiments on various separation shear layer geometries in hypervelocity flows will inform the dependence of the measured frequencies on the proposed length scales.

BIBLIOGRAPHY

Acosta, A. R., Davis, B. W., Austin, J. M., and Hornung, H. G. (2023). "Experimental investigation of the unsteadiness boundary of supersonic flow over double cones". In: *Proceedings of the 34th International Symposium on Shock Waves*.

Almodovar, C. A., Su, W.-W., Strand, C. L., and Hanson, R. K. (2019). "R-branch line intensities and temperature-dependent line broadening and shift coefficients of the nitric oxide fundamental rovibrational band". In: *AIAA Journal* 239.106612.

Aupoix, B. (2004). "Modelling of compressibility effects in mixing layers". In: *Journal of Turbulence* 5.1, p. 007.

Awasthi, M., McCreton, S., Moreau, D., and Doolan, C. (2022). "Supersonic cylinder wake dynamics". In: *Journal of Fluid Mechanics* 945.

Bathel, B. F., Weisberger, J. M., Herring, G. C., King, R. A., Jones, S. B., Kennedy, R. E., and Laurence, S. J. (2020). "Two-point, parallel-beam focused laser differential interferometry with a nomarski prism". In: *Applied Optics* 59.2, pp. 244–252.

Behrens, W. (1963). "Viscous interaction effects on a static pressure probe at M = 6". In: *AIAA Journal* 1.12, pp. 2864–2866.

Belanger, J. (1993). "Studies of mixing and combustion in hypervelocity flows with hot hydrogen injection". In: *California Institute of Technology, PhD Dissertation*.

Benitez, E. K., Borg, M. P., Dungan, S., Brehm, C., and Jewell, J. S. (2024). "Focused laser differential interferometry performance over an axisymmetric model". In: *AIAA SciTech 2024 Forum*, p. 1931.

Benitez, E. K., Esquieu, S., Jewell, J. S., and Schneider, S. P. (2020). "Instability measurements on an axisymmetric separation bubble at Mach 6". In: *AIAA Aviation 2020 Forum*, p. 3072.

Benitez, E. K. and Jewell, J. S. (2022). "Simulated focused laser differential interferometry of time-varying signals". In: *AIAA SciTech 2022 Forum*, p. 1312.

Benitez, E. K., Jewell, J. S., and Schneider, S. P. (2021). "Focused laser differential interferometry with contoured tunnel windows". In: *AIAA Journal* 59.2, pp. 419–429.

Benitez, E. K., Leger, T. J., Tufts, M. W., Borg, M. P., and Hill, J. L. (2023). "Hypersonic transitional boundary-layer profile using a linear-array FLDI". In: *AIAA Aviation 2023 Forum*, p. 4253.

Bernal, L. P. (1988). "The statistics of the organized vortical structure in turbulent mixing layers". In: *The Physics of Fluids* 31.9, pp. 2533–2543.

Bitter, N. P. (2015). "Stability of hypervelocity boundary layers". PhD thesis. California Institute of Technology.

Bose, D. and Candler, G. V. (1996). "Thermal rate constants of the N2+O → NO+N reaction using *ab initio* 3A″ and 3A′ potential energy surfaces". In: *The Journal of Chemical Physics* 104.8, pp. 2825–2833.

Bose, D. and Candler, G. V. (1997). "Thermal rate constants of the O2+N → NO+O reaction based on the A2′ and A4′ potential-energy surfaces". In: *The Journal of Chemical Physics* 107.16, pp. 6136–6145.

Brown, G. L. and Roshko, A. (1974). "On density effects and large structure in turbulent mixing layers". In: *Journal of Fluid Mechanics* 64.4, pp. 775–816.

Browne, S., Ziegler, J., and Shepherd, J. E. (2006). "Numerical solution methods for shock and detonation jump conditions". In: *California Institute of Technology, GALCIT - FM2006-006*.

Butler, C. S. and Laurence, S. J. (2021). "Interaction of second-mode disturbances with an incipiently separated compression-corner flow". In: *Journal of Fluid Mechanics* 913, R4.

Candler, G. (2005). "Hypersonic nozzle analysis using an excluded volume equation of state". In: *Proceedings of 38th AIAA Thermophysics Conference*. Toronto, Ontario Canada: AIAA.

Candler, G., Doraiswamy, S., and Kelley, J. (2010). "The potential role of electronically-excited states in recombining flows". In: *48th AIAA Aerospace Sciences Meeting Including the New Horizons Forum and Aerospace Exposition*, p. 912.

Canny, J. (1986). "A computational approach to edge detection". In: *IEEE Transactions on Pattern Analysis and Machine Intelligence* 6, pp. 679–698.

Catris, S. and Aupoix, B. (2000). "Density corrections for turbulence models". In: *Aerospace Science and Technology* 4.1, pp. 1–11.

Ceruzzi, A. and Cadou, C. P. (2017). "Turbulent air jet investigation using focused laser differential interferometry". In: *53rd AIAA/SAE/ASEE Joint Propulsion Conference*, p. 4834.

Ceruzzi, A. and Cadou, C. P. (2019). "Simultaneous velocity and density gradient measurements using two-point focused laser differential interferometry". In: *AIAA SciTech 2019 Forum*, p. 2295.

Ceruzzi, A., Callis, B., Weber, D., and Cadou, C. P. (2020). "Application of focused laser differential interferometry (FLDI) in a supersonic boundary layer". In: *AIAA SciTech 2020 Forum*, p. 1973.

Ceruzzi, A., McManamen, B., and Cadou, C. P. (2021a). "Demonstration of two-point focused laser differential interferometry (2pFLDI) in a mach 18 flow". In: *AIAA SciTech 2021 Forum*, p. 0983.

Ceruzzi, A., Neisess, C., McManamen, B., and Cadou, C. P. (2021b). "Investigation of focused laser differential interferometry (FLDI) sensitivity function". In: *AIAA SciTech 2021 Forum*, p. 1299.

Ceruzzi, A. P. and Cadou, C. P. (2022). "Interpreting single-point and two-point focused laser differential interferometry in a turbulent jet". In: *Experiments in Fluids* 63.7, p. 112.

Chaudhry, R. S., Boyd, I. D., and Candler, G. V. (2020a). "Vehicle-scale simulations of hypersonic flows using the MMT chemical kinetics model". In: *AIAA Aviation 2020 Forum*, p. 3272.

Chaudhry, R. S., Boyd, I. D., Torres, E., Schwartzentruber, T. E., and Candler, G. V. (2020b). "Implementation of a chemical kinetics model for hypersonic flows in air for high-performance CFD". In: *AIAA SciTech 2020 Forum*, p. 2191.

Clemens, N. and Mungal, M. (1995). "Large-scale structure and entrainment in the supersonic mixing layer". In: *Journal of Fluid Mechanics* 284, pp. 171–216.

Crane, L. (1957). "The laminar and turbulent mixing of jets of compressible fluid. part ii the mixing of two semi-infinite streams". In: *Journal of Fluid Mechanics* 3.1, pp. 81–92.

Crane, L. and Pack, D. (1957). "The laminar and turbulent mixing of jets of compressible fluid. part i flow far from the orifice". In: *Journal of Fluid Mechanics* 2.5, pp. 449–455.

Davies, L. and Wilson, J. L. (1969). "Influence of reflected shock and boundary-layer interaction on shock-tube flows". In: *The Physics of Fluids* 12, pp. 1–37.

Davis, J.-P. and Sturtevant, B. (2000). "Separation length in high-enthalpy shock/boundary-layer interaction". In: *Physics of Fluids* 12.10, pp. 2661–2687.

Davis, J. (1999). "High-enthalpy shock boundary layer interaction on a double wedge". In: *Ph. D. Dissertation, California Institute of Technology*.

Demetriades, A. (1977). *Laminar boundary layer stability measurements at Mach 7 including wall temperature effects*. Ford Aerospace & Communications Corporation, Aernutronic Division.

Dimotakis, P. E. (1991). "Turbulent free shear layer mixing and combustion". In: *GALCIT Report FM91–2*.

Dimotakis, P. E. and Brown, G. L. (1976). "The mixing layer at high reynolds number: large-structure dynamics and entrainment". In: *Journal of Fluid Mechanics* 78.3, pp. 535–560.

Druguet, M.-C., Candler, G. V., and Nompelis, I. (2005). "Effects of numerics on navier-stokes computations of hypersonic double-cone flows". In: *AIAA journal* 43.3, pp. 616–623.

Ebrahim, N. A. and Hornung, H. G. (1975). "High-enthalpy nonequilbrium carbon dioxide nozzle and wedge flows: experiment and calculations". In: *AIAA Journal* 13.7, pp. 845–846.

Edney, B. E. (1968). "Effects of shock impingement on the heat transfer around blunt bodies". In: *AIAA Journal* 6.1, pp. 15–21.

Fedorov, A. V. (2003). "Receptivity of a high-speed boundary layer to acoustic disturbances". In: *Journal of Fluid Mechanics* 491, pp. 101–129.

Finch, P. M., Schwartz, T., Granowitz, Z. N., Yu, W. M., Gross, T., Strand, C. L., Schwartzentruber, T. E., Austin, J. M., Hornung, H. G., and Hanson, R. K. (2023a). "Near-body measurements in hypersonic wedge flows in the T5 reflected shock tunnel by tunable diode laser absorption spectroscopy". In: *AIAA SciTech 2023 Forum*, p. 2518.

Finch, P. M., Girard, J., Strand, C. L., Hanson, R. K., Yu, W. M., Austin, J. M., and Hornung, H. G. (2023b). "Measurements of T5 shock tunnel freestream temperature, velocity, and composition". In: *AIAA Journal*.

Flaherty, W. P. (2010). "Experimental surface heat flux measurement in hypervelocity flows". PhD thesis. University of Illinois at Urbana-Champaign.

Freymuth, P. (1966). "On transition in a separated laminar boundary layer". In: *Journal of Fluid Mechanics* 25.4, pp. 683–704.

Gardiner, W., Hidaka, Y., and Tanzawa, T. (1981). "Refractivity of combustion gases". In: *Combustion and Flame* 40, pp. 213–219.

Gaydon, A. G. and Hurle, I. R. (1963). "The shock tube in high-temperature chemical physics". In: Reinhold Publishing Corporation.

Gilvey, J. J., Goldenstein, C. S., Downing, C., Lyon, B. T., Lynch, K. P., and Wagner, J. L. (2024). "Characterization of non-equilibrium no in hypersonic air via laser absorption spectroscopy". In: *AIAA SciTech 2024 Forum*, p. 2832.

Girard, J. J., Finch, P. M., Strand, C. L., Hanson, R. K., Yu, W. M., Austin, J. M., and Hornung, H. G. (2021). "Measurements of reflected shock tunnel freestream nitric oxide temperatures and partial pressure". In: *AIAA Journal* 59.12, pp. 5266–5275.

Gladstone, J. H. and Dale, T. P. (1863). "Xiv. researches on the refraction, dispersion, and sensitiveness of liquids". In: *Philosophical Transactions of the Royal Society of London* 153, pp. 317–343.

Goebel, S. G. and Dutton, J. C. (1991). "Experimental study of compressible turbulent mixing layers". In: *AIAA Journal* 29.4, pp. 538–546.

Gollan, R. J. and Jacobs, P. A. (2013). "About the formulation, verification and validation of the hypersonic flow solver eilmer". In: *Intl J. Numer. Meth. Fluids* 73, pp. 19–57.

Goodman, J. W. (2015). *Statistical optics*. John Wiley & Sons.

Gupta, R. N., Yos, J. M., Thompson, R. A., and Lee, K.-P. (1990). "A review of reaction rates and thermodynamic and transport properties for an 11-species air model for chemical and thermal nonequilibrium calculations to 30000 K". In: *NASA Technical Report*.

Hameed, A. (2023). "Spectral analysis of hypersonic boundary-layer instability". PhD thesis. Stevens Institute of Technology.

Hameed, A. and Parziale, N. J. (2021). "Focused laser differential interferometer response to a controlled phase object". In: *AIAA SciTech 2021 Forum*, p. 0602.

Hameed, A. and Parziale, N. J. (2022). "Focused laser differential interferometric investigation of turbulent jet spectra". In: *Journal of Spacecraft and Rockets* 59.5, pp. 1565–1573.

Hameed, A., Shekhtman, D., Parziale, N., Paquin, L. A., Skinner, S., Laurence, S. J., Yu, W. M., and Austin, J. M. (2022). "Hypersonic boundary-layer instability on a highly cooled cone. Part I: Q-FLDI measurement and instability calculations". In: *AIAA SciTech 2022 Forum*, p. 0734.

Hanson, R. K., Spearrin, R. M., and Goldenstein, C. S. (2016). "Spectroscopy and optical diagnostics for gases". In: Springer International Publishing.

Hao, J., Fan, J., Cao, S., and Wen, C.-Y. (2022). "Three-dimensionality of hypersonic laminar flow over a double cone". In: *Journal of Fluid Mechanics* 935, A8.

Hao, J. and Wen, C.-Y. (2018). "Numerical investigation of oxygen thermochemical nonequilibrium on high-enthalpy double-cone flows". In: *International Journal of Heat and Mass Transfer* 127, pp. 892–902.

Hao, J. and Wen, C.-Y. (2020). "Hypersonic flow over spherically blunted double cones". In: *Journal of Fluid Mechanics* 896, A26.

Hashimoto, T., Rowan, S., Komuro, T., Sato, K., Itoh, K., Robinson, M., Schramm, J., and Hannemann, K. (2009). "Application of HEG static pressure probe in HIEST". In: *26th International Symposium on Shock Waves*.

Hayes, W. D. and Probstein, R. F. (1958). *Hypersonic Flow Theory*. New York and London: Academic Press. Chap. IX.

Helmholtz (1868). "On discontinuous movements of fluids". In: *The London, Edinburgh, and Dublin Philosophical Magazine and Journal of Science* 36.244, pp. 337–346.

Hernan, M. A. and Jimenez, J. (1982). "Computer analysis of a high-speed film of the plane turbulent mixing layer". In: *Journal of Fluid Mechanics* 119, pp. 323–345.

Hinman, W. S. and Johansen, C. T. (2018). "Mechanisms in the hypersonic laminar near wake of a blunt body". In: *Journal of Fluid Mechanics* 839, pp. 33–75.

Holloway, M. E., Chaudhry, R. S., and Boyd, I. D. (2022). "Assessment of hypersonic double-cone experiments for validation of thermochemistry models". In: *Journal of Spacecraft and Rockets* 59.2, pp. 389–400.

Hornung, H. (1992). "Performance data of the new free-piston shock tunnel at GALCIT". In: *17th AIAA Aerospace Ground Testing Conference*. Nashville, TN: AIAA.

Hornung, H. (2004). "Response of pressure tap". In: *California Institute of Technology, Internal Report*.

Hornung, H. (2023). “T5 nozzle computation with specified throat-condition history”. In: *Eilmer Technical Notes*.

Hornung, H. G. (2010). “Ground testing for hypervelocity flow, capabilities and limitations”. In: *AVT-186 RTO AVT/VKI Lecture Series*, pp. 1–26.

Hornung, H., Gollan, R., and Jacobs, P. (2021). “Unsteadiness boundaries in supersonic flow over double cones”. In: *Journal of Fluid Mechanics* 916, A5.

Houpt, A. W. and Leonov, S. B. (2018). “Focused laser differential interferometer for supersonic boundary layer measurements on flat plate geometries”. In: *2018 Plasmadynamics and Lasers Conference*, p. 3434.

Huang, M.-K. and Inger, G. (1983). “Application of the triple-deck theory of viscous-inviscid interaction to bodies of revolution”. In: *Journal of Fluid Mechanics* 129, pp. 427–441.

Hurst, A., Olsen, T., Goodman, S., VanDeWeert, J., and Shang, T. (2014). “An experimental frequency response characterization of MEMSpiezoresistive pressure transducers”. In: *Proceedings of ASME Turbo Expo 2014*. Dusseldorf, Germany: ASME.

Jackson, T. and Grosch, C. (1989). “Inviscid spatial stability of a compressible mixing layer”. In: *Journal of Fluid Mechanics* 208, pp. 609–637.

Jacobs, P. A. (1991). “Single-block Navier–Stokes integrator”. In: *ICASE Interim Rep. 18, NASA Langley Research Center*.

Jans, E., Lynch, K. P., Wagnild, R., Swain, W. E., Downing, C., Kearney, S. P., Wagner, J. L., Gilvey, J. J., and Goldenstein, C. S. (2024). “Laser-based characterization of reflected shock tunnel freestream velocity and multi-species thermal nonequilibrium with comparison to modeling”. In: *AIAA SciTech 2024 Forum*, p. 1753.

Jewell, J., Wagnild, R., Leyva, I., Candler, G., and Shepherd, J. (2013). “Transition within a hypervelocity boundary layer on a 5-degree half-angle cone in Air/CO2 mixtures”. In: *51st AIAA Aerospace Sciences Meeting Including the New Horizons Forum and Aerospace Exposition*, p. 523.

Karl, S. (2011). “Numerical investigation of a generic scramjet configuration”. In: *Technical University of Dresden, PhD Dissertation*.

Kim, H. and Durbin, P. (1988). “Observations of the frequencies in a sphere wake and of drag increase by acoustic excitation”. In: *The Physics of Fluids* 31.11, pp. 3260–3265.

Knight, D., Chazot, O., Austin, J., Badr, M. A., Candler, G., Celik, B., Rosa, D. de, Donelli, R., Komives, J., Lani, A., et al. (2017). “Assessment of predictive capabilities for aerodynamic heating in hypersonic flow”. In: *Progress in Aerospace Sciences* 90, pp. 39–53.

Knisely, A. M. (2016). “Experimental investigation of nonequilibrium and separation scaling in double-wedge and double-cone geometries”. PhD thesis. University of Illinois at Urbana-Champaign.

Kragh, H. (1991). “Ludvig Lorenz and nineteenth century optical theory: the work of a great Danish scientist”. In: *Applied optics* 30.33, pp. 4688–4695.

Lawson, J. M. and Austin, J. M. (2020). “Expansion tube freestream disturbance measurements using a focused laser differential interferometer”. In: *AIAA SciTech 2020 Forum*, p. 1064.

Lawson, J. M. and Austin, J. M. (2023a). “Recovering density disturbance spectra from FLDI. part 1”. In: *Applied Optics* 62.12, pp. 3042–3053.

Lawson, J. M. and Austin, J. M. (2023b). “Recovering density disturbance spectra from FLDI. part 2: comparisons with previous methods”. In: *Applied Optics* 62.12, pp. 3054–3061.

Lawson, J. M., Neet, M. C., Grossman, I. J., and Austin, J. M. (2019). “Characterization of a focused laser differential interferometer”. In: *AIAA SciTech 2019 Forum*, p. 2296.

Lawson, J. M., Neet, M. C., Grossman, I. J., and Austin, J. M. (2020). “Static and dynamic characterization of a focused laser differential interferometer”. In: *Experiments in Fluids* 61, pp. 1–11.

Lawson, J. M., Neet, M. C., Hofferth, J. W., and Austin, J. M. (2022). “Supersonic freestream density fluctuations from focused laser differential interferometry and pitot-probe measurements”. In: *AIAA Journal* 60.9, pp. 5173–5186.

Lawson, J. M. (2021). “Focused laser differential interferometry”. PhD thesis. California Institute of Technology.

Leonov, B. S., Dean, T. S., McGruder, D. E., Bowersox, R. D., Limbach, C., and Miles, R. (2023). “Burst-mode nitric oxide PLIF for visualization and mode spectral analysis of hypersonic shear layers”. In: *AIAA AVIATION 2023 Forum*, p. 4382.

Liou, M.-S. and Van Leer, B. (1988). “Choice of implicit and explicit operators for the upwind differencing method”. In: *26th Aerospace Sciences Meeting*, p. 624.

Mack, L. M. (1984). “Boundary-layer linear stability theory”. In: *AGARD Report* 709.3, pp. 1–3.

Mack, L. M. (1990). “On the inviscid acoustic-mode instability of supersonic shear flows: Part 1: Two-dimensional waves”. In: *Theoretical and Computational Fluid Dynamics* 2.2, pp. 97–123.

MacLean, M., Holden, M., and Dufrene, A. (2014). “Comparison between CFD and measurements for real-gas effects on laminar shock wave boundary layer interaction, i”. In: *Oral Presentation, AIAA Aviation* 2014.

MacLean, M., Holden, M., Wadhams, T., and Parker, R. (2007). "A computational analysis of thermochemical studies in the lens facilities". In: *45th AIAA Aerospace Sciences Meeting and Exhibit*, p. 121.

Mark, H. (1958). "The interaction of a reflected shock wave with the boundary layer in a shock tube". In: *NASA Technical Report*.

Martens, S., Kinzie, K. W., and McLaughlin, D. K. (1994). "Measurements of Kelvin-Helmholtz instabilities in a supersonic shear layer". In: *AIAA Journal* 32.8, pp. 1633–1639.

Massa, L. and Austin, J. (2008). "Spatial linear stability of a hypersonic shear layer with nonequilibrium thermochemistry". In: *Physics of Fluids* 20.8.

Matsuo, K., Kawagoe, S., and Kage, K. (1974). "The interaction of a reflected shock wave with the boundary layer in a shock tube". In: *Bulletin of JSME* 17.110, pp. 1039–1046.

Matthews, M. L. (1958). "An experimental investigation of viscous effects on static and impact pressure probes in hypersonic flow". In: *California Institute of Technology, Hypersonic Research Project Memo*.

Maydew, R. and Reed, J. (1963). "Turbulent mixing of compressible free jets". In: *AIAA Journal* 1.6, pp. 1443–1445.

Merzkirch, W. and Gersten, K. (1987). "Techniques of flow visualization". In: AGARD.

Milonni, P. W. and Eberly, J. H. (2010). *Laser Physics*. John Wiley & Sons.

Moore, D. and Saffman, P. (1975). "The density of organized vortices in a turbulent mixing layer". In: *Journal of Fluid Mechanics* 69.3, pp. 465–473.

Mouton, C. A. (2007). "Transition between regular reflection and Mach reflection in the dual-solution domain". PhD thesis. California Institute of Technology.

Nompelis, I. and Candler, G. (2010). "Numerical investigation of double-cone flow experiments with high-enthalpy effects". In: *48th AIAA Aerospace Sciences Meeting Including the New Horizons Forum and Aerospace Exposition*, p. 1283.

Nompelis, I., Candler, G. V., and Holden, M. S. (2003). "Effect of vibrational nonequilibrium on hypersonic double-cone experiments". In: *AIAA Journal* 41.11, pp. 2162–2169.

Olejniczak, J., Candler, G., Hornung, H., Olejniczak, J., Candler, G., and Hornung, H. (1997). "Computation of double-cone experiments in high enthalpy nitrogen". In: *32nd Thermophysics Conference*, p. 2549.

Olejniczak, J., Candler, G., Wright, M., Hornung, H., and Leyva, I. (1996). "High enthalpy double-wedge experiments". In: *Advanced Measurement and Ground Testing Conference*, p. 2238.

Pandey, A., Casper, K. M., Guildenbecher, D. R., Beresh, S. J., Bhakta, R., DeZetter, M. E., and Spillers, R. (2022). "Instability measurements in hypersonic flow on a three-dimensional cone-slice-ramp geometry". In: *AIAA SciTech 2022 Forum*, p. 1578.

Papamoschou, D. and Roshko, A. (1988). "The compressible turbulent shear layer: an experimental study". In: *Journal of Fluid Mechanics* 197, pp. 453–477.

Paquin, L. A., Skinner, S. N., and Laurence, S. J. (2023). "Hypersonic boundary-layer disturbances on a cooled, slender cone at Mach 6". In: *Journal of Spacecraft and Rockets* 60.2, pp. 533–544.

Park, C. (1993). "Review of chemical-kinetic problems of future NASA missions. I-earth entries". In: *Journal of Thermophysics and Heat Transfer* 7.3, pp. 385–398.

Parziale, N., Shepherd, J., and Hornung, H. (2012). "Reflected shock tunnel noise measurement by focused differential interferometry". In: *42nd AIAA Fluid Dynamics Conference and Exhibit*, p. 3261.

Parziale, N. J. (2013). "Slender-body hypervelocity boundary-layer instability". PhD thesis. California Institute of Technology.

Parziale, N. J., Schmidt, B. E., Wang, P., Hornung, H., and Shepherd, J. (2015a). "Pulsed laser diode for use as a light source for short-exposure, high-frame-rate flow visualization". In: *53rd AIAA Aerospace Sciences Meeting*, p. 0530.

Parziale, N., Shepherd, J., and Hornung, H. (2014). "Free-stream density perturbations in a reflected-shock tunnel". In: *Experiments in Fluids* 55, pp. 1–10.

Parziale, N., Shepherd, J., and Hornung, H. (2015b). "Observations of hypervelocity boundary-layer instability". In: *Journal of Fluid Mechanics* 781, pp. 87–112.

Paull, A. (1996). "A simple shock tunnel driver gas detector". In: *Shock Waves* 6, pp. 309–312.

Paull, A. and King, M. (1995). "A driver gas detection device for shock tunnels". In: *Shock Waves* 4, pp. 289–291.

Pirozzoli, S. and Grasso, F. (2006). "Direct numerical simulation of impinging shock wave/turbulent boundary layer interaction at m= 2.25". In: *Physics of Fluids* 18.6.

Rasheed, A., Hornung, H., Fedorov, A., and Malmuth, N. (2002). "Experiments on passive hypervelocity boundary-layer control using an ultrasonically absorptive surface". In: *AIAA Journal* 40.3, pp. 481–489.

Ray, J., Blonigan, P., Phipps, E. T., and Maupin, K. (2023). "An assessment of the laminar hypersonic double-cone experiments in the lens-xx tunnel". In: *AIAA Journal* 61.8, pp. 3298–3312.

Reinert, J. D., Candler, G. V., and Komives, J. R. (2020). "Simulations of unsteady three-dimensional hypersonic double-wedge flow experiments". In: *AIAA Journal* 58.9, pp. 4055–4067.

Roshko, A. (1993). “Free shear layers, base pressure and bluff-body drag”. In: *Proceedings of the Symposium on Developments in Fluid Dynamics and Aerospace Engineering*, pp. 9–10.

Royston, P. (1992). “Approximating the Shapiro-Wilk W-test for non-normality”. In: *Statistics and Computing* 2, pp. 117–119.

Sanderson, S. and Sturtevant, B. (2002). “Transient heat flux measurement using a surface junction thermocouple”. In: *Review of Scientific Instruments* 73.7, pp. 2781–2787.

Schmidt, B. and Shepherd, J. (2015a). “Oscillations in cylinder wakes at Mach 4”. In: *Journal of Fluid Mechanics* 785, R3.

Schmidt, B. E. and Shepherd, J. (2015b). “Analysis of focused laser differential interferometry”. In: *Applied Optics* 54.28, pp. 8459–8472.

Settles, G. S. and Fulghum, M. R. (2016). “The focusing laser differential interferometer, an instrument for localized turbulence measurements in refractive flows”. In: *Journal of Fluids Engineering* 138.10, p. 101402.

Shapiro, S. S. and Wilk, M. B. (1965). “An analysis of variance test for normality (complete samples)”. In: *Biometrika* 52.3-4, pp. 591–611.

Shin, D. and Ferziger, J. (1993). “Linear stability of the compressible reacting mixing layer”. In: *AIAA Journal* 31.4, pp. 677–685.

Smeets, G. and George, A. (1973). “Laser-differential interferometer applications in gas dynamics”. In: *Translation of ISL Internal Report* 28, p. 73.

Smith, K. and Dutton, J. (1999). “Evolution and convection of large-scale structures in supersonic reattaching shear flows”. In: *Physics of Fluids* 11.8, pp. 2127–2138.

Smits, A. J. and Dussauge, J.-P. (2006). *Turbulent shear layers in supersonic flow*. Springer Science & Business Media.

Spalart, P. and Allmaras, S. (1992). “A one-equation turbulence model for aerodynamic flows”. In: *30th Aerospace Sciences Meeting and Exhibit*, p. 439.

Stalker, R. (1968). “A driver gas contamination probe for shock tunnels”. In: *Aeronautical Quarterly* 19.2, pp. 183–191.

Stalker, R. and Crane, K. (1978). “Driver gas contamination in a high-enthalpy reflected shock tunnel”. In: *AIAA Journal* 16.3, pp. 277–279.

Steger, J. L. and Warming, R. (1981). “Flux vector splitting of the inviscid gas-dynamic equations with application to finite-difference methods”. In: *Journal of Computational Physics* 40.2, pp. 263–293.

Stetson, K. F., Thompson, E. R., Donaldson, J. C., and Siler, L. G. (1984). “Laminar boundary layer stability experiments on a cone at Mach 8. II-Blunt cone”. In: *American Institute of Aeronautics and Astronautics, Aerospace Sciences Meeting, 22 nd, Reno, NV*.

Stewartson, K. and Williams, P. (1969). "Self-induced separation". In: *Proceedings of the Royal Society of London. A. Mathematical and Physical Sciences* 312.1509, pp. 181–206.

Sudani, N. and Hornung, H. (1998). "Gasdynamical detectors of driver gas contamination in a high-enthalpy shock tunnel". In: *AIAA Journal* 36.3.

Sundqvist, B. (1992). "Thermal diffusivity and thermal conductivity of chromel, alumel, and constantan in the range 100–450 k". In: *Journal of Applied Physics* 72.2, pp. 539–545.

Swantek, A. and Austin, J. (2015). "Flowfield establishment in hypervelocity shock-wave/boundary-layer interactions". In: *AIAA Journal* 53.2, pp. 311–320.

Sychev, V. (1982). "Asymptotic theory of separation flows". In: *Fluid Dynamics* 17.2, pp. 179–188.

Thomson, W. (1871). "Xlvi. hydrokinetic solutions and observations". In: *The London, Edinburgh, and Dublin Philosophical Magazine and Journal of Science* 42.281, pp. 362–377.

Thurow, B., Samimy, M., and Lempert, W. (2003). "Compressibility effects on turbulence structures of axisymmetric mixing layers". In: *Physics of fluids* 15.6, pp. 1755–1765.

Weisberger, J. M., Bathel, B. F., Herring, G. C., Buck, G. M., Jones, S. B., and Cavone, A. A. (2020). "Multi-point line focused laser differential interferometer for high-speed flow fluctuation measurements". In: *Applied Optics* 59.35, pp. 11180–11195.

Weisberger, J. M., Bathel, B. F., Herring, G. C., King, R. A., Chou, A., and Jones, S. (2019). "Two-point focused laser differential interferometry second-mode measurements at mach 6". In: *NASA Technical Report*.

Welch, P. (1967). "The use of fast Fourier transform for the estimation of power spectra: a method based on time averaging over short, modified periodograms". In: *IEEE Transactions on Audio and Electroacoustics* 15.2, pp. 70–73.

Winant, C. D. and Browand, F. K. (1974). "Vortex pairing: the mechanism of turbulent mixing-layer growth at moderate Reynolds number". In: *Journal of Fluid Mechanics* 63.2, pp. 237–255.

Wright, M. J., Candler, G. V., and Bose, D. (1998). "Data-parallel line relaxation method for the Navier-Stokes equations". In: *AIAA Journal* 36.9, pp. 1603–1609.

Yu, W. M., Austin, J. M., and Hornung, H. G. (2022a). "Freestream static pressure measurements in the T5 reflected shock tunnel". In: *AIAA SciTech 2022 Forum*. San Diego, CA: AIAA. DOI: 10.2514/6.2022-1658.

Yu, W. M., Luo, Y., Austin, J. M., and Hornung, H. G. (2022b). "Temporal freestream measurements in the T5 free piston shock tunnel". In: *23rd Australasian Fluid Mechanics Conference*. [Non-Listed]. Sydney, Australia: AFMS.

Yu, W. M., Luo, Y., Austin, J. M., Hornung, H. G., Finch, P. M., Schwartz, T., Strand, C. L., and Hanson, R. K. (2023). "Comparison of static pressure measurement techniques in the T5 free-piston reflected shock tunnel". In: *The 34th International Symposium on Shock Waves*. [Accepted]. Daegu, Korea: ISSW34.

Yu, W. M., Luo, Y., Austin, J. M., Hornung, H. G., Finch, P. M., Schwartz, T., Strand, C. L., and Hanson, R. K. (2024). "High-frequency static pressure measurements in the T5 reflected shock tunnel". In: *AIAA SciTech 2024 Forum*. Orlando, FL: AIAA. DOI: 10.2514/6.2024-2884.

Appendix A

T5 TEST CONDITIONS

Table A.1: T5 Facility Conditions

Shot	Condition	h_0 (MJ/kg)	U_s (m/s)	P_1 (kPa)	P_R (MPa)	T_R (K)	P_4 (MPa)
2903	H18-Air-A	17.9	4221	35.0	56.1	8676	115.5
2904	H8-Re2-Air	8.20	2987	45.0	20.5	5149	39.70
2905	H18-Air-A	19.9	4350	35.0	50.6	8888	117.7
2906	H18-Air-A	19.9	4356	35.0	53.4	8991	116.0
2907	H18-Air-A	20.2	4398	35.0	53.4	8991	117.8
2914	H8-Re2-Air	7.5	2845	45.0	18.1	4954	34.40
2915	H18-Air	16.9	4098	45.0	56.1	8342	110.2
2916	H18-Air	17.2	4128	45.0	54.2	8348	111.8
2919	H18-Air	16.9	4089	45.0	55.6	8321	111.7
2920	H13-Air	11.3	3745	18.0	13.8	6949	30.80
2921	H8-Re2-Air	8.01	2942	45.0	17.5	4900	38.50
2922	H21-Air	20.7	4557	27.0	53.5	9256	111.1
2923	H21-Air	21.1	4599	27.0	53.7	9311	111.3
2934	H8-Re2-Air	7.80	2913	45.0	17.9	5058	39.80
2935	H8-Re2-Air	7.90	2932	45.0	18.1	5096	40.20
2936	H8-Re2-Air	8.10	3001	45.0	18.6	5234	40.60
2937	H18-Air	16.2	4091	45.0	52.4	8254	112.1
2938	H18-Air	16.6	4125	45.0	54.1	8346	114.2
2939	H18-Air	16.1	4062	45.0	52.1	8207	110.1
2940	H18-Air	16.2	4066	45.0	53.7	8247	112.3
2941	H18-Air	16.5	4101	45.0	54.6	8319	113.4
2943	H8-Re2-Air	7.90	2984	45.0	16.2	5095	39.90
2944	H18-Air	16.3	4113	45.0	51.0	8259	111.1
2945	H8-Re2-Air	8.00	2955	45.0	17.7	5117	40.10
2946	H18-Air	16.1	4071	45.0	50.1	8177	107.9
2972	H18-Air	15.7	3917	45.0	50.9	8110	108.6
2973	H8-Re2-Air	7.80	2895	45.0	18.7	5063	39.60

2977	H8-Re2-Air	7.70	2858	45.0	19.0	5014	39.10
2978	H8-Re2-Air	7.90	2888	45.0	19.3	5075	41.40
2979	H8-Re2-Air	7.80	2899	45.0	18.9	5076	40.00
2994	H8-Re2-Air	8.30	3003	45.0	19.4	5270	40.10
2995	H8-Re2-Air	8.10	2961	45.0	19.2	5191	39.50
2996	H13-Air	13.4	3789	18.0	14.5	7070	31.60
2997	H8-Re2-Air	7.92	2917	45.0	19.2	5119	38.90
2998	H8-Re2-Air	8.00	2935	45.0	19.2	5148	39.60
2999	H8-Re2-Air	7.90	2903	45.0	19.2	5096	38.80
3000	H8-Re2-Air	7.95	2934	45.0	18.7	5125	39.10
3001	H8-Re2-Air	8.30	3014	45.0	18.7	5257	39.50
3002	H8-Re2-Air	7.91	2920	45.0	18.8	5107	38.50
3003	H13-Air	12.9	3702	18.0	14.0	6890	29.50
3004	H13-Air	12.9	3709	18.0	13.9	6894	30.10
3005	H13-Air	13.1	3749	18.0	13.9	6961	31.30
3006	H13-Air	13.2	3761	18.0	14.1	6995	30.40
3007	H13-Air	12.9	3715	18.0	13.9	6904	30.70
3008	H18-Air-T	16.5	4026	38.0	54.9	8326	104.2
3009	H18-Air	16.3	4091	45.0	52.9	8266	108.1
3010	H18-Air-T	17.4	4171	38.0	53.5	8514	104.9
3011	H18-Air-T	17.2	4152	38.0	52.6	8476	107.3
3012	H8-Re2-Air	8.30	3008	45.0	18.9	5256	39.70
3013	H8-Re2-Air	8.20	2997	45.0	18.9	5238	40.50
3014	H8-Re2-Air	7.80	2888	45.0	18.8	5059	39.80
3015	H8-Re2-Air	8.10	2968	45.0	18.3	5163	40.80
3029	H8-Re2-Air	7.70	2865	45.0	19.1	5030	35.70
3030	H18-Air	16.3	4090	45.0	53.3	8273	110.4
3031	H18-Air-T	16.9	4127	38.0	51.1	8399	111.3
3041	H8-Re2-Air	8.19	3019	45.0	17.3	5200	40.00
3042	H8-Re2-Air	8.23	3018	45.0	17.8	5222	40.90
3043	H8-Re2-Air	8.25	3014	45.0	18.2	5234	39.90
3044	H8-Re2-Air	8.03	2965	45.0	18.0	5145	39.60
3045	H8-Re2-N2	8.57	3055	45.0	18.4	6440	40.20
3046	H8-Re2-N2	8.69	3067	45.0	19.0	6494	41.30

3047	H8-Re2-N2	8.75	3091	45.0	18.6	6517	40.80
3048	H8-Re2-Air	8.07	2959	45.0	18.8	5171	39.50
3049	H8-Re2-N2	8.65	3056	45.0	19.1	6479	40.00
3050	H8-Re2-Air	8.00	2947	45.0	18.6	5142	39.60
3051	H8-Re6-Air	8.24	2945	130.0	61.8	5473	108.0
3052	H8-Re2-Air	7.97	2952	45.0	18.1	5128	39.60
3053	H8-Re2-N2	8.66	3065	45.0	18.8	6480	40.40
3054	H8-Re2-Air	8.21	3001	45.0	18.4	5222	40.40
3055	H8-Re2-Air	7.93	2927	45.0	18.8	5118	39.20
3056	H8-Re2-N2	8.82	3108	45.0	18.6	6547	40.60
3057	H8-Re2-Air	7.94	2929	45.0	18.8	5121	39.90

Table A.2: T5 Freestream Conditions

Shot	Test Gas	M_∞ (MJ/kg)	U_∞ (m/s)	P_∞ (kPa)	T_∞ (K)	$T_{v,\infty}$ (K)	ρ_∞ (kg/m^3)	Re$_{x,\infty}$ 10^6/m	Diagnostic
2903	Air	4.82	5153	30.3	2575	2575	0.0378	2.74	TDLAS Freestream
2904	Air	5.40	3628	8.76	1102	1110	0.0273	2.25	TDLAS Freestream
2905	Air	4.83	5299	26.9	2656	2656	0.0319	2.34	TDLAS Freestream
2906	Air	4.85	5355	27.3	2673	2673	0.0322	2.38	TDLAS Freestream
2907	Air	4.85	5354	27.5	2677	2677	0.0323	2.39	TDLAS Freestream
2914	Air	5.51	3544	7.19	1015	1022	0.0243	2.06	TDLAS Freestream
2915	Air	4.91	4977	28.8	2355	2355	0.0377	2.78	TDLAS Freestream
2916	Air	4.91	4982	27.7	2354	2354	0.0385	2.84	TDLAS Freestream
2919	Air	4.91	4964	28.7	2347	2347	0.0398	2.93	TDLAS Freestream
2920	Air	5.27	4431	5.96	1594	1603	0.0120	0.98	TDLAS Freestream
2921	Air	5.54	3531	5.34	991	1002	0.0184	1.57	TDLAS Freestream
2922	Air	4.82	5519	28.1	2825	2825	0.0308	2.28	TDLAS Freestream
2923	Air	4.81	5550	28.3	2861	2861	0.0306	2.26	TDLAS Cylinder
2934	Air	5.49	3600	7.06	1048	1057	0.0231	1.95	TDLAS Cylinder
2935	Air	5.47	3616	7.15	1063	1071	0.0230	1.93	TDLAS Cylinder
2936	Air	5.44	3684	7.50	1116	1122	0.0230	1.91	TDLAS Cylinder
2937	Air	4.92	4940	26.6	2305	2305	0.0376	2.78	TDLAS Cylinder
2938	Air	4.91	4986	27.8	2353	2353	0.0384	2.83	TDLAS Cylinder

2939	Air	4.93	4918	26.5	2282	2282	0.0378	2.80	TDLAS Cylinder
2940	Air	4.93	4933	27.2	2302	2302	0.0386	2.85	TDLAS Cylinder
2941	Air	4.91	4968	28.0	2342	2342	0.0389	2.87	TDLAS Cylinder
2943	Air	5.47	3617	6.42	1063	1071	0.0207	1.74	Static Probe V1
2944	Air	4.92	4947	25.9	2304	2304	0.0366	2.71	Static Probe V1
2945	Air	5.47	3626	7.03	1071	1080	0.0224	1.88	Static Probe V1
2946	Air	4.94	4905	25.3	2263	2263	0.0365	2.71	Static Probe V1
2972	Air	4.94	4870	25.8	2237	2237	0.0377	2.79	Static Probe V2
2973	Air	5.49	3596	7.38	1049	1058	0.0242	2.04	Static Probe V2
2977	Air	5.51	3571	7.45	1029	1038	0.0249	2.11	Static Probe V2 w/ TDLAS
2978	Air	5.48	3601	7.63	1053	1061	0.0249	2.09	Static Probe V2 w/ TDLAS
2979	Air	5.48	3603	7.50	1055	1062	0.0244	2.05	Static Probe V2 w/ TDLAS
2994	Air	5.43	3697	7.87	1129	1138	0.0238	1.97	Schlieren 48° Wedge w/ Static Probe V2 and Pitot
2995	Air	5.45	3659	7.71	1100	1108	0.0240	2.00	Schlieren 48° Wedge w/ Static Probe V2 and Pitot
2996	Air	5.25	4485	6.30	1637	1644	0.0123	1.00	Schlieren 38° Wedge w/ Static Probe V2 and Pitot
2997	Air	5.47	3624	7.64	1071	1079	0.0245	2.05	TDLAS 48° Wedge w/ Static Probe V2 and Pitot
2998	Air	5.46	3638	7.67	1083	1090	0.0243	2.03	TDLAS 48° Wedge w/ Static Probe V2 and Pitot
2999	Air	5.48	3612	7.61	1062	1071	0.0246	2.06	TDLAS 48° Wedge w/ Static Probe V2 and Pitot
3000	Air	5.47	3628	7.45	1074	1082	0.0238	1.99	TDLAS 48° Wedge w/ Static Probe V2 and Pitot
3001	Air	5.43	3693	7.57	1126	1135	0.0230	1.91	TDLAS 48° Wedge w/ Static Probe V2 and Pitot

3002	Air	5.48	3619	7.47	1067	1076	0.0240	2.01	TDLAS 48° Wedge w/ Static Probe V2 and Pitot
3003	Air	5.26	4403	6.06	1583	1591	0.0123	1.00	TDLAS 38° Wedge w/ Static Probe V2 and Pitot
3004	Air	5.26	4405	6.01	1583	1591	0.0122	0.99	TDLAS 38° Wedge w/ Static Probe V2 and Pitot
3005	Air	5.26	4436	6.02	1601	1610	0.0121	0.98	TDLAS 38° Wedge w/ Static Probe V2 and Pitot
3006	Air	5.26	4451	6.12	1613	1611	0.0122	0.99	TDLAS 38° Wedge w/ Static Probe V2 and Pitot
3007	Air	5.26	4410	6.02	1586	1595	0.0122	0.99	TDLAS 38° Wedge w/ Static Probe V2 and Pitot
3008	Air	4.91	4971	28.1	2345	2345	0.0390	2.88	TDLAS 38° Wedge w/ Static Probe V2 and Pitot
3009	Air	4.92	4945	27.0	2313	2313	0.0380	2.81	TDLAS 38° Wedge w/ Static Probe V2 and Pitot
3010	Air	4.89	5075	27.6	2434	2434	0.0366	2.70	TDLAS 38° Wedge w/ Static Probe V2 and Pitot
3011	Air	4.90	5052	27.1	2409	2409	0.0363	2.68	Schlieren 38° Wedge w/ Static Probe V2 and Pitot
3012	Air	5.43	3692	7.65	1125	1132	0.0233	1.93	Schlieren 38° Opposing-Wedge
3013	Air	5.44	3683	7.64	1118	1126	0.0234	1.94	Shadowgraph 38° Opposing-Wedge
3014	Air	5.49	3594	7.46	1048	1055	0.0245	2.06	Shadowgraph 38° Opposing-Wedge
3015	Air	5.46	3648	7.32	1090	1097	0.0230	1.92	Shadowgraph 38° Opposing-Wedge
3029	Air	5.50	3579	7.52	1036	1043	0.0249	2.10	Static Probe V3
3030	Air	4.92	4948	27.1	2315	2315	0.0381	2.82	Static Probe V3
3031	Air	4.91	5020	26.1	2370	2370	0.0356	2.64	Static Probe V3
3041	Air	5.44	3669	6.96	1105	1114	0.0215	1.79	FLDI on Double-Cone w/ Static Probe V3
3042	Air	5.44	3678	7.18	1114	1122	0.0221	1.83	FLDI on Double-Cone w/ Static Probe V3
3043	Air	5.44	3683	7.35	1118	1126	0.0225	1.87	DFLDI on Double-Cone w/ Static Probe V3

3044	Air	5.46	3639	7.20	1084	1091	0.0228	1.90	DFLDI on Double-Cone w/ Static Probe V3
3045	N2	6.63	3835	4.55	802	3075	0.0191	2.01	DFLDI on Double-Cone w/ Static Probe V3
3046	N2	6.62	3859	4.71	815	3080	0.0194	2.05	DFLDI on Double-Cone w/ Static Probe V3
3047	N2	6.61	3870	4.62	820	3096	0.0189	1.99	DFLDI on Double-Cone w/ Static Probe V3
3048	Air	5.45	3650	7.54	1093	1110	0.0236	1.97	DFLDI on Double-Cone w/ Static Probe V3
3049	N2	6.62	3852	4.73	811	3074	0.0196	1.91	DFLDI on Double-Cone w/ Static Probe V3
3050	Air	5.46	3636	7.44	1082	1089	0.0236	1.97	DFLDI on Double-Cone w/ Static Probe V3
3051	Air	5.46	3729	25.2	1150	1150	0.0758	6.27	DFLDI on Double-Cone w/ Static Probe V3
3052	Air	5.47	3631	7.23	1077	1085	0.0230	1.92	DFLDI on Double-Cone w/ Static Probe V3
3053	N2	6.62	3853	4.66	812	3080	0.0193	2.03	DFLDI on Double-Cone w/ Static Probe V3
3054	Air	5.44	3677	7.42	1113	1121	0.0228	1.90	DFLDI on Double-Cone w/ Static Probe V3
3055	Air	5.47	3624	7.50	1072	1080	0.0240	2.01	DFLDI on Double-Cone w/ Static Probe V3
3056	N2	6.61	3884	4.62	827	3107	0.0188	1.97	DFLDI on Double-Cone w/ Static Probe V3
3057	Air	5.46	3625	7.50	1073	1081	0.0239	2.00	DFLDI on Double-Cone w/ Static Probe V3

Appendix B

HEAT FLUX AND STATIC PRESSURE MEASUREMENTS

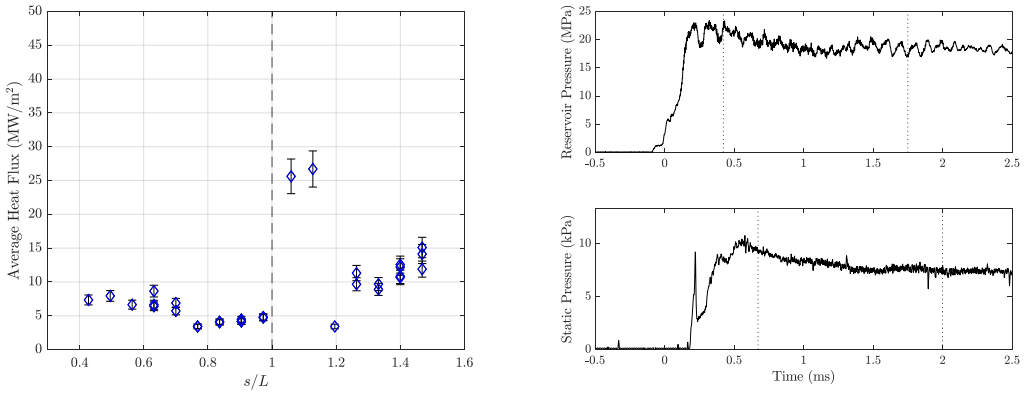

Figure B.1: Double-cone average heat flux during test time **(left)**, marked by the vertical dotted lines in the plots of reservoir and static pressure **(right)** from Shot 3043, H8-Re2-Air. The vertical dashed line marks the corner of the double-cone. The streamwise normalized positions are the same as given in Knisely, 2016.

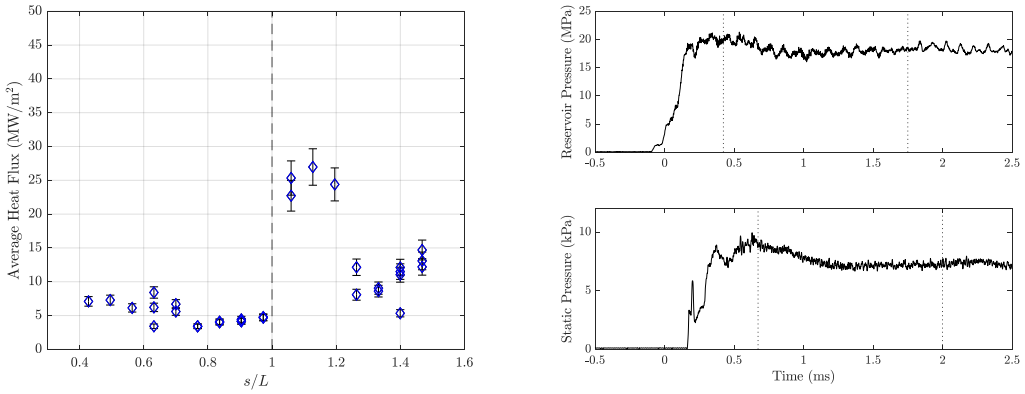

Figure B.2: Shot 3044, H8-Re2-Air.

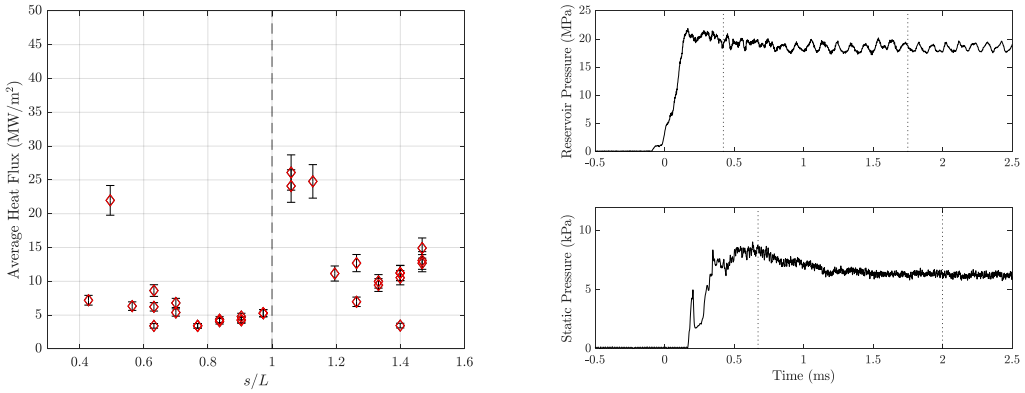

Figure B.3: Shot 3045, H8-Re2-N2.

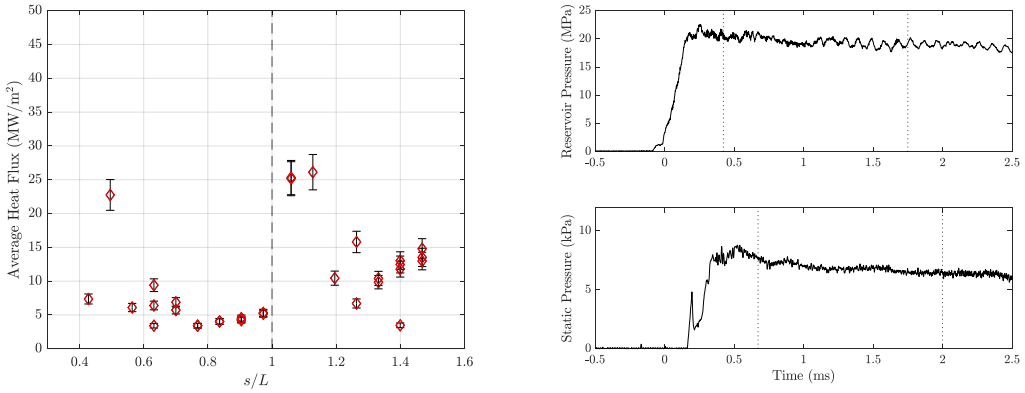

Figure B.4: Shot 3046, H8-Re2-N2.

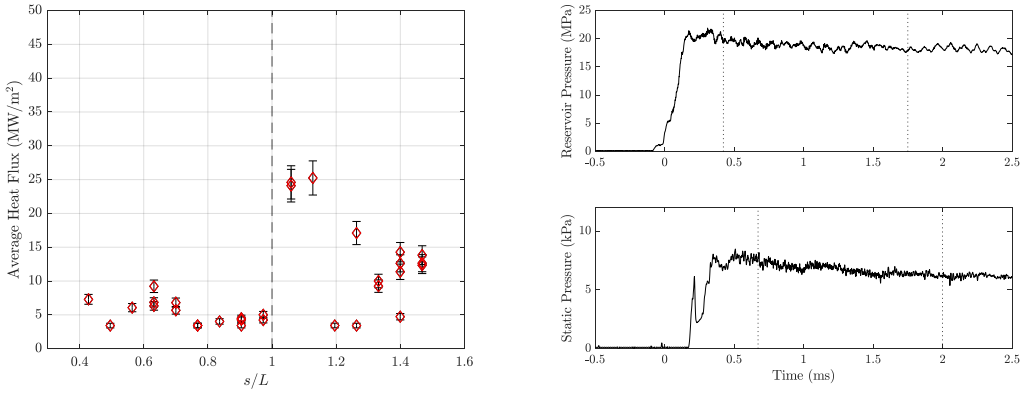

Figure B.5: Shot 3047, H8-Re2-N2.

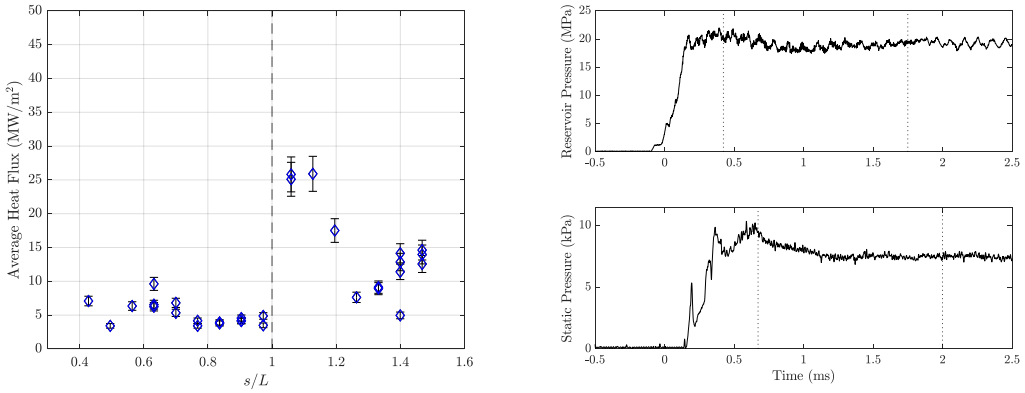

Figure B.6: Shot 3048, H8-Re2-Air.

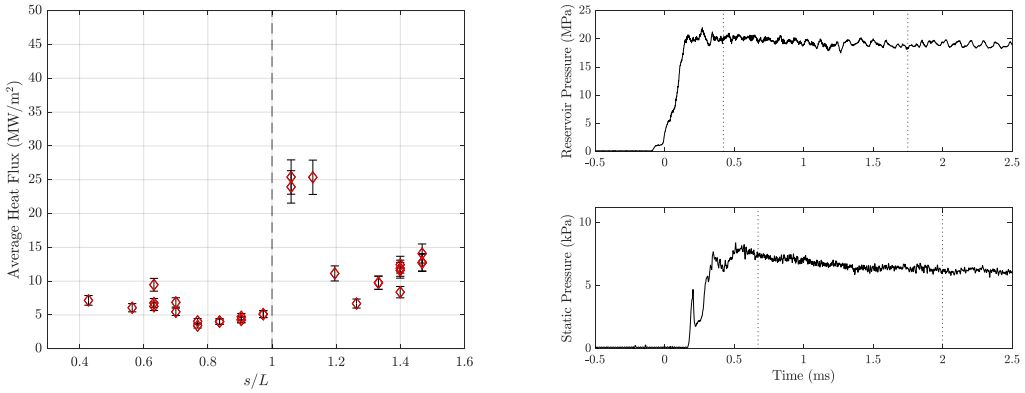

Figure B.7: Shot 3049, H8-Re2-N2.

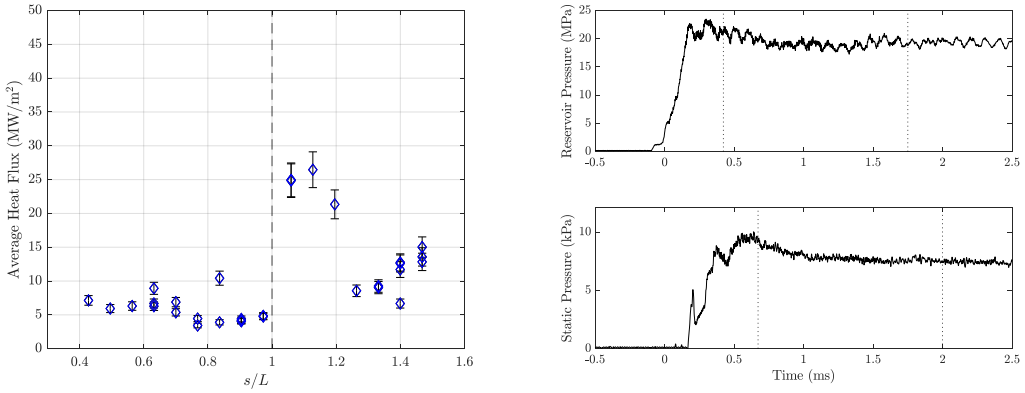

Figure B.8: Shot 3050, H8-Re2-Air.

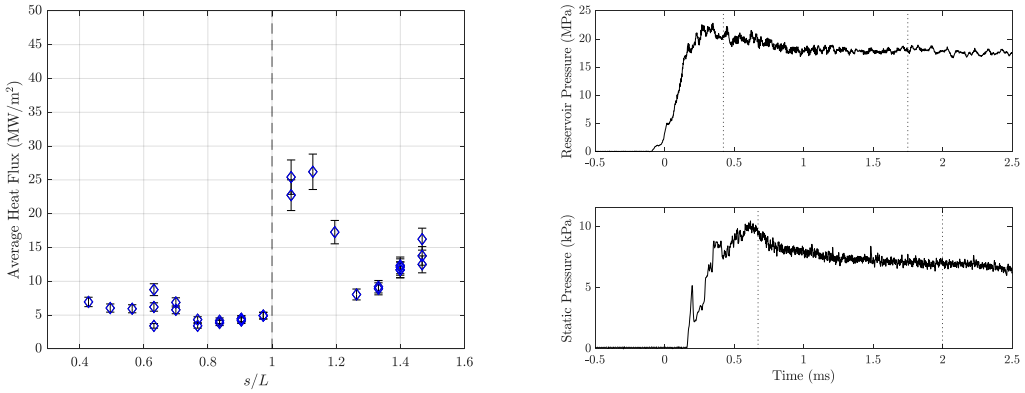

Figure B.9: Shot 3052, H8-Re2-Air.

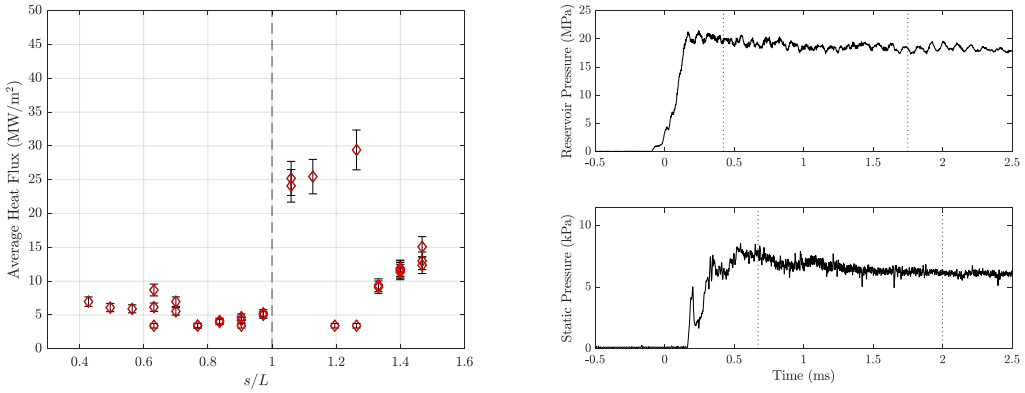

Figure B.10: Shot 3053, H8-Re2-N2.

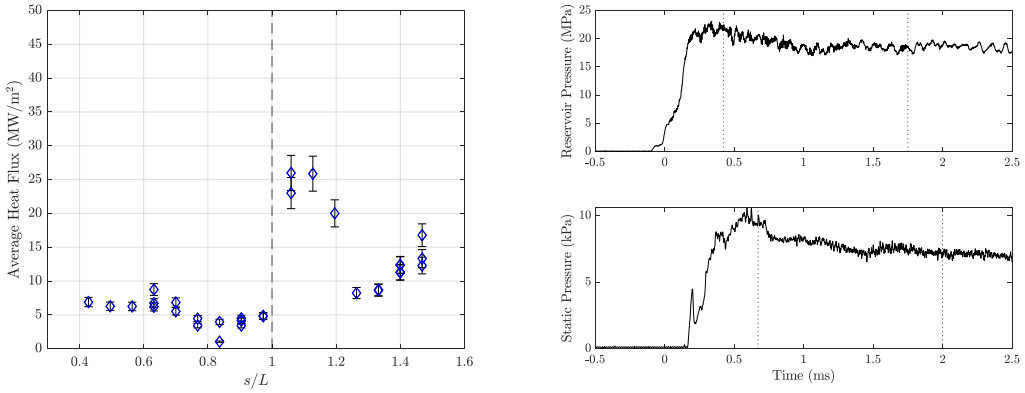

Figure B.11: Shot 3054, H8-Re2-Air.

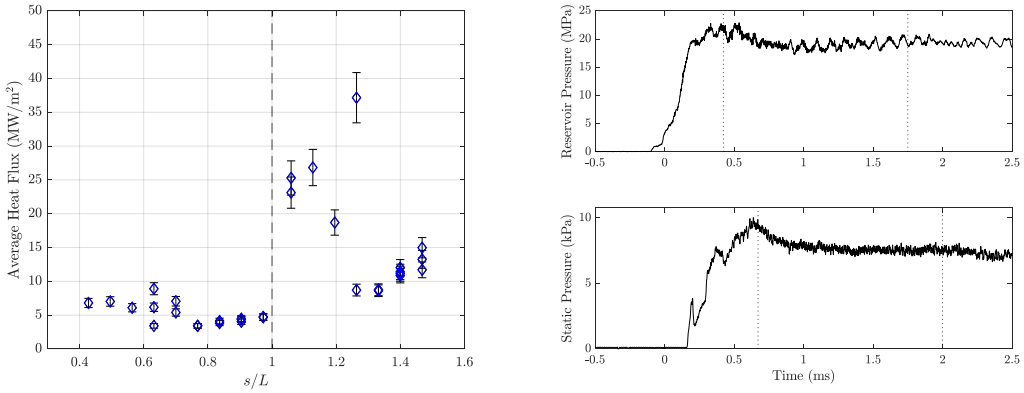

Figure B.12: Shot 3055, H8-Re2-Air.

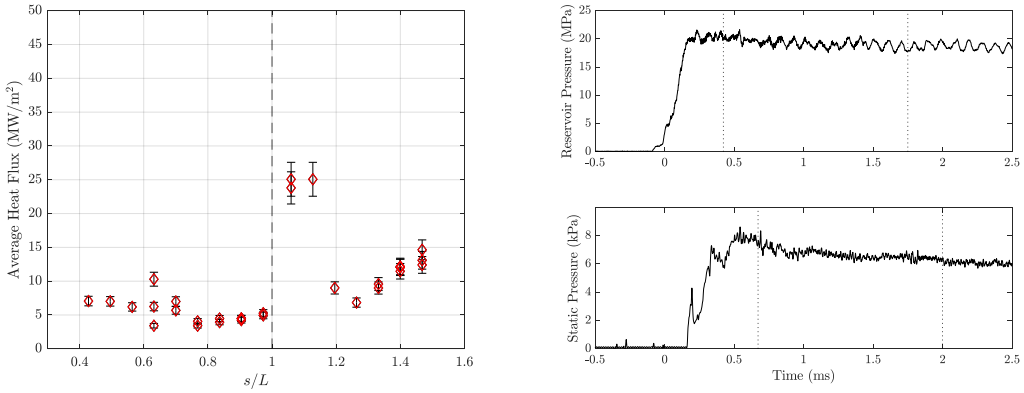

Figure B.13: Shot 3056, H8-Re2-N2.

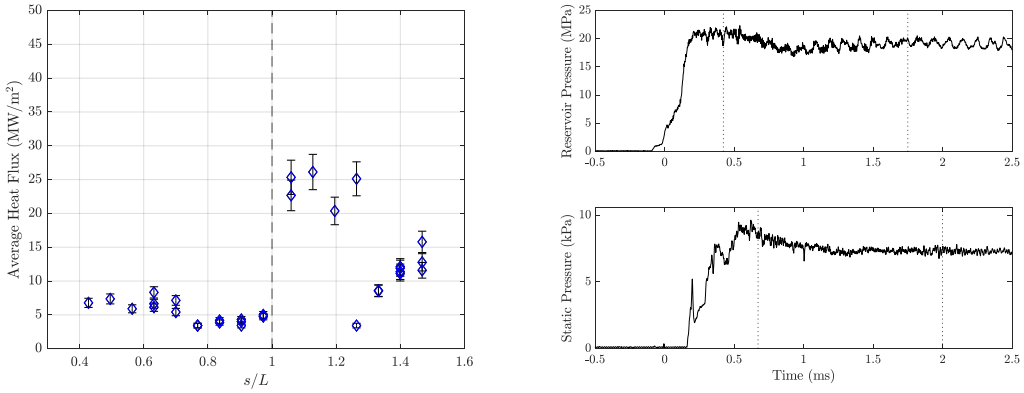

Figure B.14: Shot 3057, H8-Re2-Air.

Appendix C

TIME-RESOLVED NOZZLE SIMULATIONS

While the UMNAEM Nozzle Code calculates a steady-state freestream condition as described in Chapter 2, there are temporal changes in the T5 freestream are evident in the static pressure traces and TDLAS-inferred pressures. A recent effort was made by Hornung (2023) to model a time-varying freestream by using the measured reservoir pressure as a time-varying input. The nozzle flow is simulated in Eilmer4 using `nenzf1d` and the Bose-Candler five-species air model (Bose and Candler, 1996, 1997). The H8-Re2-Air and H18-Air test conditions were simulated and the respective simulated time-resolved static pressure traces are plotted against the static probe and TDLAS traces in Figs. C.1 and C.2. generally, there is good agreement in magnitude and temporal behavior in both conditions. To decrease the runtime and increase temporal resolution, additional work is needed to automate this process and package the simulation so it can be used more efficiently alongside future experiments in T5.

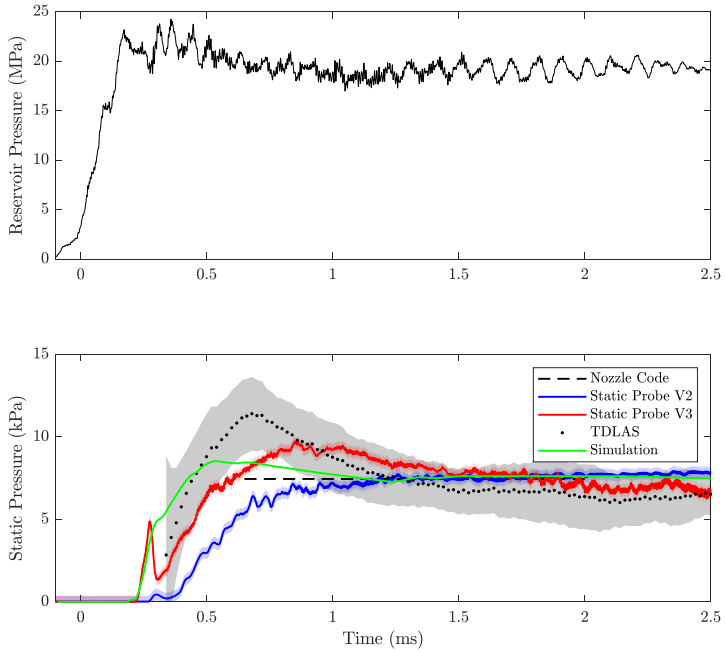

Figure C.1: 8 MJ/kg condition comparisons with Eilmer4 simulation.

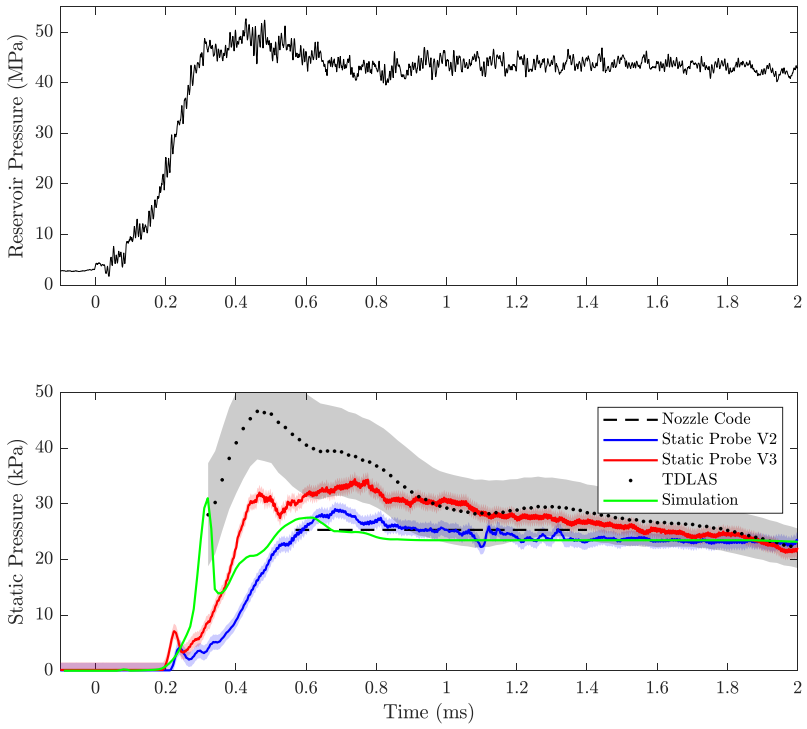

Figure C.2: 16 MJ/kg condition comparisons with Eilmer4 simulation.

Appendix D

FLDI FREQUENCY-RESPONSE CHARACTERIZATION

Since a new laser system and optical components were used in this setup compared to the FLDI/DFLDI system described in Lawson (2021), extensive benchtop testing was needed to characterize the expected frequency-response to acoustic disturbances. The two main issues to address were the spatial filtering of the FLDI and the frequency response dependence on resting DC voltage. The following two sections cover these topics, respectively, and discuss the implications on the data collected during the T5 experimental campaign.

D.1 Spatial Filtering

In order to characterize the FLDI response to acoustic disturbances, it is useful to generate a direction, constant-frequency, sinusoidal plane wave so that sharp peaks on a PSD can be observed. Lawson (2021) used a commercial electrostatic ultrasonic transducer (Senscomp Series 600) driven by a Stanford Research Systems Model DS335 waveform generator amplified by an A.A. Lab Systems A-301/HS amplifier, and directed the acoustic beam along the x-axis of the FLDI beams to induce a response. The transducer was then translated along the z-axis to characterize the spatial filtering of the FLDI at different frequencies (30–100 kHz). A similar setup using the same acoustic generating equipment is utilized in the current work.

Since the resonant frequency of the transducer is 50 kHz, the transmission response from 50–100 kHz is relatively flat, while there is significant signal drop-off below 50 kHz. The low SNR at these lower frequencies causes measured photodetectors to be quite noisy, so for this reason, the current tests are limited to 50–100 kHz (at 10 kHz increments). The acoustic pattern from the transducer is multi-lobed, and changes with frequency, generating acoustic waves in off-center axis directions. Thus, a thin aluminum mask with a 3 mm aperture is placed on the transducer to minimize these effects during the test. The transducer is centered at $y = 0$ mm, and translated along the z-axis between the two focusing lenses from -400 to 400 mm by 10 mm increments, keeping $x \approx 60$ mm from the optical axis. At each measurement location, the photodetector signal is recorded on the Yokogawa DL850E oscilloscope at 5 MHz for 100 µs.

The PSD for the measured FLDI responses for all locations and frequencies is calculated using the method outlined in Section 5.2 with a Hann window (50% overlap, $\Delta f = 1$ kHz). The peak magnitude at the respective frequency is then taken and plotted versus the z-position of the measurement, normalized to the maximum response for each frequency since the acoustic beam power for each frequency is unknown. The compilation of these normalized data is shown in Fig. D.1. As observed by Lawson (2021), the FLDI response for the higher-frequency disturbances are more spatially filtered, with the 100 kHz signal decaying to the noise floor in approximately 40% of the distance from the focus as with the 50 kHz case.

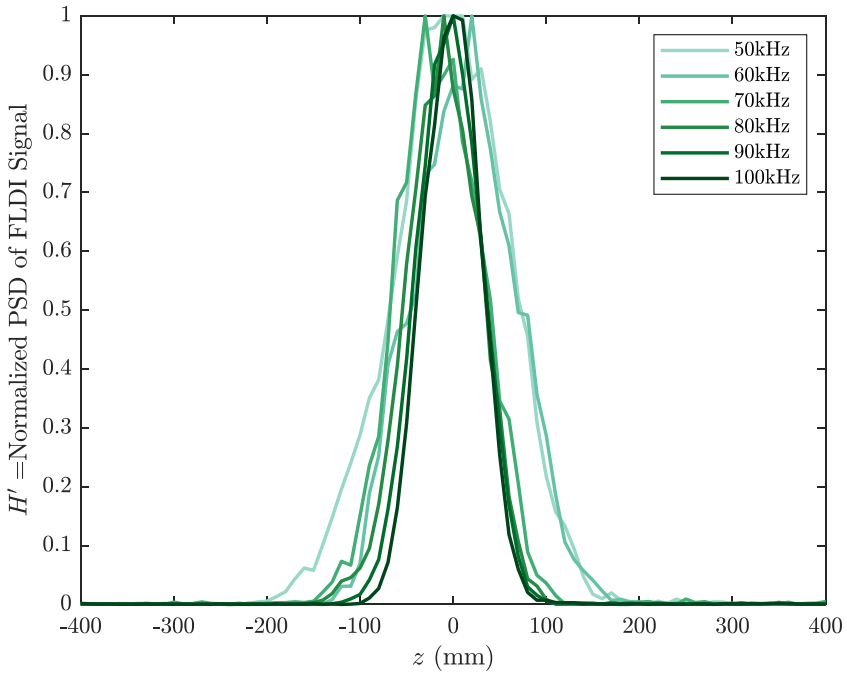

Figure D.1: Normalized PSD of FLDI response to ultrasonic acoustic excitation.

To complete the comparison with Lawson (2021), the data is collapsed using the analytical transfer function developed by Schmidt and Shepherd (2015b) for sinusoidal plane-waves. From Chapter 1, the transfer function is repeated here:

$$H(k) = \frac{2}{k\Delta x} \sin\left(\frac{k\Delta x}{2}\right) \times \exp\left(-\frac{w^2 k^2}{8}\right) \tag{D.1}$$

The PSD of a $\Delta\Phi(t,z)$ time-series is defined as $|\Delta\Phi(k,z)|^2$. Thus the PSD of the FLDI focal plane signal at the driving frequency f_0 is $|\Delta\Phi(k_0,z)|^2$, and when normalized as plotted in Fig. D.1 and compared to the transfer functions from Schmidt and Shepherd (2015b):

$$H'(k_0,z) = \frac{|\Delta\Phi(k_0,z)|^2}{|\Delta\Phi(k_0,0)|^2} \approx \frac{H^2(k_0,z)}{H^2(k_0,0)} \tag{D.2}$$

Eqn. D.1 can then be substituted to get:

$$H'\left(k_0,z\right) = \exp\left(-\frac{\left[w^2(z) - w_0^2\right]k_0^2}{4}\right) \tag{D.3}$$

The measured acoustic data can then be collapsed using this transform by potting $\log(H')$ vs. $-z_0^2 f_0^2$ (Lawson, 2021), shown in Fig. D.2. Despite the larger scatter than observed by Lawson (2021), likely due to differences in the acoustic generator setup, the transfer function describes the system well and shows the spatial sensitivity of FLDI on disturbance frequency.

D.2 DC Voltage Offset

An important factor to consider for DLFDI is the impact of resting voltage of the system on the measured photodetector signal. If quantitative comparisons are to be made between two simultaneous FLDI beams, care must be taken to ensure the signals from the respective photodetectors are as closely matched as possible. Early iterations of the current DFLDI system had channels with different resting DC voltages (essentially phase shifted along a fringe). So a quick test was performed to analyze the effect of the resting voltage on signal strength. The same acoustic generating system was used as before, at 100 kHz, and the FLDI signals were recorded with three different resting DC voltages (0–5.2 V DC dynamic range) during calibration. The PSD's of these cases are plotted in Fig. D.3, and the non-ideal behaviors in the signal are immediately noticed. In the 0.1 V case, the absolute signal strength is the lowest, albeit with a much lower noise floor due to the low overall intensity. In the 5.0 V offset case, the noise floor is comparable to the 2.5 V case but has an order of magnitude lower peak at the driving frequency. The 2.5 V case gives the best overall performance, as expected, since it is resting in the center of a fringe, yielding the largest and most symmetrical dynamic range before phase wrapping.

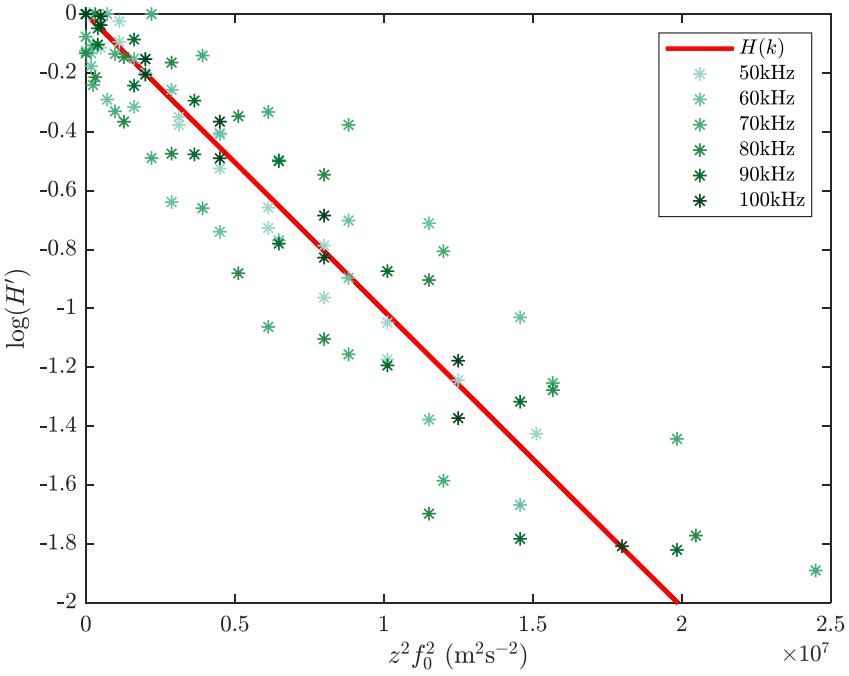

Figure D.2: Data points from Fig. D.1 plotted vs. variables from the analytical transfer function model.

The results from the acoustic test, while at the extrema of the dynamic rage, suggest that the photodetector signal is affected by the resting voltage of the system, and is reflected in the eventual PSD peak strength. This can have adverse effects on the signal correlation during experiments if two simultaneous FLDI beams are compared quantitatively without ensuring their resting voltages are matched. This is demonstrated by Shots 3041 and 3042, where the resting voltage was roughly 3.5 V for Shot 3041, and the typical 2.5 V for Shot 3042. The respective PSD's are plotted in Fig. D.4, and a significant difference in the peak structure is observable, despite the two shots being repeats of each other. Shot 3041 has a higher noise floor but comparable peak height, suggesting the same trend noticed in the acoustic tests. This comparison demonstrates the importance of keeping all FLDI channels at the same resting DC voltage near the center of the dynamic range, or drastically different results can be obtained from simultaneous measurements. In the subsequent shots in the experimental campaign discussed in Chapter 5, the DFLDI system was calibrated during each shot to have matching resting DC voltages so that the two FLDI signals could be compared.

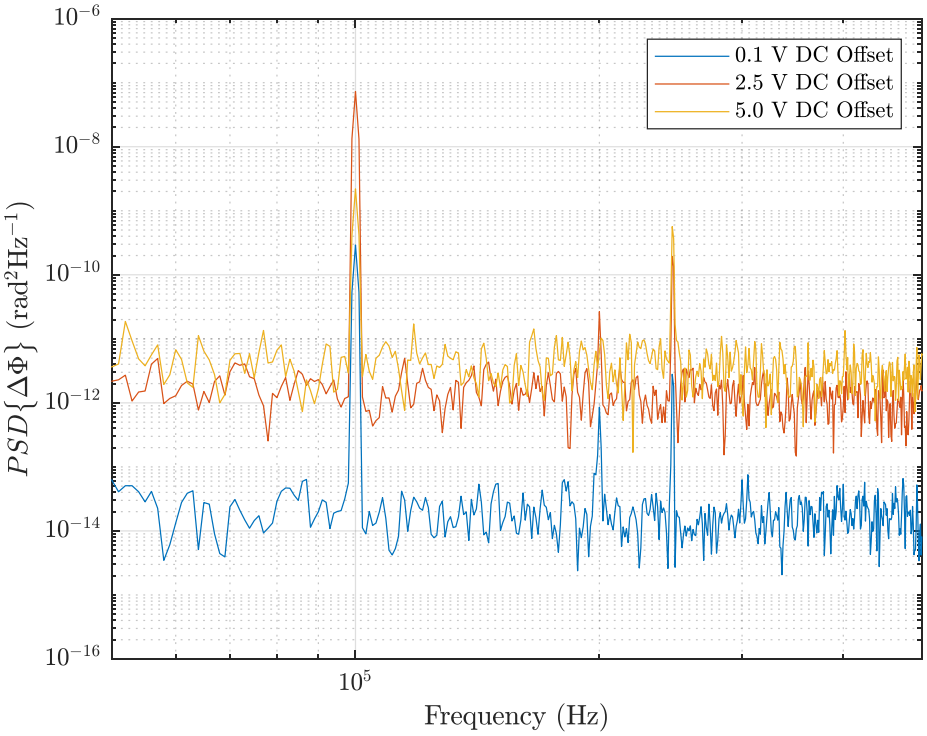

Figure D.3: PSD's of FLDI response to a 100 kHz sinusoidal acoustic disturbance, with three different DC offset voltages.

D.3 Laser Noise Floor

While FLDI is useful in quantifying small magnitude density disturbances, it is important to characterize the laser noise floor when analyzing signals from freestream tunnel noise. A useful metric to compare the noise content between signals is an RMS value, which can be calculated for a certain frequency bandwidth by:

$$RMS\{\Delta\Phi\} = \sqrt{\int_{f_1}^{f_2} PSD\{\Delta\Phi\}\mathrm{d}f} \tag{D.4}$$

In the current work, $[f_1, f_2] = [10\text{kHz}, 10\text{MHz}]$ is used as the integration window as the frequencies of interest fall well within this range. The calculated $RMS\{\Delta\Phi\}$ for all of the experiments are plotted in Fig. D.5 for the wind-off laser noise, freestream, and shear layer measurements. The freestream tunnel noise is roughly two to three times higher than the laser noise floor outside of the uncertainty bounds, while the shear layer noise content is roughly an order of magnitude higher than the laser

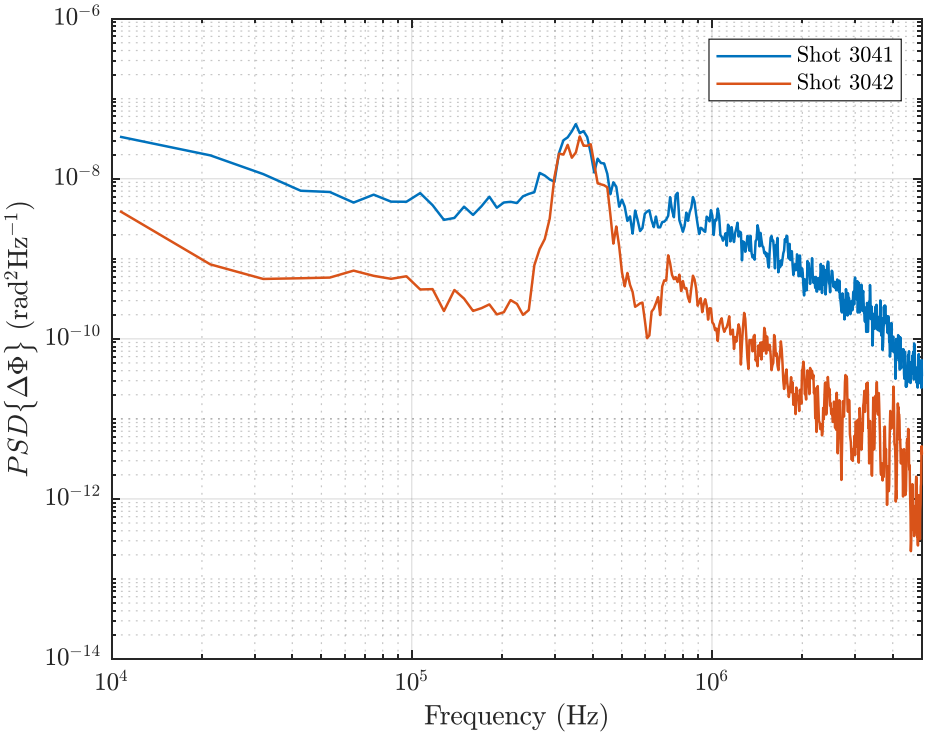

Figure D.4: PSD's of FLDI signal from Shots 3041 and 3042.

noise floor. It is important to note that one shot (3055) had a RMS value at the laser noise floor within uncertainty, so quantification of tunnel noise should not include that experiment.

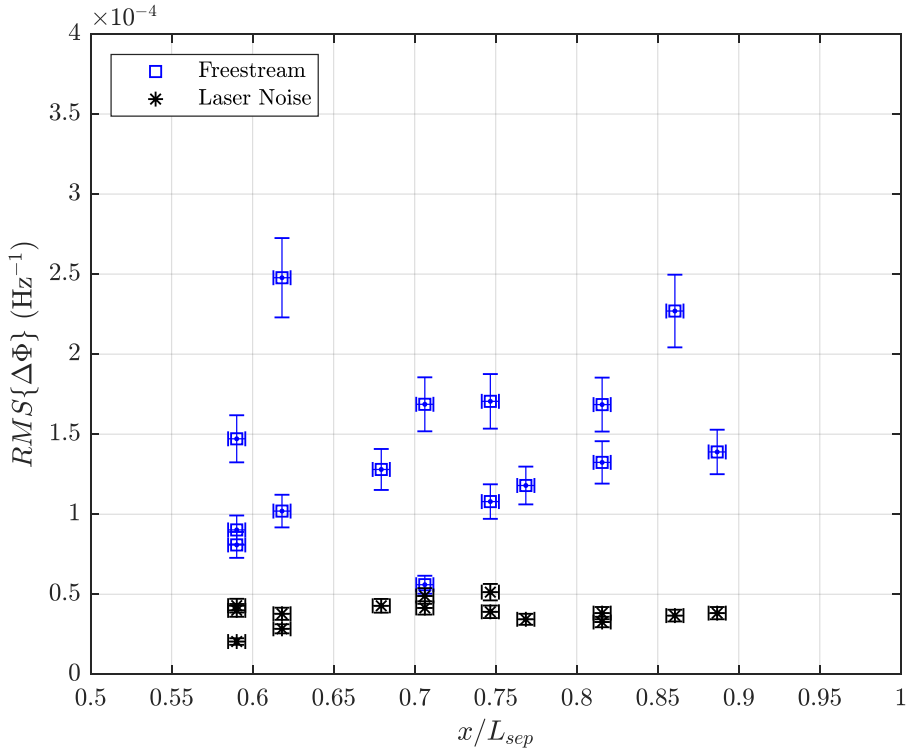

Figure D.5: RMS values of noise content in FLDI measurements.

Appendix E

ENGINEERING DRAWINGS

Detailed engineering drawings for the static probes (V1–V3) as well as the opposing-wedge model are included in this Appendix. Drawings for the 25°–55° double-cone model are provided in Knisely (2016).

Drawings for Static Probe V1:

1. Molybdenum tip
2. Main body
3. Sting
4. Full assembly

Drawings for Static Probe V2:

1. Molybdenum tip
2. Main body (hypodermic tubing)
3. Sting adapter
4. Kulite adapter
5. Body-Sting adapter
6. Extension tube
7. Mounting clamp
8. Full assembly

Most of the parts between Static Probes V2 and V3 are shared, changed parts are:

1. Molybdenum tip
2. Main body (hypodermic tubing)

3. Sting adapter

Drawings for Opposing-Wedge model:

1. 38° symmetric wedge
2. Support plate
3. Rear support
4. Sting adapter

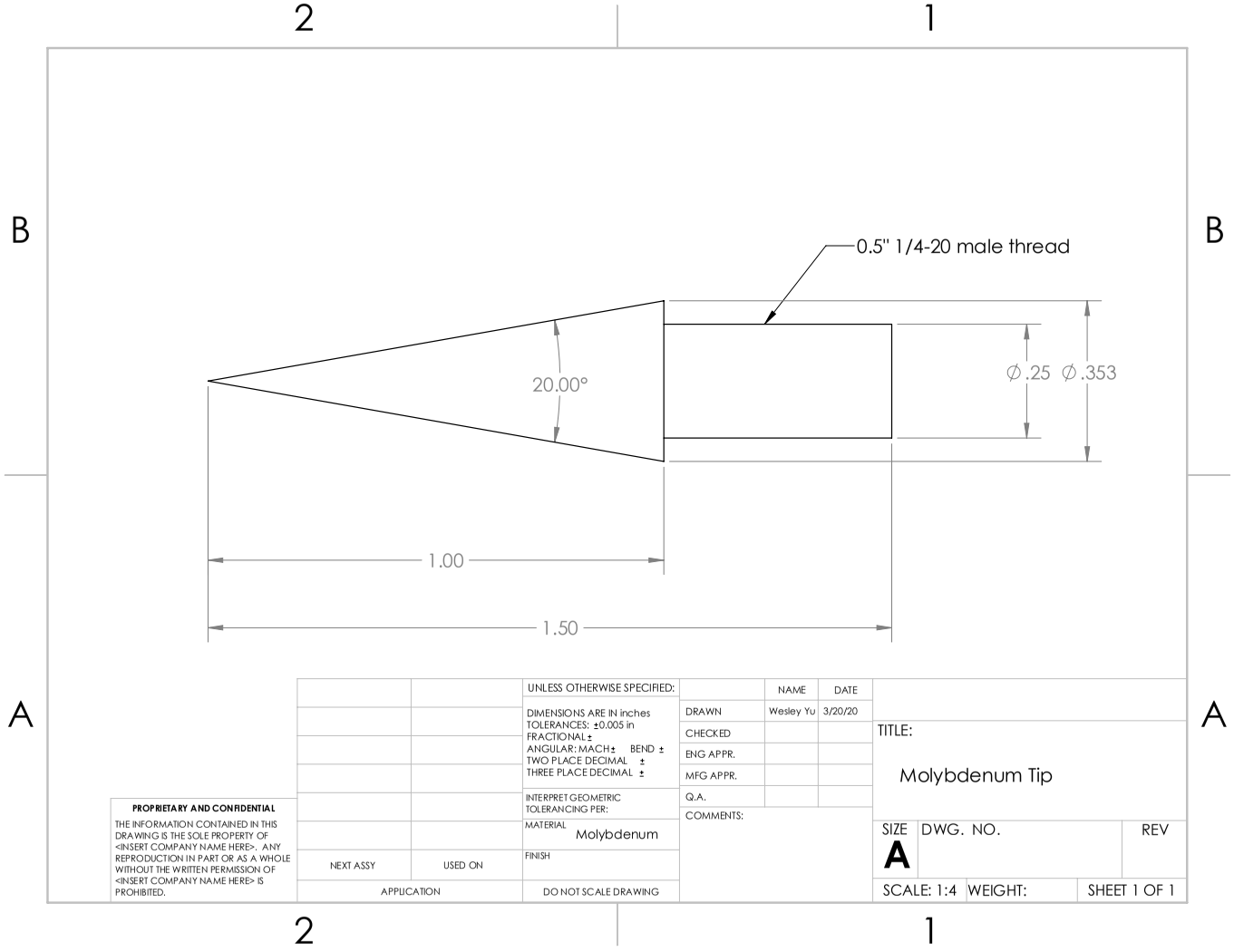

Figure E.1: Static Probe V1 Molybdenum Tip

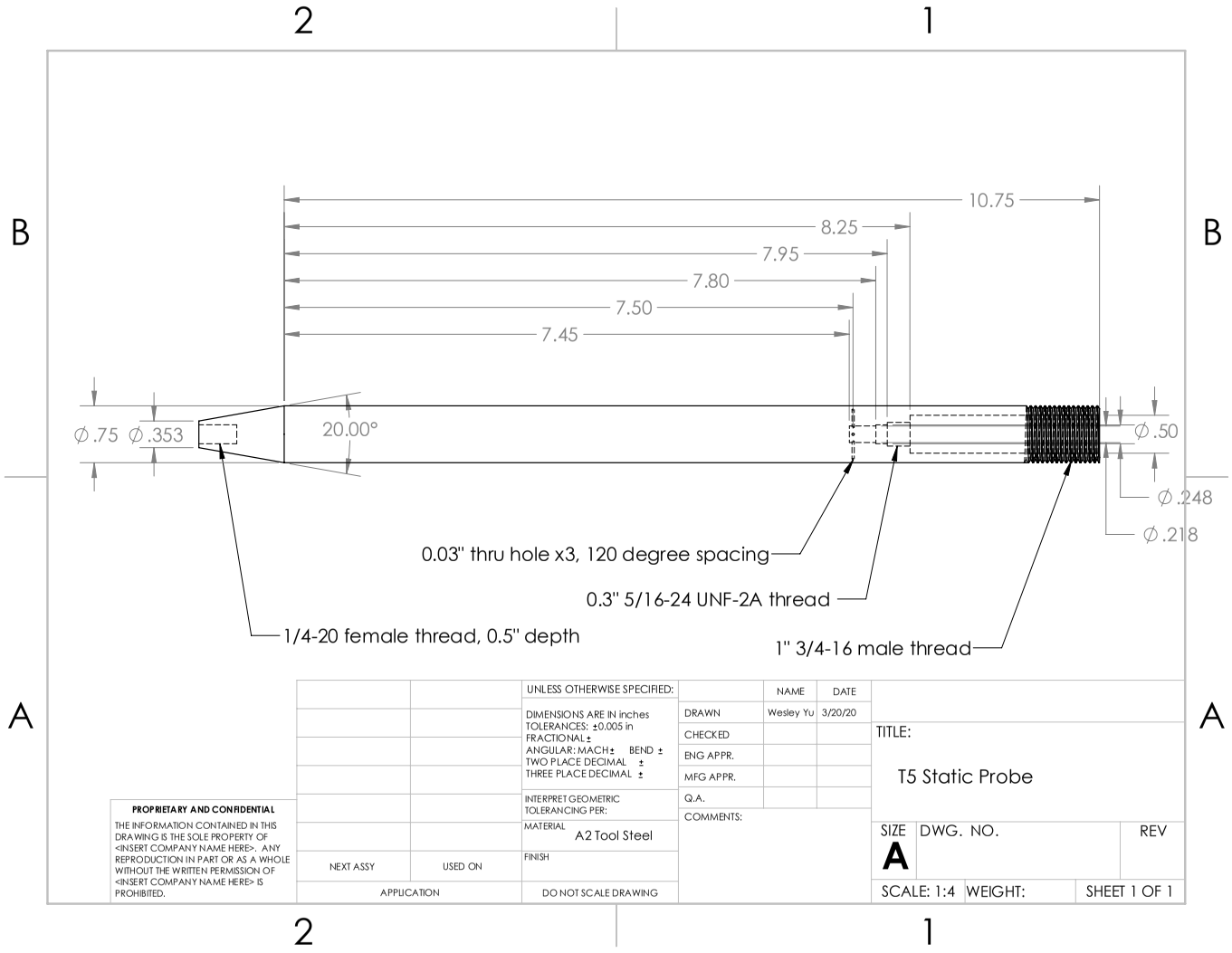

Figure E.2: Static Probe V1 Main Body

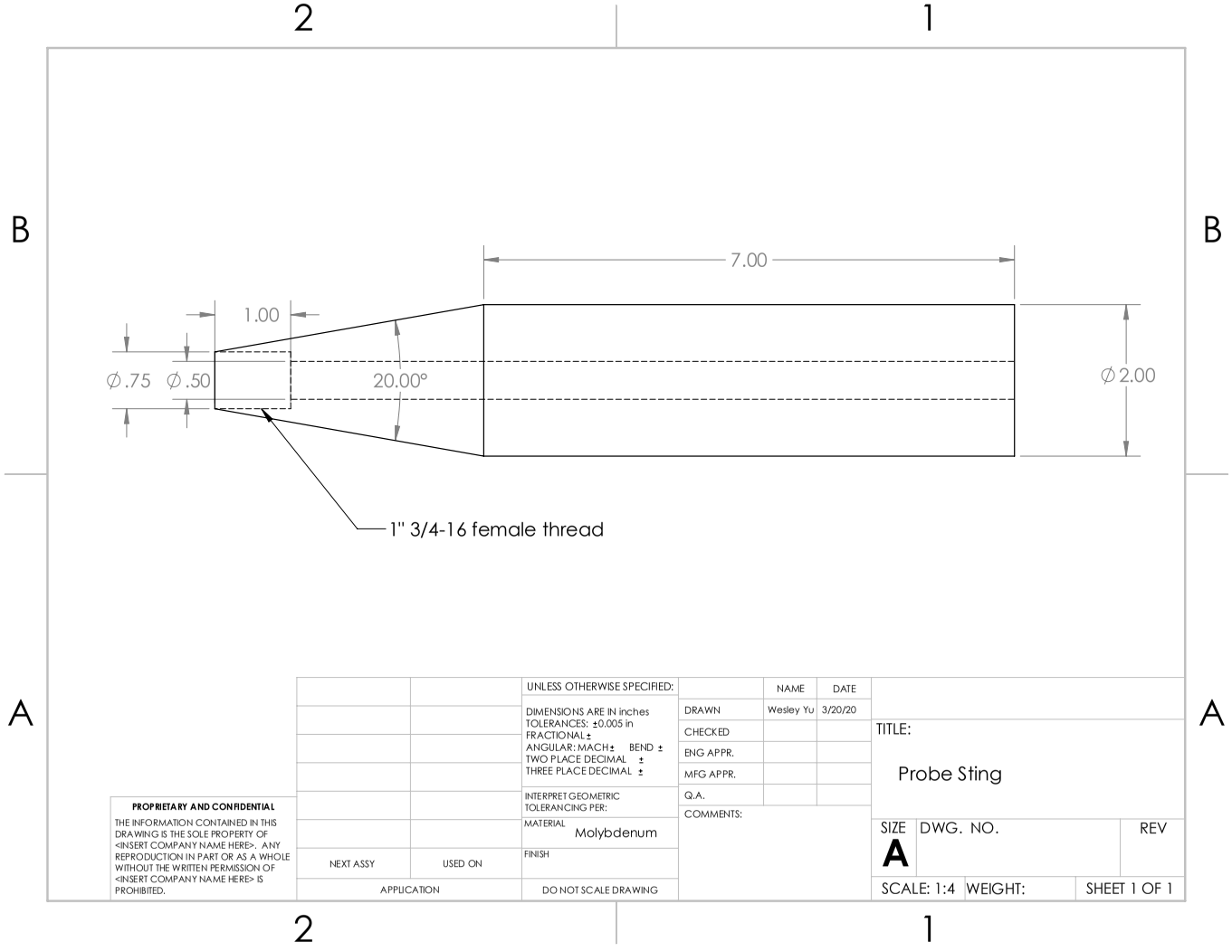

Figure E.3: Static Probe V1 Sting

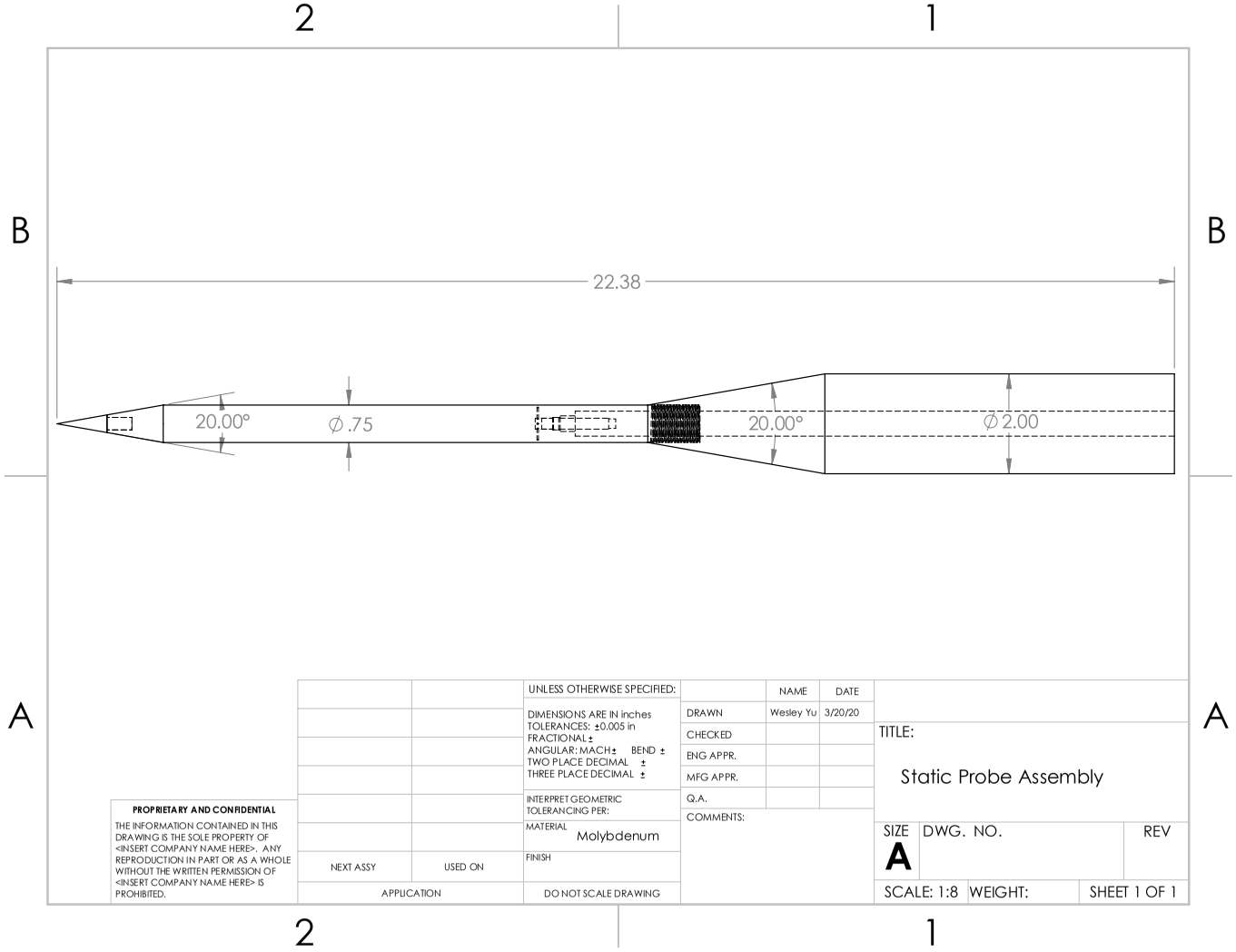

Figure E.4: Static Probe V1 Assembly

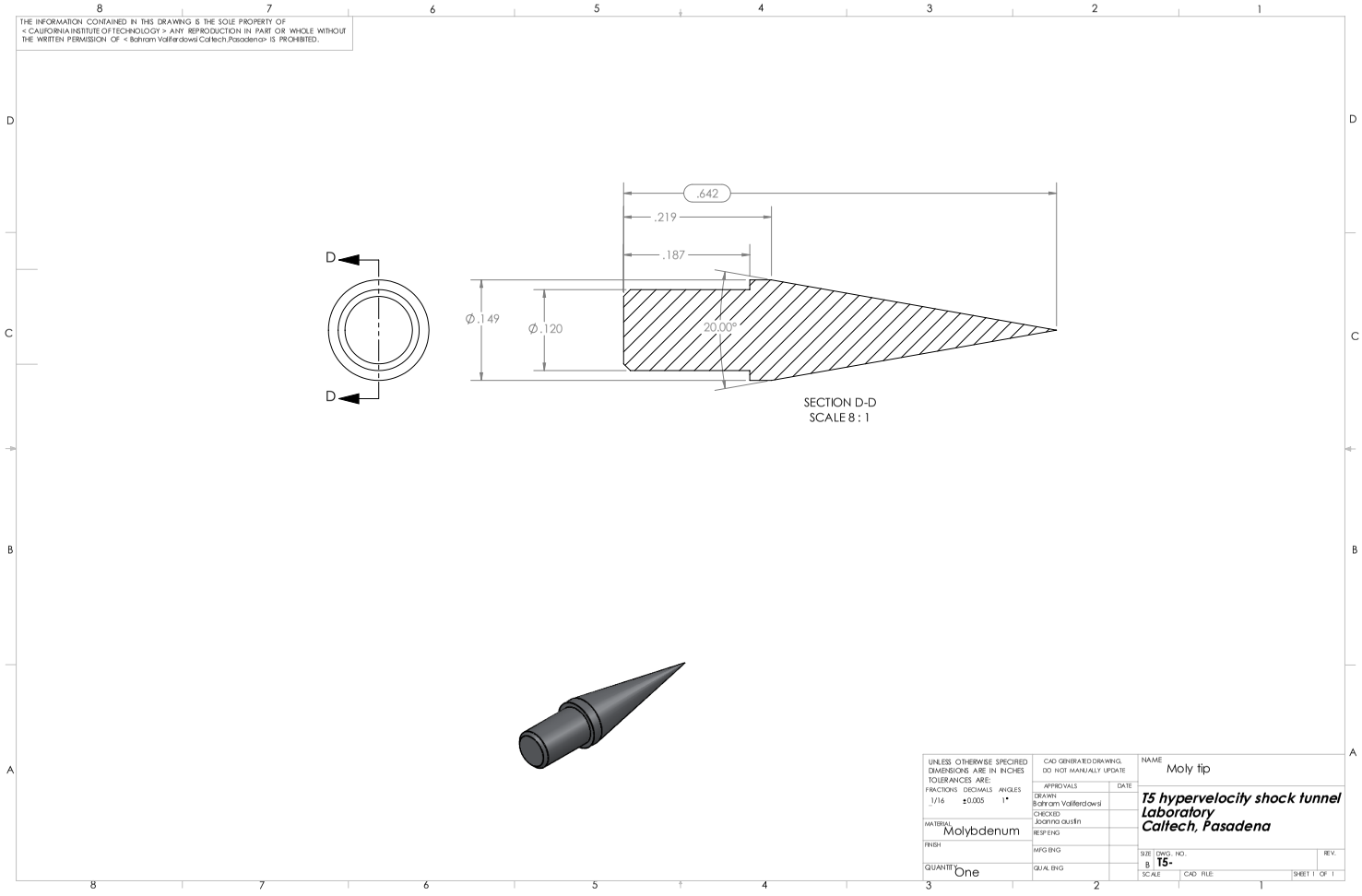

Figure E.5: Static Probe V2 Molybdenum Tip

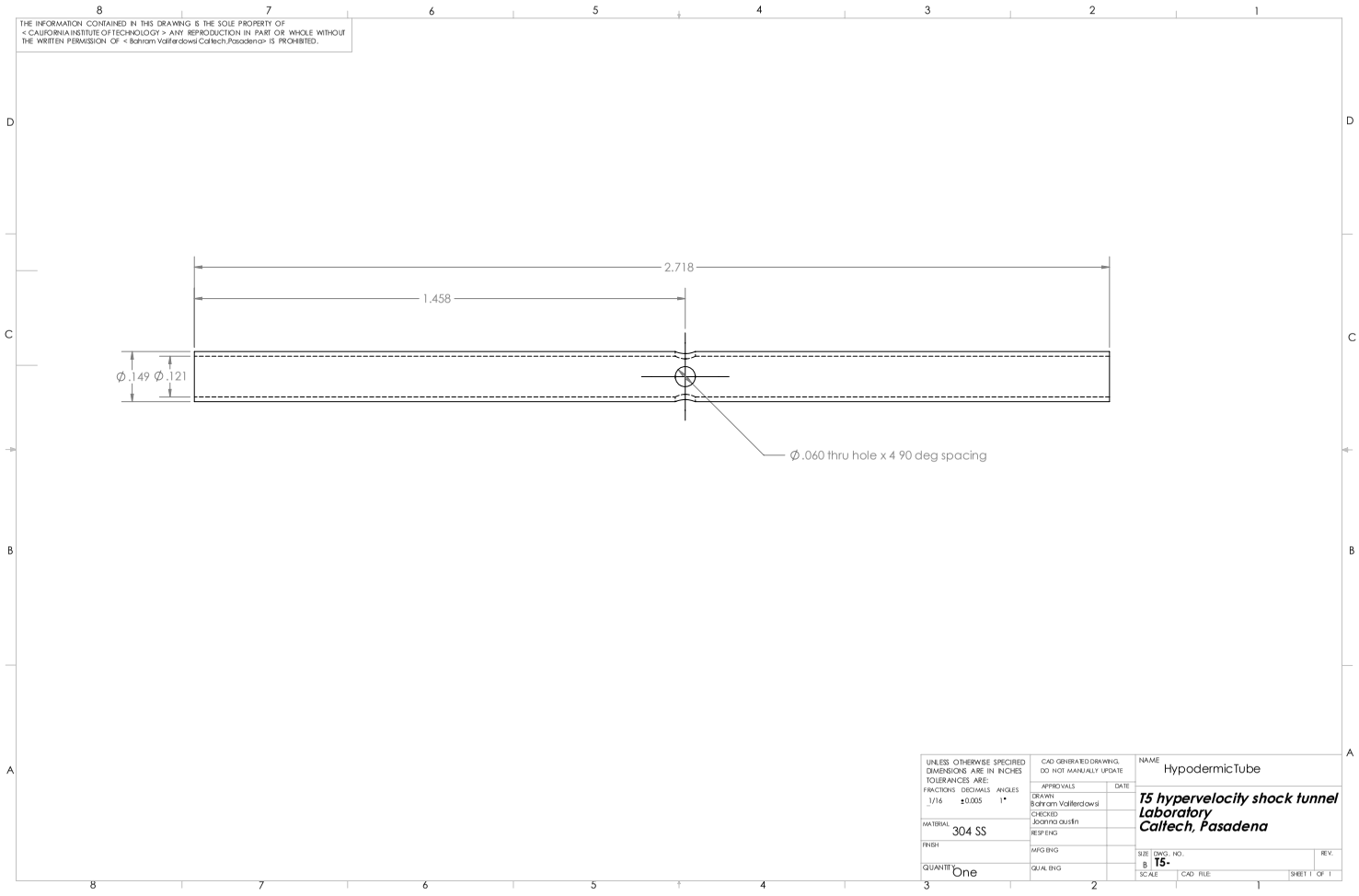

Figure E.6: Static Probe V2 Main Body

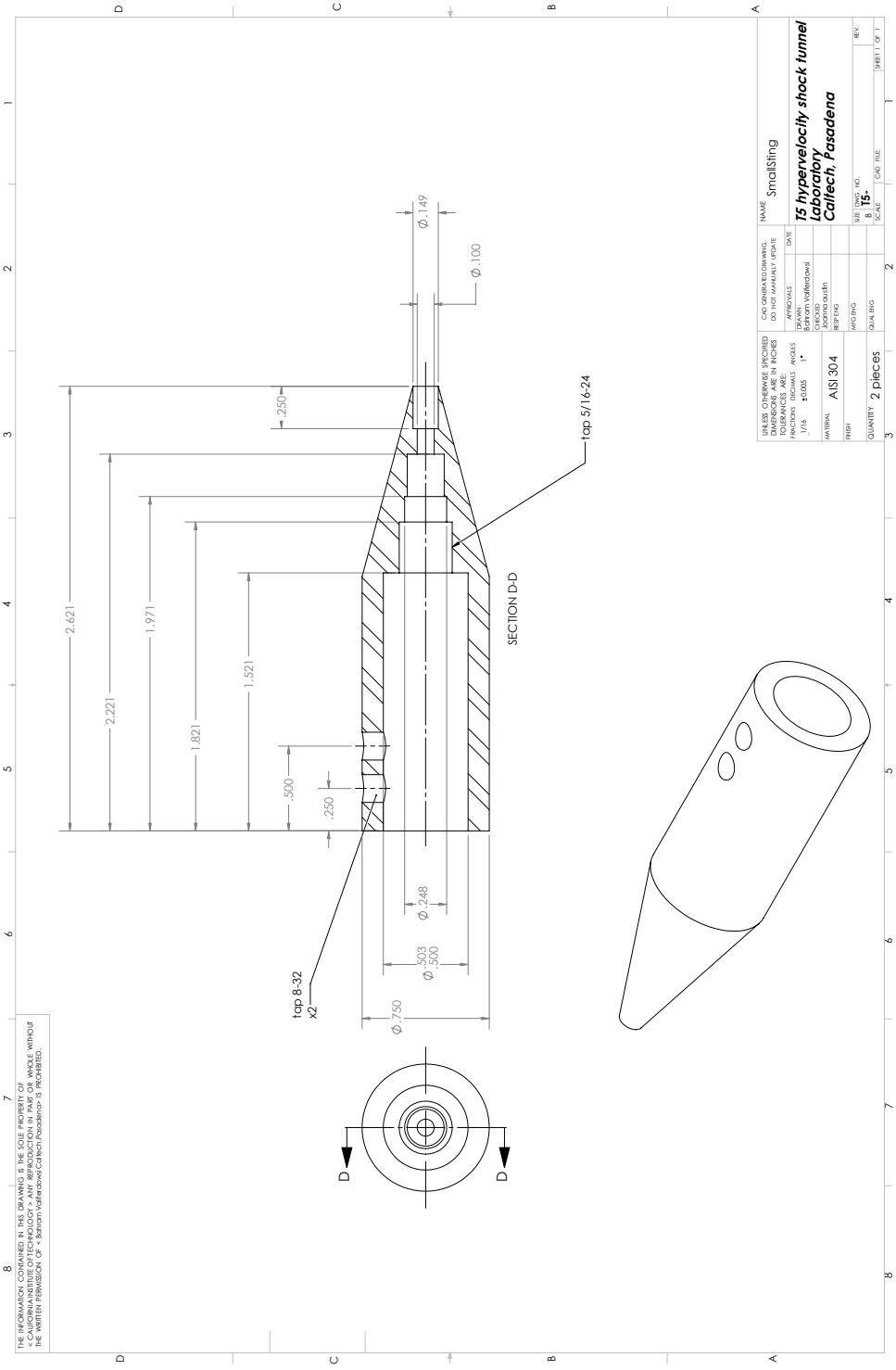

Figure E.7: Static Probe V2 Sting Adapter

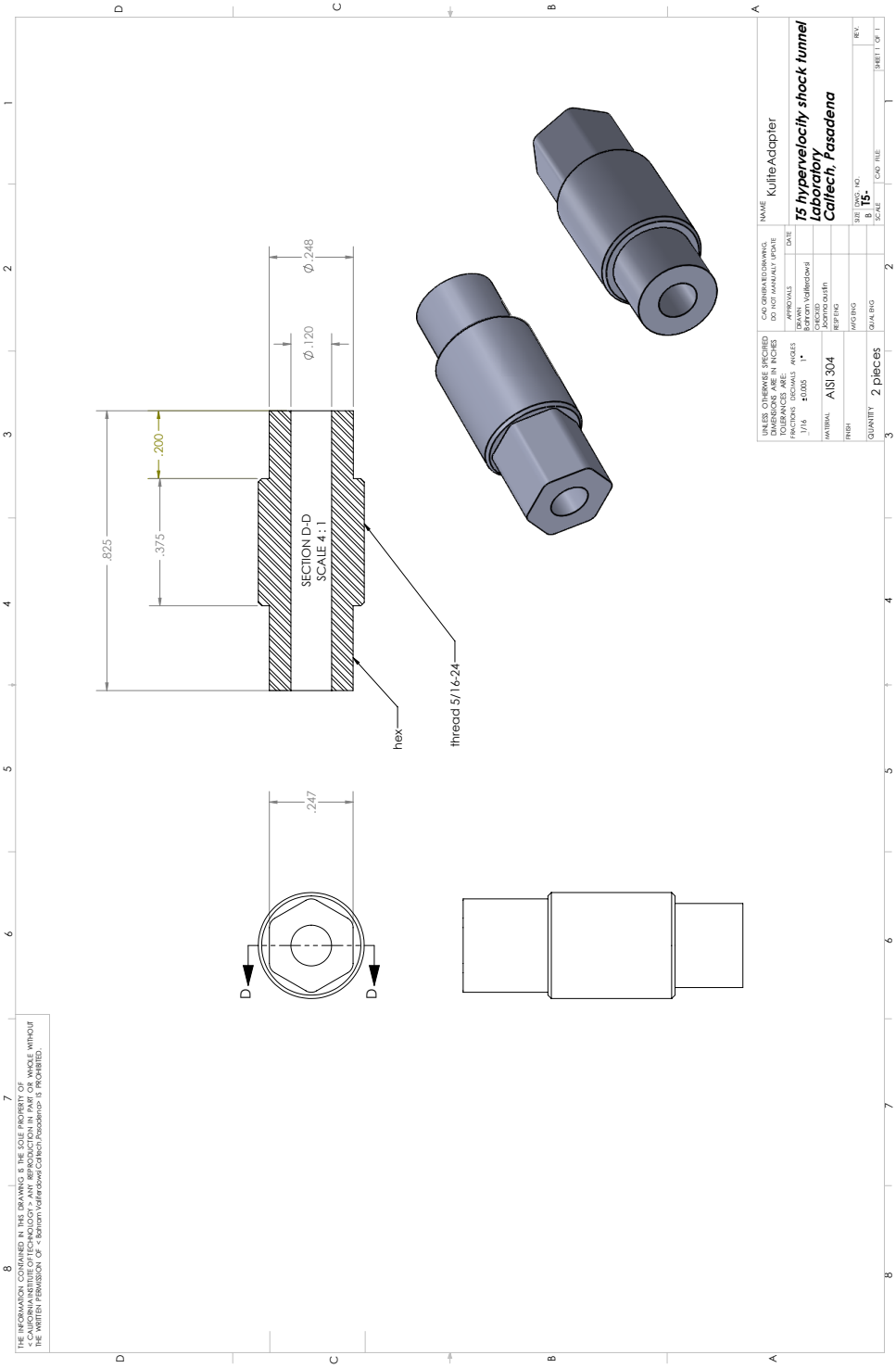

Figure E.8: Static Probe V2 Kulite Adapter

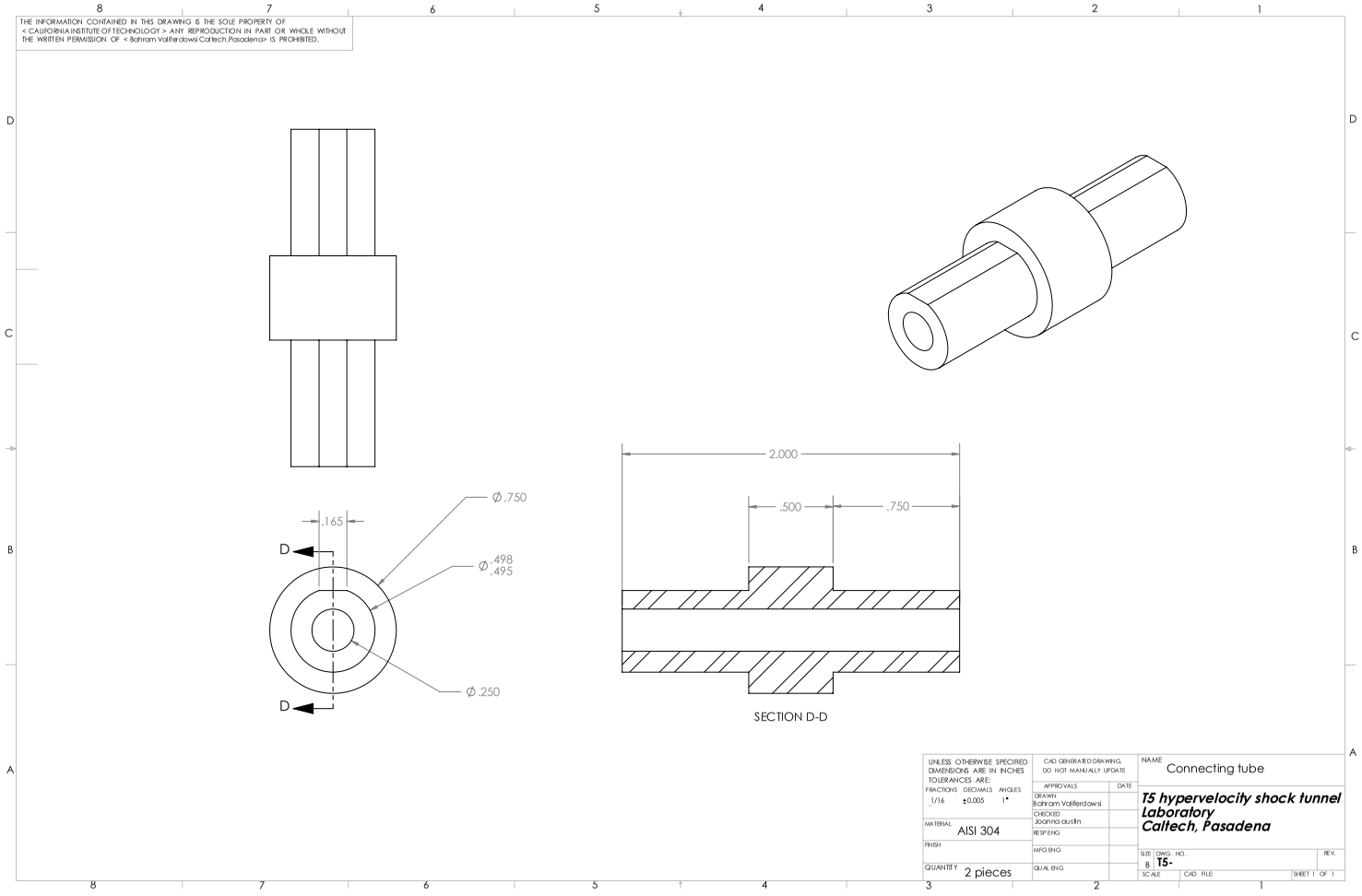

Figure E.9: Static Probe V2 Connection Tube

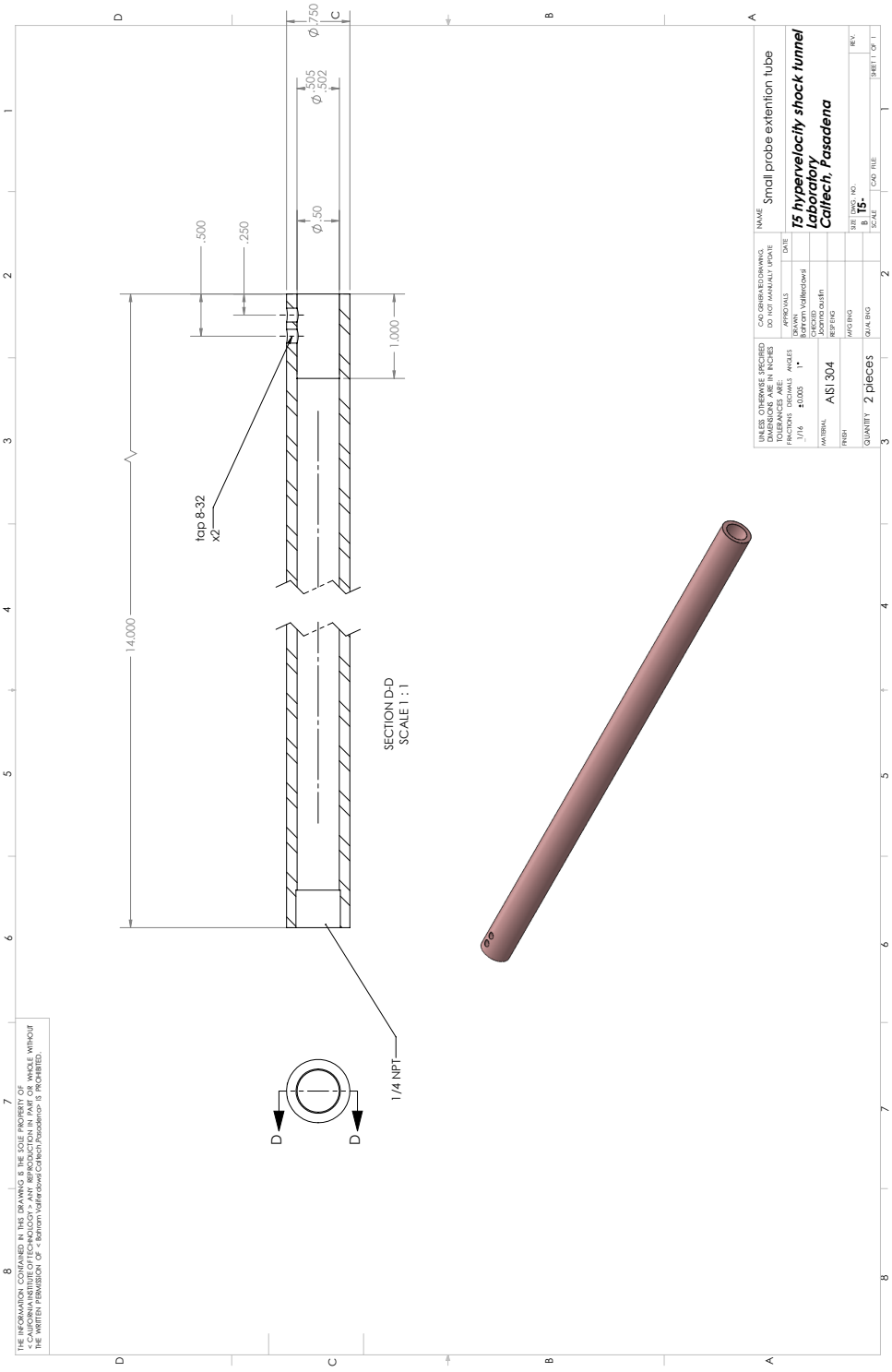

Figure E.10: Static Probe V2 Extension Tube

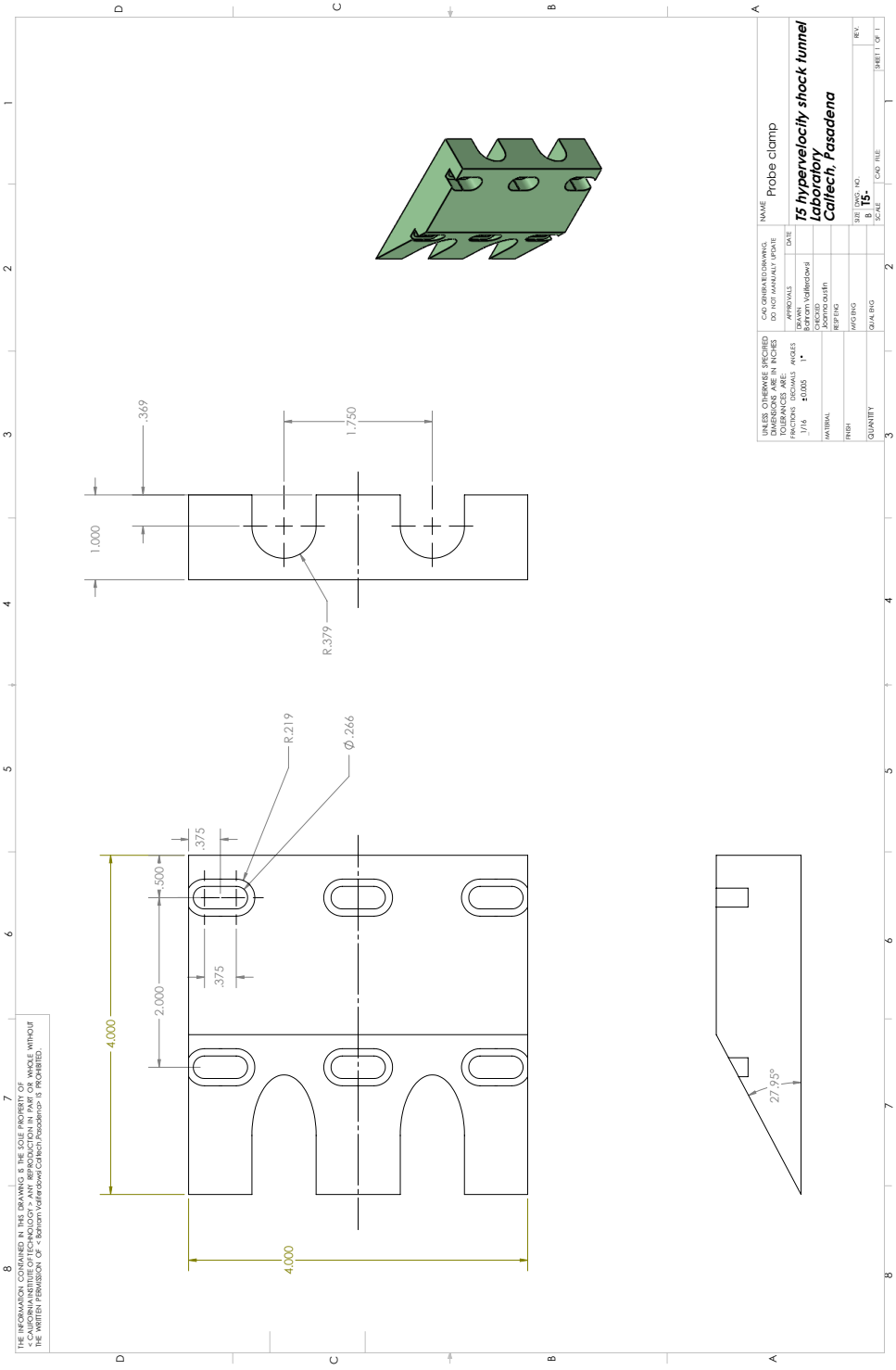

Figure E.11: Static Probe V2 Probe Clamp

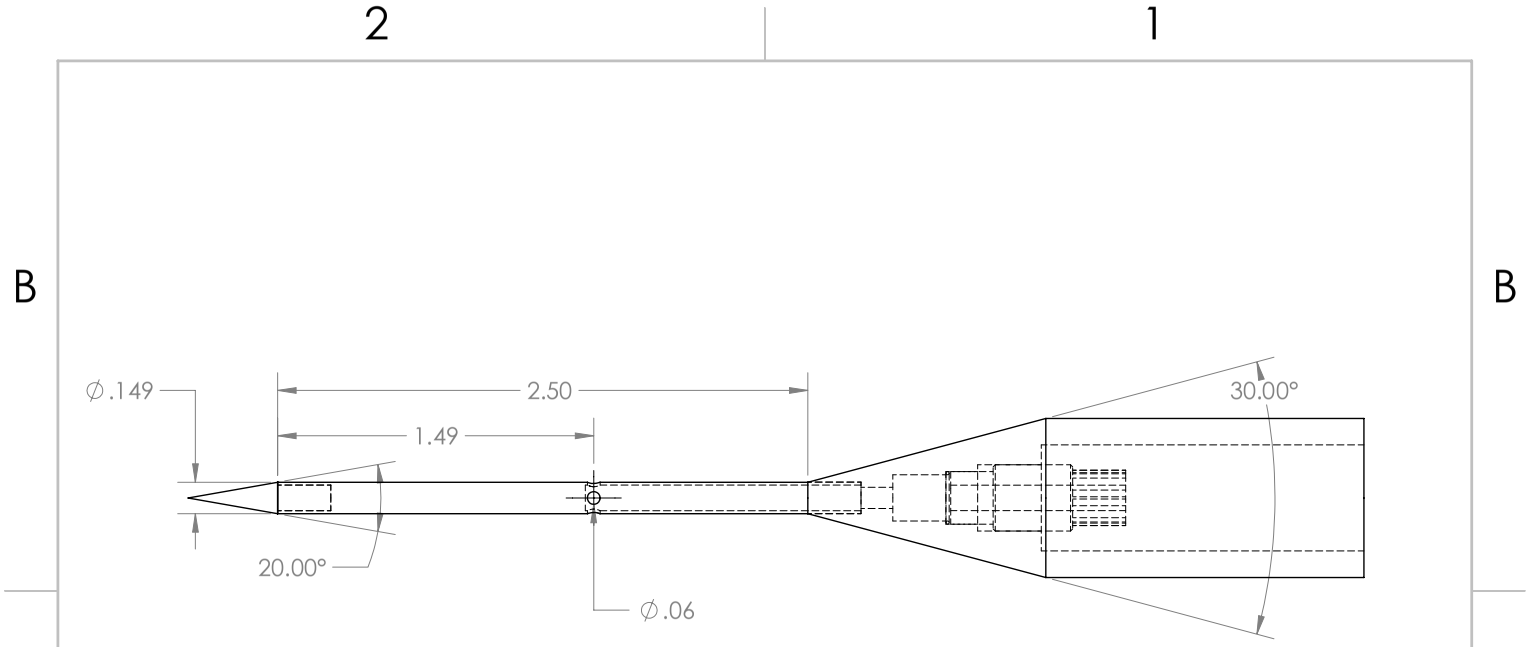

		UNLESS OTHERWISE SPECIFIED:		NAME	DATE
		DIMENSIONS ARE IN inches TOLERANCES: ±0.005 in FRACTIONAL ± ANGULAR: MACH ± BEND ± TWO PLACE DECIMAL ± THREE PLACE DECIMAL ±	DRAWN	Wesley Yu	4/2/20
			CHECKED		
			ENG APPR.		
			MFG APPR.		
		INTERPRET GEOMETRIC TOLERANCING PER:	Q.A.		
		MATERIAL Molybdenum	COMMENTS:		
NEXT ASSY	USED ON	FINISH			
APPLICATION		DO NOT SCALE DRAWING			

PROPRIETARY AND CONFIDENTIAL

THE INFORMATION CONTAINED IN THIS DRAWING IS THE SOLE PROPERTY OF <INSERT COMPANY NAME HERE>. ANY REPRODUCTION IN PART OR AS A WHOLE WITHOUT THE WRITTEN PERMISSION OF <INSERT COMPANY NAME HERE> IS PROHIBITED.

TITLE:

Small Static Probe Assembly

SIZE	DWG. NO.	REV
A		
SCALE: 1:2	WEIGHT:	SHEET 1 OF 1

Figure E.12: Static Probe V2 Assembly

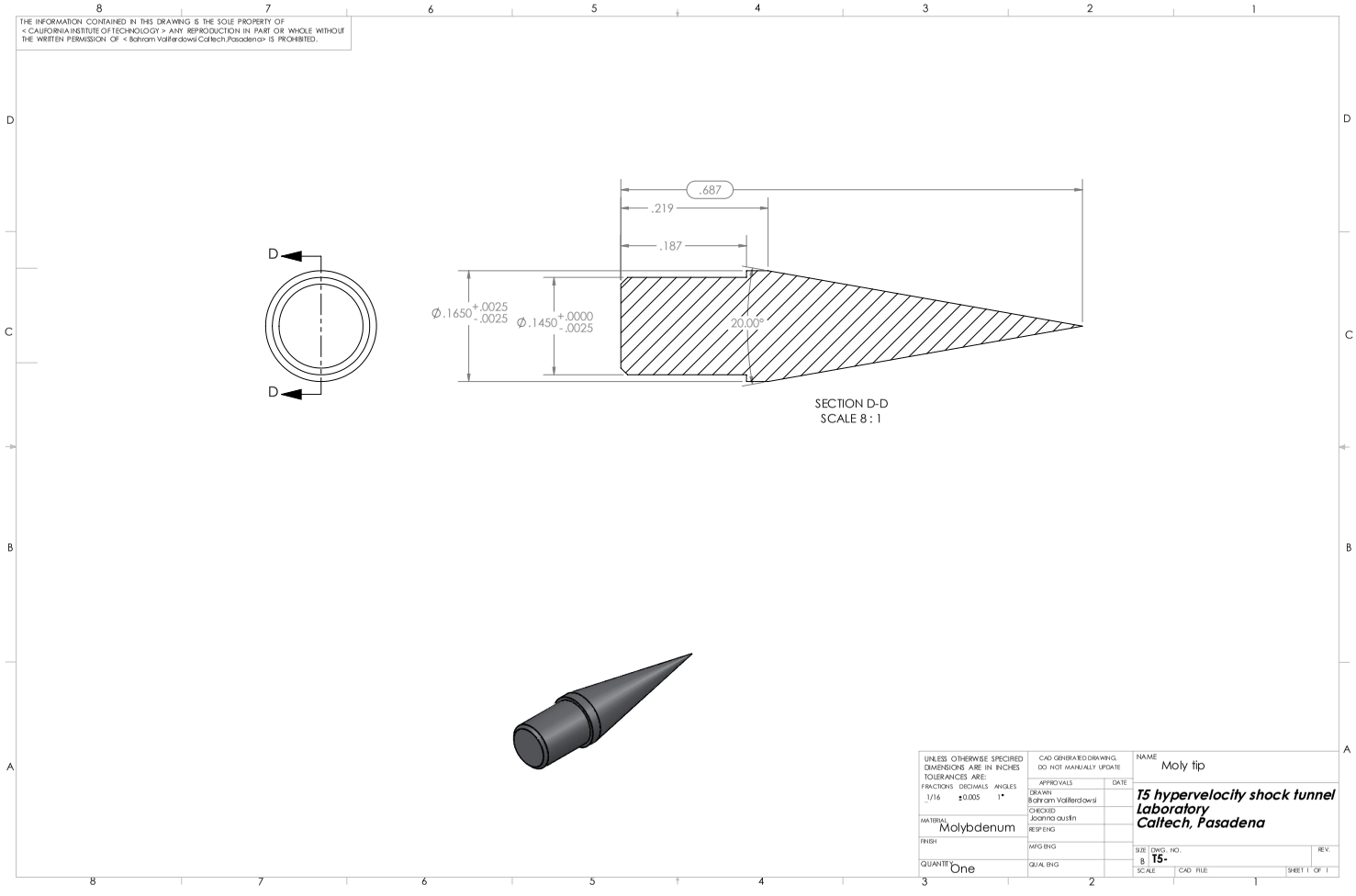

Figure E.13: Static Probe V3 Molybdenum Tip

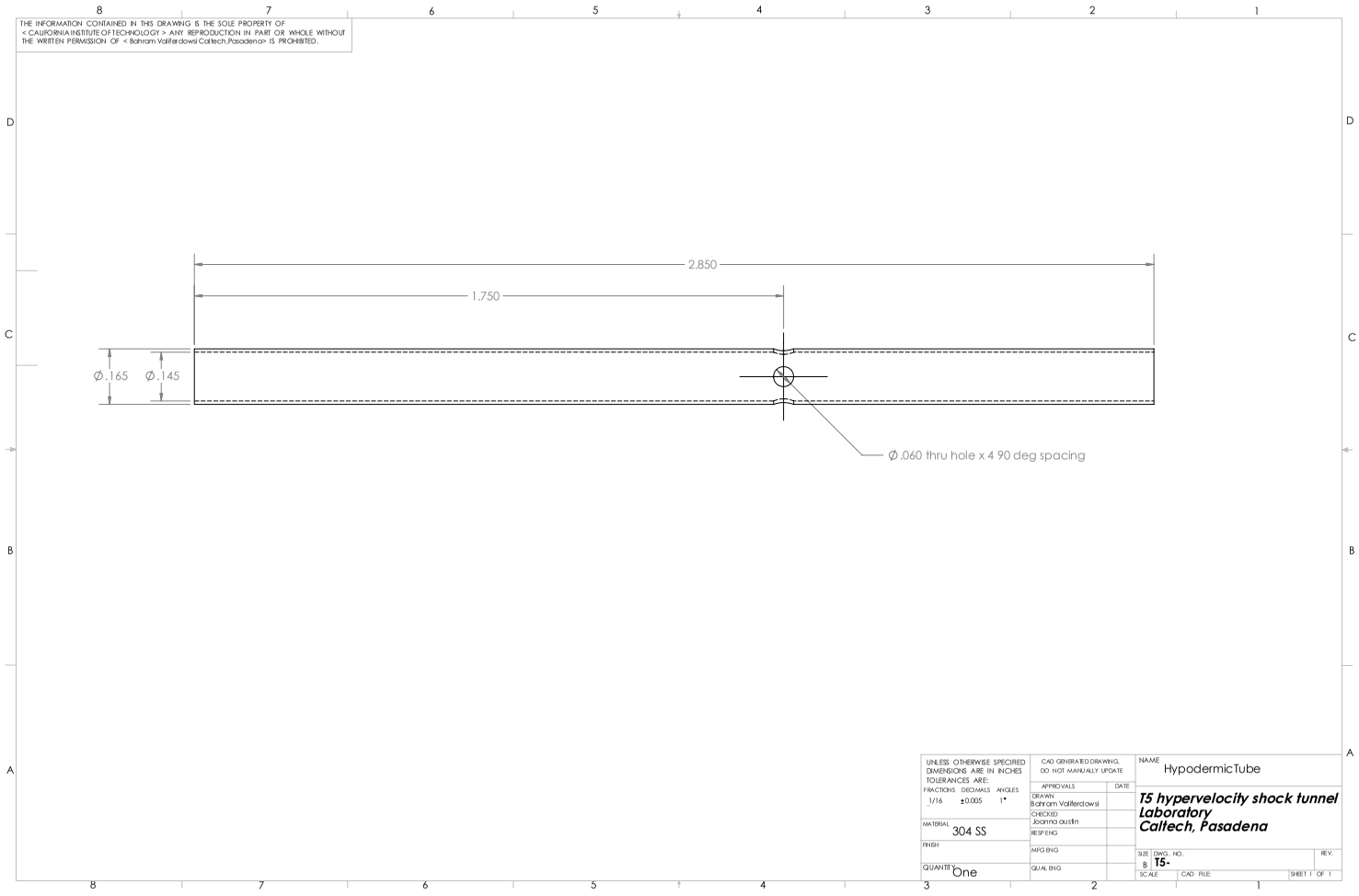

Figure E.14: Static Probe V3 Main Body

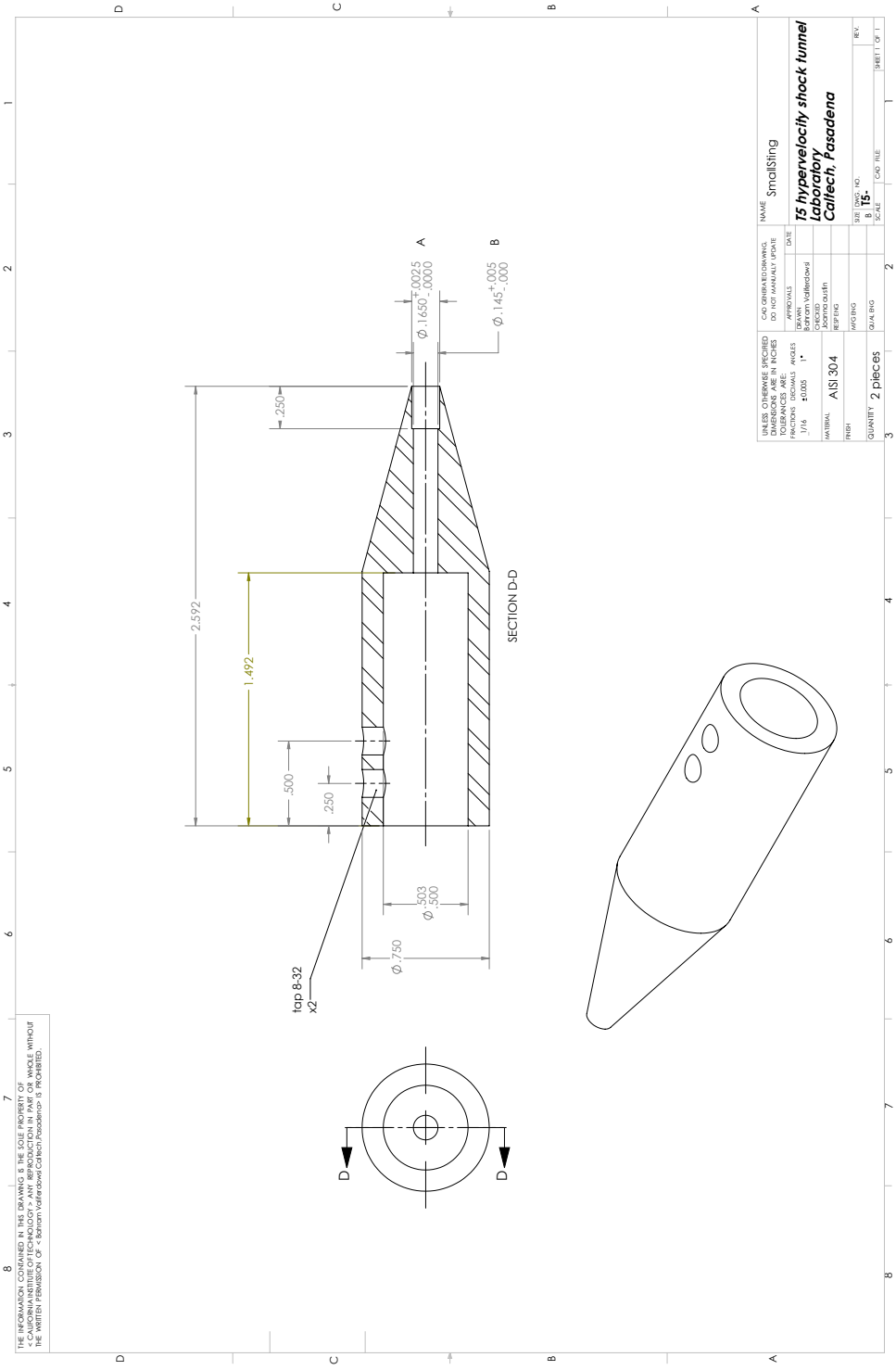

Figure E.15: Static Probe V3 Sting Adapter Modification

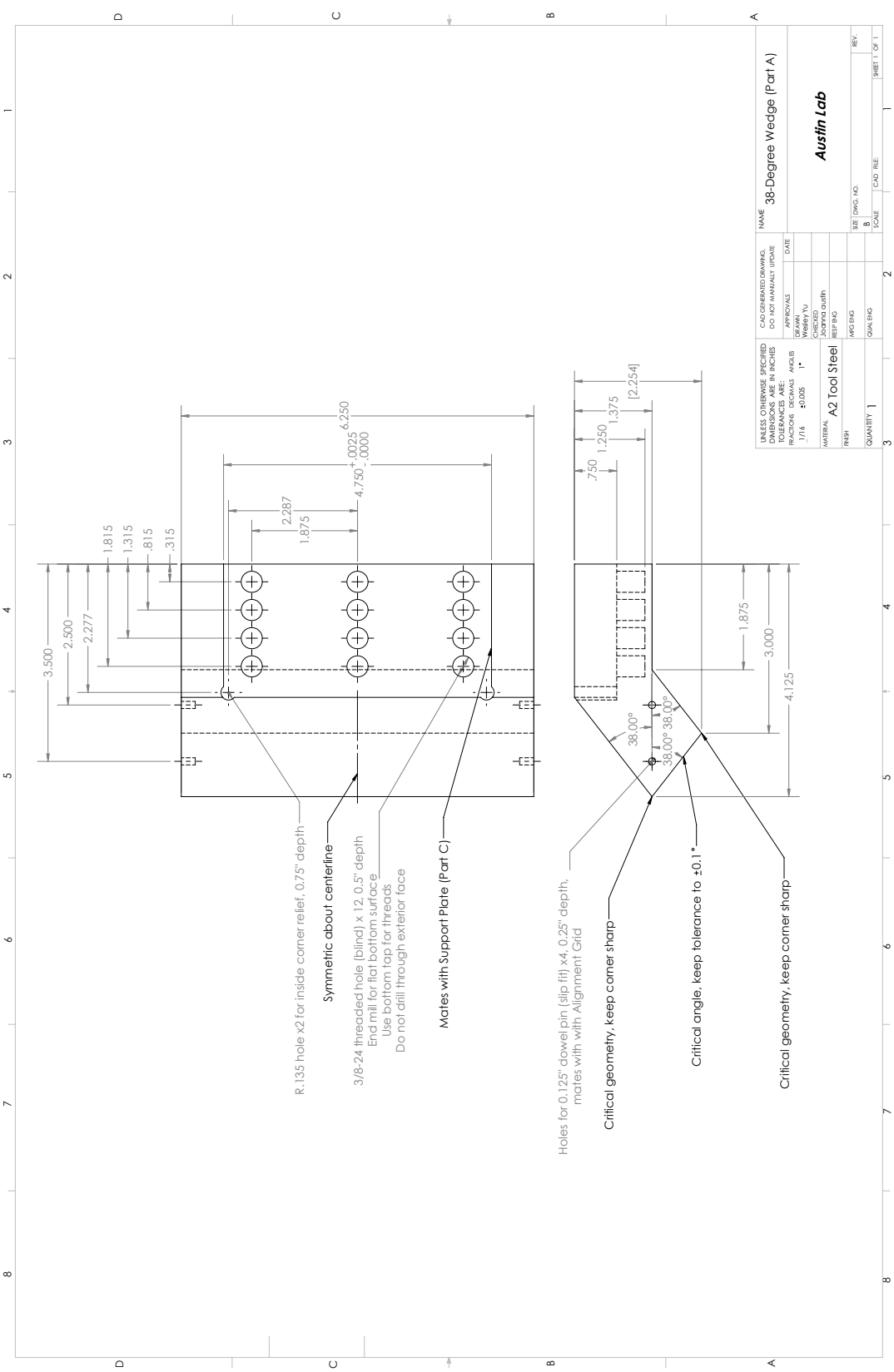

Figure E.16: 38-Degree Symmetric Wedge

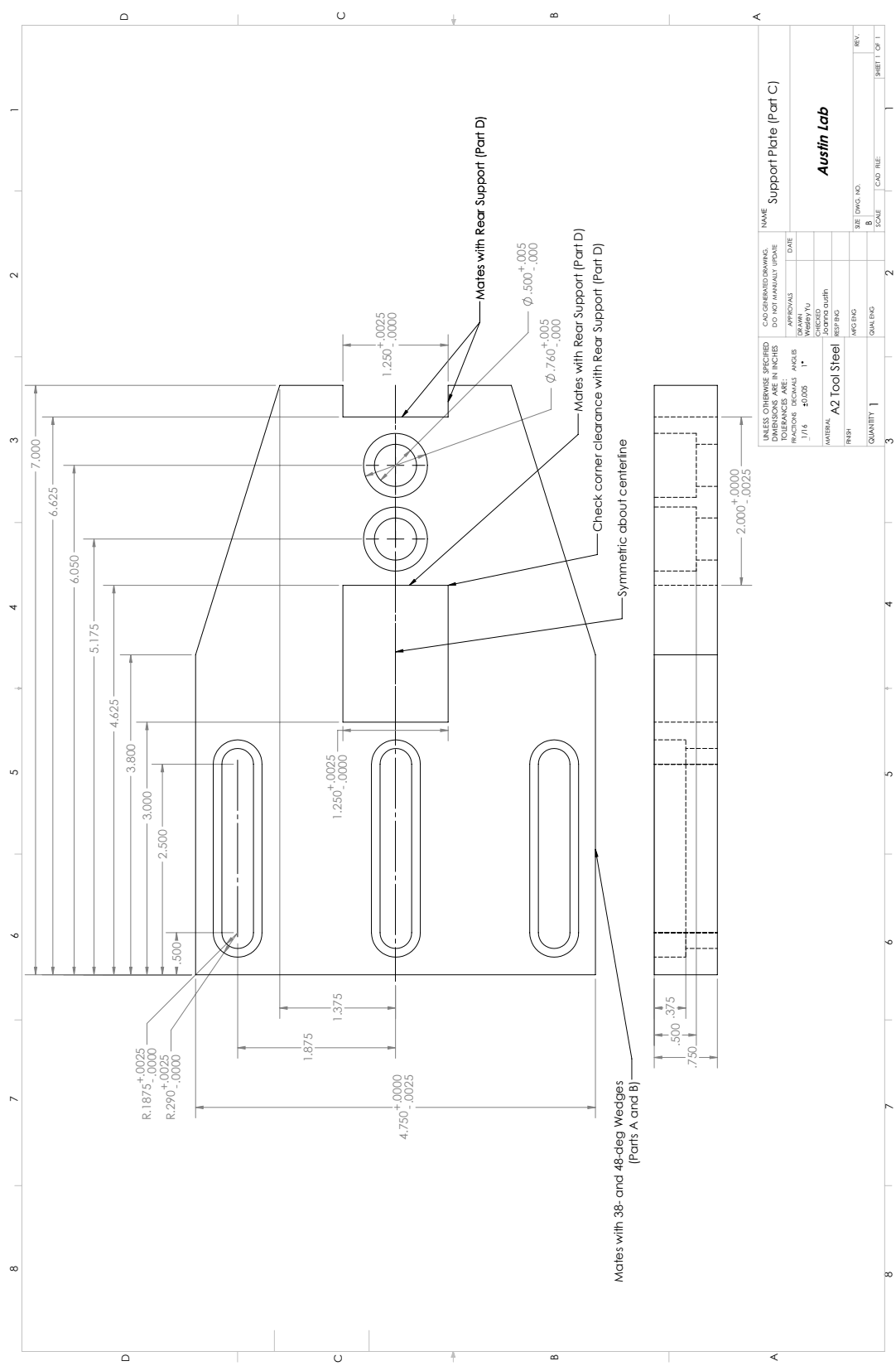

Figure E.17: Opposing-Wedge Support Plate

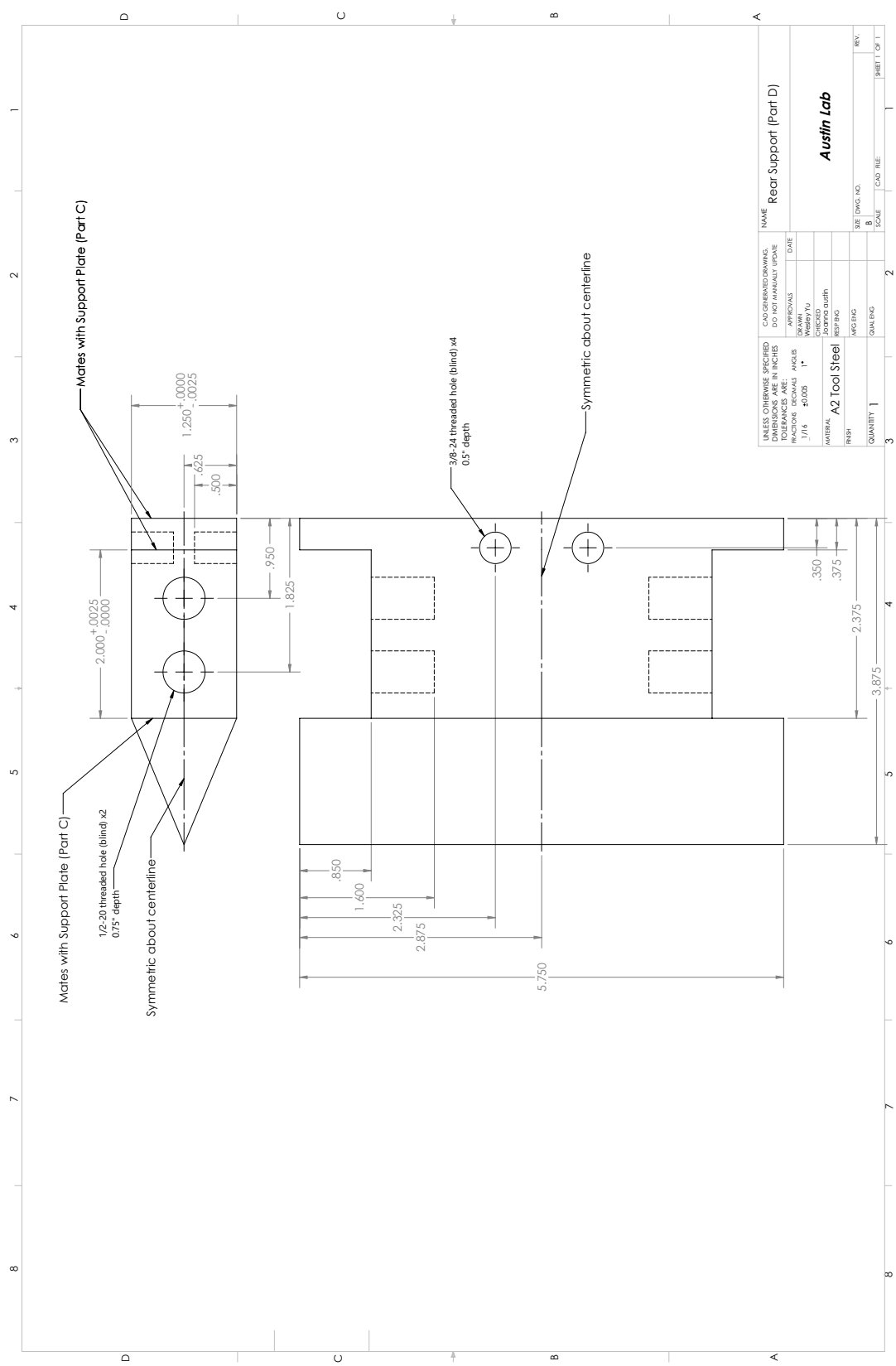

Figure E.18: Opposing-Wedge Rear Support

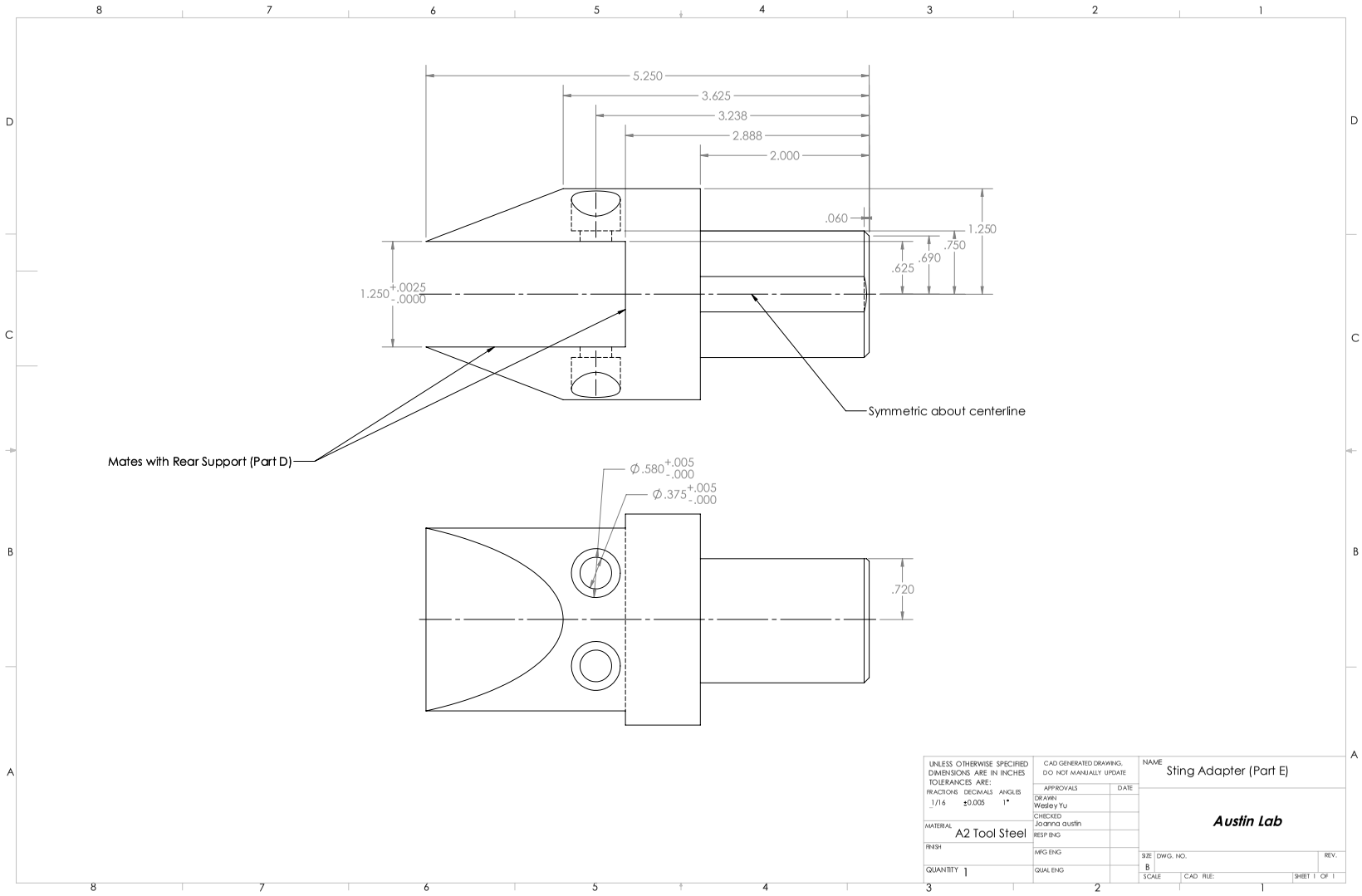

Figure E.19: Opposing-Wedge Sting Adapter